

# **The Design of High Entropy Ultra-high Temperature Ceramics for Oxidation Resistance**

---

A Dissertation

Presented to

the faculty of the School of Engineering and Applied Science

University of Virginia

---

in partial fulfillment  
of the requirements for the degree

Doctor of Philosophy

by

Lavina Backman

May 2020

# APPROVAL SHEET

This Dissertation  
is submitted in partial fulfillment of the requirements  
for the degree of  
Doctor of Philosophy

Author Signature: Lavinia Baltman

This Dissertation has been read and approved by the examining committee:

Advisor: Elizabeth Opila

Committee Member: Bi-Cheng Zhou

Committee Member: William Soffa

Committee Member: Patrick Hopkins

Committee Member: Mark Opeka, Ph. D.

Committee Member: \_\_\_\_\_

Accepted for the School of Engineering and Applied Science:



Craig H. Benson, School of Engineering and Applied Science

May 2020

## Acknowledgements

The work compiled in this dissertation would not be possible without many people. First and foremost, I would like to extend my deepest gratitude to my advisor, Dr. Elizabeth J. Opila, for fostering a learning culture, for teaching me how to ask the right questions, and for her patient guidance. I am grateful for her commitment to my growth as a researcher, scientist and communicator. Her encouragement and support both in and out of the lab were essential to any success to which I may lay claim.

This work is funded by the U.S. Office of Naval Research MURI, *The Science of Entropy-Stabilized Ultra-High Temperature Ceramics* (Grant no.: N00014-15-1-2863), under program manager, Dr. Eric Wuchina. This work is also partially funded by the Virginia Space Grant Consortium Graduate Research Fellowship Program. Further, I would like to acknowledge Tyler Harrington, Dr. Kenneth Vecchio, Joshua Gild and Dr. Jian Luo from the University of California San Diego (UCSD) for providing the high entropy carbides and boride materials used in this study. All synthesis and a bulk of the characterization of the base materials were completed at UCSD. I would also like to thank the rest of the MURI team for their work, expertise and discussions which have informed so much of the direction of this work: Dr. Don Brenner, Sam Daigle and Mina Lim at North Carolina State University; Dr. Stefano Curtarolo, Dr. Cormac Toher, Dr. Corey Oses, and Pranab Sarkar at Duke University; Dr. Patrick Hopkins, and Dr. Jeff Braun at the University of Virginia. I'd especially like to thank Dr. Tina Rost for her excellent training on X-ray diffraction and for the many, many helpful discussions.

I'd like to thank Dr. Mark Weaver, Dr. Greg Thompson and Brett Hunter at the University of Alabama for graciously providing their expertise, time and efforts in conducting transmission electron microscopy (TEM) energy dispersive spectroscopy (EDS) work when needed. The finite element analysis simulation models for the resistive heating system were created by Dr. Michael Dion and colleagues at Materials Research & Design, Inc. I am grateful for their guidance and

help in understanding the methodology and interpreting the data. I would also like to acknowledge insight and guidance provided by Dr. Bill Fahrenholtz, and from the committee members, Dr. Bill Soffa, Dr. Bi-Cheng Zhou, Dr. Patrick Hopkins and Dr. Mark Opeka.

Barry Baber, Ig Jakovac, Jeannie Reese, Kari Werres, Tonya Reynolds, Bryana Amador and Sherri Sullivan provided indispensable assistance with respect to the logistical aspects of conducting research, and I am grateful for their help. I would like to especially thank Tanner Fitzgerald, who helped provide several improvements to my experimental set-up and helped me find creative solutions to many lab-equipment related hiccups. I'd also like to acknowledge and thank Kim Fitzhugh-Higgins as a tremendous source of support. Further, the guidance and insight from the Nanoscale Materials Characterization Facility (NMCF) at UVA was essential to this work. I'd like to thank Helge Heinrich, in particular, for his help with conducting TEM and focused ion beam milling work.

I am also grateful to the Opila research group members, past and present, for the excellent guidance, insightful scientific discussions and friendship, all of which made for a wonderful five years. I'd like to acknowledge Niquana Smith for her help in conducting some of the resistive heating oxidation experiments on  $ZrB_2$ , Dom Pinnissi and Kendall Mueller for their help with labwork, and Maddy Morales and Rachel McNamara for her help with imaging.

Finally, I would like to thank my family and friends. I am incredibly thankful for my husband, Eric, who supported me through these intense five years in every way and made this achievement possible. My mother-in-law, parents, and Terri and John Heib reminded me what I was capable of when I floundered. I would also like to thank Christy, who went above and beyond to help life happen while I was writing this dissertation.

## Abstract

Ultra-high temperature ceramics (UHTCs), most notably transition metal carbides and borides, exhibit melting temperatures exceeding 3000 °C, making them appropriate candidates to withstand the extreme temperatures (~2000 °C) expected to occur at the leading edges of hypersonic vehicles. However, their propensity to react rapidly with oxygen limits their sustained application. Oxidation resistant materials require formation of dense, adherent and solid oxides that provide an effective barrier, slowing the diffusion of oxygen and/or metal atoms to the reaction interface under ultra-high temperature conditions. The work completed was part of a collaborative effort to identify new UHTCs with the potential for improved properties based on entropic stabilization of the base material. The goals of this work were to determine the parameters influencing the oxidation behavior of group IV, V and VI transition metal HE-UHTCs at ultra-high temperatures. Candidate compositions for oxidation studies were identified based on initial thermodynamic assessments to be HfZrTiTaNb, HfZrTiTaMo and HfZrTiMoW carbides and diborides. The bulk of the analytical and experimental studies were performed on HfZrTiTaNb carbide and diboride.

Thermodynamic calculations using FactSage software and databases were performed for oxidation reactions of the constituents in equimolar, five-component carbide and diboride ceramics in the group IV, V and VI elemental palette. Periodic trends in oxide stability and phase were observed. The relative stability of the oxide phases formed from the constituent carbides and from binary carbide solutions were used to investigate preferential oxidation. This analysis was extended to ternary and higher order alloys and carbides. The thermodynamic models thus developed were compared to the experimentally determined oxidation behavior of the five-component HfZrTiTaNb carbide and diboride. Experimental results verified that the thermodynamically favorable group IV oxides dominated in the observed oxide scale. It was concluded that, given any high entropy material, even a slight relative favorability for a given

oxide formation reaction will result in preferential oxidation, reducing the configurational entropy in the underlying substrate material.

Specimen thermal gradients generated during oxidation in a unique resistive heating system (RHS) capable of achieving ultra-high temperatures ( $>1700^{\circ}\text{C}$ ) were evaluated using finite element analysis models. Thermal gradients on the order of the uncertainty in temperature measurements were calculated, confirming the RHS suitability for conducting ultra-high temperature oxidation exposures on HE-UHTCs. The oxidation kinetics of the high entropy group IV+V (HfZrTiTaNb)C and (HfZrTiTaNb) $\text{B}_2$  materials were extensively evaluated at  $1500^{\circ}\text{C}$ - $1800^{\circ}\text{C}$  using the RHS in one atmosphere 0.1%-1% oxygen/argon gas mixtures for times up to 15 minutes. Possible mechanisms based on the resulting time, temperature and oxygen partial pressure dependence underscored the complex oxidation behavior of these materials. The carbides formed porous and intergranular oxides. Oxidation resistance was improved upon external scale formation. The diborides formed dense external scales and exhibited better oxidation resistance compared to the carbides. This improvement was attributed to the formation of liquid boria. Both compositions showed an unexpected reduction in material consumption at  $1800^{\circ}\text{C}$  for all times tested, compared to the lower temperatures tested. An in-depth analysis of the composition and morphology of the oxide scale and sub-surface regions for specimens tested at  $1800^{\circ}\text{C}$  revealed that the formation of denser group IV-rich (Hf, Zr, Ti) oxides mitigated the formation of the otherwise detrimental liquid-forming group V (Ta, Nb) oxides, leading to the improved oxidation resistance.

Group IV+V+VI (HfZrTiTaMo) and group IV+VI (HfZrTiMoW) carbides and borides, were exposed at  $1700^{\circ}\text{C}$  in 1% $\text{O}_2$  for five minutes, conditions at which group IV+V HfZrTiTaNb compositions exhibited the poorest oxidation resistance. Oxidation behavior of the high entropy compositions were also compared to the baseline ZrC and Zr $\text{B}_2$  ceramics. All compositions exhibited preferential oxidation of the group IV elements. Group V (Ta) element-containing

carbides were found to exhibit the lowest oxidation resistance, which was attributed to the tendency to form intergranular and liquid oxides, while (HfZrTiTaMo)C performed comparably with ZrC. All the diboride compositions exhibited similar material consumption, reinforcing the hypothesis that the oxidation behavior under these conditions is at least partly attributable to liquid boria acting as an oxidant diffusion barrier.

The findings in this study demonstrate that the oxidation behavior of HE-UHTCs can be understood primarily with thermodynamic principles, with minimal application of kinetic considerations. Further, they show that the oxidation behavior of HE carbides are compositionally driven, with the most promising composition being (HfZrTiMoW)C. Therefore, the thermodynamic models developed in this work can be used to tailor the design of a carbide HE-UHTC composition for oxidation resistance. Under the conditions explored in this study, the boride HE-UHTCs exhibited better oxidation resistance. Further studies are recommended at temperatures above the boiling point of boria ( $>1860^{\circ}\text{C}$ ) to probe the oxidation behavior of boride HE-UHTCs without the influence of boria acting as a diffusion barrier.

# Table of Contents

|   |           |
|---|-----------|
| <b>1. Introduction .....</b>  | <b>1</b>  |
| <b>1.1. Ultra-high temperature ceramics for hypersonic vehicle applications.....</b>            | <b>1</b>  |
| <b>1.2. High entropy UHTCs .....</b>  | <b>2</b>  |
| 1.2.1. The four core effects in high entropy ceramics.....                                      | 4         |
| <b>2. Thermodynamic Considerations in High Entropy Materials .....</b>                          | <b>8</b>  |
| <b>2.1. Background and motivation.....</b>  | <b>8</b>  |
| <b>2.2. Thermodynamic stabilities of constituent oxide products .....</b>                       | <b>9</b>  |
| 2.2.1. Methodology.....   | 9         |
| 2.2.2. Results.....   | 11        |
| 2.2.3. Discussion .....   | 16        |
| <b>2.3. Thermodynamic Predictions of Preferential Oxidation in High Entropy Materials .....</b> | <b>24</b> |
| 2.3.1. Background and introduction.....   | 24        |
| 2.3.2. Methodology.....   | 27        |
| 2.3.3. Results.....   | 34        |
| 2.3.4. Discussion .....   | 44        |
| <b>2.4. Experimental Verification of Preferential Oxidation Predictions .....</b>               | <b>47</b> |
| 2.4.1. Methodology.....   | 47        |
| 2.4.2. Results.....   | 48        |
| 2.4.3. Discussion .....   | 55        |
| <b>2.5. Conclusions.....</b>  | <b>58</b> |
| <b>3. Oxidation Kinetics of (HfZrTiTaNb)C and (HfZrTiTaNb)B<sub>2</sub>.....</b>                | <b>60</b> |
| <b>3.1. Introduction.....</b>   | <b>60</b> |

|  |            |
|--|------------|
| <b>3.2. Methodology.....</b>   | <b>64</b>  |
| 3.2.1. Experimental set-up.....  | 64         |
| <b>3.3. Results .....</b>  | <b>69</b>  |
| 3.3.1. Temperature control .....   | 69         |
| 3.3.2. Sample variation .....  | 70         |
| 3.3.3. Kinetics.....   | 78         |
| 3.3.4. Microstructure and Oxide Composition .....  | 85         |
| <b>3.4. Discussion.....</b>  | <b>102</b> |
| 3.4.1. Oxide/substrate compositional and microstructural changes.....  | 102        |
| 3.4.2. Destabilization of the solid solution in high entropy carbides and borides due to preferential oxidation..... | 105        |
| 3.4.3. Possible rate controlling mechanisms.....   | 109        |
| <b>3.5. Conclusions.....</b>   | <b>114</b> |
| <b>3.6. Future Work .....</b>  | <b>115</b> |
| <b>4. Comparison of Oxidation Resistance of (HfZrTiTaNb) Carbide and Diboride to Other UHTC Compositions.....</b>    | <b>117</b> |
| <b>4.1. Introduction.....</b>  | <b>117</b> |
| <b>4.2. Methodology.....</b>   | <b>120</b> |
| <b>4.3. Results .....</b>  | <b>121</b> |
| 4.3.1. Starting materials (high entropy compositions).....   | 121        |
| 4.3.2. Oxidation Results .....   | 126        |
| <b>4.4. Discussion.....</b>  | <b>149</b> |
| 4.4.1. Carbides.....   | 149        |
| 4.4.2. Diborides.....  | 151        |

|        |  |            |
|--------|--|------------|
| 4.4.3. | Design of oxidation-resistant HE-UHTCs .....   | 153        |
| 4.5.   | Conclusions.....   | 155        |
| 4.6.   | Recommendations for future work .....  | 156        |
| 5.     | <i>Analysis of Test Specimen Temperature Gradients in the Resistive Heating System .....</i>                                 | <i>158</i> |
| 5.1.   | Introduction.....  | 158        |
| 5.2.   | Resistive heating system .....   | 160        |
| 5.3.   | Estimated temperature gradient through oxide thickness .....   | 167        |
| 5.4.   | Thermal electric model of RHS specimen temperature gradients.....  | 168        |
| 5.4.1. | Modeling work .....  | 169        |
| 5.5.   | Results .....  | 174        |
| 5.6.   | Discussion.....  | 181        |
| 5.7.   | Conclusions.....   | 183        |
| 6.     | <i>References .....</i>  | <i>184</i> |
|        | <i>Appendix A: Volatility of Ta oxides.....</i>  | <i>203</i> |
|        | <i>Appendix B: Pyrometer Data for Resistive Heating System Experiments .....</i>   | <i>204</i> |
|        | <i>Appendix C: Detailed Experimental Results from Oxidation Studies on (HfZrTiTaNb)C and (HfZrTiTaNb)B<sub>2</sub> .....</i> | <i>207</i> |

# 1. Introduction

## 1.1. Ultra-high temperature ceramics for hypersonic vehicle applications

There is a need for ultra-high temperature materials for use in applications such as engine cowl inlets<sup>1</sup>, wing leading edges and nose tips on hypersonic vehicles, and propulsion systems<sup>2</sup>. In particular, any advancement in hypersonic flight technology requires sharp wing leading edges, defined as having a radius much smaller than the length scale of the feature, in order to improve maneuverability, performance and safety<sup>3</sup>. During hypersonic flight, convective heating of the surface increases as the radius decreases, bringing the surface of the stagnation region to temperatures in excess of 2000 °C<sup>3,4</sup>.

Leading candidates for ultra-high temperature ceramics (UHTCs) are the carbides and borides of group IV, V and VI transition metal elements. UHTCs exhibit melting temperatures exceeding 3000 °C, making them appropriate candidates to withstand the extreme temperatures experienced by some areas of the craft during hypersonic flight (Figure 1.1). However, the propensity for UHTCs to react rapidly with oxygen limits their sustained application in reusable vehicles. Researchers have attempted to address this limitation through improvements in processing monolithic UHTCs and by exploring composite design<sup>5-7</sup>. Many UHTC systems incorporate SiC to promote the formation of a silica layer, however, pure silica melts at ~1723 °C. The addition of SiC as a secondary phase to boride UHTCs, such as ZrB<sub>2</sub> for example, improves oxidation resistance in diborides up to 1600 °C in oxidation experiments<sup>1,2,4</sup>; however, this resistance is due to the formation of a borosilicate glass layer, which can be liquid even at temperatures less than 1000 °C. Thus, relying on the formation of silica or borosilicate glass is not a viable strategy for promoting oxidation resistance above 2000 °C, as these liquid oxides will shear off during hypersonic flight. Without SiO<sub>2</sub>, the oxidation of hafnium and zirconium diborides is mainly limited by diffusion through boron below about 1800 °C<sup>8</sup>. The oxidation of hafnium and zirconium carbides results in a non-protective,

porous oxide below 1800°C. Above 1800°C, oxidation behavior improves as the oxides start to sinter. The formation of an oxycarbide layer, which may slow oxygen diffusion to the reaction front, has been reported in HfC at temperatures below 900°C<sup>2,9,10</sup>.

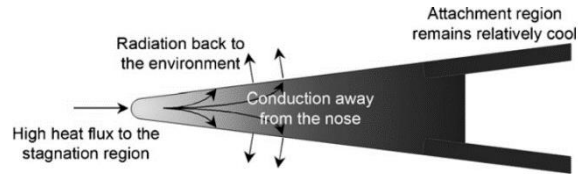


*Figure 1.1: Schematic of an ultra-high temperature ceramic wing leading edge concept and the expected temperature distribution. Figure from Squire et al.<sup>3</sup>*

## 1.2. High entropy UHTCs

Traditional materials engineering for UHTCs relies on the enthalpic contribution to the free energy of the material to achieve stability at high temperatures; UHTCs are characterized by strong covalent bonds and high melting temperatures, for instance. An alternative and promising approach, which was initially demonstrated with metal alloys<sup>11</sup>, explores the effect of entropy in phase stabilization, but this approach is still in its infancy. High entropy alloys (HEAs) have been defined as alloys with four or more components in concentrations of 5-35 at% in solid solution, or a minimum additional configurational entropy of  $S_{config} = 1.5R$ <sup>12</sup>.

Configurational entropy is maximized as the number of components is increased in equimolar amounts (Figure 1.2).

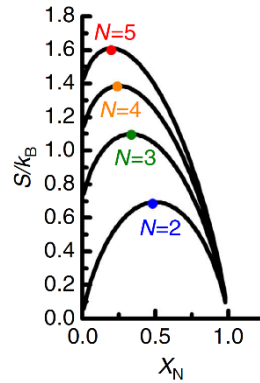


Figure 1.2: The effect of composition and number of components on the configurational entropy in a material. Figure from Rost et al.<sup>13</sup>

This approach has subsequently been applied to oxides<sup>13</sup>, and carbide<sup>14</sup> and boride<sup>15</sup> UHTCs.

In metallic alloys, assuming the ideal case, each site in the lattice is randomly occupied. In

ionic and covalent compounds, only the metal sub-lattice is disordered as shown in Figure 1.3.

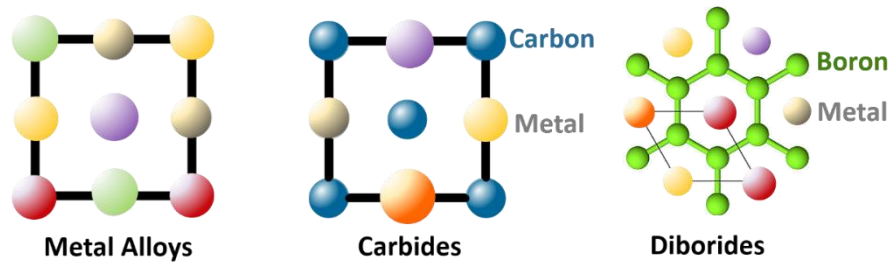


Figure 1.3: Crystal plans showing the differences between a high entropy alloy and high entropy carbide and boride materials. The multi-colored spheres are metal atom species, the blue spheres are carbon atoms and the bright green spheres are boron atoms. In carbide and borides, there is a non-metal sub-lattice and a disordered metal sub-lattice. Graphics adapted from Alling et al.<sup>16</sup>

High entropy materials are hypothesized to manifest the following effects: (a) the high entropy effect, in which a high configurational entropy stabilizes the solid solution over the formation of competing phases; (b) the lattice distortion effect, which arises from the disparate

atom sizes in solid solution and can affect material properties such as hardness; (c) the sluggish diffusion effect, which is thought to be a result of the complex chemical landscape and lattice distortion; and (d) the cocktail effect, which is a term used to describe the properties of the HEA arising from the interactions of multiple elements being mixed together<sup>11</sup>. The following sections discuss these effects in terms of high entropy UHTCs (HE-UHTCs).

### 1.2.1. The four core effects in high entropy ceramics

#### *The high entropy effect*

The high entropy effect in metallic alloys has been critically reviewed<sup>17,18</sup>. Existing HEAs deviate from ideality significantly and demonstrate short-range ordering, clustering or phase separation that reduces the overall configurational entropy of the system. Rost et al.<sup>13</sup> have proposed that short range ordering is mitigated in high entropy ceramics due to the presence of the non-metal sub-lattice, e.g., the oxygen sub-lattice in a rock-salt entropy-stabilized oxide. The oxygen atoms act as "shields" for the metal atoms, rendering each metal lattice site equivalent to a first nearest neighbor approximation, unlike in a high entropy alloy. Similar sub-lattices exist in the carbides and borides as shown in Figure 1.3. The contribution of configurational entropy to the free energy of the base material scales with temperature. Thus, the study of high entropy UHTCs provides an opportunity to gain new insight into the role of configurational entropy on the base material stability, particularly at high temperatures.

#### *The lattice distortion effect*

There is significant evidence in the HEA literature showing the improvement in mechanical properties such as hardness in HEAs compared to conventional alloys, summarized by Zhang et al.<sup>19</sup>. These improvements have been attributed to strain in the lattice

due to lattice distortion. Similar improvements have been shown for HE-UHTCs. (HfZrTaNb)C fabricated and tested by Castle et al.<sup>14</sup> and high entropy diborides fabricated and tested by Gild et al.<sup>15</sup> exhibited higher hardness and elastic modulus when compared to the monocarbides or monodiborides, as well as when compared to the value that would be expected from rule of mixtures. The distorted lattice is also proposed to result in sluggish diffusion in HEAs. Evidence for lattice distortion has been little studied for HEAs<sup>17</sup>, but has been measured by Rost et al.<sup>20</sup> in oxides with the rock-salt structure.

### *The sluggish diffusion effect*

Oxygen solubility in the diborides and carbides have been reported<sup>1,10</sup>. In UHTCs, which are highly covalent materials, oxidation proceeds via oxygen diffusion into the UHTC lattice. While the sluggish diffusion effect is one that has perhaps the least consensus in the HEA literature, it is also an effect that could result in improvement in oxidation resistance: sluggish diffusion kinetics could mean slower transport of reactants to the reaction front. Review of the literature on sluggish diffusion was recently conducted by Miracle<sup>12,17</sup>, and he concluded that expected diffusion rates did slow, but only if one considered the reduced melting temperature of high entropy materials. He also surveyed self-diffusion in elements and alloys having the face-centered cubic (FCC) lattice and found that diffusion in FCC HEAs is faster than in some non-HEA compositions such as Cu-Pt alloys<sup>17</sup>. Other observations including many instances of rapid precipitation of secondary phases in HEAs, even upon rapid cooling from high temperatures<sup>18</sup>, contradict the sluggish diffusion hypothesis. A computational study<sup>21</sup> explored the sluggish diffusion hypothesis from the standpoint of the chemical potential landscape and driving forces. It was concluded that the cross-diffusion terms could not be ignored, and that a pseudo-binary diffusion study was at best an approximation of the resulting diffusion kinetics.

One of the proposed mechanisms for sluggish diffusion is lattice distortion, discussed above. The other proposed mechanism is a trapping effect, which arises from specific sites having favorable bonding conditions, which keep the diffusing atom in place. The trapping effect may not be a factor in HE-UHTCs due to the non-metal sub-lattice acting as a shield so that each metal site in the metal sub-lattice is approximately equivalent.

### *The cocktail effect*

A high entropy material, with five or more components, vastly expands the space for composition-based materials design. For example, a refractory high entropy alloy containing Al improves on the current high temperature capabilities (melting temperature, high temperature strength) of conventional superalloys<sup>22</sup>. Designing materials with multiple principle elements have, in theory, the ability to bring together key properties from the different components, instead of incremental improvements from alloying additions seen in conventional alloys<sup>23</sup>. An HE-UHTC therefore could have the benefit of leveraging the desirable properties of Hf- and Zr-based compounds, while mitigating their rapid oxidation rates. On the other hand, given lack of adequate thermodynamic data and phase diagrams, the design of five component materials for the desired properties is challenging.

### *Designing for oxidation resistance*

It is hypothesized that a UHTC with improved oxidation resistance can be engineered by using the multiple principal element approach. Oxidation resistant materials require formation of dense, adherent and solid oxides that provide an effective barrier, slowing the diffusion of oxygen inward and/or metal atoms outward to the reaction interface under ultra-high temperature conditions. The ideal composition for a UHTC is one that can form an oxide that meets these requirements at temperatures greater than 1700 °C. Importantly, the resulting

oxides themselves must have high melting temperatures. A review was conducted of the oxidation behaviors of each of the group IV, V and VI transition metals, as described in the next chapter. An important conclusion from this work is that the oxidation behavior of the candidate constituents exhibits periodic trends. Group IV elements form the most stable oxides with the highest melting temperatures, group V formed oxides with intermediate melting temperatures, while group VI elements formed oxides that readily volatilize at high temperatures.

This work investigated a multi-prong approach to inform the design of oxidation resistant HE-UHTCs. The thermodynamically expected products from oxidation of high entropy UHTCs were explored. These thermodynamic predictions were then verified with experimental data. The oxidation kinetics of one high entropy carbide and corresponding boride composition were explored in detail, and where possible, the mechanisms for the oxidation of HE-UHTCs were elucidated. Finally, the effects of systematic compositional variation on oxidation mechanisms were experimentally explored.

## 2. Thermodynamic Considerations in High Entropy Materials

### 2.1. Background and motivation

Most of the research in the high entropy alloy community has focused on finding new compositions based on their ability to form single phase solid solutions and testing their properties, usually mechanical properties, afterward. The focus of this work is the development of tools to aid the design of a high entropy ceramic with oxidation resistance as a primary requirement. To do this, the equilibrium phases that could form during an oxidation reaction must first be determined. When a multi-component material is exposed to a sufficiently oxidizing environment, it is expected that all species in contact with the environment will initially oxidize<sup>24</sup>. As equilibrium is achieved, the oxide products that result are governed by their relative thermodynamic stability and oxidation kinetics.

The Ellingham diagram<sup>25</sup> is a useful and straightforward predictive tool, enabling the comparison of the relative thermodynamic stabilities of the oxides that form in a multi-component system. An Ellingham diagram, in the context of oxidation, plots the change in negative free energy of an oxidation reaction, normalized to one mole of oxygen, as a function of temperature. Each reaction is represented by a straight line in this plot, wherein the slope is the negative of the entropy of the oxidation reaction, and the intercept at 0K is the enthalpy of the reaction. The lower the line on the plot, the more thermodynamically favored the oxide product. However, existing Ellingham diagrams in literature<sup>26,27</sup> do not provide an adequate thermodynamic comparison of the oxidation reactions of the group IV, V and VI early transition metals, namely Hf, Zr, Ti, V, Nb, Ta, Mo and W, as well as their carbides, nitrides and borides. These elements are not only of significant interest to the study of HE-UHTCs, but also to existing studies that seek to understand the oxidation behavior of refractory HEAs<sup>22,28,29</sup>. No such diagrams exist for this set of materials, and as such are needed to provide guidance for oxidation-informed materials design.

These Ellingham diagrams provide an understanding of how each component might individually behave when exposed to an oxidizing environment and provide an initial method for component selection. However, even in the ideal case, it is not straightforward to understand how these components might behave in solution. A rigorous study of the thermodynamics of oxidation reactions from a multiple principle element solid solution phase is not available in literature. Such a study is necessary to further inform the component selection for oxidation-resistant high entropy materials.

The objectives of this study are to a) develop Ellingham diagrams for component M, MC, MB<sub>2</sub> and MN (where M is a transition metal), b) determining the expected products of oxidation from a solid solution containing group IV, V and/or VI elements and compounds, and c) verify the thermodynamic predictions using experimental data from oxidation exposures conducted on high entropy carbides and borides.

## 2.2. Thermodynamic stabilities of constituent oxide products

### 2.2.1. Methodology

The thermodynamic stability of oxide phases pertinent for UHTCs were calculated using FactSage<sup>30</sup>, a free energy minimization software. A two-step calculation method was employed. First, the equilibrium module was used with the Fact Pure Substance (FactPS) database to determine the equilibrium assemblage of reactants and oxide products that represented the minimum free energy of the system. Calculations were performed from 100 °C-3000 °C in 100 °C increments at a pressure of one atmosphere and fixed volume of one liter. In the second step, the free energies of formation for the oxides that were predicted to form for each M-O system in the previous step were calculated using the reaction module in FactSage for the temperature range of 100 °C to 3000 °C and a pressure of one atmosphere. The values of  $\Delta G^\circ$ , which were normalized to one mole of oxygen, were plotted versus

temperature, providing an Ellingham diagram for each M-O system. The lowest bound in each M-O system was identified (Figure 2.4) and plotted on the comparative Ellingham diagram for the metal-oxide reactions. The Fe-O system was used to test the chosen methodology as the oxidation behavior of iron is well understood<sup>31</sup>. It was found that an input of one mol each of Fe and O resulted in an activity of less than unity for iron once the calculation was complete, indicating that the high stability of the oxides tends towards complete oxidation of the metal. The calculation was conducted again, fixing the activity of iron at one to ensure the Fe reactant was not depleted. This strategy of fixing the metal activity at one in performing the equilibrium calculations with a 1:1 M:O ratio of reactants was thus utilized to identify potential product oxide phases for other metal-oxygen systems.

The oxides that formed or had a potential of forming, as determined by the equilibrium calculation, in the Fe-O system were FeO, Fe<sub>2</sub>O<sub>3</sub>, Fe<sub>3</sub>O<sub>4</sub>, as expected from previous studies<sup>31,32</sup>. The oxide formation reactions on a per mol O<sub>2</sub> basis are as shown by Equations (2.1)-(2.3) below



This approach, confirmed with the well-known Fe-O system, was then used to study the metal-oxygen systems of each of the group IV, V and VI early transition metals, as well as for the carbides, nitrides and borides of the same elements. In addition, where available, previously published observations of metal oxide products and their kinetics of formation are reviewed and discussed in the context of these diagrams. Finally, strategies are identified for optimizing design of high entropy UHTCs, for oxidation resistance above 1700 °C.

## 2.2.2. Results

### Validation of methods using Fe-O system

The reactions for the formations of the stable oxides in the Fe-O system,  $\text{Fe}_2\text{O}_3$ ,  $\text{Fe}_3\text{O}_4$  and  $\text{FeO}$ , normalized to 1 mol  $\text{O}_2(\text{g})$  are summarized in the Ellingham diagram in Figure 2.1.

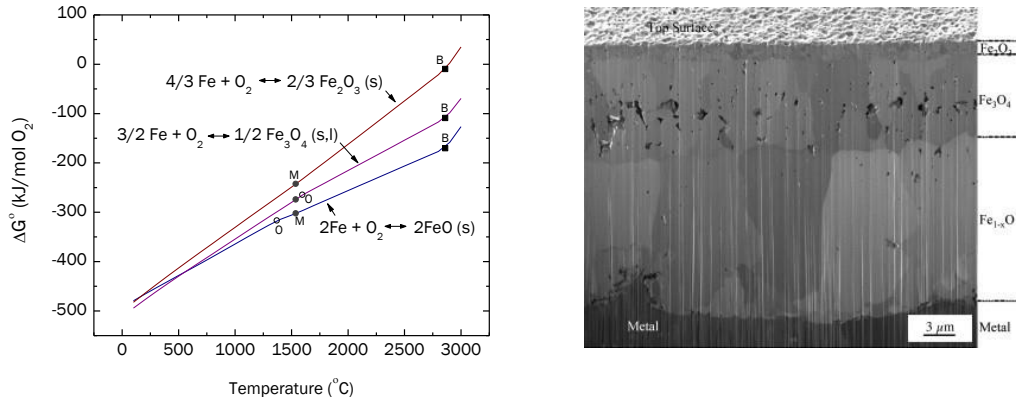


Figure 2.1: (Left) Ellingham diagram showing the formation reactions of Fe oxides, normalized to 1 mol  $\text{O}_2$ . Closed circles indicate melting point of the metal, open circles that of the oxide. Closed squares indicated boiling point of the metal; (Right) Layered oxide formed on Fe from Pujilaksono et al.<sup>32</sup>

Points of interest have been labeled on the Ellingham diagram; namely, “M” indicates the melting point of the metal, “O” indicates the melting point of the oxides and “B” indicates the boiling point of the metal. The order of thermodynamic stability demonstrated by the diagram corresponds with the order of layering of the oxides shown in Figure 2.1 (Right) from the work of Pujilaksono et al.<sup>32</sup>, in accordance with the equilibrium activities of oxygen at each interface, an observation that has previously been noted<sup>31</sup>. The free energy-temperature space occupied by a given metal-oxide equilibrium system can thus be thought of as a band on an Ellingham diagram, enveloping multiple oxidation reactions.

The kinetics of the oxidation reaction must be considered in conjunction with thermodynamics, as it can influence the observation of the predicted equilibrium phases. An

expression has been derived<sup>31,33</sup> establishing a relationship between the relative thicknesses of the different oxides formed and their parabolic oxidation rate constants. Specifically, the ratio of the thicknesses of two oxides that form in the case of a layered oxide is proportional to the square root of the ratio of their respective rate constants. The oxidation rate constant is related to diffusivity by Wagner's equation<sup>34</sup> shown by Equation (2.4). In this equation,  $k'_p$  is the parabolic rate constant,  $p_{O_2}$  is the partial pressure of oxygen, and  $D_M$  and  $D_O$  are the diffusivities of the metal species and oxygen respectively. The prime (' and ') modifiers on  $p_{O_2}$  indicate the maximum and minimum values governed by the fixed oxygen activities at the relevant interface, and  $z_c$  and  $z_a$  are the valences of the cations and anions respectively.

$$k'_p = \frac{1}{2} \int_{p_{O_2}'}^{p_{O_2}''} \left( \frac{z_c}{|z_a|} D_M + D_O \right) d \ln p_{O_2} \quad (2.4)$$

This is highlighted by the differences in thicknesses of the different oxide layers on Fe, wherein FeO with the highest defect concentration and highest diffusivities forms the thickest layer<sup>32,35,36</sup>. This combined consideration of thermodynamic stability and kinetics becomes important in the analysis of some of the metal-oxygen systems presented later, particularly that of Ti-O.

#### *Oxidation of group IV, V and VI metals*

The thermodynamically stable oxide products and temperature range of oxide stability for the group IV, V and VI metals under consideration as components for high temperature high entropy materials were determined and are summarized in Figure 2.2.

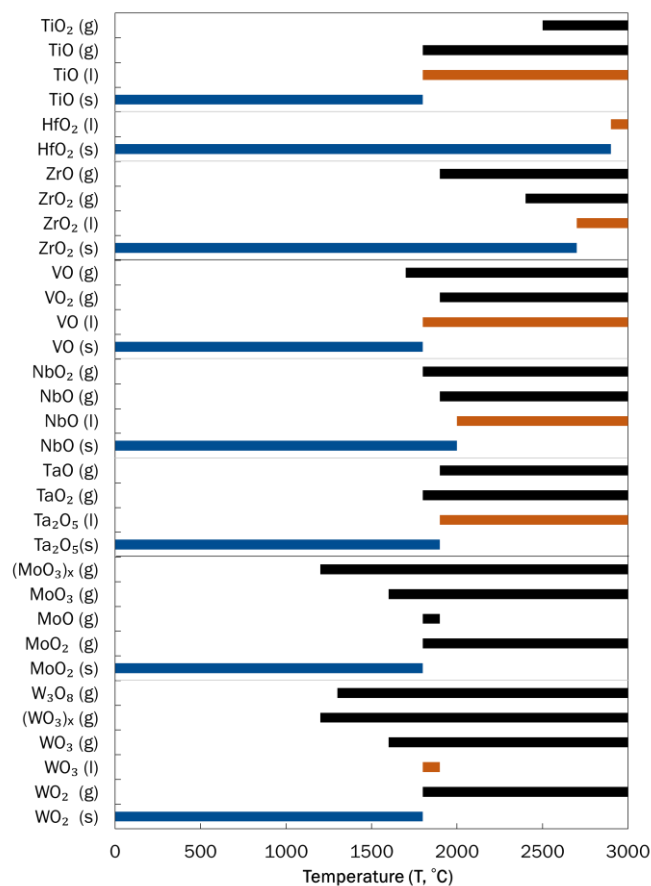


Figure 2.2: Summary of equilibrium calculations showing the thermodynamically stable products for each temperature range up to 3000 °C. Blue bars indicate solid oxides, orange bars indicate liquid oxides and black bars indicate gaseous oxides.

The most thermodynamically stable reaction in each M-O system was then identified and plotted on a comparative Ellingham diagram for the metal-oxide reactions shown in Figure 2.3. Additionally, TiO<sub>2</sub> and Nb<sub>2</sub>O<sub>5</sub> (dotted lines) were added as they are commonly observed despite being less thermodynamically favored than their corresponding suboxide. Identification of the lower bound for the formation of the oxides of the group IV and V metals was relatively straightforward, as the most thermodynamically stable product did not change across the temperature range of interest. However, the stable oxide products of the group VI metals were more complex. Figure 2.4 shows the Mo-O system as an example.

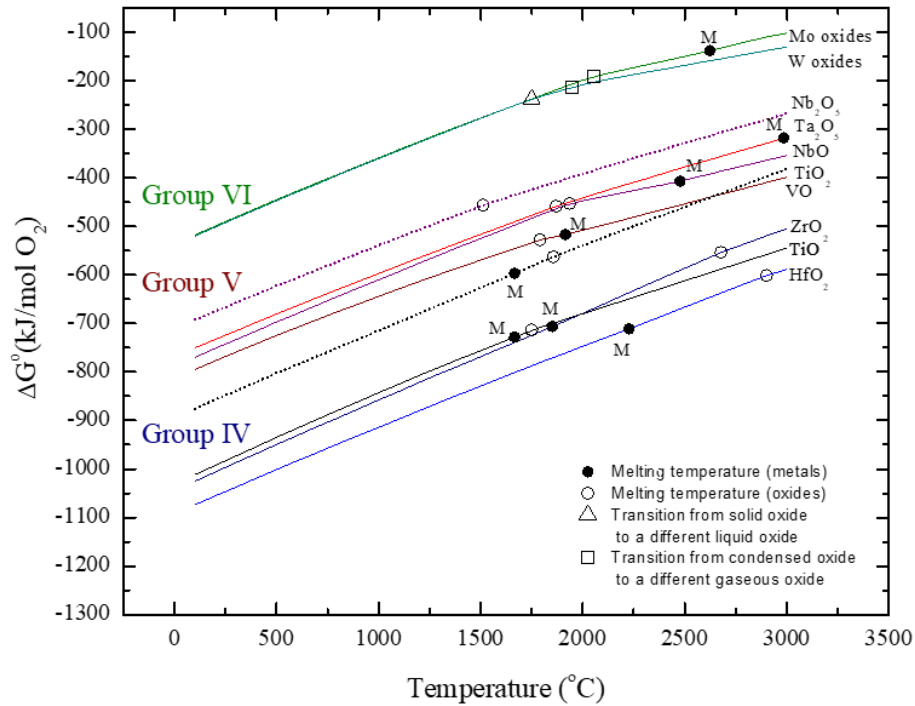


Figure 2.3: Ellingham diagram showing the formation reactions of the group IV, V and VI early transition metals. Filled circles indicate the melting temperatures of the metals; open circles indicate melting temperatures of the oxides. The triangle indicates transition to a liquid oxide,  $T_L$ , and squares indicate transition to gaseous oxides,  $T_V$ .

The most thermodynamically stable oxide of Mo transitions from  $\text{MoO}_2$  (s) to  $(\text{MoO}_3)_3$  (g), at  $2052^\circ\text{C}$  and then transitions to  $\text{MoO}_2$  (g) at  $2980^\circ\text{C}$ . The lower bound of the Mo-O oxide formation band, shown in Figure 2.4, therefore, consists of different oxides. The transition at  $2052^\circ\text{C}$  is from a solid oxide to a different, gaseous oxide. Such transitions also necessitated new symbols, which are shown in Figure 2.3, namely the solid triangle and open square. The solid triangle indicates transition from a solid oxide to a different oxide in the liquid phase,  $T_L$ , while the open square indicates a transition from a solid oxide to a different oxide in the vapor phase,  $T_V$ .

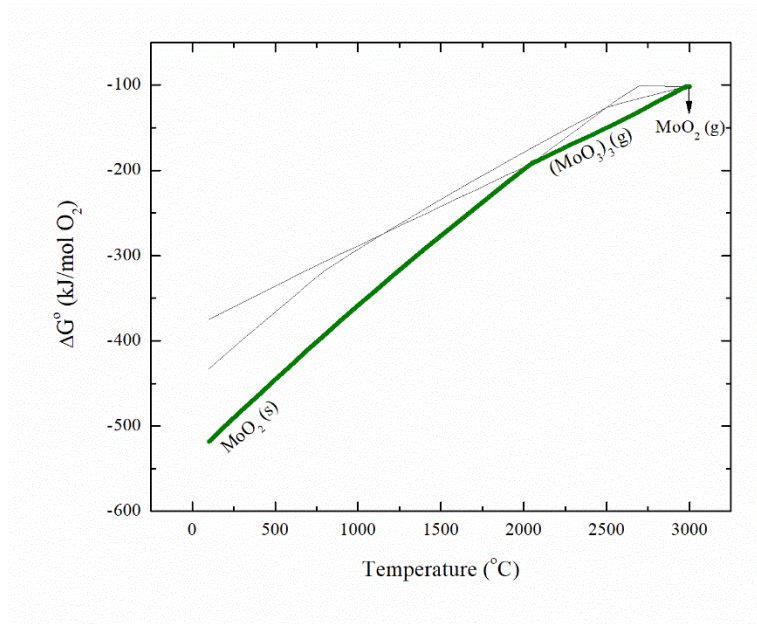
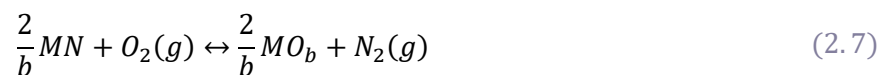
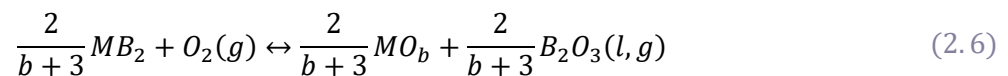
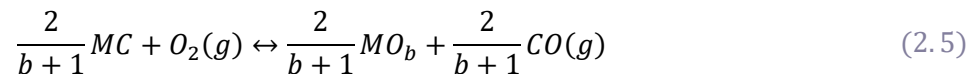


Figure 2.4: Ellingham diagram showing the delineation of the “lower bound” of the Mo-O system (bold, green line).

#### Oxidation of transition metal carbides, borides and nitrides

The development of diagrams for the oxidation of the refractory carbides, borides and nitrides was primarily conducted with the oxides of Hf and Zr, given that these M-O systems are relatively less complex, each consist of one oxide, and can therefore serve as model systems to understand how the free energy of oxide formation from the  $M + O_2$  reaction differs from that formed from the  $MX + O_2$  reaction (where X stands for C, N, B or  $B_2$ ). The results are presented in Figure 2.5. Generalized oxidation reactions for carbides, borides and nitrides were shown in Reactions (2.4)-(2.6), respectively.



The *relative* thermodynamic stability of HfO<sub>2</sub> and ZrO<sub>2</sub>, whether formed from the metal, boride, carbide or nitride, are largely unchanged in all temperature regimes. The only exception is the carbide-oxygen system, wherein the lines for HfO<sub>2</sub> and ZrO<sub>2</sub> are barely distinguishable from each other at lower temperatures (<2000 °C). The enthalpic contributions to the free energies of oxide formation for oxides formed from the carbides, borides and nitrides are all within a range of ~200 kJ/mol O<sub>2</sub> and are much less negative than that formed from the pure metals. The entropic contributions for oxide formation are lower for the oxides formed from carbides and nitrides, as can be seen by the shallower slopes.

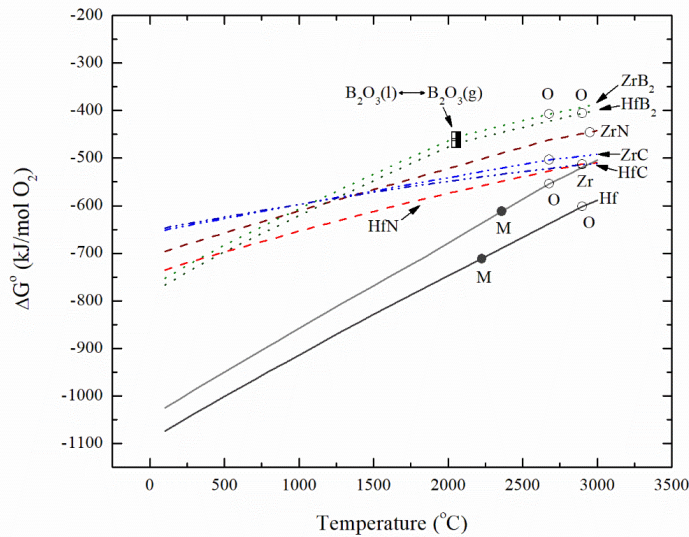


Figure 2.5: Comparison of HfO<sub>2</sub> and ZrO<sub>2</sub> stability when formed from the pure metal, or from carbide, nitride and boride. Open circles indicate oxide melting temperatures, and closed circles indicate metal melting temperatures.

### 2.2.3. Discussion

The constructed Ellingham diagram in Figure 2.3 shows clear periodic trends. Lines for the group IV, V and VI metals, respectively are clustered within their group, demonstrating the similarity in the enthalpies of formation (y-intercept at 0 K) for their most thermodynamically

stable oxides. Group IV oxides are the most thermodynamically stable, while those of group VI are the least thermodynamically stable. If the same logic described for the Fe-O system were to be applied, it would be expected that, for oxidation of systems containing multiple transition metals and ignoring kinetic effects, the group VI oxides would be found at the oxide/gas interface, while the group IV oxides would be located at the metal/oxide interface.

The group IV metals also tend to form oxides with melting temperatures higher than the melting temperature of the metal. On the other hand, group V metals form oxides with low melting temperatures, lower than the metal itself. The group VI metal oxides were primarily gaseous at high temperatures. This trend is important to note as dimensional stability is required for many high temperature applications. For example, in hypersonic vehicle wing leading edges and rocket nozzles, the form of the structure is critical to their function. A system that forms a solid oxide at these high temperatures is more desirable than one that forms liquid oxides that can easily shear away or volatilize during operation.

Changes in the slope of the line on an Ellingham diagram represent the negative of the change in entropy and are largely dominated by changes due to the consumption or production of the number of gas molecules in the oxidation reaction. The slopes for the carbide and nitride reactions are much shallower than that for the metal reactions due to formation of gaseous products (Reactions (2.4) and (2.6)). A similarly shallow slope is observed in the boride reaction lines at high temperatures, as boron is now forming as a gas (Reaction (2.5)). These shallower slopes indicate a reduced temperature dependence for the oxidation reactions, allowing for the extrapolation of oxidation behavior at 2000°C, to temperatures as high as 3000°C. The enthalpies of the oxidation reactions for the boride, carbide and nitride reactions are all much less negative (per mol O<sub>2</sub>) than that for the pure metal reactions.

The Ellingham diagrams also indicate thermodynamically stable oxides that are not always observed at oxidizing temperatures at atmospheric pressure, such as TiO. The Fact

Pure Substance database used to calculate these diagrams is a collection of data from standard compilations as well as additional data evaluated from the literature. The values for the enthalpy and entropy of formation used in these calculations at high temperatures (typically  $T > 1200\text{ }^{\circ}\text{C}$  for most oxides) were extrapolated by FactSage from lower temperature data where thermodynamic data at those temperatures for these materials were not available. In addition, these thermodynamic calculations do not account for oxidation kinetics. It is therefore useful to compare these predictions to oxide phases observed in prior studies from the literature.

#### *Group IV elements*

Hafnium is reported to only have one oxide,  $\text{HfO}_2$ <sup>37-39</sup>. Likewise, although the JANAF database has thermochemical data for  $\text{ZrO}(\text{g})$ ,  $\text{ZrO}_2$  is considered the only oxide of import<sup>37,38,40,41</sup> in the oxidation of zirconium. In the Ti-O system, the most thermodynamically stable oxide according to the calculations in this study is TiO, but  $\text{TiO}_2$  is primarily observed in oxidation studies of titanium<sup>37</sup> and was therefore added to Figure 2.3. TiO formation on titanium has been observed at temperatures less than  $1000\text{ }^{\circ}\text{C}$  at near atmospheric pressures. Kofstad et al.<sup>35</sup> have reported that at low partial pressures of oxygen, the oxides of titanium form in a layered manner, similar to the Fe-O system. The generally limited observations of TiO may be attributed to the relative kinetics of oxygen transport in TiO and  $\text{TiO}_2$ , as suggested by Yurek et al.'s work<sup>33</sup>. TiO is likely not always observed due to the transport of oxygen in  $\text{TiO}_2$  being much faster<sup>42,43</sup>. It is well known that  $\text{TiO}_2$  is highly nonstoichiometric relative to its suboxides and that the large oxide defect concentration should result in rapid oxidation kinetics. Kinetics can therefore play a large role in what is observed versus what is predicted by thermodynamics.

### Group V elements

Thermochemical analyses<sup>44</sup> and oxidation studies of tantalum<sup>45</sup> have shown that  $Ta_2O_5$  is the only stable condensed phase in the Ta-O system, which is reflected in the calculated Ellingham diagram in Figure 2.3. Gulbransen's analysis<sup>44</sup> shows  $TaO_2$  to be the major volatile species in that system, with an additional volatile species being TaO, and this is likewise reflected in the calculations summarized in Figure 2.2. Similarly, Gulbransen reports  $Nb_2O_5$  as being the stable condensed oxide formed on niobium at high temperatures and near atmospheric pressures and was therefore added to Figure 2.3. The suboxides were present as volatile species. Oxidation studies of niobium have shown the formation of the sub-oxides, particularly  $NbO_2$ <sup>39,45,46</sup> forming at lower temperatures and pressures (<500°C) and then subsequently oxidizing to  $Nb_2O_5$ <sup>45</sup>. This observation suggests that NbO is the most thermodynamically stable oxide, consistent with our representation of the Nb-O system in Figure 2.3. Studies of the oxidation of vanadium<sup>47-51</sup> up to 1050 °C at varying pressures show that the pentoxide,  $V_2O_5$ , readily forms. Mukherjee reports that  $VO_2$  forms at low pressures and above 500 °C<sup>51</sup>. Both Westman<sup>52</sup> and Stringer and Price<sup>48</sup> have reported on the formation of VO on vanadium at varying pressures and temperatures above 500 °C. Specifically, Stringer and Price reported the formation of VO in an experiment where a fixed volume of  $O_2$  was admitted into the system, and the pressure drop from the gas consumption was measured with time. The computations performed in this study predict that VO is the most thermodynamically stable oxide, followed by  $VO_2$  and  $V_2O_5$ . It can thus be expected that similarly to Ta and Nb, VO will oxidize to  $VO_2$  and  $V_2O_5$ .  $V_2O_5$  melts at 670 °C. In the case of Nb and V, the sub-oxides are shown in Figure 2.3 because these condensed oxides have been previously observed, and are expected to form prior to further oxidation to  $M_2O_5$ .

### *Group VI elements*

Studies of the oxidation of molybdenum<sup>44,53-58</sup> and tungsten<sup>55,59-64</sup> show that gaseous oxide species dominate the high temperature oxidation behavior of these metals, which is consistent with the results in Figure 2.2. Note that most of the high temperature data available were collected at low total pressures. Pressure is a significant variable as it affects both the equilibrium partial pressure and transport of the volatile species through the gas boundary layer<sup>44</sup>. Gulbransen et al.<sup>54</sup> found that the temperature at which the oxide will volatilize as fast as it forms on the metal changes with total pressure. Below this transition, both condensed and volatile species coexist.  $\text{MoO}_3(\text{c})$  is reported to be the primary condensed phase oxide formed on molybdenum, especially at higher pressures, but  $\text{MoO}_2(\text{s})$  has also been observed<sup>57</sup>, usually as an inner layer in the thermally grown oxide scale at lower temperatures, consistent with the calculations in this study as shown in Figure 2.3. Similarly, the condensed oxides of tungsten form in a layered manner, consisting primarily of the trioxide<sup>44,45</sup>. The dioxide has been reported<sup>65</sup>, but Kellett and Rogers<sup>64</sup> have suggested that what was previously reported as  $\text{WO}_2(\text{c})$  is defective or non-stoichiometric  $\text{WO}_3(\text{c})$ . The difference between the free energies of formation for  $\text{WO}_3(\text{c})$  and  $\text{WO}_2(\text{c})$  lines was found to be insignificant, and the presence of a condensed oxide layer at high temperatures is negligible to non-existent.

### *Kinetic considerations*

The role of kinetics in the high temperature oxidation of high entropy ceramics, as mentioned earlier, must be considered. Existing reviews of kinetics parameters<sup>66,67</sup> do not consider all the available data for oxygen diffusion in the oxides of group IV, V and VI. As such, an updated review of the diffusivity data in literature<sup>50,51,62,68-74</sup> for the oxides of interest was conducted and summarized in Figure 2.6. Most of the data shown are for oxygen diffusion in the oxide; oxidation in these strongly bonded materials tends to be controlled by oxygen

diffusion inward. The available data were obtained at low or intermediate temperatures (relative to a maximum of 3000 °C). Data for some of the oxides of the group IV, V and VI oxides are not available, such as the sub-oxides of titanium, or the condensed oxides of molybdenum. Consideration of the highest temperature data available shows that diffusion in zirconia, which is among the more thermodynamically stable oxides, is rapid. Therefore, it can be expected that  $ZrO_2$ , which has a high melting temperature will readily form if included in the material. Similar conclusions may be drawn for the formation of  $Ta_2O_5$ . Oxygen diffusion in  $Nb_2O_5$  and  $TiO_2$  is slower than the former two oxides. Thus, if a material containing Zr, Ta, Ti and Nb were to form a layered oxide scale, the  $ZrO_2$  and  $Ta_2O_5$  layers would be expected to be thicker than the oxides of the other two elements.

The formation of complex oxides are extremely likely, based on the similar diffusivities of the group IV and V oxides, the respective phase diagrams showing the solubility of group IV and V oxides in each other, and the existence of mixed stoichiometric oxides such as  $Hf_6Ta_2O_{17}$ <sup>75,76</sup>. As far as the authors are aware, there are no data available for the diffusivities of oxygen in the complex oxides.

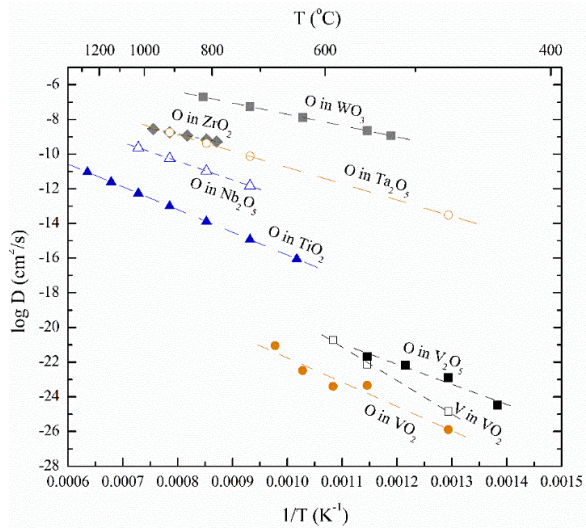


Figure 2.6: Diffusivities of oxygen in the oxides of group IV, V and VI transition metals, from data available in literature:  $\text{TiO}_2$ <sup>69,77</sup>;  $\text{ZrO}_2$ <sup>68</sup>;  $\text{VO}_2$ <sup>50,51</sup>;  $\text{V}_2\text{O}_5$ <sup>70</sup>;  $\text{Nb}_2\text{O}_5$ <sup>71</sup>,  $\text{Ta}_2\text{O}_5$ <sup>72-74</sup>;  $\text{WO}_3$ <sup>62</sup>.

### Implications for HE-UHTCs

This study has only considered the thermodynamic stabilities and kinetics of binary oxides of individual reactants and has not considered the complex oxides (Table 2.1). Given the requirement for the formation of a solid oxide, Hf, Zr, or Ti, or a combination of them, should be primary components of an HE-UHTC. Both the thermodynamics and kinetics suggest that these components will tend to oxidize first among the group IV, V and VI elements; therefore, using them as the basis for an HE-UHTC, especially for ultra-high temperature applications, is a viable strategy. Group V containing compounds should be minimized, as they both exhibit rapid kinetics of formation, are next in the order of thermodynamic stability, and have low melting temperatures.

Table 2.1: Known complex oxides that could form in the material systems under study, based on a review of available phase diagrams.

|    | Hf  | Ti   | Zr   | Nb  | Ta  |
|----|---|--|--|---|---|
| Hf |   |  |  |   |   |
| Ti | HfTiO <sub>4</sub> <sup>78</sup>                              |  |  |   |   |
| Zr |   | ZrTiO <sub>4</sub> <sup>79-81</sup>  |  |   |   |
| Nb | Hf <sub>6</sub> Nb <sub>2</sub> O <sub>17</sub> <sup>82</sup> | Nb <sub>2</sub> TiO <sub>7</sub> <sup>83</sup><br>Nb <sub>10</sub> Ti <sub>2</sub> O <sub>29</sub> <sup>83</sup><br>Nb <sub>6</sub> Ti <sub>2</sub> O <sub>19</sub> <sup>83</sup><br>TiNb <sub>6</sub> O <sub>17</sub> <sup>75</sup> | Zr <sub>6</sub> Nb <sub>2</sub> O <sub>17</sub> <sup>75</sup>  |   |   |
| Ta | Hf <sub>6</sub> Ta <sub>2</sub> O <sub>17</sub> <sup>76</sup> | TiTa <sub>2</sub> O <sub>7</sub> <sup>84</sup>   | ZrTa <sub>6</sub> O <sub>17</sub> <sup>85</sup><br>Zr <sub>6</sub> Ta <sub>2</sub> O <sub>19</sub> <sup>85</sup> | Nb <sub>4</sub> Ta <sub>2</sub> O <sub>15</sub> <sup>86</sup> |   |
| V  |   |  | ZrV <sub>2</sub> O <sub>7</sub> <sup>87</sup>  | VNb <sub>9</sub> O <sub>25</sub> <sup>88</sup>                | VTa <sub>9</sub> O <sub>25</sub> <sup>89,90</sup> |
| Mo |   |  |  |   |   |
| W  | HfW <sub>2</sub> O <sub>8</sub> <sup>91</sup>                 |  | ZrW <sub>2</sub> O <sub>8</sub> <sup>91</sup>  |   |   |

In addition, their phase diagrams indicate the potential for the formation of low melting oxide eutectics (Table 2.2), e.g. an eutectic in the ZrO<sub>2</sub>-V<sub>2</sub>O<sub>5</sub><sup>87</sup> is noted at 665 °C, which is dramatically lower than the melting temperature of ZrO<sub>2</sub> (~2700 °C). Group VI element additions can be expected to promote the formation of oxides with high vapor pressures, which may result in porosity in the oxide. This may not be an issue with carbides and nitrides, which already form porous oxides. Small amounts of group VI additions such as WC have previously been explored as a method to promote oxidation resistance<sup>92</sup>; however, recent research<sup>93</sup> has shown that at temperatures above 1650 °C, the volatility of W oxides precludes any protection.

Table 2.2: Table summarizing the lowest melting temperatures in pseudo binary systems.

| $T_m$ (°C)                     | HfO <sub>2</sub> | ZrO <sub>2</sub> | TiO <sub>2</sub> | VO <sub>2</sub> | V <sub>2</sub> O <sub>5</sub> | Nb <sub>2</sub> O <sub>5</sub> | NbO  | NbO <sub>2</sub> | Ta <sub>2</sub> O <sub>5</sub> | MoO <sub>2</sub> | MoO <sub>3</sub> | WO <sub>3</sub> |
|--------------------------------|------------------|------------------|------------------|-----------------|-------------------------------|--------------------------------|------|------------------|--------------------------------|------------------|------------------|-----------------|
| HfO <sub>2</sub>               | 2900             |                  |                  |                 |                               |                                |      |                  |                                |                  |                  |                 |
| ZrO <sub>2</sub>               |                  | 2678             |                  |                 |                               |                                |      |                  |                                |                  |                  |                 |
| TiO <sub>2</sub>               | 1740             | 1845             | 1857             |                 |                               |                                |      |                  |                                |                  |                  |                 |
| VO <sub>2</sub>                |                  |                  |                  | 1360            |                               |                                |      |                  |                                |                  |                  |                 |
| V <sub>2</sub> O <sub>5</sub>  |                  | 670              |                  | 665             | 670                           |                                |      |                  |                                |                  |                  |                 |
| Nb <sub>2</sub> O <sub>5</sub> |                  | 1436             | 1477             |                 | 648                           | 1512                           |      |                  |                                |                  |                  |                 |
| NbO                            |                  |                  |                  |                 |                               |                                | 1937 |                  |                                |                  |                  |                 |
| NbO <sub>2</sub>               |                  |                  |                  |                 |                               | 1830                           |      | 1902             |                                |                  |                  |                 |
| Ta <sub>2</sub> O <sub>5</sub> |                  |                  | 1620             |                 |                               |                                |      |                  | 1870                           |                  |                  |                 |
| MoO <sub>2</sub>               |                  |                  |                  |                 |                               |                                |      |                  |                                | 2680             |                  |                 |
| MoO <sub>3</sub>               |                  |                  |                  |                 | 618                           |                                |      |                  | 781                            |                  | 801              |                 |
| WO <sub>3</sub>                | 1227             | 1231             | 1233             |                 |                               | 1335                           |      |                  |                                |                  | 770              | 1472            |

This work suggests that in the compositional design of an HE-UHTC for oxidation resistance, group IV elements are the best option as primary components. The rapid formation of the group IV oxides will be beneficial in establishing a solid scale. On the other hand, their rapid formation will likely lead to excessive consumption of the substrate. Kinetic considerations do not provide substantial guidance for compositional choices, as oxygen transport in all the group IV, V and VI oxides considered here are rapid. The kinetics involving the formation of complex oxides are poorly understood in the literature.

## 2.3. Thermodynamic Predictions of Preferential Oxidation in High Entropy Materials

### 2.3.1. Background and introduction

Limited data exists for the high temperature oxidation resistance of refractory HEAs<sup>94,95</sup> and carbides<sup>96</sup>, including an understanding of the oxide phases formed. A more rigorous understanding of the thermodynamic driving forces in the oxidation process is therefore needed. Further, the effects of oxidation on the stability of the underlying material, the

configurational entropy stabilizing the phases and its attendant properties, still need to be further understood to aid in the design of oxidation-resistant high entropy materials.

Assuming a generic oxidation reaction for species M,  $M + O_2(g) = MO_2$ , the driving force for the oxidation reaction is given by the familiar free energy equation,

$$\Delta G_{\text{rxn}}^{\circ} = \Delta H_{\text{rxn}}^{\circ} - T\Delta S_{\text{rxn}}^{\circ} \quad (2.8)$$

where the free energy of reaction is given by the difference in free energies of formation of the products and reactants, as shown in Equation (2.9).

$$\Delta G_{\text{rxn}}^{\circ} = \sum \Delta G_{\text{f,prod}}^{\circ} - \sum \Delta G_{\text{f,react}}^{\circ} \quad (2.9)$$

Entropy can be further described as in Equation (2.10).

$$\Delta S = \Delta S_{\text{vib}} + \Delta S_{\text{config}} \quad (2.10)$$

High entropy materials are characterized by additional configurational entropy, given by Equation (2.11):

$$\Delta S_{\text{config}} = -R \sum_{i=1}^N x_i \log x_i \quad (2.11)$$

$R$  refers to the ideal gas constant,  $N$  is the number of species, and  $x_i$  is the mole fraction of each species. The maximum configurational entropy occurs when all species in the alloy occur at equimolar fractions and is given by Equation (2.12).

$$\Delta S_{\text{config,max}} = R \log N \quad (2.12)$$

The determination of the products that form during an oxidation reaction is a necessary step in the design of a multi-component, oxidation resistant, ultra-high temperature system, as discussed in depth in the previous section<sup>97</sup>. Considering Equations (2.8), (2.9) and (2.10),

along with the reasonable assumption that a high entropy alloy does not form a high entropy oxide scale, one could write Equation (2.13) and simplify to Equation (2.14).

$$\Delta G_{\text{rxn,HE}}^{\circ} = (\Delta H_{\text{f,prod}}^{\circ} - \Delta H_{\text{f,react}}^{\circ}) - T[\Delta S_{\text{f,prod}}^{\circ} - (\Delta S_{\text{f,react}}^{\circ} + \Delta S_{\text{config}})] \quad (2.13)$$

$$\Delta G_{\text{rxn,HE}}^{\circ} = \Delta G_{\text{rxn}}^{\circ\text{ox}} + T\Delta S_{\text{config}} \quad (2.14)$$

Any changes in vibrational entropy due to the mixing are assumed to be negligible, as in a prior analysis<sup>17</sup>. In Equations (2.13) and (2.14),  $\Delta G_{\text{rxn,HE}}^{\circ}$  is the driving force for oxidation from a high entropy material. Equation (2.14) suggests that configurational entropy has the potential to reduce the driving force for oxidation, i.e.,  $\Delta G_{\text{rxn}}^{\circ}$  becomes less negative, however the magnitude of this reduction is minimal. For a five-component equimolar solution,  $S_{\text{config}}=1.61R$ . At 2073K, a relevant temperature for refractory materials, this results in a  $T\Delta S$  of +27.7kJ, and the  $\Delta G_{\text{rxn,HE}}^{\circ}$  (Equation (2.14)) becoming more positive by this amount.

As the reaction progresses and approaches equilibrium, the final product is dependent on the relative thermodynamic stability of the oxides, and the kinetics of their formation. Note the substantial differences in relative thermodynamic stabilities of the oxides of the group IV, V and VI transition metals (Figure 2.3). The enthalpy for formation of  $\text{HfO}_2$  (most favorable) at 2073K is  $-1115.8\text{kJ/mol}$  and  $(\text{WO}_3)_3(\text{g})$  (least favorable) is  $-438.1\text{kJ/mol}$ . The reduction in driving force due to the contribution of the configurational entropy is at least an order of magnitude less than the relative differences in the enthalpy of oxidation. It is therefore not expected that the additional configurational entropy will provide a significant advantage in reducing the driving force for oxidation. It is further hypothesized that given the number of components and the large differences in thermodynamic favorability of the oxides of interest, that a large tendency towards preferential oxidation will be exhibited in refractory high entropy materials. Both a first-principle surface oxidation study<sup>98</sup> and an experimental study on bulk material<sup>95</sup> have observed preferential oxidation consistent with the thermodynamic favorability

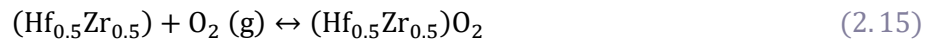
indicated in Figure 2.3. This demonstrates the need for a deeper understanding of the extent to which this phenomenon can be expected to occur in high entropy materials. Preferential oxidation also has implications for the stability of the underlying substrate, leading to the destabilization of the solid solution phase or formation of undesirable phases, due to the reduction in configurational entropy as some components are preferentially depleted.

In this section, a thermodynamic approach is described to provide a quantitative analysis of preferential oxidation in multi-principal component refractory materials as a function of elemental composition. These computed results are compared to experiments. The calculations are idealized, first to simplify the complex compositional and phase assemblages, and second, because thermodynamic data are not available for these multicomponent systems and complex oxides. The overall objective of these calculations is to predict the oxidation products of multi-principal component materials and thereby provide insight into the mechanisms that govern their oxidation behavior.

### 2.3.2. Methodology

#### *Thermodynamic Calculations – Equilibrium Constants*

The equilibrium composition of the oxide scale formed from multi-component base materials is sought. The equilibrium oxide formed will not have the same composition (on a cation basis) as the underlying material due to varying constituent thermodynamic favorability. Consider a binary Hf-Zr alloy. One might expect this alloy to oxidize according to the reaction:



This reaction suggests that a 50-50 (at%) Hf-Zr alloy will yield a 50-50 (at%) solution of HfO<sub>2</sub> and ZrO<sub>2</sub>. However, HfO<sub>2</sub> is more thermodynamically favored compared to ZrO<sub>2</sub>

( $\Delta G_{f,\text{HfO}_2}^0 = -779.4$  kJ/mol and  $\Delta G_{f,\text{ZrO}_2}^0 = -715.6$  kJ/mol at 2073K), and the remaining Hf could

reduce any ZrO<sub>2</sub> that forms. This difference in stabilities will be reflected in the oxide composition. When an Hf-Zr alloy oxidizes, it will be in equilibrium with a solid solution of HfO<sub>2</sub> and ZrO<sub>2</sub>, with a corresponding equilibrium pO<sub>2</sub>. The relevant reactions for each alloy constituent are:



Following Gaskell's approach<sup>99</sup>, the pertinent reaction describing the equilibrium between the base metal constituents and their oxides can be written by combining Equations (2.16) and (2.17) as



Assuming ideal solid solution thermodynamics, where each activity coefficient,  $\gamma$ , is equal to unity, the equilibrium constant for this equation yields the following relationship for the relative concentrations in mole fraction ( $X_i$ ) of the components

$$K = \frac{[X_{\text{HfO}_2}][X_{\text{Zr}}]}{[X_{\text{ZrO}_2}][X_{\text{Hf}}]} \quad (2.19)$$

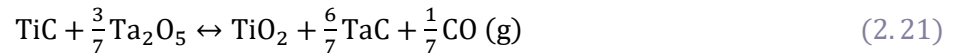
For a fixed temperature,  $K$  is constant; therefore, for a given alloy composition, e.g. a 50-50 alloy, the composition of the oxide will be fixed as well.

$$K * \frac{[X_{\text{Hf}}]}{[X_{\text{Zr}}]} = \frac{1 - [X_{\text{ZrO}_2}]}{[X_{\text{ZrO}_2}]} \quad (2.20)$$

Using Equation (2.20), the mole fractions of oxides in equilibrium with a range of alloy compositions can be plotted for Hf-Zr at a given temperature in a *composition balance diagram*. Using tabulated data, e.g. FactSage databases<sup>30</sup>, to determine  $K$ , the analysis shown in Equations (2.18) to (2.20) was also conducted for Zr-Ti, Ti-Ta and Ta-Mo, in equilibrium with the predominantly observed, condensed binary oxides in the respective systems. The elements

were chosen as representatives of the elements that make up refractory high entropy materials. In the case of the Ta-Mo alloy, MoO<sub>2</sub> was chosen as the representative oxide since it is the thermodynamically stable condensed oxide in the Mo-O system<sup>97</sup>, and has been observed to exist in the sublayers of thermally grown oxides or other conditions with reduced oxygen partial pressures<sup>100,101</sup>. At higher temperatures and oxygen partial pressures, the highly volatile, less thermodynamically favored MoO<sub>3</sub> (l) is formed<sup>54</sup>.

These analyses are then extended to the more complex refractory carbide systems. Equations (2.21) and (2.22) demonstrate the governing reactions and the resulting equilibrium constant, using the example of a TiC-TaC solid solution. Note the formation of the additional product, CO (g).



$$K_c = \frac{[X_{\text{TiO}_2}][X_{\text{TaC}}]^6 p_{\text{CO}}^{\frac{1}{7}}}{[X_{\text{Ta}_2\text{O}_5}]^{\frac{3}{7}}[X_{\text{TiC}}]} \quad (2.22)$$

Oxygen solubility in the metallic systems is not considered, which can be as high as 30%, as in the Ti-O system<sup>102</sup>. Similarly, oxygen solubility in the rock-salt carbide lattice<sup>103</sup> is also neglected. The computational tools described in this section preclude these effects, as the underlying assumption of this approach is predicated on the existence of an external oxide scale and the equilibrium between the metal (or alloy) and their respective condensed oxides. Furthermore, oxygen solubility in high entropy alloy and ceramic systems has not been studied<sup>104</sup>. Experimental studies were undertaken to gauge the applicability of these tools to real systems, and the results reported in the following section and chapter. It is expected that this thermodynamic assessment method (Equations (2.18)-(2.22)) will aid in oxide phase identification and prediction of preferential oxidation, which are essential for understanding

the oxidation mechanisms of refractory high entropy materials, and thereby aid design efforts for oxidation-resistant materials.

The focus of this work will be on equimolar multi-principal component materials. Temperatures used in the following calculations were chosen to be as high as possible while maintaining all constituents in the solid state. Solid states were chosen over liquid so that temperatures remained within the realm of experimental verification described in the next section. Partial pressures (oxygen activity) reported in this study are those that exist between the external oxide scale and substrate at equilibrium.

### *Free energy minimization calculations*

The analytical method outlined by Gaskell<sup>99</sup> provides a useful, visual way to consider the binary ideal solution case, and develop hypotheses with respect to real, multicomponent cases. These hypotheses can be further refined by leveraging the computational capabilities of FactSage, a free energy minimization software<sup>30</sup>, and the accompanying databases. The FactSage Equilibrium module allows for the definition of the solid solution phases, both ideal and real, for the reactants as well as the products, provided the pertinent databases are available. In both the real and ideal cases, the appropriate phase diagrams, mostly pseudo-binary, were consulted to identify the most likely phases and components of the solution at the temperature under consideration. Current research is addressing the gaps for ternary oxides<sup>105,106</sup>, but further information on solid solubility is needed.

Like the analytical approach in the prior section, an equimolar solid solution substrate is defined to be in equilibrium with an equimolar oxide solid solution (on a cation basis) in an isolated system based on the Gibbs isolation chamber construct. Assumptions include ideal solution thermodynamics, unless otherwise stated, approximating ideal solid solutions formed from phases not of the same crystal structure (as input), due to the use of Fact Pure Substance

database. The Gibbs free energy of the assemblage of substrate and oxide constituents is then minimized, with a resulting output of equilibrium phases. Metals with more thermodynamically favored oxides such as the group IV oxides, reduce the less stable oxides (e.g. group V and VI) until equilibrium is achieved. The equilibrium  $pO_2$  between the resultant oxide and substrate is also calculated. In cases where sub-oxides are predicted to form, the calculation is repeated with input of the suboxides in the oxide solid solution phase.

The case of the Hf-Zr binary alloy oxidizing to  $HfO_2$ - $ZrO_2$  in an ideal solid solution phase was compared to results from free energy minimization calculations in FactSage to test this methodology. Once tested, the approach was extended to study ternary (Hf-Zr-Ti) and quinary (Hf-Zr-Ti-Ta-Nb) alloy compositions.

The ideal solution assumptions described above allow for a first approximation in the understanding of the tendency towards preferential oxidation in high entropy materials, which will be shown in section 2.4 to have good agreement with experimental results. This simplified approach relies on thermodynamic data available in the database for pure substances and assumes that all oxide compounds will go into solution without applying an enthalpy correction for a change in crystal structures. Formation of extensive solid solutions has been demonstrated for the refractory metal high entropy alloys, carbides and diborides. The constituents of the high entropy  $Hf_{0.2}Zr_{0.2}Ti_{0.2}Ta_{0.2}Nb_{0.2}$  all form stable body-centered cubic (BCC) structures (although the temperature ranges of the BCC phase stability vary). The high entropy alloy itself forms a stable single phase BCC solid solution with no indication of intermetallic phases after annealing at 1473K for 3 hours<sup>107-109</sup>. The constituent carbides form stable rocksalt MC structures (where M=Hf,Zr,Ti,Ta,Nb) structure, and available binary and ternary diagrams indicate complete mutual solubility above 1000 °C<sup>110</sup>, with the exception of HfC-TiC and ZrC-TiC, which exhibit mutual solubility above approximately 2000 °C<sup>111,112</sup>. Calculations performed by Sarker et al.<sup>113</sup> show that  $(Hf_{0.2}Zr_{0.2}Ti_{0.2}Ta_{0.2}Nb_{0.2})C$  does in fact form

a solid solution. Similarly, the constituents of the high entropy diboride, which is a hexagonal  $AlB_2$ -type structure, each also form stable  $AlB_2$ -type diborides<sup>15,114</sup>. Available phase diagrams (isothermal sections at 1400 °C for B and two of Hf, Zr, Ti or Nb) indicate complete mutual solubility of the diboride phases in the  $HfB_2$ - $TiB_2$ ,  $HfB_2$ - $ZrB_2$ ,  $TiB_2$ - $ZrB_2$  and  $TiB_2$ - $NbB_2$  systems.<sup>115,116</sup>

In the FactSage calculations performed, the activity of the oxide solution phase is constrained to be unity. This approximation imposes the coexistence of, for instance, a rutile Ti oxide constituent in solution with the tetragonal Hf and Zr oxides; without this constraint, the free energy minimization calculations will result in the most stable product phase being  $HfO_2$ , i.e.,  $HfO_2$  as having an activity of one, and the other oxide phases as having been reduced by  $HfO_2$ . This approach is reasonable as the enthalpy correction would be negligible compared to the free energy of formation of the oxides under consideration, or their relative stabilities<sup>117-119</sup>.

Additionally, in non-ideal thermodynamics, the activity of a component in a solution varies from the mole fraction according to the activity coefficient,  $\gamma$ . While this non-ideality will affect the reactant solid solution as well as the overall reaction free energy, it is hypothesized these differences are not so large compared to the difference in the stabilities between oxides from different groups (Figure 2.3). These large differences are expected to persist when comparing the relative stabilities of oxides using thermodynamic data for real solutions. If this is the case, use of ideal solution thermodynamics is sufficient to understand the preferential oxidation phenomenon in HE materials. To probe this, the case of an ideal Zr-Ti alloy to form real oxidation products, rather than ideal products, was considered. The Zr-Ti system was chosen due to the availability of thermodynamic data for their oxides. While Zr and Ti metals are soluble in each other, the binary phase diagram for their oxides (Figure 2.7) exhibits more complex phase behavior<sup>79</sup>.

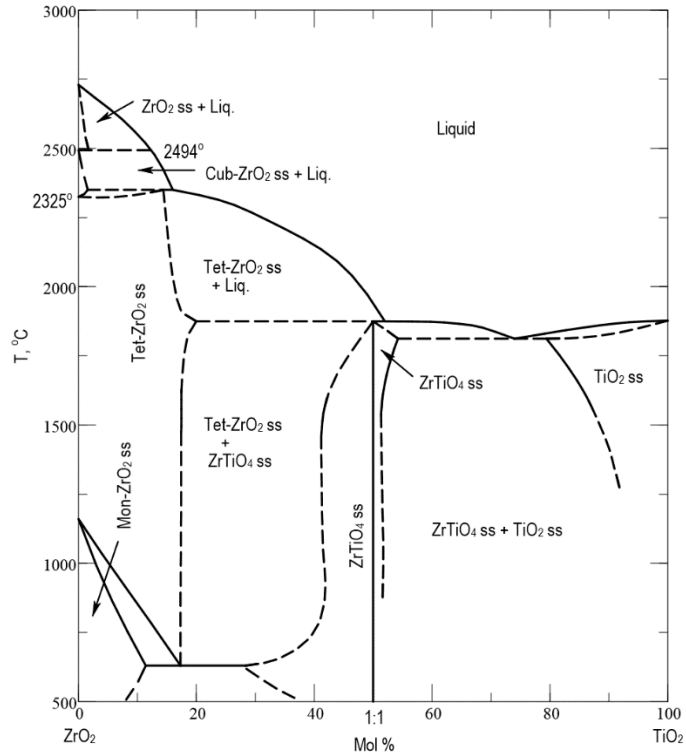


Figure 2.7: ZrO<sub>2</sub>-TiO<sub>2</sub> pseudobinary phase diagram, based on the work of Noguchi and Mizuno<sup>79</sup> and obtained from the Phase Equilibria Diagrams Database (NIST Standard Reference Database 31), The American Ceramic Society and the National Institute of Standards and Technology, 2020. Figure Number 04452; [www.nist.gov/srd/nist31.cfm](http://www.nist.gov/srd/nist31.cfm) .

Zr and Ti oxides also exhibit a significant difference in their relative thermodynamic favorability. The calculation was performed at the Zr-Ti equimolar alloy composition at 1773K, assuming the alloy to be an ideal solution, where the temperature was chosen below the melting temperature of Ti. The FTOxid database, which contains thermodynamic data for real oxide solutions such as (Zr,Ti)O<sub>2</sub> tetragonal oxide solution phase and a rutile oxide phase, was used to calculate the oxide composition in the non-ideal case.

### 2.3.3. Results

#### *Composition Balance Diagrams: Ideal Binary Metal Alloys and Ideal Oxide Solutions*

Figure 2.8, Figure 2.9 and Figure 2.10 show the composition balance diagrams for Hf-Zr, Ti-Ta and Ta-Mo respectively, assuming ideal solution behavior in both binary metal alloys and their oxides. Results for the formation of real oxide solutions ( $\gamma \neq 1$ ) are presented later. The composition balance diagram can be read as follows. Take for example Figure 2.8, the top x-axis, shown in mole fraction, ranges from pure HfO<sub>2</sub> on the left side to pure ZrO<sub>2</sub> on the right. The bottom x-axis, also in mole fraction, ranges from pure Hf on the left to pure Zr on the right. The y-axis height is set arbitrarily to display the slopes of the tie lines joining the metal alloy composition with the corresponding equilibrium oxide composition, assuming that both alloy and the oxides are in an ideal solid solution respectively. The tie lines are also oxygen isobars, representing the equilibrium partial pressure of oxygen (based on a reference state of 1 atm) that corresponds to each specific alloy-oxide activity ratio. The lines joining the pure Hf to pure HfO<sub>2</sub>, and that joining pure Zr to pure ZrO<sub>2</sub>, correspond to the equilibrium pO<sub>2</sub> for the respective oxidation reactions, given by Equations (2.16) and (2.17).

Figure 2.8 shows the case of an alloy consisting of two elements from the same group in the periodic table, Hf and Zr, whose oxides have similar thermodynamic stability (Figure 2.3). The diagram shows that more than 97% zirconium in the alloy is needed to form ~50% ZrO<sub>2</sub>. Taking the equimolar case, a 50-50 mol% Hf-Zr alloy will yield at equilibrium an oxide scale with 2.4% ZrO<sub>2</sub> (Figure 2.8). If one follows the red dotted line on Figure 2.8 upward, each intersection with a black tie-line represents a higher partial pressure of oxygen encountered. When the alloy is in the initial state, the composition is 50 mol% Zr. At this composition, the equilibrium partial pressure (oxygen activity) between the alloy and the oxide scale is  $4 \times 10^{-20}$  (with respect to 1 atm), and the oxide composition is 2.4 mol% ZrO<sub>2</sub>. Correspondingly, as one moves upwards along the red dotted line, an oxide increasingly enriched in the less stable

oxide, in this case  $ZrO_2$ , is encountered. As Hf preferentially oxidizes, and is depleted from the base alloy, the alloy composition will traverse to the right on the lower x-axis in the depletion zone. This results in traversing to the right on the top x-axis (oxide composition), i.e., assuming an inward growing oxide, the Hf-depleted regions become richer in Zr, forming more  $ZrO_2$ , with a concomitant increase in the equilibrium partial pressure of oxygen.

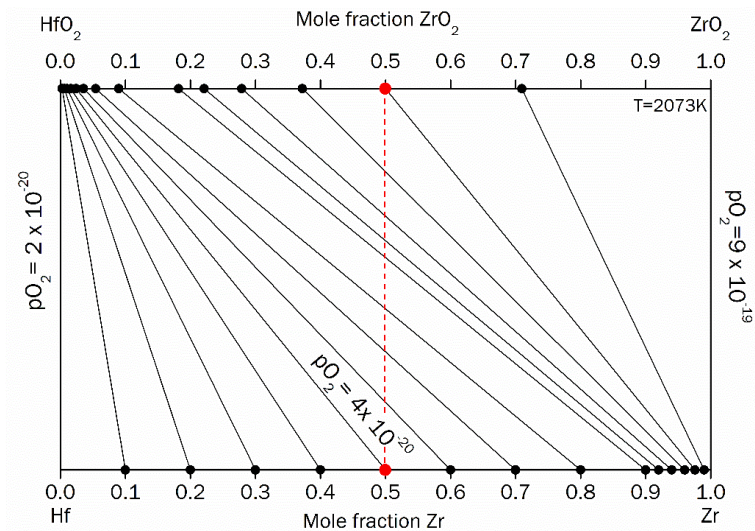


Figure 2.8: Composition balance diagram showing the equilibrium concentrations of the oxides in a binary solution when formed from a binary metal alloy, Hf-Zr. Results are shown in increments of 10 mol % with respect to alloy composition at 2073K. The red dotted line is a reference line, which goes from the 50 mol% Zr composition in the alloy to the 50 mol %  $ZrO_2$  in the oxide.

Figure 2.9 and Figure 2.10 represent the oxidation of alloys in which the constituents are members of adjacent groups in the periodic table with more widely differing oxide stabilities. In both these cases, the oxide composition is comprised entirely or almost entirely by the element with the most thermodynamically stable oxide. The grey, shaded regions shown on the top x-axis in Figure 2.9 indicate the solubility of the respective oxides in real systems. A

similar shaded region is not shown in Figure 2.10 due to the relevant phase diagram being unavailable.

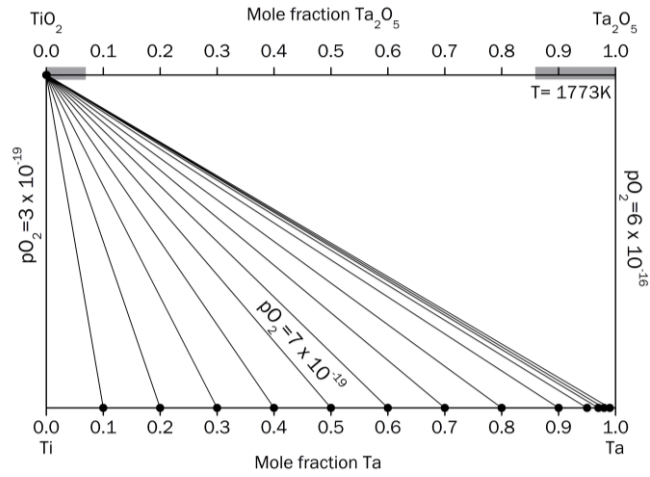


Figure 2.9: Composition balance diagram showing the equilibrium concentrations of the oxides in a binary solution when formed from a binary metal alloy, Ti-Ta (groups IV and V), of varying compositions at 1773K. Note that even at 99% tantalum in the alloy, the oxide composition is 0.08% Ta<sub>2</sub>O<sub>5</sub> at equilibrium. TiO<sub>2</sub> is assumed to be in the rutile phase. Grey shaded areas on the oxide axis indicate regions of solid solubility in the real system<sup>120</sup>.

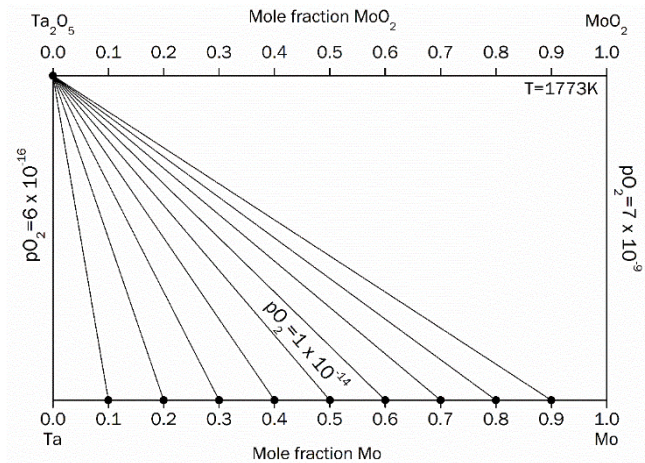


Figure 2.10: Composition balance diagram showing the equilibrium concentrations of the oxides in a binary solution when formed from a binary metal alloy, Ta-Mo, of varying compositions at 1773K. The larger difference in thermodynamic favorability in the oxides when comparing different groups (group V vs VI) results in a large tendency towards preferential oxidation to form  $Ta_2O_5$ , the more thermodynamically favored oxide.

#### Composition Balance Diagrams: Ideal Transition Metal Carbide and Ideal Oxide Solution

A similar approach was followed to calculate the composition balance diagram for the refractory carbides, where the additional product, CO (g), must be considered. In the case of HfC-ZrC, which would oxidize to  $HfO_2$  and  $ZrO_2$  respectively, the condensed phases have the same oxygen stoichiometry and the  $pCO$  term will cancel out. Results are shown in Figure 2.11. Note the increased equilibrium  $pO_2$  for the end members compared to Figure 2.8. However, for TiC-TaC: $TiO_2$ - $Ta_2O_5$ , the  $pCO$  term remains (Equation (2.22)). To simplify the analysis, the value of  $pCO$  was fixed at 1. The resulting diagram is shown in Figure 2.12. Note that for the HfC-ZrC oxidizing to  $HfO_2$ - $ZrO_2$  (Figure 2.11), the oxide solution is more reflective of substrate composition (on a cation basis), compared to the metallic alloy case (Figure 2.8). Note that the equilibrium  $pO_2$ s for HfC- $HfO_2$  and ZrC- $ZrO_2$  are the same order of magnitude and are both significantly higher than those of the end members in the alloy case (Figure 2.8). For TiC-TaC oxidizing to  $TiO_2$ - $Ta_2O_5$  (Figure 2.12), the tendency towards preferential formation of  $TiO_2$  also

decreases relative to the metallic alloy case (Figure 2.9). However,  $\text{TiO}_2$  is still strongly favored over  $\text{Ta}_2\text{O}_5$ .

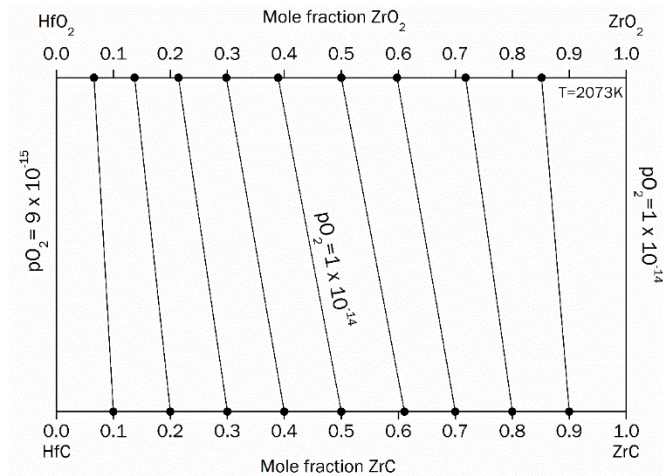


Figure 2.11: Composition balance diagram showing the equilibrium concentrations of the oxides in a binary solution when formed from a binary carbide,  $\text{HfC-ZrC}$ , of varying compositions at 2073K.

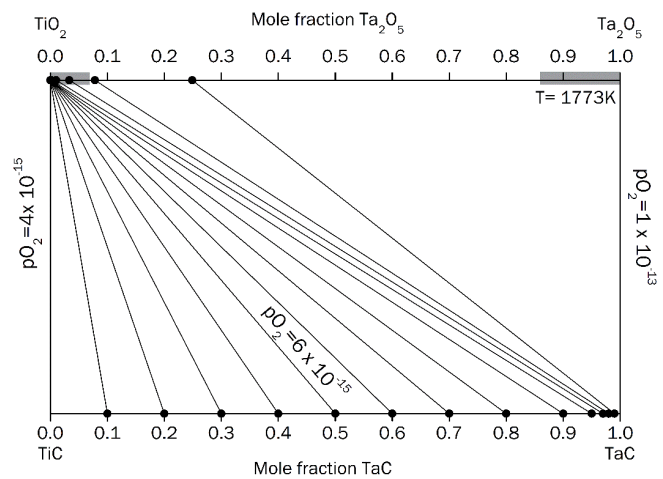


Figure 2.12: Composition balance diagram showing the equilibrium concentrations of the oxides in a binary solution when formed from a binary carbide,  $\text{TiC-TaC}$ , of varying compositions. Note that the tendency towards preferential formation of  $\text{TiO}_2$  decreases relative to the metallic alloy case (Figure 2.9).  $p\text{CO}$  was assumed to be 1.  $\text{TiO}_2$  is assumed to be in the rutile phase. Grey shaded areas on the oxide axis indicate regions of solid solubility in the real system<sup>120</sup>.

### *Free Energy Minimization: Ideal Ternary and Quinary Substrate and Oxide Solutions*

The predictions using the FactSage free energy minimization software were confirmed by comparison to the analytical results for the Hf-Zr system (Figure 2.8). Thus validated, this approach was then used to generate predictions for systems with more than two components. The equimolar cases for a ternary alloy, Hf-Zr-Ti, and a quinary alloy, Hf-Zr-Ti-Ta-Nb, at 1773K were studied as examples. Both the ternary and quinary alloys under consideration are known to be in the BCC phase at this temperature<sup>107,121,122</sup>. In the ternary case, the HfZrTi alloy is assumed in equilibrium with an ideal solid solution containing HfO<sub>2</sub>, ZrO<sub>2</sub> and TiO<sub>2</sub>. Similarly, the HfZrTiTaNb alloy is assumed in equilibrium with an ideal solid solution containing HfO<sub>2</sub>, ZrO<sub>2</sub>, TiO<sub>2</sub>, Ta<sub>2</sub>O<sub>5</sub> and Nb<sub>2</sub>O<sub>5</sub>. There are no data on the quinary phase equilibria for the corresponding oxide phases; therefore, the most stable, condensed phase for each oxide according to available data was assumed, regardless of crystal structure.

Table 2.3 and Table 2.4 summarize the results of the calculations performed for the alloy cases. In the ternary case (Table 2.3), the oxide consists primarily of Hf and Zr and contains very little Ti; the alloy is depleted in Hf. In the quinary case (Table 2.4), note the preferential formation of group IV oxides (Hf, Zr, Ti) and corresponding depletion of those constituents in the alloy. Ti suboxides (TiO, Ti<sub>2</sub>O<sub>3</sub>) are also predicted to form. Table 2.5 shows the results for the free energy minimization calculation for (Hf<sub>0.2</sub>Zr<sub>0.2</sub>Ti<sub>0.2</sub>Ta<sub>0.2</sub>Nb<sub>0.2</sub>)C and (Hf<sub>0.2</sub>Zr<sub>0.2</sub>Ti<sub>0.2</sub>Ta<sub>0.2</sub>Nb<sub>0.2</sub>)B<sub>2</sub> each in equilibrium with an equimolar solid solution containing HfO<sub>2</sub>, ZrO<sub>2</sub>, TiO<sub>2</sub>, TaO<sub>2.5</sub>, and NbO<sub>2.5</sub>, conducted at 1700 °C (to allow for comparison to experimental data, section 2.4). The calculation predicts the formation of an oxide primarily rich in the group IV elements (Hf, Zr and Ti), with Ta and Nb content in the oxide below experimentally determinable limits for both the carbide and the boride.

It is also interesting to note that the calculation for the high entropy carbide resulted in the prediction of Nb<sub>8</sub>C<sub>7</sub> (NbC<sub>0.87</sub>), which is enriched in Nb relative to the rock-salt high entropy

carbide phase constituent. Smith et al.<sup>123</sup> reported the diffraction patterns for a range of sub-stoichiometric niobium carbide, and found the X-ray diffraction peaks to occur at the same or similar 2-theta values as stoichiometric NbC. Therefore, it is possible that the peaks corresponding to a secondary carbide shown in Figure 2.15 are an indication that a sub-stoichiometric niobium carbide exists.

*Table 2.3: Equilibrium calculation showing the final composition of the oxide scale that results from an equimolar HfZrTi ternary alloy at 1773K in equilibrium with an equimolar oxide ideal solution containing HfO<sub>2</sub>, ZrO<sub>2</sub> and TiO<sub>2</sub>, as well as the depletion of Hf from the underlying alloy.*

| Constituents                 | Input (mol) | Input (mol%) | Output (mol %)        |
|------------------------------|-------------|--------------|-----------------------|
| <b>Alloy, Ideal Solution</b> |             |              |                       |
| Hf                           | 1           | 33.3         | 1.03                  |
| Zr                           | 1           | 33.3         | 32.3                  |
| Ti                           | 1           | 33.3         | 66.7                  |
| <b>Oxide, Ideal Solution</b> |             |              |                       |
| HfO <sub>2</sub>             | 1           | 33.3         | 65.6                  |
| ZrO <sub>2</sub>             | 1           | 33.3         | 34.4                  |
| TiO <sub>2</sub>             | 1           | 33.3         | 4.70x10 <sup>-3</sup> |

Table 2.4: Calculation results showing the final composition of the oxide scale from an input of equimolar quinary alloy  $Hf_{0.2}Zr_{0.2}Ti_{0.2}Ta_{0.2}Nb_{0.2}$  at 1773K in equilibrium with an equimolar (cation atom basis) oxide ideal solid solution containing  $HfO_2$ ,  $ZrO_2$ ,  $TiO_2$ ,  $Ta_2O_5$ ,  $Nb_2O_5$ , as well as the depletion of Hf, Zr and Ti from the underlying alloy.

| Constituents                        | Input (mol) | Input (mol%) | Output (mol %)        |
|-------------------------------------|-------------|--------------|-----------------------|
| <b>Alloy Ideal Solution</b>         |             |              |                       |
| Hf                                  | 1           | 20           | $7.87 \times 10^{-8}$ |
| Zr                                  | 1           | 20           | $4.72 \times 10^{-6}$ |
| Ti                                  | 1           | 20           | $8.05 \times 10^{-3}$ |
| Ta                                  | 1           | 20           | 48.4                  |
| Nb                                  | 1           | 20           | 51.5                  |
| <b>Oxide Ideal Solution</b>         |             |              |                       |
| $HfO_2$                             | 1           | 20           | 35.9                  |
| $ZrO_2$                             | 1           | 20           | 35.9                  |
| $TiO_2$                             | 1           | 20           | 4.05                  |
| Ti sub-oxides ( $TiO$ , $Ti_2O_3$ ) | -           | -            | 23.2                  |
| $TaO_{2.5}$                         | 1           | 10           | 1.05                  |
| $NbO_{2.5}$                         | 1           | 10           | $6.32 \times 10^{-5}$ |

Table 2.5: Equilibrium calculation showing the final composition of the oxide scale and underlying substrate that results from an inputs of equimolar quinary alloy  $(\text{Hf}_{0.2}\text{Zr}_{0.2}\text{Ti}_{0.2}\text{Ta}_{0.2}\text{Nb}_{0.2})\text{C}$  and  $(\text{Hf}_{0.2}\text{Zr}_{0.2}\text{Ti}_{0.2}\text{Ta}_{0.2}\text{Nb}_{0.2})\text{B}_2$ , respectively, at 1700 °C in equilibrium with an equimolar (cation atom basis) oxide ideal solid solution containing  $\text{HfO}_2$ ,  $\text{ZrO}_2$ ,  $\text{TiO}_2$ ,  $\text{Ta}_2\text{O}_5$ ,  $\text{Nb}_2\text{O}_5$ . † indicates a separate phase not part of the substrate or oxide solid solution.

| Constituents                          | Input (mol) | Input (mol%) | Carbide<br>Output (mol %) | Boride<br>Output (mol %) |
|---------------------------------------|-------------|--------------|---------------------------|--------------------------|
| <b>Carbide/Boride Ideal Solution</b>  |             |              |                           |                          |
| Hf                                    | 1           | 20           | 0.015                     | 0.025                    |
| Zr                                    | 1           | 20           | 0.022                     | 0.180                    |
| Ti                                    | 1           | 20           | 14.1                      | 15.5                     |
| Ta                                    | 1           | 20           | 44.7                      | 42.2                     |
| Nb                                    | 1           | 20           | 41.1                      | 42.2                     |
| <b>Nb<sub>8</sub>C<sub>7</sub></b>    | -           | -            | †                         | -                        |
| <b>B<sub>2</sub>O<sub>3</sub> (l)</b> | -           | -            | -                         | †                        |
| <b>Oxide Ideal Solution</b>           |             |              |                           |                          |
| HfO <sub>2</sub>                      | 1           | 20           | 39.9                      | 42.7                     |
| ZrO <sub>2</sub>                      | 1           | 20           | 39.9                      | 42.6                     |
| TiO <sub>2</sub>                      | 1           | 20           | 20.2                      | 8.50                     |
| Ti <sub>3</sub> O <sub>5</sub>        | -           | -            | -                         | 6.19                     |
| TaO <sub>2.5</sub>                    | 1           | 20           | 8.22x10 <sup>-4</sup>     | 9.89x10 <sup>-3</sup>    |
| NbO <sub>2.5</sub>                    | 1           | 20           | 4.38x10 <sup>-7</sup>     | 5.32x10 <sup>-9</sup>    |
| <b>Equilibrium pO<sub>2</sub></b>     | -           | -            | 2.55x10 <sup>-13</sup>    | 3.70x10 <sup>-13</sup>   |

*Free Energy Minimization: Ideal Alloy and Real Oxide Solid Solution*

Thus far, both the alloy and oxide were assumed to be in ideal solid solutions respectively. Comparison of the predictions from the ideal case for a given system to the real case offer insight into the suitability of the ideal solution approximation. Table 2.6 compares the resulting oxide compositions calculated using the ideal solid solution approximation, and real solid solution data, for the oxide solid solution. In both cases, the alloy is assumed to be an ideal solid solution. Using the real oxide solution data, the predicted oxide is tetragonal ZrO<sub>2</sub> with small amounts of TiO<sub>2</sub>, like the ideal solution case.

*Table 2.6: Results for stable oxides formed from ideal equimolar Zr-Ti solution when considering the oxide solid solution as an ideal solution (first column) compared to the results using the real oxide solution database (second column) at 1773K. In both cases, the alloy is considered as an ideal solid solution. Note partial depletion of Zr from the underlying alloy is predicted.*

| <b>Constituents</b>          | <b>Output (mol%)</b>   | <b>Output (mol %)</b>   |
|------------------------------|--|---|
|                              | <b><u>Ideal</u> Oxide Solution in equilibrium with ideal alloy</b> | <b><u>Real</u> Oxide Solution in equilibrium with ideal alloy</b> |
| <b>Alloy, Ideal Solution</b> |  |   |
| Zr                           | 24.6   | 22.2  |
| Ti                           | 75.4   | 77.8  |
| <b>Oxide Solution</b>        |  |   |
| ZrO <sub>2</sub>             | 99.9   | 99.9  |
| TiO <sub>2</sub>             | 2.03x10 <sup>-2</sup>  | 1.97x10 <sup>-2</sup>   |

### 2.3.4. Discussion

#### *Composition balance diagrams: binary metal alloys*

The composition balance diagrams shown in the preceding sections provide a visual method to illustrate the extent of preferential oxidation expected. They also demonstrate the strong sensitivity of preferential oxidation to the difference in relative thermodynamic stability between the oxides of interest. This sensitivity is best seen when comparing Figure 2.8 and Figure 2.9 where the periodic trend in the thermodynamic stabilities of the oxides of the elements under consideration is shown.  $\text{HfO}_2$  and  $\text{ZrO}_2$ , formed from elements in the same periodic table group, have similar thermodynamic stabilities ( $\Delta G_{\text{HfO}_2}^{\circ} = -779.4 \text{ kJ/mol}$  and  $\Delta G_{\text{ZrO}_2}^{\circ} = -715.6 \text{ kJ/mol}$  at 2073K), as shown in Figure 2.3. Even so, this small difference in thermodynamic stability has a large effect on the thermodynamic prediction for preferential oxidation (Figure 2.8). Given the result for Hf-Zr alloy oxidation which forms two oxides with similar thermodynamic stabilities, it is not surprising to see that for the oxidation of a Ti-Ta alloy (group IV-V alloy) oxidizing, the tendency towards preferential oxidation of Ti is greater. The difference in the free energy for oxidation per mole of  $\text{O}_2$  is smaller when comparing between two elements in the same group, Hf-Zr, versus two elements in different groups, Ti-Ta. This is again seen in Figure 2.10, wherein Ta in Ta-Mo alloy is expected to dominate the composition of resulting oxide scale, even for alloy compositions rich in Mo.

It is to be noted that in the cases shown in Figure 2.9 and Figure 2.10, the choice of oxides to represent the end members of the oxide side of the diagram were based on the predominantly observed oxide in each M-O system, where  $M = \text{Ti, Ta}$ . In reality, the existence of suboxides and complex oxides in the Ti-Ta-O system may result in a more complex scale. However, it is unlikely that consideration of these oxides will result in a significantly reduced tendency towards preferential oxidation, given the large difference in thermodynamic stabilities between their oxides. Park and Butt<sup>124</sup> experimentally studied the oxidation of a Ti-Ta alloy at

varying compositions from 0-60 wt% Ta, and found that generally speaking, the oxide scale consisted of a  $\text{TiO}_2$  scale with increasing Ta content as one moved towards the metal-oxide interface, suggesting the  $\text{Ta}_2\text{O}_5$  formed when Ti was depleted from the alloy. This is consistent with the diagram shown in Figure 3 wherein, as more Ti is depleted due to oxidation, the alloy composition becomes Ta-rich, allowing for the formation of Ta-rich oxides.

It is also interesting to compare the composition balance diagram for the metal alloys oxidizing to that of their corresponding carbides oxidizing. Take the case of HfC-ZrC (Figure 2.11), wherein the oxide composition now more closely reflects that of the base material composition compared to the oxide composition for the corresponding alloy (Figure 2.8). The spread of the tie lines indicates that preferential oxidation of the HfC component in the carbide solid solution will be much less significant than Hf in the Hf-Zr alloy (50 mol% ZrC yields a 39 mol%  $\text{ZrO}_2$  oxide compared to 50 mol % Zr yielding 3 mol%  $\text{ZrO}_2$ ). This is also the case for TiC-TaC where we see again a larger spread in the tie lines compared to the metal alloy case. Section 2.2 discussed the differences in thermodynamic stabilities when considering the alloy, carbide, and boride cases for any two given elements, (Figure 2.5). The relative difference in the thermodynamic stability of the oxides formed from Hf and Zr carbides is significantly reduced compared to the metal case, due to the formation of the gaseous oxide, CO (g) and the increase in equilibrium  $p\text{O}_2$ . The difference in the oxide formation energy from HfB<sub>2</sub> and ZrB<sub>2</sub> fall between these values (Figure 2.5). Thus, the oxide formation from the metal and the carbide serve as bounding cases for the purposes of predicting preferential oxidation.

### *Free energy minimization*

Calculations for the ternary case using the ideal solid solution approximation showed that the oxidation of the equimolar group IV HfZrTi alloy would result in a HfO<sub>2</sub>-ZrO<sub>2</sub> rich scale. Very small amounts of TiO<sub>2</sub> are predicted in the final state, well within the solubility limits in

both  $\text{HfO}_2$  and  $\text{ZrO}_2$ <sup>78,79</sup>. If the trend exhibited in the ternary case is extrapolated to the high entropy  $\text{Hf}_{0.2}\text{Zr}_{0.2}\text{Ti}_{0.2}\text{Ta}_{0.2}\text{Nb}_{0.2}$  alloy case, insignificant amounts of Ta and Nb oxides would be expected. Indeed, preferential oxidation of the group IV elements is predicted, and the oxide scale contains 1 mol% or less of  $\text{Ta}_2\text{O}_5$  and  $\text{Nb}_2\text{O}_5$  (Table 2.4, Table 2.5). The equilibrium  $p_{\text{O}_2}$  at the oxide/alloy interface due to the assemblage of the different oxides that are expected to form in the initial stages of oxidation ( $\text{HfO}_2$ ,  $\text{TiO}_2$ ,  $\text{ZrO}_2$ ,  $\text{Ta}_2\text{O}_5$ ,  $\text{Nb}_2\text{O}_5$ ) is higher than that due to only the most stable oxides (e.g.  $\text{HfO}_2$ ,  $\text{ZrO}_2$ ), and will influence the final oxide composition determined via the free energy minimization approach. Similar results obtain for the high entropy carbides and diborides. The computational results for the high entropy carbide and diboride will also be discussed in more detail in section 2.4 along in the context of experimental results.

#### *Ideal solution vs real solution thermodynamics*

The tendency towards preferential oxidation is highly sensitive to the relative difference in the standard Gibbs free energy of formation for the oxides. Figure 2.3 shows a sizable difference in the relative thermodynamic favorability of  $\text{ZrO}_2$  and  $\text{TiO}_2$ , similar to the difference between  $\text{Ta}_2\text{O}_5$  and  $\text{TiO}_2$  (Figure 2.3 and Figure 2.9). This suggests that for a ZrTi alloy, preferential oxidation of Zr is expected. Calculations using both the ideal solid solution approximation and real solid solution data indeed show that the oxide composition is dominated by  $\text{ZrO}_2$  (Table 2.6). Gaps in current knowledge and available data have driven the need to assume ideal thermodynamic behavior for most of the calculations presented here. The result in Table 2.6 confirms that the ideal solution approximation can sufficiently predict the extent of preferential oxidation in refractory materials.

### *Effect on underlying material*

An estimated reduction in configurational entropy due to the reduced number of components in the solid solution alloy or compound can be calculated using Equations (2.11) and (2.12). For the refractory high entropy alloy case shown in Table 2.4 calculated at 1773K, where the HfZrTiTaNb alloy effectively goes from  $N=5$  to  $N=2$  due to preferential oxidation, this results in a change in  $S_{\text{config}}$  from 13.4 J/mol·K to 5.8 J/mol·K (using Equation (2.11)), which is an approximately 60% reduction in configurational entropy. If configurational entropy is required to stabilize the alloy solid solution phase<sup>125</sup>, then such a reduction may result in the destabilization of this phase, and the formation of other, competing alloy phases. This will be accompanied by a corresponding change in material properties. For example, the preferential oxidation of group IV elements in the high entropy carbide may result in the formation of secondary phases such as Ta<sub>2</sub>C and Nb<sub>2</sub>C, which have different crystal structures compared to the original rock-salt. On the other hand, if the remaining components form a thermodynamically stable solid solution, then the effects may include a reduction in melting temperature or in the originally enhanced mechanical properties. The work presented here and previously<sup>97</sup> indicates that such preferential oxidation of refractory alloys and compounds is closely correlated with groups in the periodic table; if the remaining elements all belong to the same periodic group, they may remain in solid solution.

## 2.4. Experimental Verification of Preferential Oxidation Predictions

### 2.4.1. Methodology

A brief description of the methodology is provided here for the tests used to verify the thermodynamic predictions, and detailed descriptions for the materials and methods will be given in the next chapter. The partial pressure of oxygen is not defined as an input but is a result from the free energy minimization calculations given the initial condition the substrate

solid solution at equilibrium with an oxide solid solution. The materials chosen for the study are carbides and borides containing group IV and group V elements: Hf, Zr, Ti, Ta and Nb. The  $(\text{Hf}_{0.2}\text{Zr}_{0.2}\text{Ti}_{0.2}\text{Ta}_{0.2}\text{Nb}_{0.2})$  carbide and diboride were also among the first compositions for which single phase, UHTC solid solutions were made<sup>15,126</sup>. The experimental results will be compared to computational predictions calculated for the high entropy carbide and diboride at 1700 °C (Table 2.5).

The  $(\text{Hf}_{0.2}\text{Zr}_{0.2}\text{Ti}_{0.2}\text{Ta}_{0.2}\text{Nb}_{0.2})$  carbide and diboride were exposed to flowing ( $\sim 1\text{L}/\text{min}$ ) 1%O<sub>2</sub> in argon at a nominal temperature of 1700 °C for 5 minutes using the resistive heating system (Chapter 3, 5). After the oxidation, the samples were characterized in plan view and cross-section with scanning electron microscopy (SEM), energy dispersive spectroscopy (EDS) and X-ray diffraction (XRD). For cross-section examination, the samples were then manually fractured across the hot zone, and the cross-sections were examined in an SEM. Focused ion beam (FIB) milling was also used to obtain selected samples for further EDS analysis.

## 2.4.2. Results

### *Carbides: after oxidation at 1700 °C, 1%O<sub>2</sub>, 5 minutes*

Figure 2.13 shows light optical (a-c) and back-scattered electron images (d) of the exposed  $(\text{Hf}_{0.2}\text{Zr}_{0.2}\text{Ti}_{0.2}\text{Ta}_{0.2}\text{Nb}_{0.2})\text{C}$  specimen. The hot zone can be discerned by a dark gray region in the middle of the specimen surrounded by a lighter gray oxide. These images highlight the temperature gradients inherent in the experimental set-up, which will be addressed in more detail in Chapter 4. The current chapter focuses on results obtained from the center of the hot zone, well within the boundary of the pyrometer sighting zone.

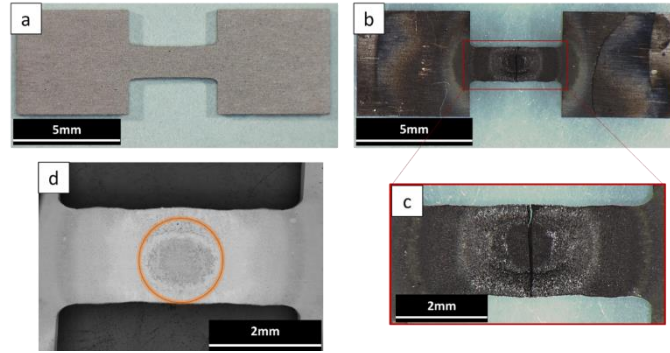


Figure 2.13: Plan view light optical images showing (HfZrTiTaNb)C (a) before oxidation, (b-c) after oxidation at a nominal temperature of 1700 °C in 1%O<sub>2</sub> for 5 minutes, and manual fracture along the hot zone, and (d) back-scattered electron image (plan view) of the hot zone before fracture. The orange circle is added to (d) to show the estimated size and location of the pyrometer sighting zone.

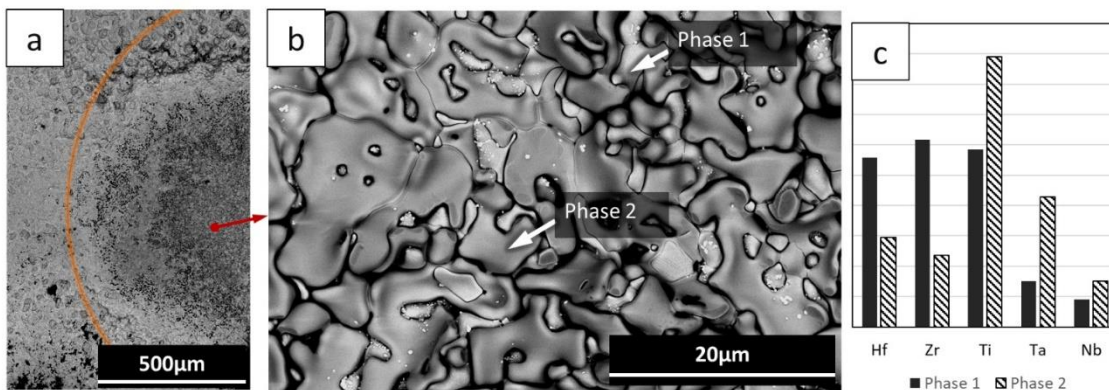


Figure 2.14: Plan view images of (HfZrTiTaNb)C after oxidation at a nominal temperature of 1700 °C in 1%O<sub>2</sub>/bal Ar for 5 minutes. (a) A low-magnification image of the hot zone on one half of a dogbone (orange line indicates approximate boundary of the pyrometer sighting zone), (b) higher magnification, back-scattered electron image obtained at 5kV of the microstructure in center of the pyrometer sighting zone (c) semi-quantitative composition of the two phases apparent in this region from EDS obtained at 10kV.

Two phases can be discerned from the microstructure in the hot zone as shown in Figure 2.14: one that is rich in the group IV elements, and the other rich in Ti, but now with

increased Ta and, to a lesser extent, Nb. The morphology indicates the occurrence of melting, particularly the Ti-rich phase. The first phase, rich in group IV elements, is likely a titanate (see Table 2.7). A eutectic between  $\text{HfO}_2$  and  $\text{TiO}_2$  exists at  $\sim 1740 \pm 15^\circ\text{C}$  in the  $\text{TiO}_2$  rich side<sup>80</sup>, which is within the uncertainty range of the test temperature. Figure 2.15 shows the corresponding indexed X-ray diffraction pattern of oxide formed on  $(\text{Hf}_{0.2}\text{Zr}_{0.2}\text{Ti}_{0.2}\text{Ta}_{0.2}\text{Nb}_{0.2})\text{C}$ . The composition of Phase 1 is consistent with a titanate. The composition and morphology of Phase 2 in Figure 2.14 is a good match for  $\text{TiTa}_2\text{O}_7$ , which melts at  $1674^\circ\text{C}$ <sup>84</sup>. Other possible phases are listed in Table 2.7, given that substitution of elements from the same periodic group are likely, as discussed later.

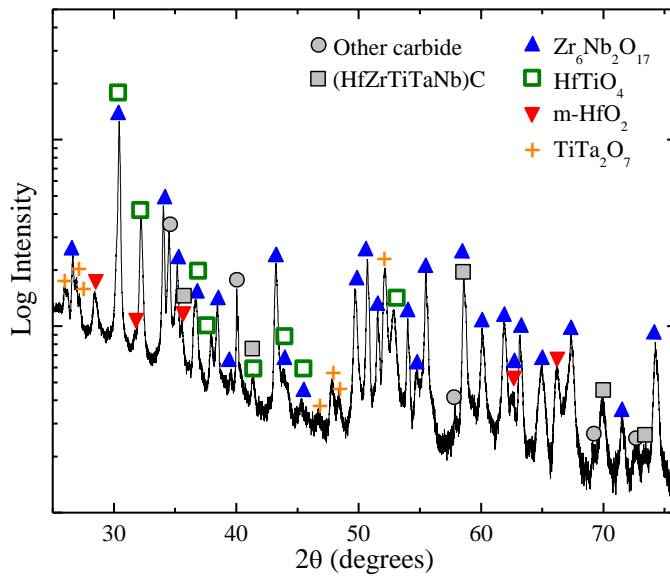


Figure 2.15: X-ray diffraction spectra taken after oxidation for  $(\text{Hf}_{0.2}\text{Zr}_{0.2}\text{Ti}_{0.2}\text{Ta}_{0.2}\text{Nb}_{0.2})\text{C}$  exposed for 5 mins at  $1700^\circ\text{C}$  in 1 mol %  $\text{O}_2/\text{bal Ar}$ .

Figure 2.16 shows the ion conversion and electron (ICE) detector secondary electron (SE) image and EDS maps of oxide scale fracture cross-section, wherein the gas-oxide surface is underneath the carbon layer deposited during the FIBing process. A white circle is added to

focus on an area of interest, which is a partially oxidized carbide grain. The oxygen lean areas correspond with an enrichment of Ta and Nb, whereas the oxygen rich areas are mostly rich in the group IV elements.

*Table 2.7: Possible phase matches for the x-ray diffraction pattern (Figure 2.15) collected from (Hf<sub>0.2</sub>Zr<sub>0.2</sub>Ti<sub>0.2</sub>Ta<sub>0.2</sub>Nb<sub>0.2</sub>)C oxidized at 1700°C (actual 1715°C) in 1% O<sub>2</sub>/Ar for 5 mins. PDF numbers are indicated in parentheses and references as superscripts.*

| Indicated Phase   | Crystal System | Possible alternate phases  |
|---|----------------|--|
| Zr <sub>6</sub> Nb <sub>2</sub> O <sub>17</sub> (04-011-2890) | Orthorhombic   | (Hf,Zr) <sub>6</sub> (Ta,Nb) <sub>2</sub> O <sub>17</sub> <sup>127</sup> |
| HfTiO <sub>4</sub> (01-080-2977)                              | Orthorhombic   | (Hf,Zr)TiO <sub>4</sub> <sup>80</sup>                                    |
| HfO <sub>2</sub> (00-034-0104)                                | Monoclinic     | (Hf,Zr)O <sub>2</sub> <sup>128,129</sup>                                 |
| TiTa <sub>2</sub> O <sub>7</sub> (01-084-8891)                | Monoclinic     | Ti(Ta,Nb) <sub>2</sub> O <sub>7</sub> <sup>130</sup>                     |
| Other carbide   | Cubic          | NbC <sub>0.92</sub> O <sub>0.01</sub> (04-022-7393)                      |
|   |                | Nb <sub>0.80</sub> Ta <sub>0.20</sub> C (01-085-4222)                    |
|   |                | Zr <sub>0.20</sub> Ta <sub>0.80</sub> C (04-002-6875)                    |
|   |                | Nb <sub>x</sub> C <sub>x-1</sub> <sup>123</sup>                          |
|   |                | NbC (00-038-1364)  |
|   |                | NbC <sub>0.87</sub> (04-008-3212)  |

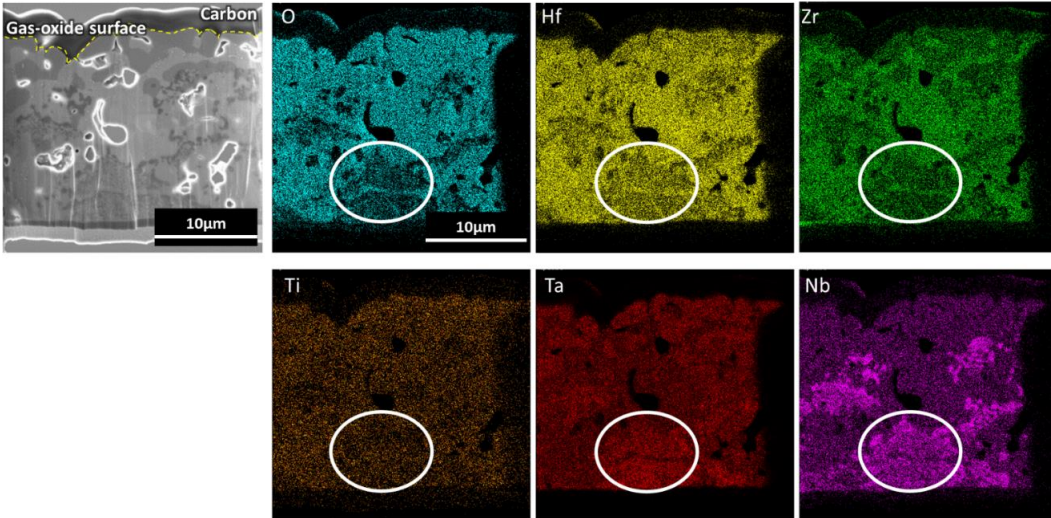


Figure 2.16: FIB lift out from the hot zone in  $(\text{Hf}_{0.2}\text{Zr}_{0.2}\text{Ti}_{0.2}\text{Ta}_{0.2}\text{Nb}_{0.2})\text{C}$  oxidized for 5 mins at  $1700\text{ }^{\circ}\text{C}$  in 1 mol%  $\text{O}_2/\text{bal Ar}$ . [Left] Secondary electron image of the focus ion beam (FIB) cross section of part of the oxide scale. [Right] EDS maps showing elemental distribution of oxygen, titanium, tantalum, hafnium, zirconium and niobium. The white circle is added to help guide the eye to a partially oxidized grain.

**Borides: after oxidation at  $1700\text{ }^{\circ}\text{C}$ , 1% $\text{O}_2$ , 5 minutes**

Figure 2.17 shows low and high magnification BSE images of the oxide formed in the hot zone region of the  $(\text{Hf}_{0.2}\text{Zr}_{0.2}\text{Ti}_{0.2}\text{Ta}_{0.2}\text{Nb}_{0.2})\text{B}_2$  specimen. In contrast to the carbide, the diboride specimen exhibits a uniform scale in plan view. This scale is composed largely of Hf, Zr and Ti, with very little Ta and almost no Nb. Analysis of the FIB cross section (Figure 2.18) taken from the oxidized diboride specimen shows that the surface oxide is dominated by Hf and Zr. Figure 2.19 shows a detail image of partially oxidized boride grains approximately  $3\text{ }\mu\text{m}$  below the surface, depleted in Hf and Zr. The oxide around these grains is rich in Hf, Zr and Ti. A Ti composition gradient in the grain is also observed, with a depleted region in the center of the grain. XRD results shown in Figure 2.20 and summarized in Table 2.8 confirm the preferential oxidation of group IV elements, and indicate the possibility of a secondary group V rich boride.

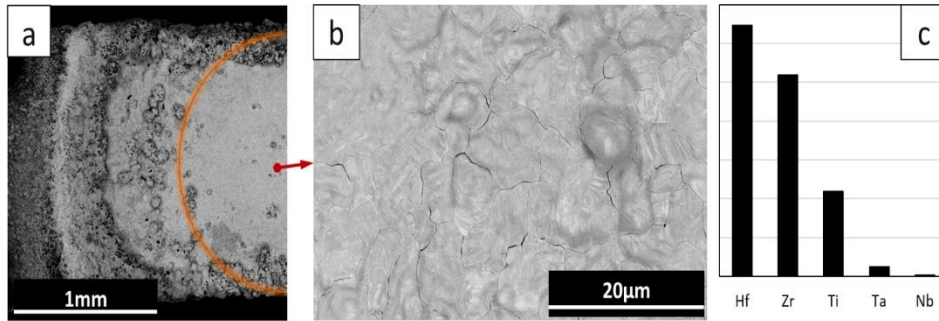


Figure 2.17: (a) Back-scattered electron image showing the plan view of the  $(\text{Hf}_{0.2}\text{Zr}_{0.2}\text{Ti}_{0.2}\text{Ta}_{0.2}\text{Nb}_{0.2})\text{B}_2$  dogbone specimen; the orange curve shows the approximate size and location of the hot zone. (b) Higher magnification plan view image of the microstructure in the pyrometer sighting zone. (c) Semi-quantitative EDS results for the elemental composition of the oxide in plan view.

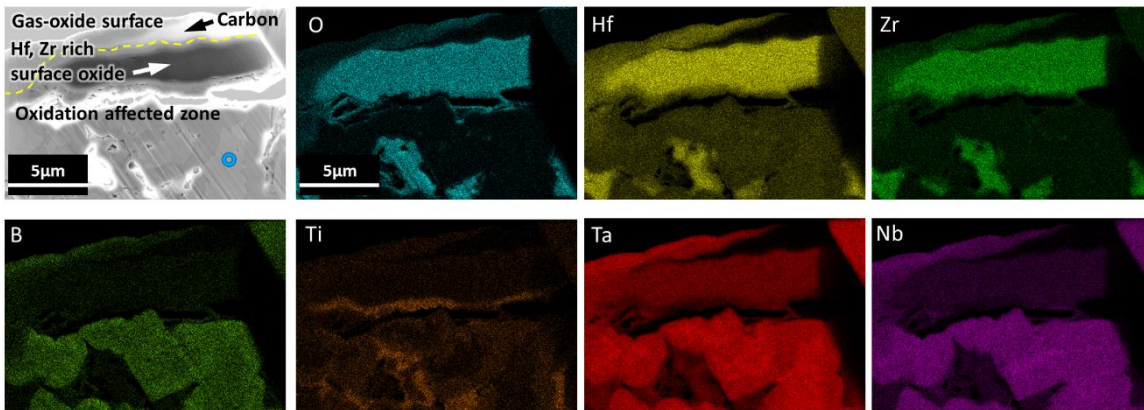


Figure 2.18:  $(\text{Hf}_{0.2}\text{Zr}_{0.2}\text{Ti}_{0.2}\text{Ta}_{0.2}\text{Nb}_{0.2})\text{B}_2$  oxidized for 5 mins at  $1700^\circ\text{C}$  in 1%  $\text{O}_2$ . Backscattered electron image in cross section of the top of the oxide scale at the hot zone, shown in the top left along with EDS maps showing elemental distribution of boron, oxygen, titanium, tantalum, hafnium, zirconium and niobium. The blue circular marker indicates the same location in Figure 2.19.

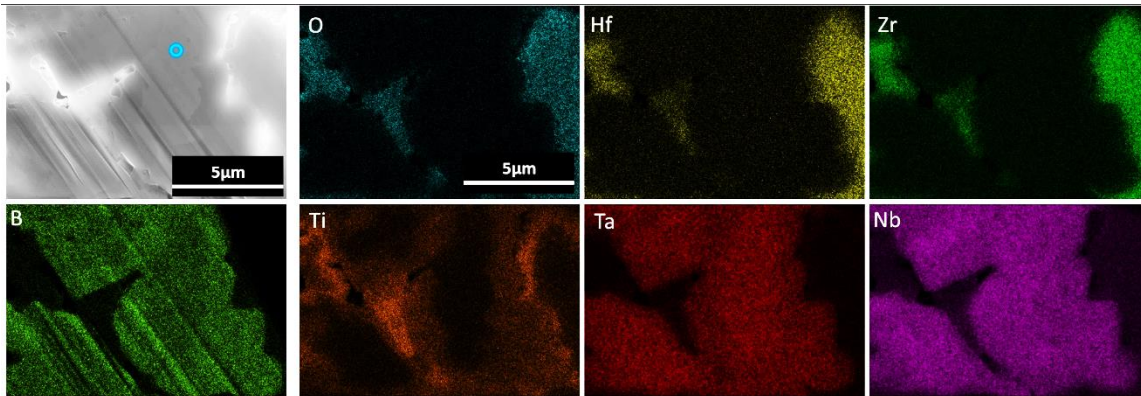


Figure 2.19:  $(\text{Hf}_{0.2}\text{Zr}_{0.2}\text{Ti}_{0.2}\text{Ta}_{0.2}\text{Nb}_{0.2})\text{B}_2$  oxidized for 5 mins at  $1700^\circ\text{C}$  in 1 mol%  $\text{O}_2/\text{bal Ar}$ . [Left] Secondary electron image of the focus ion beam (FIB) cross section of part of the oxide scale  $3\ \mu\text{m}$  below the surface in the hot zone, and EDS maps showing elemental distribution of boron oxygen, titanium, tantalum, hafnium, zirconium and niobium. The blue circular marker shown in Figure 2.18 is repeated here for reference.

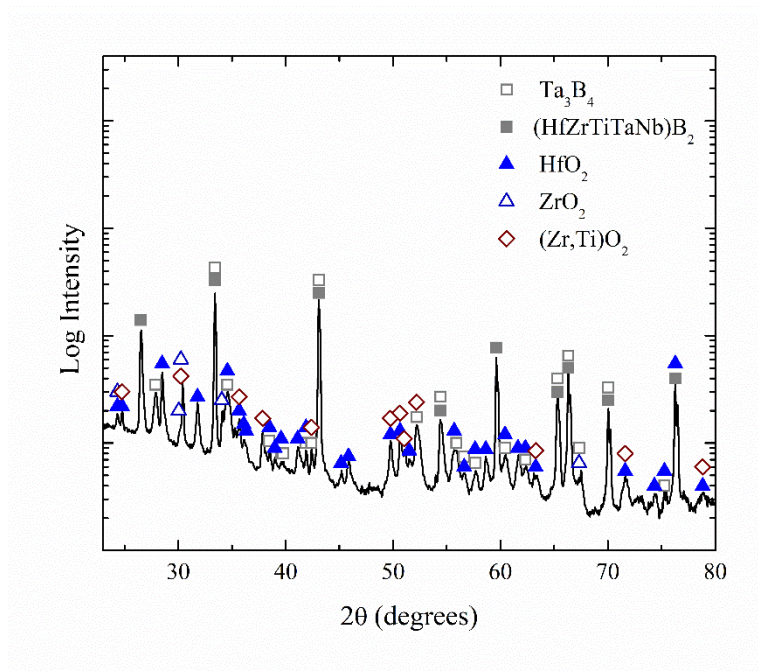


Figure 2.20: X-ray diffraction spectra taken after oxidation for  $(\text{Hf}_{0.2}\text{Zr}_{0.2}\text{Ti}_{0.2}\text{Ta}_{0.2}\text{Nb}_{0.2})\text{B}_2$  oxidized for 5 mins at  $1700^\circ\text{C}$  in 1 mol %  $\text{O}_2/\text{bal Ar}$ .

Table 2.8: Possible phase matches for the x-ray diffraction pattern (Figure 2.20) collected from  $(\text{Hf}_{0.2}\text{Zr}_{0.2}\text{Ti}_{0.2}\text{Ta}_{0.2}\text{Nb}_{0.2})\text{B}_2$  oxidized at 1700°C in 1%  $\text{O}_2/\text{Ar}$  for 5 mins. PDF numbers are indicated in parentheses, references in superscripts.

| Indicated Phase                           | Crystal System | Possible alternate phases/overlaps  |
|---|----------------|---|
| $\text{HfO}_2$ (00-034-0104)              | Monoclinic     | $(\text{Hf, Zr})\text{O}_2$ <sup>128,129</sup><br>$(\text{Hf, Zr, Ti})\text{O}_2$ <sup>80</sup>             |
| $\text{ZrO}_2$ (00-042-1164)              | Tetragonal     | $(\text{Hf, Zr})\text{O}_2$ <sup>128,129</sup><br>$(\text{Hf, Zr, Ti})\text{O}_2$ <sup>80</sup>             |
| $(\text{Zr, Ti})\text{O}_2$ (04-002-8273) | Orthorhombic   | $(\text{Hf, Zr, Ti})\text{O}_2$ <sup>80</sup><br>$(\text{Hf, Zr})_{1-x}\text{Ti}_x\text{O}_2$ <sup>80</sup> |
| $\text{Ta}_3\text{B}_4$ (04-003-3812)     | Orthorhombic   | $(\text{Nb, Ta})_3\text{B}_4$ <sup>130</sup>  |

### 2.4.3. Discussion

#### *Comparison of experimental results to calculated predictions*

The computational results (Table 2.5) predicted the oxidation of group IV elements is thermodynamically favored and therefore preferentially oxidize. The borides were expected to exhibit behavior like the carbides, except the secondary phase,  $\text{B}_2\text{O}_3$  (l,g) formed would also be condensed, albeit with a high vapor pressure. The formation of a carbon-poor, Nb rich phase was also predicted for the carbide system, suggesting that the original carbide may phase separate into the rock-salt phase and an  $\text{Nb}_8\text{C}_7$  phase in the oxidation affected regions.

The experimental observations are in generally good agreement with the calculated predictions for the oxide composition formed on the carbide and the diboride; the group IV elements preferentially oxidize over the group V elements, while the substrate is enriched in group V elements. Hf and Zr, which are the most stable, oxidize preferentially, followed by Ti. Within these groups, the extent of oxidation of the different elements also corresponds to their thermodynamic favorability. Of the group V elements,  $\text{Ta}_2\text{O}_5$  is more stable than  $\text{Nb}_2\text{O}_5$ , and thus Ta is expected to preferentially oxidize over Nb.

The Ta content in the oxide formed on the carbide (Phase 2 in Figure 2.14) is higher than both the calculated predictions and the experimental observations for the oxidized boride. This result is best explained by the non-protective nature of the oxide formed on the carbide, indicated by the porosity and extensive intergranular oxidation. This porosity, attributed to the formation and release of  $\text{CO}(\text{g})$ <sup>131,132</sup> through the oxide, results in a higher oxygen partial pressure at the reaction interface. This porous, non-protective oxide could result in the retention of any Ta oxide which initially forms upon exposure of the high entropy material to the oxidizing environment and the further oxidation of Ta over Nb ( $\text{Ta}_2\text{O}_5$  is more stable than  $\text{Nb}_2\text{O}_5$ ). The EDS maps in Figure 2.16 show that Ta is present in some of the oxygen rich regions, but almost no Nb. XRD matches for Nb-rich carbides are consistent with this interpretation and calculated predictions. In comparison, the formation of liquid bororia attending the oxidation of diborides may seal pores and defects in the oxide and result in a more protective scale<sup>2,8,133</sup>.

The more protective scale formed on the diboride, relative to the carbide, reduces the oxygen partial pressure at the reaction interface. This not only results in the predicted low tantalum content in the oxide, but also in the titanium compositional gradient shown in the boride grains in Figure 2.18 and Figure 2.19. Hf and Zr oxides are significantly more thermodynamically stable than  $\text{TiO}_2$ ; Hf and Zr oxidize preferentially from the boride, leading to Ti “lagging” the other group IV elements in extent of oxidation. The depletion zone in the Ti map (Figure 2.19) indicates that some Ti is still retained in the diboride. The  $\text{Ta}_3\text{B}_4$  boride phase indicated by the XRD results is consistent with a tantalum rich composition, in contrast with the Nb rich sub-stoichiometric carbide in the high entropy carbide case.

### *Complex oxide formation*

The thermodynamic predictions assume that the carbide or boride is in equilibrium with a solid solution oxide. The lack of available thermodynamic data for complex or ordered compounds limited consideration of these phases. A review of the relevant phase diagrams indicates that only Hf- and Zr- oxides exhibit complete solubility. Other binary and/or ternary oxide systems under consideration exhibit only partial solid solubility and complex oxide formation. Further, the XRD patterns for the oxidized samples indicate that oxide compounds such as  $Zr_6Nb_2O_{17}$  and titanates form. Table 2.1 summarizes known complex oxides which are likely to form based on a review of the available phase diagrams. As presented in the results, the actual oxides formed on the high entropy ceramics are complex variations of the compounds shown in Table 2.1, due to the possibility of ionic substitutions. For example, Hf and Zr are known to form substitutional solid solutions in alloys and oxides, and in their computational work, Hautier et al.<sup>105,130</sup> found that Ta and Nb have a high likelihood to substitute for each other. In fact, an analogous phase to  $Zr_6Nb_2O_{17}$  exists with Hf and Ta:  $Hf_6Ta_2O_{17}$ <sup>76,127</sup>.

It has been posited by Butler et al.<sup>95</sup> and Gorr et al.<sup>134</sup> that the formation of complex oxide phases may promote oxidation resistance, and therefore be an advantage of high entropy materials relative to conventional alloys and ceramics. Consideration of the complex oxide phases was outside the scope of this work at the time due to the lack of thermodynamic data. However, it can be seen from the experimental results that despite the formation of complex oxides, the elemental composition of the assemblage of oxides still followed the predicted trend, wherein the group IV elements dominated in the thermally grown oxide.

### *Implications for use of HE-UHTCs in oxidizing environments*

Oxides formed from group IV elements (Hf, Zr, Ti) have the highest melting temperatures ( $T_m$ ) and are most thermodynamically favored among the refractory elements. The predicted and observed preferential oxidation of these elements demonstrate that an HE-UHTC can be designed to form an oxide scale containing these elements. Further, the retention of elements with lower  $T_m$  oxides ( $Nb_2O_5$ ,  $Ta_2O_5$ ) as carbides or borides ensures a material with a high thermal stability overall, as Nb and Ta carbides and borides have melting temperatures greater than  $2000^\circ C$ <sup>115</sup>. The thermodynamic framework presented in this chapter can further be used to optimize such a composition as a multi-principal component material that is not equimolar but promotes a targeted oxide and substrate composition.

On the other hand, the preferential oxidation of several elements from the substrate can destabilize the underlying substrate and promote the formation of other phases, such as sub-stoichiometric Nb carbides. This destabilization can result in the loss of properties that might be gained from the high entropy design concept.

## 2.5. Conclusions

The relative thermodynamic stabilities of the oxides of the elements of interest were evaluated and summarized using Ellingham diagrams. Periodic trends in the thermodynamic stability of the oxides were noted. Group IV oxides are the most thermodynamically stable, followed by group V and VI respectively. The rapid formation and the thermodynamic stability of the group IV oxides are expected to be beneficial in promoting a solid scale at ultra-high temperatures. These periodic trends are expected to result in a tendency towards preferential oxidation in HE-UHTCs. Analytical and computational approaches using free energy minimization were used to quantify the extent of preferential oxidation in binary, ternary and quinary systems. The results indicate that the tendency for preferential oxidation is highly

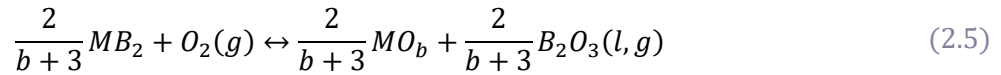
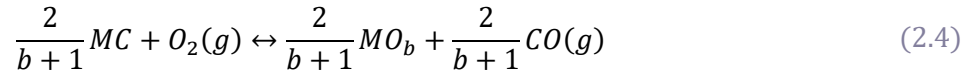
sensitive to the difference in relative thermodynamic stabilities of the constituent oxides. The differences in relative thermodynamic stabilities of oxides from the same periodic group, though small, were enough to result in a significant tendency towards preferential oxidation; this effect was dramatically more pronounced in systems with elements from different periodic groups (e.g., group IV-V alloys). The thermodynamic predictions were found to be in generally good agreement with experimental results for both the carbide and the diboride cases. However, non-protective oxide formation was observed to result in the oxidation of elements with relatively less thermodynamically favored oxides.

These findings provide guiding principles for the design of HE-UHTCs. Refractory high entropy materials (alloys, carbides, borides) will inevitably be comprised of constituents whose oxides span a wide range in relative thermodynamic stability. Thermodynamics will drive preferential oxidation, reducing the effect of configurational entropy in stabilizing the material. Therefore, while configurational entropy stabilizes the solid solution phase in the base material, this effect is not expected to hold in the oxidation affected zone during high temperature oxidation.

### 3. Oxidation Kinetics of (HfZrTiTaNb)C and (HfZrTiTaNb)B<sub>2</sub>

#### 3.1. Introduction

The oxidation mechanisms of group IV, V and VI carbides and diborides have been studied extensively due to their potential aerospace applications<sup>2</sup>. Equations (2.4) and (2.5), repeated here for reference, describe the expected generalized form of the reactions that take place upon exposure of carbides and borides, respectively, to oxidizing environments at high temperatures.



During the oxidation of carbides at high temperatures, gaseous products such as CO(g) are released, which results in a porous, non-protective oxide scale<sup>135</sup>. HfC, ZrC and TiC form HfO<sub>2</sub>, ZrO<sub>2</sub> and TiO<sub>2</sub> respectively. Additionally, solid solution refractory metal ceramics such as (Hf,Ta)C<sup>136,137</sup>, and other solid solution or composite carbide- and boride materials<sup>138,139</sup> form complex oxides such as Hf<sub>6</sub>Ta<sub>2</sub>O<sub>17</sub>. An oxycarbide interlayer has been reported for the three group IV oxides, although the exact nature of this interlayer has been debated<sup>140</sup>. In the case of TiC, Ti suboxides are also predicted, based on results using the methodology outlined in Chapter 2 (see Figure 3.1) to be stable, and have been observed to form as additional products<sup>141,142</sup>. Oxidation studies of the TaC<sup>143</sup> as well as HfC-TaC solutions<sup>136</sup> report the formation of an oxycarbide. Attempts to determine whether oxygen dissolves in the carbide lattice for NbC were inconclusive based on available data<sup>144</sup>. Oxidation studies on NbC at up to 600 °C exhibited the formation of Nb sub-oxides<sup>145</sup> and reduction of NbC to sub-stoichiometric carbides. Szökefalvi-Nagy and Jehn<sup>146</sup> proposed that C preferentially oxidizes from NbC. At higher temperatures (1827 °-2000 °C), they observe the formation of a metal layer at the oxide-gas interface on NbC and TaC.

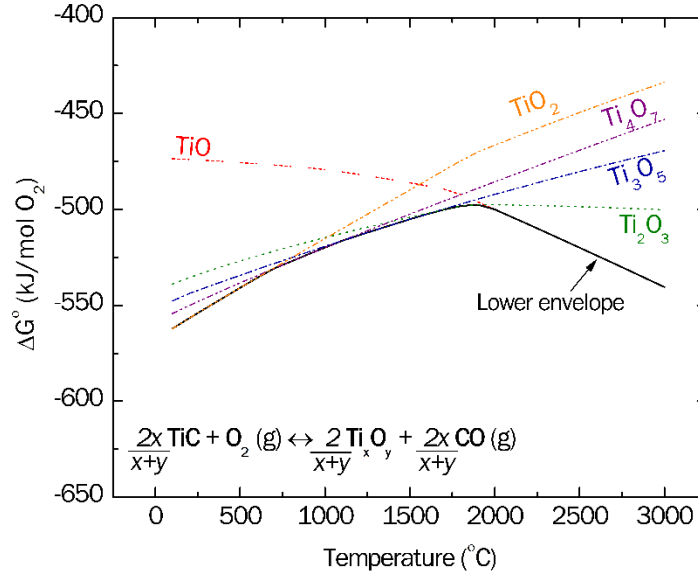


Figure 3.1: Ellingham diagram showing the possible sub-oxides that may form upon oxidation of TiC.

The oxidation of borides results in the formation of liquid boria which has been reported to boil at  $T=1860^{\circ}\text{C}$ <sup>133,147</sup>. The rate limiting mechanism for group IV metal diborides is expected to be oxygen transport through boria-filled pores and channels in the refractory oxide. However, it is hypothesized that the protectiveness due to liquid boria is limited to temperatures below about  $1850^{\circ}\text{C}$ ; above this temperature, Parthasarathy et al.'s model has shown boria to volatilize as soon as it forms<sup>8</sup>. This skeleton/pore-filling microstructure is not seen for the group V diborides<sup>148</sup>. At temperatures at or above  $1500^{\circ}\text{C}$ , the oxidation of TaB<sub>2</sub> resulted in the formation of Ta oxides, which were reported to have volatilized<sup>148</sup>. Kofstad also observed weight loss due to volatilization during the high temperature oxidation of tantalum<sup>149</sup>. However, the vapor pressures of Ta oxides at  $1500^{\circ}\text{C} - 1800^{\circ}\text{C}$ , calculated using FactSage and shown in Appendix A, are on the order of  $10^{-8}$  (atm), which contradicts this observation. Silvestroni et al.<sup>148</sup> proposed, based on the work of Jehn and Olzi<sup>150</sup>, that the dissociation of Ta<sub>2</sub>O<sub>5</sub> into  $\alpha$ -Ta and a volatile liquid phase occurs above  $1600^{\circ}\text{C}$ . At temperatures above  $1000^{\circ}\text{C}$ , NbB<sub>2</sub> oxidized to form Nb borates which were not adherent<sup>151</sup>.

Prior work to improve the oxidation resistance of UHTC carbides and borides have focused on the addition of SiO<sub>2</sub> formers, such as SiC<sup>152</sup>. However, this protectiveness is not viable at ultra-high temperatures due to the melting of SiO<sub>2</sub> (~1723 °C) or the formation of SiO (g) (>1600 °C)<sup>1</sup>.

The high entropy design paradigm has been employed to broaden the compositional palette for UHTC carbides<sup>153,154</sup> and diborides<sup>15</sup>. In addition to the potential for improved mechanical and thermal properties, this expansion of compositional space could lead to the discovery of more oxidation resistant compositions. The increased configurational entropy in high entropy alloys has been credited with the stabilization of solid solution phases. In the previous chapter, the preferential oxidation of one or more components was predicted and verified. If a high entropy material is stabilized by configurational entropy, it stands to reason that preferential oxidation occurring in an oxidizing environment will deplete the substrate of one or more constituents and destabilize the solid solution. It is not clear how the changing substrate composition affects the oxidation mechanisms and kinetics of HE-UHTC carbide and borides.

An in-depth oxidation study of these complex, multi-principal component materials is therefore warranted. The compositions chosen are based on group IV and V elements: Hf, Zr, Ti, Ta and Nb. Group IV carbides and borides, particularly those based on Hf and Zr, have long been considered the best-performing UHTCs<sup>2</sup>. Group V additions to group IV ceramics in various forms, mainly as Ta compounds, have resulted in some limited improvement in oxidation behavior, whether through liquid phase sintering of the group IV oxides, the doping of group IV oxides with higher valence ions to limit oxygen transport through oxygen vacancies, or the formation of ordered compounds such as A<sub>6</sub>B<sub>2</sub>O<sub>17</sub> (A = Hf, Zr; B = Ta, Nb)<sup>139,155</sup>. On the other hand, liquid oxide formation at more aggressive conditions and ultra-high temperatures

have shown to be detrimental to the oxidation behavior of UHTCs. It is not known at this time whether the better candidate for an oxidation resistant HE-UHTC is a carbide or boride.

The work presented here explores the time, temperature and oxygen partial pressure dependence of these high entropy ceramics to elucidate the mechanisms governing their oxidation behavior. There are several possibilities for the rate limiting oxidation mechanism, given the formation of solid, liquid and gaseous products. Likely possibilities are (i) diffusion of oxygen inward or metal species outward through a dense, solid oxide, (ii) diffusion of oxygen through the pores or channels in a porous oxide, (iii) diffusion of oxygen or metal species through a liquid oxide, or (iv) reaction control. Each of these may be identified through a time, oxygen partial pressure and temperature dependence<sup>24,37</sup> as shown in Table 3.1. Given the complexity of the composition, it is expected that the oxidation behavior of high entropy ceramics will also be complex, and it is not known to what extent the known mechanisms of carbide or diboride oxidation will prevail.

Table 3.1: Possible mechanisms in the oxidation of carbides and borides

| Mechanism  | Time dependence  | Temperature dependence   | pO <sub>2</sub> dependence   |
|--|--|--|--|
| Reaction control                                 | Linear<br>$x = kt$   | Exponential<br>$k_l \propto \exp(-\Delta H/RT)$  | $k \propto pO_2^m$   |
| Solid state diffusion through oxide              | Linear if scale has constant thickness<br>$x = kt$<br><br>Parabolic if scale is growing<br>$x = k_p t^{0.5}$ | Exponential<br>$k_p \propto \exp(-\Delta H/RT)$  | p-type oxide only<br>$k \propto pO_2^{1/n}$<br><br>molecular oxidant transport<br>$k \propto pO_2$ |
| Transport through porous oxide product           | Linear if scale has constant thickness<br>$x = kt$<br><br>Parabolic if scale is growing<br>$x = k_p t^{0.5}$ | Reactant in<br>$k \propto T^{-1/2}$<br><br>Product out<br>$\log k \propto (-\Delta H/RT)$            | molecular oxidant transport<br>$k \propto pO_2$  |
| Diffusion or permeation through a liquid product | Similar considerations to solid state (based on diffusion path length)                                       | $D \propto T \exp(-\Delta H/RT)$   | ionic transport<br>$k \propto pO_2^{1/n}$<br><br>molecular transport<br>$k \propto pO_2$           |
| Gas phase diffusion                              | $x = kt$   | Rate constant exhibits weak T dependence in a log-log plot <sup>156</sup><br><br>$D \propto T^{3/2}$ | $k \propto pO_2^m$   |

## 3.2. Methodology

### 3.2.1. Experimental set-up

All materials tested in this work were prepared and characterized by collaborators at UCSD prior to receipt for oxidation studies; further characterization was done at University of Virginia (UVA) when needed. (Hf<sub>0.2</sub>Zr<sub>0.2</sub>Ti<sub>0.2</sub>Ta<sub>0.2</sub>Nb<sub>0.2</sub>)C bulk samples were prepared by high energy ball milling and spark plasma sintering (SPS) commercially available powders (Alfa

Aesar Haverhill, MA) to ~99% relative density as described by Harrington et al.<sup>126,154</sup> The  $(\text{Hf}_{0.2}\text{Zr}_{0.2}\text{Ti}_{0.2}\text{Ta}_{0.2}\text{Nb}_{0.2})\text{B}_2$  samples were prepared primarily from powders prepared via borocarbothermal reduction described by Gild et al. and consolidated via SPS to approximately 99% relative density.<sup>157</sup> However, an early set of samples exhibiting 92% relative density was prepared by sintering commercially available powders (Alfa Aesar Haverhill, MA, USA and Goodfellow, PA, USA), as described by Gild et al.<sup>15</sup>. All sintered samples were machined at Bomas Machine Specialties (Somerville, MA) into 0.5mm thick dogbone specimens shown in Figure 3.2 for the oxidation studies described next.

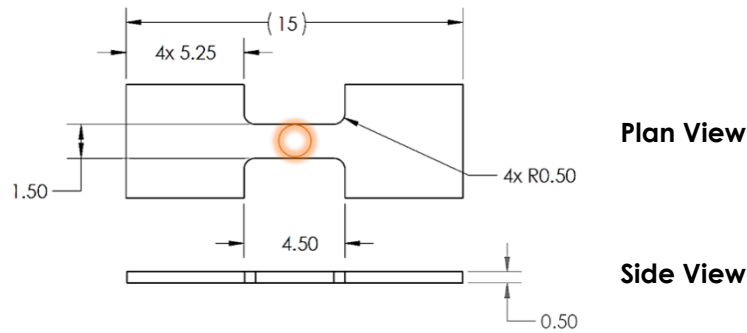


Figure 3.2: Dogbone specimen configuration. The approximate hot zone, or pyrometer sighting zone (diameter 1.5 mm), is shown in orange. Dimensions shown are in millimeters (mm).

Oxidation studies were conducted by loading dogbone specimens into a resistive heating system, modified from Karlsdottir and Halloran<sup>158</sup>, and Shugart and Opila<sup>159</sup>, schematic shown in Figure 3.3.

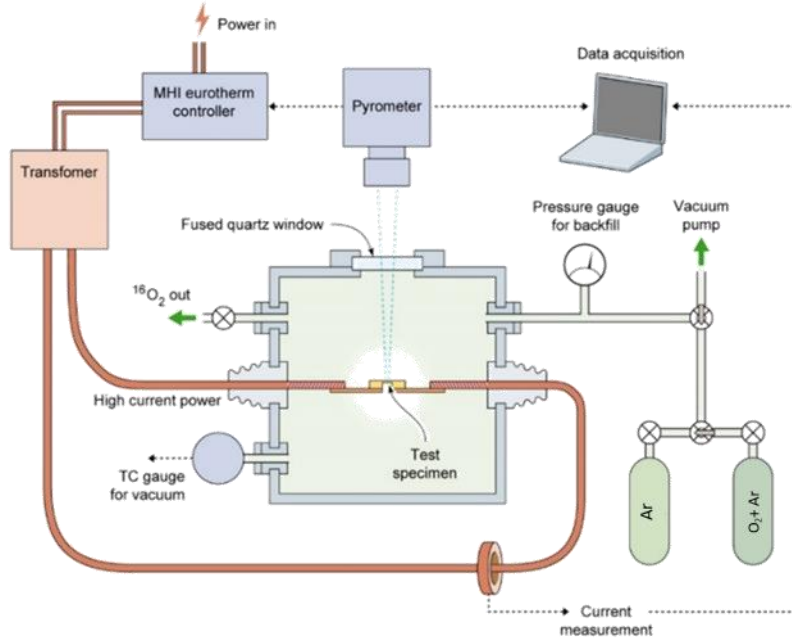


Figure 3.3: Schematic of the resistive heating experimental set-up. Specimen shown is of different configuration for clarity.

The samples were heated to the desired temperature through Joule heating. The temperature was controlled by a proportional-integral-derivative (PID) controller and an emissivity correcting one-color pyrometer (Pyrofiber Lab PFL-0865-0790-2500C311, Pyrometer Instrument Company, Ewing Township, NJ). The pyrometer sights on an approximately 1.5 mm diameter zone in the middle of the dogbone specimen (Figure 3.2). The average and standard deviation of the pyrometer readings for the various oxidation tests at 1500 °C, 1700 °C and 1800 °C discussed in Chapters 2, 3 and 4 are provided in Appendix B; sample values are provided in Table 3.2. The samples were ramped from room temperature to target temperature in approximately 2 minutes (~10-20 °C per second) in flowing (~1L/min) ultra-high purity argon (2 ppmv O<sub>2</sub> maximum impurity, Praxair, Danbury, CT). Gas mixtures with certified oxygen content of 0.1%, 0.5% and 1% in argon (Praxair, Danbury, CT) were used to explore dependence of the oxidation kinetics on partial pressure. The oxidizing gas was turned on (~1L/min) once the test

temperature was achieved. Isothermal oxidation exposures were conducted for 2-15 minutes from the time the oxidizing gas began to flow. The low partial pressures of oxygen used result in lower oxidation rates allowing for longer exposures and time dependent studies than those in 1 atm O<sub>2</sub>.

After oxidation, the oxide morphology in both plan view and cross section were characterized using scanning electron microscopy (SEM, FEI Quanta 650, FEI-Thermo Fisher Scientific, Hillsboro, Oregon) using the following: Everhart Thornley detector (ETD), circular backscatter detector (CBS) and ion conversion and electron (ICE) detector and energy dispersive spectroscopy (EDS, Oxford Instruments Aztec X-Max<sup>N</sup> 150, Concord, MA). The oxide phases were identified using X-ray diffraction (XRD, PANalytical X'Pert Pro MPD or PANalytical Empyrean, Almelo, The Netherlands) via conventional powder diffraction set-up and micro-focusing optics. In the latter case, the beam size was constrained to be 720µm in diameter and focused on the pyrometer sighting zone. The samples were manually fractured across the hot zone, and the cross-sections were examined in an SEM. Mechanical polishing was not generally performed due to large differences in hardness between substrate and oxide, the potential for oxide pullout, and loss of boron. Focused ion beam (FIB) milling (Helios UC G4, Thermo Fisher Scientific, Hillsboro, Oregon) was also used to obtain selected samples for further EDS analysis. Analysis via transmission electron microscopy (TEM, FEI Titan 80-300 S-Twin, Thermo Fisher Scientific, Hillsboro, OR) and selected area electron diffraction was conducted at UVA on selected samples. TEM-EDS analysis was also conducted at University of Alabama (FEI Tecnai 200kV F20 with STEM-HAADF).

The parameters used to probe the time, temperature and pressure dependence of oxidation are typically weight change, scale thickness or material consumption. The experimental set-up used to expose specimens to high temperatures result in large lateral temperature gradients (as described in Chapter 5); as such weight changes cannot be reliably

used. Oxide scale thickness could not be used due to oxide composition and porosity variations between samples of different composition. The parameter chosen to quantify oxidation kinetics was material consumption (Figure 3.4). Material consumption was measured by a combined analysis of secondary electron, backscattered electron and oxygen EDS map images to determine extent of oxidation, but final measurements were taken primarily using EDS maps. Material consumption reported in this study are the average of a minimum of ten measurements per sample and were taken in the middle of the sample to minimize data being skewed by edge effects. Error bars indicate the standard deviation in the measurements. The results presented here will focus on the region within the pyrometer sighting zone (Figure 3.2).

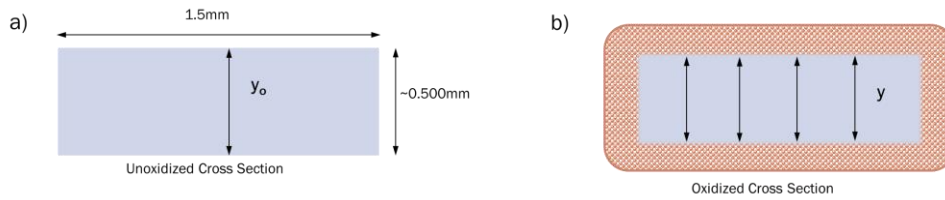


*Figure 3.4: Schematic showing the cross section of the dogbone specimen across the zone of interest (a) before oxidation, and (b) after oxidation. The solid, blue areas indicate unoxidized material, while the orange patterned areas indicate oxidized material. Material consumption is defined as half of the difference between the thickness,  $y$ , of the remaining, unoxidized material subtracted from the original thickness,  $y_0$ .*

### 3.3. Results

#### 3.3.1. Temperature control

Table 3.2 summarizes the average and standard deviation of the temperatures recorded by the pyrometer during the isothermal dwell time for samples tested for five minutes (unless otherwise noted) at each target temperature and  $pO_2$ . Data for other tests are presented more fully in Appendix B.

The poorest temperature control was observed for samples tested at the nominal temperature of 1800 °C in 0.5% $O_2$ . The best control was observed for samples tested at a nominal temperature of 1500 °C. Various factors can affect temperature control, such as proportional-integrative-derivative (PID) controller settings, material resistance, oxidation behavior, pyrometer performance, and orientation of the sample surface relative to the pyrometer head. The experimental set-up was updated with a jig that helped minimize variation of the sample surface to the pyrometer line-of-sight. The PID controller settings were determined using sintered and machined TiC samples also obtained from UCSD, and minor adjustments were made to the PID settings during the early high entropy carbide and boride tests to refine the temperature control. Due to the limited number of samples available, significant changes to the PID settings were not made. Carbide samples tested in 0.5% $O_2$  were among the latest batch of samples received (Batch C3, see next section), and had large standard deviations in temperature, particularly at 1800 °C, compared to earlier samples tested at the same PID settings. Drops in current are expected as the cross-section is reduced due to oxidation (Figure 3.5) as the test progressed; the fluctuations about the general trend indicate that higher deviation from the mean current occurred at higher temperatures.

Table 3.2: Average and standard deviation temperature values recorded by the pyrometer for carbides and borides tested for five minutes at each temperature and partial pressure for (HfZrTiTaNb)*X* where *X*=C or B<sub>2</sub>, unless otherwise noted.

| Carbides       | pO <sub>2</sub> (% in Ar) |                    |                  |
|----------------|---------------------------|--------------------|------------------|
| Nominal T (°C) | 0.1%O <sub>2</sub>        | 0.5%O <sub>2</sub> | 1%O <sub>2</sub> |
| 1500           | 1497 ± 20                 | 1511 ± 15          | 1509 ± 22        |
| 1700           | 1698 ± 56                 | 1722 ± 60          | 1715 ± 34        |
| 1800           | 1798 ± 85                 | 1836 ± 88          |                  |
| Borides        | pO <sub>2</sub> (% in Ar) |                    |                  |
| Nominal T (°C) | 0.1%O <sub>2</sub>        | 0.5%O <sub>2</sub> | 1%O <sub>2</sub> |
| 1500           | 1494 ± 11 (6 min.)        | 1504 ± 10          | 1498 ± 8         |
| 1700           | 1688 ± 36                 | 1703 ± 27          | 1701 ± 26        |
| 1800           | 1794 ± 60                 | 1801 ± 76          |                  |

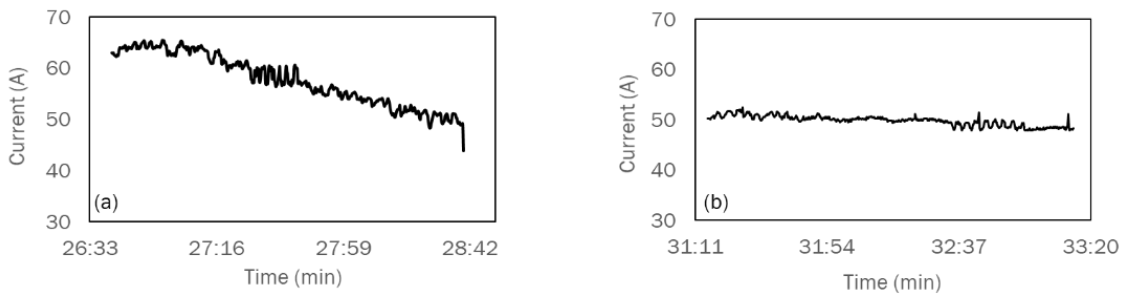


Figure 3.5: Comparison of current fluctuation during dwell time between (a) (HfZrTiTaNb)*C* tested at 1800 °C in 0.5%O<sub>2</sub> for two minutes with standard deviation of temperature reading >100 °C, and (b) (HfZrTiTaNb)*C* tested in at 1500 °C in 1%O<sub>2</sub> for 2 minutes. Sample in (a) is from Batch C3, and in (b) from Batch C1.

### 3.3.2. Sample variation

Samples from UCSD were received in multiple batches, with the process for sample synthesis changing. Some variation in the materials were observed in terms of secondary phase composition, size and distribution. In all cases, the five-component carbide or boride phases, respectively, generally appeared to be in single phase solid solution as determined via

EDS and XRD. All characterization results reported here were conducted at UVA unless otherwise noted in each figure caption.

### Carbides

Samples received earlier in the program (labeled Batch C1 and C2) generally exhibited more porosity and retained Hf and Zr oxides. A representative image, EDS maps and XRD diffractogram are shown in Figure 3.6 and Figure 3.7. Samples received later, labeled Batch C3 (Figure 3.8 and Figure 3.9) exhibited less porosity and a smaller fraction of secondary oxide phases.

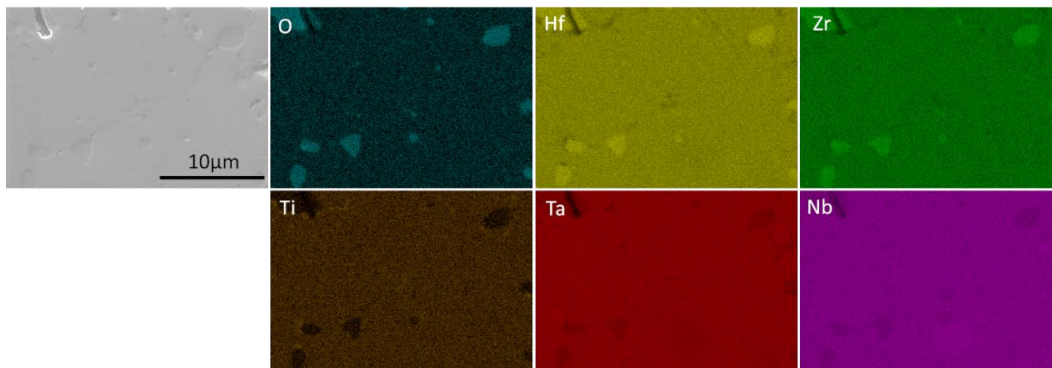


Figure 3.6: Back-scattered electron image and EDS maps of (HfZrTiTaNb)C samples made with sintered commercial powders, received early in the program (Batch C1). Hf/Zr rich areas are oxides.

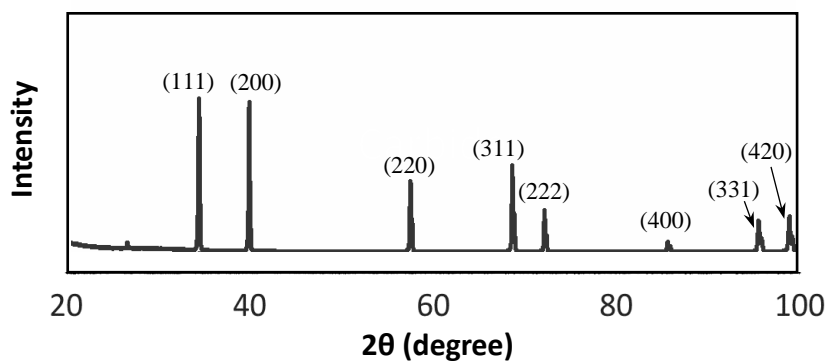


Figure 3.7: Apparent single-phase rock-salt XRD pattern from (HfZrTiTaNb)C samples made with sintered commercial powders, received early in the program (Batch C1). Small, unlabeled peak near 20-30 degrees  $2\theta$  represents Hf/Zr oxide. XRD performed and data obtained from UCSD.

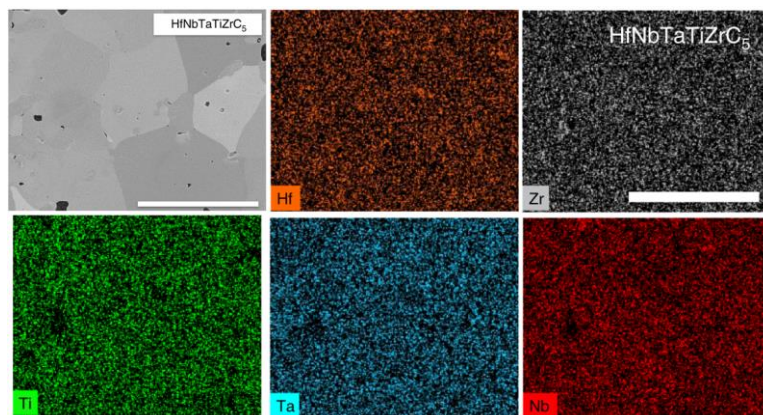


Figure 3.8: Back-scattered electron image and EDS maps representative of (HfZrTiTaNb)C samples made and received later in the program (Batch C3). Data obtained from Sarker et al.<sup>113</sup> Scale bar is 10 $\mu$ m.<sup>113,126</sup>

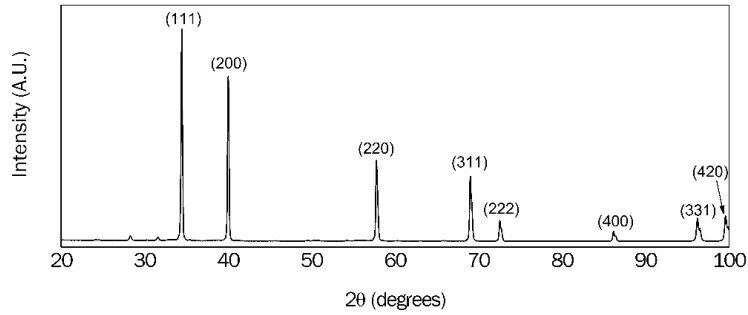


Figure 3.9: Apparent single-phase rock-salt XRD pattern from (HfZrTiTaNb)C samples made with sintered commercial powders, received late in the program (Batch C3). Small, unlabeled peak near 20-30 degrees  $2\theta$  represents Hf/Zr oxide. Data obtained from Sarker et al.<sup>113</sup>

Figure 3.10 shows a comparison of the (HfZrTiTaNb)C samples from different batches oxidized under the same conditions. The tendency for intergranular oxidation and the fact that oxidation is driven by available surface area means that some differences in extent of oxidation and morphology might be expected if there are grain size differences. However, the differences in morphology, particularly of the oxides in the intergranular regions are not significant.

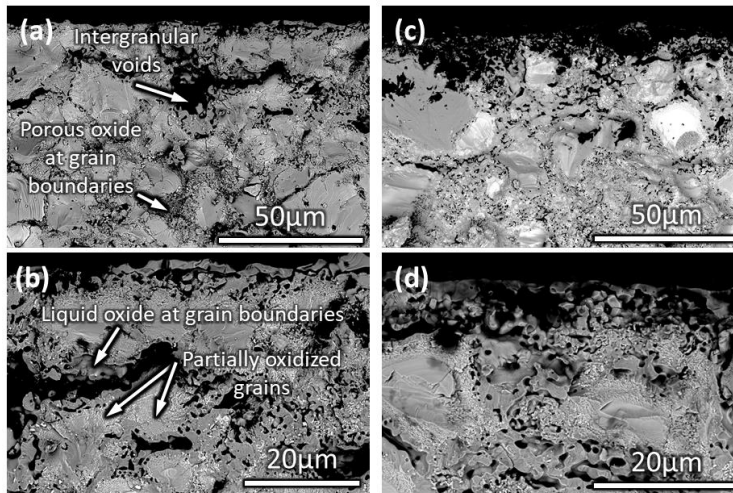
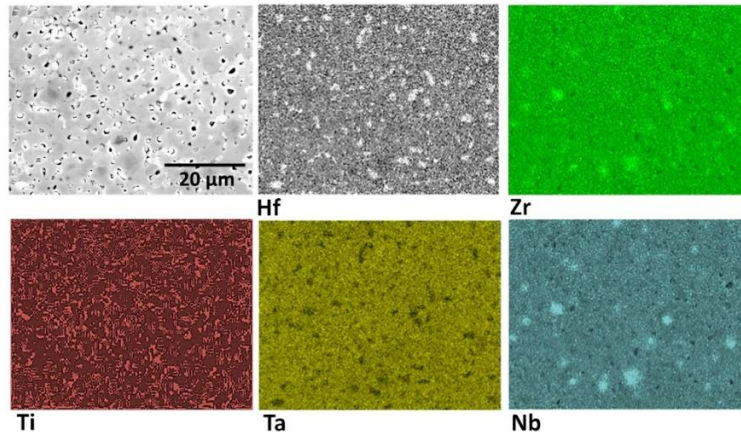


Figure 3.10: Back-scattered electron images of (HfZrTiTaNb)C samples oxidized at 1700 °C in 0.5%O<sub>2</sub> for five minutes. (a) Lower and (b) higher magnification cross sections of samples from Batch C2, and (c) lower and (d) higher magnification cross sections of samples from Batch C3.

## Borides

(HfZrTiTaNb)<sub>2</sub>B<sub>2</sub> samples received earlier in the program were synthesized using commercial powders (Batch B1). This batch of high entropy boride samples exhibited retained Hf and Zr oxides, and elemental clustering (Nb, Zr) as shown in Figure 3.11. These samples, being 92% dense, also exhibited a large volume fraction of porosity, apparent in Figure 3.11 as dark regions. XRD data, shown in Figure 3.12, indicates a single phase hexagonal high entropy diboride, with Hf/Zr oxides present as contaminants. Samples received later (Batch B2, Figure 3.13, Figure 3.14) exhibited larger grain sizes, improved homogeneity in elemental distribution, and a large fraction (~4-5 vol%) of the secondary boron carbide phase (B-rich regions in Figure 3.13), which was from borocarbothermal reduction of the precursor oxides. A very small fraction (much less than 1 vol% and can be considered a minor contamination) of a Ta-rich carbide formed due to the reduction process detectable via XRD analysis (Figure 3.14), but not readily apparent via EDS. No retained Hf and Zr oxides were observed via XRD.



*Figure 3.11: Back-scattered electron image and EDS maps of (HfZrTiTaNb)<sub>2</sub>B<sub>2</sub> samples made with sintered commercial powders, received early in the program (Batch B1). SEM and EDS data obtained from collaborators at UCSD.*

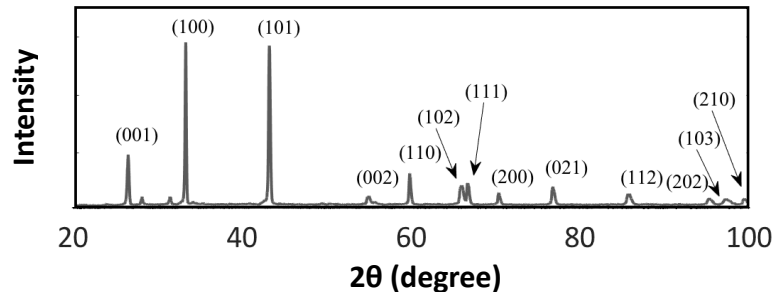


Figure 3.12: Apparent single phase hexagonal XRD pattern taken from  $(\text{HfZrTiTaNb})\text{B}_2$  samples made with sintered commercial powders (Batch B1). Small, unlabeled peak near 30 degrees  $2\theta$  are due to minor Hf and Zr oxide contamination. XRD data obtained from collaborators at UCSD.

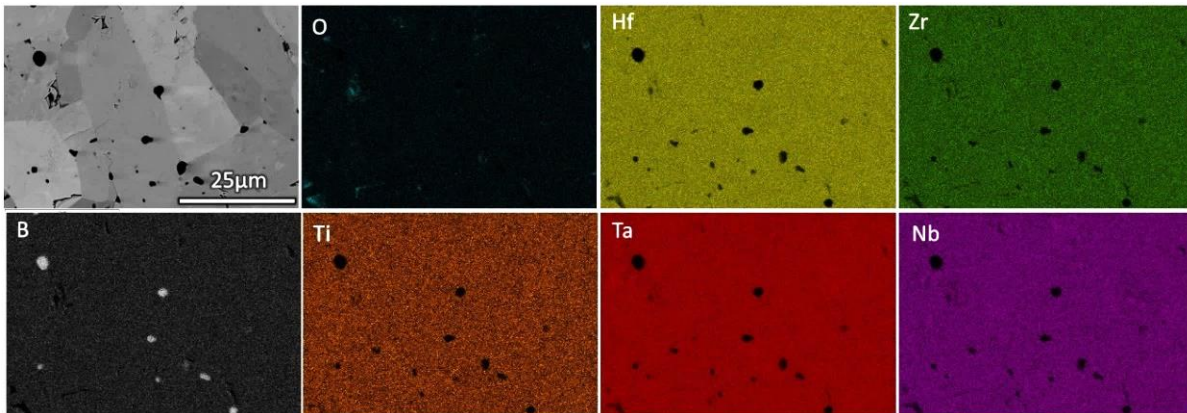


Figure 3.13: Back-scattered electron image and EDS maps of  $(\text{HfZrTiTaNb})\text{B}_2$  samples made with sintered borocarbothermally reduced powders (Batch B2).

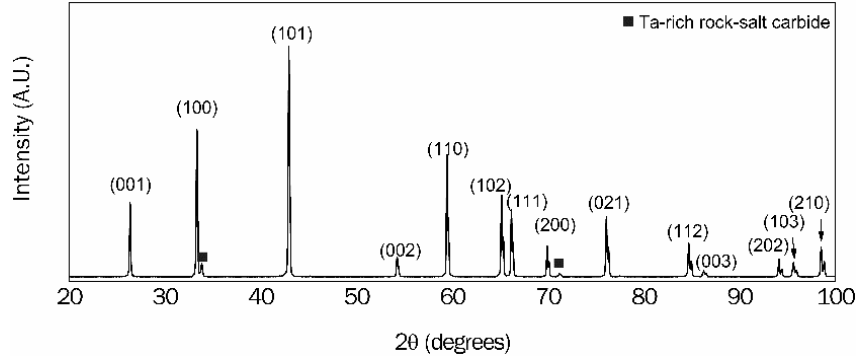


Figure 3.14: XRD pattern taken from  $(\text{HfZrTiTaNb})\text{B}_2$  samples made with borocarbothermally reduced powders (Batch B2) showing a single-phase high entropy hexagonal  $(\text{HfZrTiTaNb})\text{B}_2$  is observed, along with a cubic phase attributed to a Ta-rich rocksalt carbide present as a minor contaminant (<1 vol%). XRD data obtained from collaborators at UCSD.

Figure 3.15 and Figure 3.16 show a comparison of the morphology of the oxidized boride samples depending on the process used to synthesize the ceramics. The samples with boron carbide as the secondary phase exhibited lower material consumption, but also exhibited larger voids. These later batches had a significant volume fraction (~4-5 vol% as determined by collaborators at UCSD via ImageJ analysis) of the secondary  $\text{B}_4\text{C}$  phase retained from processing, which is expected to influence the oxidation behavior of the borides. Most of the oxidation tests discussed in this chapter were conducted with these latter samples (Batch B2).

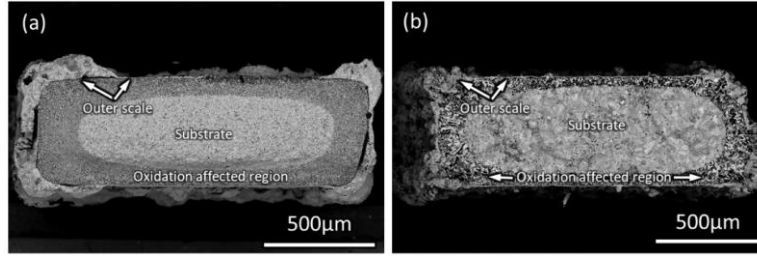


Figure 3.15: Backscattered electron images of the entire cross-section of  $(\text{HfZrTiTaNb})\text{B}_2$  oxidized at  $1700^\circ\text{C}$  in  $1\%\text{O}_2$  for five minutes. (a) Oxidized sample made with sintered commercial powders (Batch B1); and (b) oxidized sample made from sintered borocarbothermally reduced powders (Batch B2).

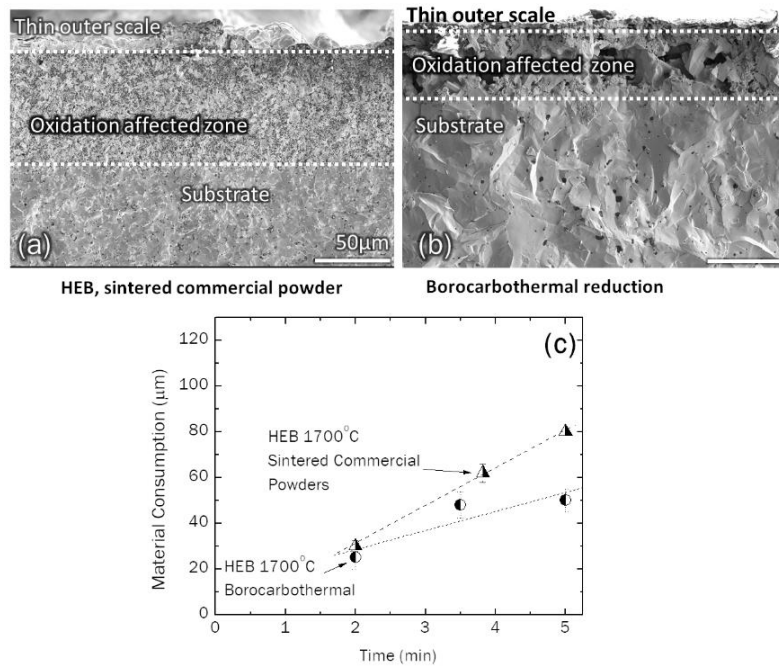


Figure 3.16: Secondary electron images showing the cross section of the oxidized  $(\text{HfZrTiTaNb})\text{B}_2$  (a) made from sintered commercial powders (Batch B1), (b) made from powders prepared via borocarbothermal reduction (Batch B2), both oxidized at  $1700^\circ\text{C}$  in  $1\%\text{O}_2$  for 5 minutes. (c) shows the difference in material consumption rates observed for both samples, tested in  $1\%\text{O}_2$ .

### 3.3.3. Kinetics

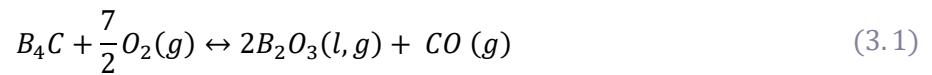
#### *Kinetics: time dependence*

Material consumption measurements are plotted versus time in Figure 3.17 for the oxidation of (HfZrTiTaNb)C and (HfZrTiTaNb)B<sub>2</sub> at 1500 °C to 1800 °C in 0.1%, 0.5% and 1%O<sub>2</sub>. The rates are linear in most cases for both the carbides and the diborides, but some deviations are noted. The rates also increase with oxygen partial pressure. Higher rates of material consumption are observed at 1700 °C relative to 1500 °C; however material consumption at 1800 °C is lower than at 1700 °C for both the carbides and diborides. The high entropy borides exhibited lower material consumption compared to the carbides in all conditions.

Several explanations exist for the observed scatter in results for the carbides. The metric used to quantify oxidation rates measures unaffected material. The time dependence presented therefore includes regions exhibiting a wide range of oxidation morphologies, e.g. external scale formation, intergranular oxidation (discussed in more detail in section 3.3.4). For the cases exhibiting intergranular oxidation, which generally was the case for the carbides at short times, the grains in the oxidation affected regions oxidize further; thus, this metric does not account for this additional intragranular oxidation at longer times. Deviations from a best fit line could be due to the interplay of further oxidation of the grains in the intergranularly oxidized region versus further penetration along grain boundaries in substrate. Data for carbide samples tested in 0.5% O<sub>2</sub> also deviates from the best fit line, and this can be attributed to additional factors. All the data points corresponding to material consumption higher than or equal to samples tested in 1%O<sub>2</sub> are from Batch C3, received later. There is significant topography in the fracture cross sections for these samples that introduce large, unquantified uncertainties in the determination of the extent to which oxidation penetrates along the grain boundaries. Second, the sample data plotted for 1700 °C in 0.5%O<sub>2</sub> for 2 minutes is from a test that exhibited a higher average temperature (pyrometer output = 1744

± 55 °C). One sample from the Batch C2 was tested in 0.5% O<sub>2</sub> and 5 minutes for comparison (boxed in red, Figure 3.17 (b)), and this exhibited lower material consumption that fits well within the trend shown by samples tested at 1% and 0.1% O<sub>2</sub> (Batch C1 and C2). Based on this, results for the 0.5%O<sub>2</sub> data from Batch C3 are not discussed in detail.

The observed material consumption for the borides also exhibits complex behavior with respect to time, temperature and oxygen partial pressure. The linear kinetics exhibited by the high entropy borides are not unexpected given boron volatility<sup>160</sup>. Deviations from linear fit that do not fit trends established by the bounding oxygen partial pressure conditions may be explained by variation in specimen synthesis between batches and the possible related effect of large fluctuations in temperature during the testing. An example is shown in Figure 3.18 of the material consumption measured after oxidation of (HfZrTiTaNb)B<sub>2</sub> at 1700 °C in 0.5%O<sub>2</sub>, which demonstrates the variation in oxidation behavior between specimens from different pellets (pellet ID BX and BY, both using the same borocarbothermally reduced powder batch, Batch B2) exposed to similar conditions. It is hypothesized that the oxidation of the relatively large volume fraction of B<sub>4</sub>C of varying size and distribution in Batch B2 influences the oxidation behavior of these materials through additional production of B<sub>2</sub>O<sub>3</sub> (l,g) and CO (g), as shown in Equation (3.1).



Variations in the size and distribution of these secondary phases can also cause changes in resistivity, leading to poorer temperature control during the resistive heating tests. Therefore, data obtained from testing materials from Batch B2 containing B<sub>4</sub>C may not be reflective of the oxidation kinetics of the pure metal diborides (Figure 3.16 (c)). However, as the increased oxidation resistance of the borides relative to the carbides is likely due to the formation and protectiveness of boron<sup>8</sup>, it is still possible to qualitatively examine the composition of the oxide

and substrate formed on these high entropy diboride specimens after exposure to oxidizing environments.

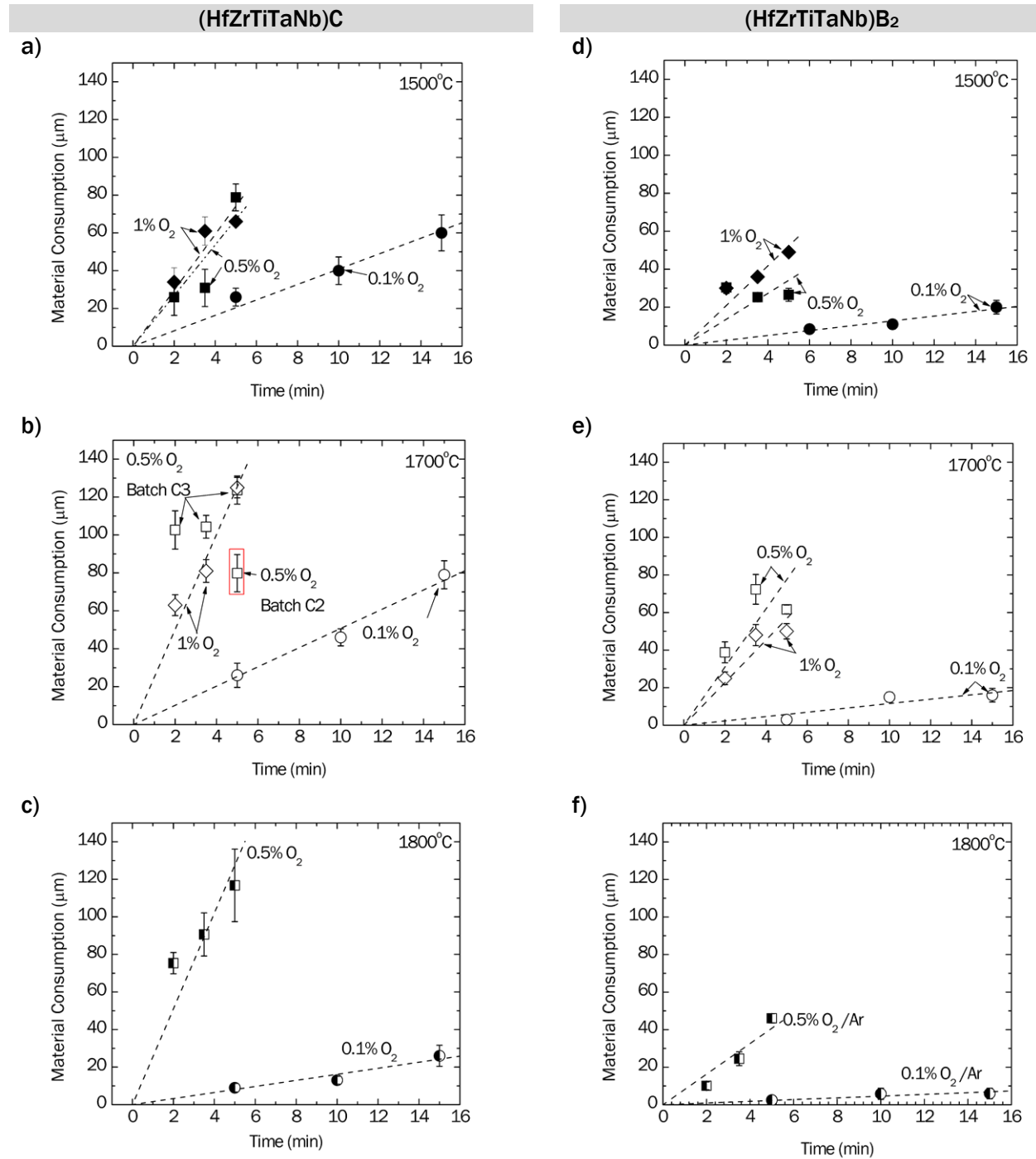


Figure 3.17: Material consumption plotted against time for  $(\text{HfZrTiTaNb})\text{C}$  specimens tested in (a) 1500 °C, (b) 1700 °C and (c) 1800 °C; and for  $(\text{HfZrTiTaNb})\text{B}_2$  specimens tested in (e) 1500 °C, (f) 1700 °C and (g) 1800 °C.

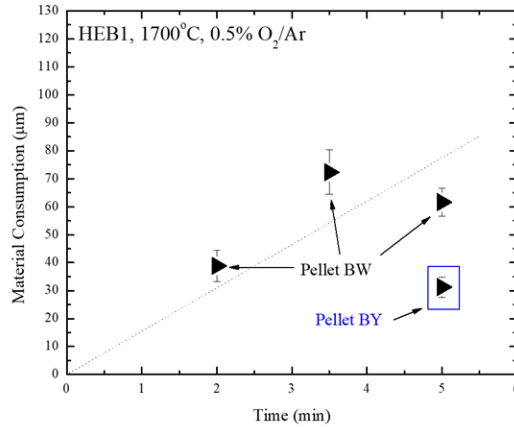


Figure 3.18: Differences in material consumption for samples oxidized under the same conditions. BX and BY are pellet identification codes. Both pellets were synthesized from the same powder batch.

The material consumption data were also plotted versus time on a log-log scale for both the carbides and borides in Figure 3.19 to further examine the time dependence. The log-log plots provide the value of  $n$  shown in Equation (3.2):

$$x = (kt)^n \quad (3.2)$$

where  $x$  is material consumption,  $k$  is the rate constant, and  $t$  is the time. In most cases, oxidation kinetics are not purely parabolic ( $n=0.5$ ) or linear ( $n=1$ ) for either carbide or boride but are in between. Some exceptions to this are observed. The carbides exhibit linear dependence ( $n=1$ ) at 1700 °C in 0.1%O<sub>2</sub>, and the borides exhibit parabolic time dependence ( $n=0.5$ ) at 1500 °C in 1%O<sub>2</sub>. The boride exhibits a negative slope for  $n$  ( $n= -0.2$ ) at 1500 °C in 0.5%O<sub>2</sub>. This apparent deviation from the trends established by other conditions may be attributable to variation between sintered pellets (see Figure 3.18), as the 2 and 3.5 minute data points were obtained from one pellet (pellet ID = BW), while the 5 minute data point was obtained from another (ID = BX). However, consideration of plots of material consumption versus time in the bounding oxygen partial pressure conditions (0.1%O<sub>2</sub> and 1%O<sub>2</sub>) shown in Figure 3.17 indicate that the results are adequately described by linear kinetics. Subsequent analysis of temperature and pO<sub>2</sub> dependence therefore assumes linear oxidation kinetics.

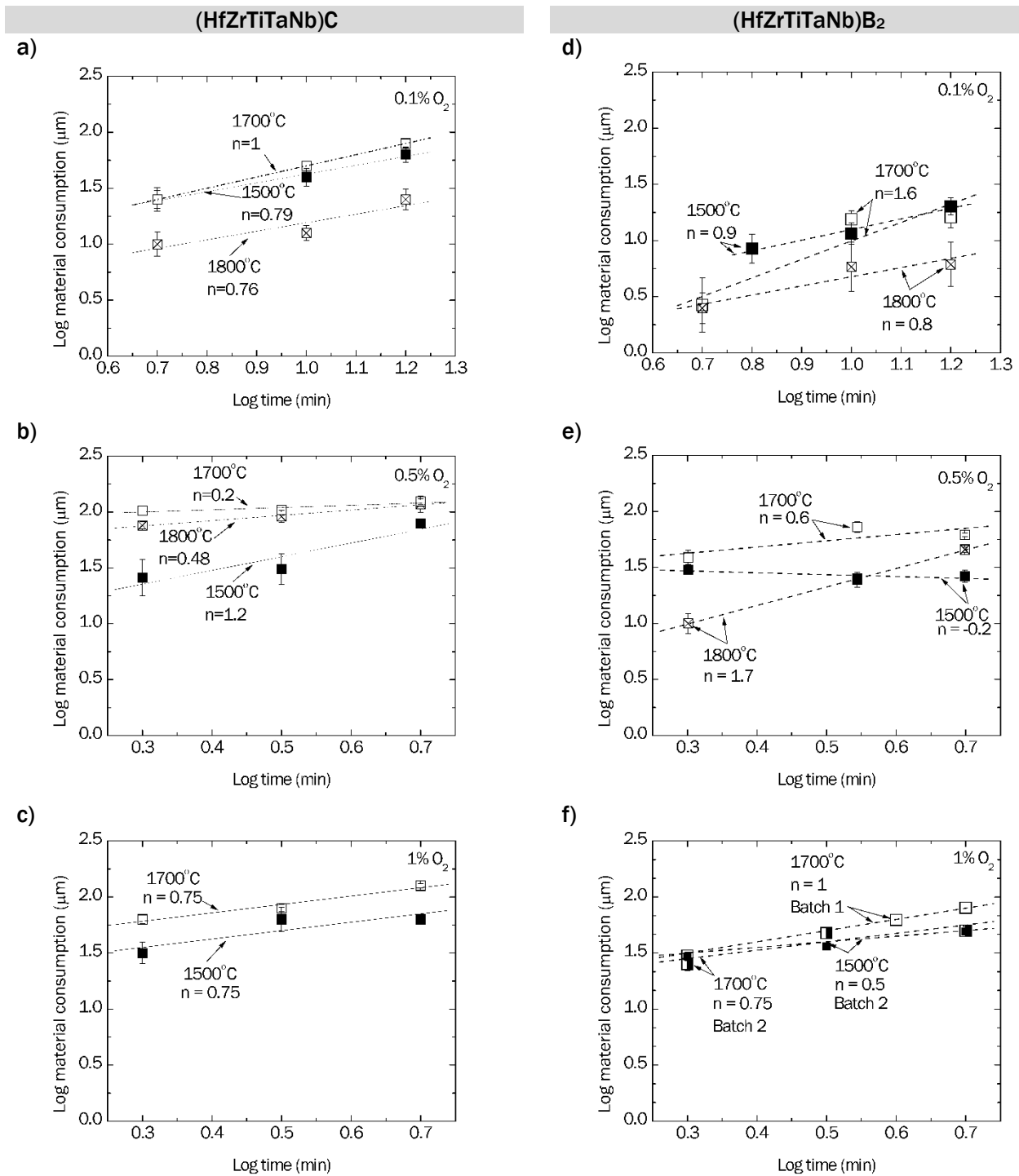


Figure 3.19: Log material consumption plotted against log time for  $(\text{HfZrTiTaNb})\text{C}$  specimens tested in (a) 0.1% $\text{O}_2$ , (b) 0.5% $\text{O}_2$  and (c) 1% $\text{O}_2$ ; and for  $(\text{HfZrTiTaNb})\text{B}_2$  specimens tested in (e) 0.1% $\text{O}_2$ , (f) 0.5% $\text{O}_2$  and (g) 1% $\text{O}_2$ .

### *Kinetics: oxygen partial pressure ( $pO_2$ ) dependence*

The linear rate constants obtained from the plots in Figure 3.17 in each  $pO_2$  and at each temperature for (HfZrTiTaNb)C and (HfZrTiTaNb) $B_2$  respectively, are summarized in Table 3.3 and Table 3.4. The  $pO_2$  dependence is also plotted in Figure 3.20. The linear rate constants are proportional to  $pO_2^m$ , where  $m$  varies from 0.59 to 1.79. This dependence of  $>0.5$  suggests that the kinetics are not likely limited by transport of ionic species but more likely by molecular oxygen transport or by a surface/interface reaction.

Errors reported are standard errors calculated from the linear regression analysis. Due to various experimental artifacts affecting kinetic data from the 0.5% $O_2$  exposures, data from these exposures must be considered with care as previously discussed. The data point for the carbide oxidized at 1700 °C in 0.5% $O_2$  (Table 3.3, Figure 3.20) was from a sample that came from an earlier batch of materials (Batch C2), similar to the other data points from the same temperature (Batch C1 and C2). This is the same data point highlighted by a red rectangle in Figure 3.17(b). Nevertheless, it fits the trend established by the other partial pressures well. The lack of data at 1% $O_2$  results in only two data points for the examination of the  $pO_2$  dependence at 1800 °C. The available data are plotted in Figure 3.20 and show a much larger  $pO_2$  dependence than noted for the lower temperatures tested, however the degree of uncertainty is large.

*Table 3.3: Summary of (HfZrTiTaNb)C oxidation kinetic parameters obtained from experiments conducted at 1500-1800 °C, linear ( $k_i$ ) kinetics. The ‘\*’ indicates a rate constant obtained from one data point.*

| (HfZrTiTaNb)C<br>Partial Pressure of Oxygen (%) | $k_i$ ( $\mu\text{m}/\text{min}$ ) |                |                |
|---|------------------------------------|----------------|----------------|
|   | 1500 °C                            | 1700 °C        | 1800 °C        |
| 0.1   | $4.1 \pm 0.2$                      | $5.1 \pm 0.2$  | $1.6 \pm 0.1$  |
| 0.5   | $13.4 \pm 2.2$                     | 16.0*          | $25.5 \pm 2.9$ |
| 1   | $14.8 \pm 1.4$                     | $25.1 \pm 1.6$ | -              |

Table 3.4: Summary of (HfZrTiTaNb)<sub>2</sub>B<sub>2</sub> oxidation kinetic parameters obtained from experiments conducted at 1500-1800 °C, linear (k<sub>i</sub>) kinetics.

| (HfZrTiTaNb) <sub>2</sub> B <sub>2</sub> | k <sub>i</sub> (μm/min) |            |           |
|--|-------------------------|------------|-----------|
| Partial Pressure of Oxygen (%)           | 1500 °C                 | 1700 °C    | 1800 °C   |
| 0.1                                      | 1.3 ± 0.1               | 1.2 ± 0.2  | 0.5 ± 0.1 |
| 0.5                                      | 6.8 ± 2.0               | 15.5 ± 2.8 | 8.2 ± 1.0 |
| 1  | 10.5 ± 1.1              | 11.4 ± 1.2 | -         |

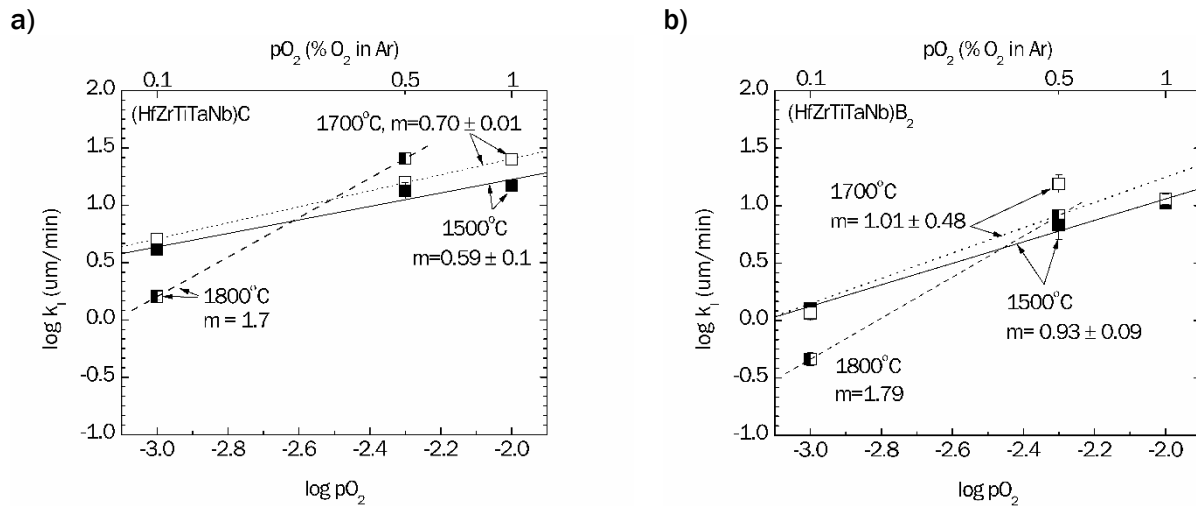


Figure 3.20: (a)  $pO_2$  dependence of (HfZrTiTaNb)C oxidized at 1500-1800 °C, assuming linear kinetics, (b)  $pO_2$  dependence of (HfZrTiTaNb)B<sub>2</sub> oxidized at 1500-1800 °C, assuming linear kinetics.

#### Kinetics: temperature dependence

The temperature dependence for both the carbides and the borides are plotted in Figure 3.21 for data obtained from oxidation exposures in 0.1% and 1%  $pO_2$ . At temperatures below 1800 °C in 0.1%  $O_2$ , the linear rate constants obtained for the diborides exhibit no significant temperature dependence at temperatures lower than 1800 °C, while those for the carbides exhibit a weak temperature dependence. Similarly, the borides exhibit almost no temperature dependence in 1%  $O_2$ , while a dependence is observed for the carbides. Both the carbides and borides exhibited significantly reduced reaction rates at 1800 °C and 0.1%  $O_2$ ,

indicating a possible change in mechanism, which will be explored in more detail in section

### 3.3.4.

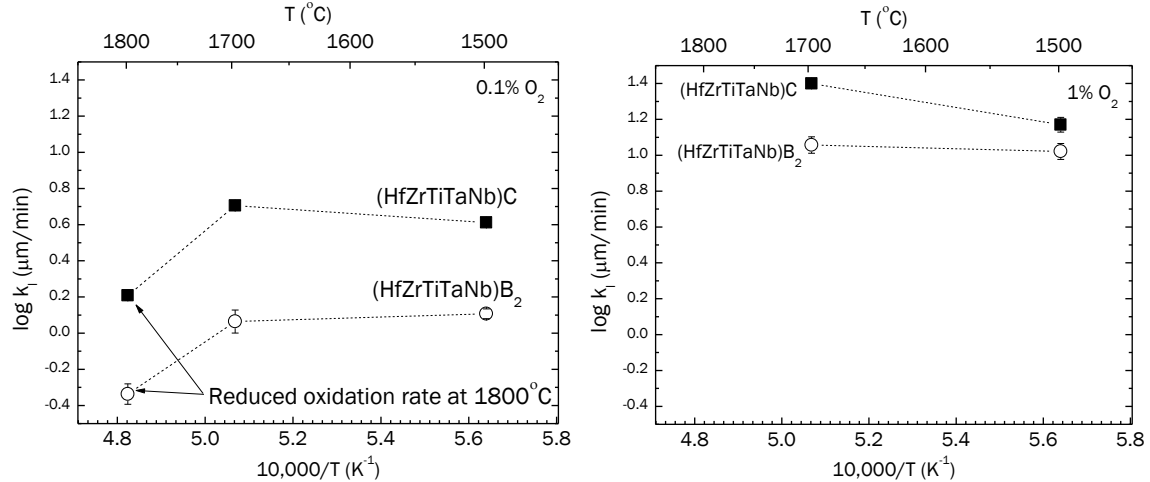


Figure 3.21: Rate reduction at  $1800^{\circ}\text{C}$  for both the  $\text{HfZrTiTaNb}$  carbides and borides tested in (left)  $0.1\% \text{O}_2$  and (right)  $1\% \text{O}_2$ .

### 3.3.4. Microstructure and Oxide Composition

Figure 3.22 shows representative micrographs of the morphologies observed in the oxidized regions in cross-section for both the carbide and diboride at  $1500^{\circ}$ ,  $1700^{\circ}$  and  $1800^{\circ}\text{C}$ . The oxide morphologies varied according to substrate composition, time, temperature and  $p\text{O}_2$ . Table 3.5 summarizes the microstructure, and related elemental composition and phases detected after exposure at each temperature and the bounding oxygen partial pressures of  $0.1\%$  and  $1\% \text{O}_2$  for  $(\text{HfZrTiTaNb})\text{C}$ , while Table 3.6 does the same for  $(\text{HfZrTiTaNb})\text{B}_2$ . Detailed micrographs, EDS maps and XRD data are provided in Appendix C; the reader is invited to review these supplements to the summary tables. Variations in composition and morphology with time are noted where appropriate. It should be noted that the oxide phases detected via XRD are the closest structural matches. Overlaps exist, along with the

possibility of cationic substitutions (Hf and Zr for each other, Ta and Nb for each other), and solid solution formation. XRD data were useful to confirm findings via EDS results.

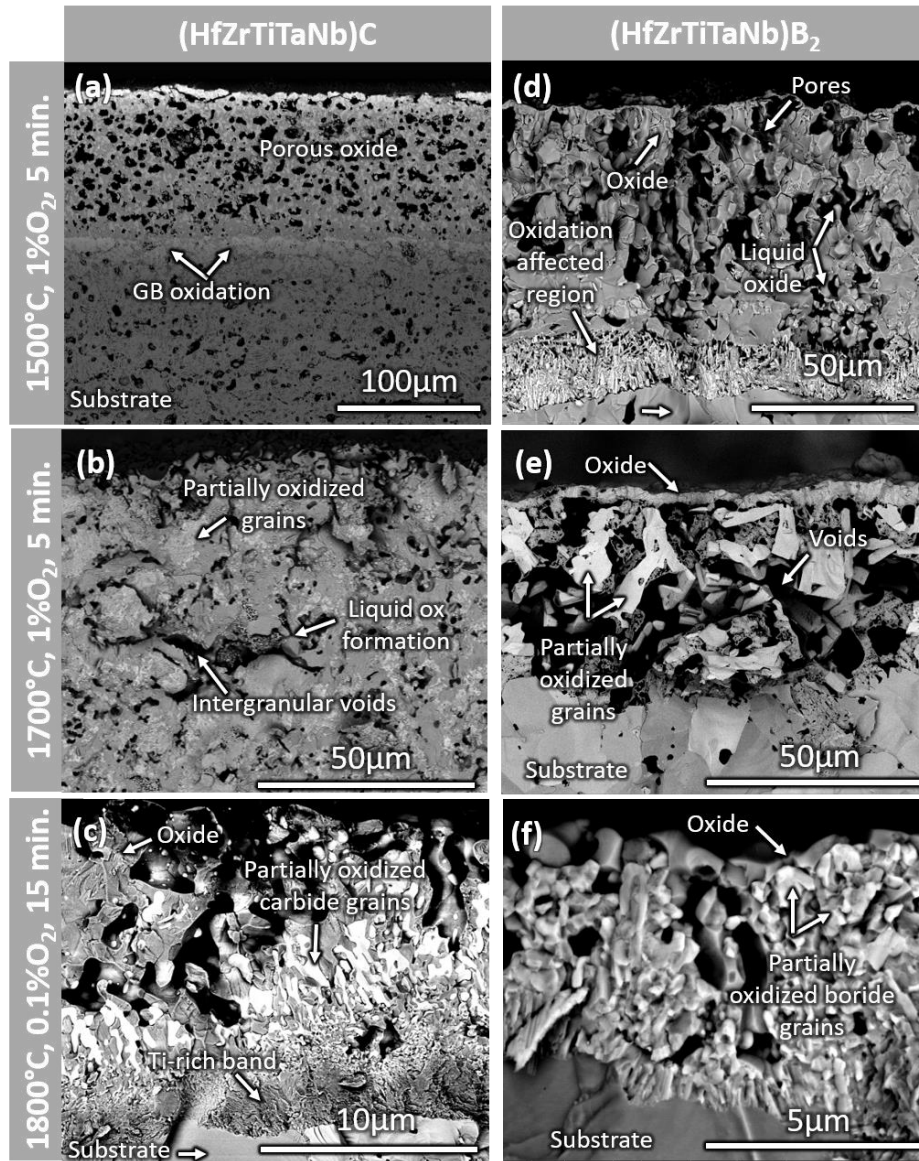


Figure 3.22: Cross-section back-scattered electron images of (a)-(c) (HfZrTiTaNb)C and (d)-(f) (HfZrTiTaNb)B<sub>2</sub> showing oxidized regions at the oxide-gas interface, summarizing the representative morphologies at each temperature. (a) and (d) 1500 °C, 1%O<sub>2</sub>, 5 minutes; (b) and (e) 1700 °C, 1%O<sub>2</sub> and 5 minutes; (c) and (f) 1800 °C, 0.1%O<sub>2</sub> and 15 minutes. Note scale bars vary for each image to show microstructural features of interest.

Table 3.5: Summary of the microstructure, elemental composition and oxide phases formed on (HfZrTiTaNb)C after oxidation at 1500 °C, 1700 °C and 1800 °C in 0.1%O<sub>2</sub> and 1%O<sub>2</sub>. XRD phases reported are those detected after 5 minutes in 1%O<sub>2</sub> and 15 minutes in 0.1%O<sub>2</sub>.

| <b>1500 °C</b>              | <b>0.1% O<sub>2</sub></b>  | <b>1%O<sub>2</sub></b>  |
|-----------------------------|--|---|
| Microstructure              | Intergranular oxidation at short times. Porous external scale at long times. Porosity observed in entirety of grains in the oxidized region  | Intergranular oxidized regions taken over by external porous oxide at long times. Porous external scale observed at all times tested. Porous scale exhibits rounded morphology indicative of solidified melt.   |
| Elemental composition       | Intergranular oxides at short times rich in Hf, Zr, and some Ti. Region underneath intergranular oxides rich in Ta and Nb, also contains oxygen. Oxidized regions contain Hf, Zr, Ti and Ta, and small amounts of Nb (~1at%, and in more than one apparent phase)  | Oxidized regions contain Hf, Zr, Ti, Ta and Nb (in more than one apparent phase).   |
| Phases detected (XRD)       | ZrO <sub>2</sub> , (Zr <sub>1.3</sub> Ti <sub>0.7</sub> )O <sub>2</sub> , TiTaO <sub>4</sub> , HfTiO <sub>4</sub> , Hf <sub>6</sub> Ta <sub>2</sub> O <sub>17</sub>  | TiTaO <sub>4</sub> , Ti <sub>2</sub> Nb <sub>2</sub> O <sub>29</sub> , TiNb <sub>2</sub> O <sub>7</sub> , HfTiO <sub>4</sub> , Hf <sub>6</sub> Ta <sub>2</sub> O <sub>17</sub>  |
| <b>1700 °C</b>              | <b>0.1% O<sub>2</sub></b>  | <b>1%O<sub>2</sub></b>  |
| Microstructure              | At short times, porous intergranular oxides. Multi-phase region observed at oxide/grain interface. At longer times and as grains oxidize further, oxides around grains densify. A discontinuous layer of porous oxide appears on the surface at longer times. Some intergranular voids observed.           | At all times, porous intergranular oxides, intergranular voids, oxide morphology consistent with melting. Multi-phase region at oxide/grain interface. At longer times the grains oxidize from the grain boundary inward, oxides around grains appear denser, although voids observed between grains. Partially oxidized grains have fine-scale microstructure in the interior. |
| Elemental composition       | Intergranular oxidized regions at short times rich in Hf, Zr, Ti. Multi-phase region at intergranular oxide/grain interface are rich in Ta and Nb. Ta observed in the oxide on the surface at longer times. Discontinuous Ti-rich region observed beneath surface oxide.                                   | Intergranular oxides are rich in Hf, Zr, some Ti at short times. Ta and Nb enriched in the multi-phase region between Hf,Zr oxides and unoxidized region in the grain. Ta detected in the oxygen rich regions at longer times.  |
| Phases detected (XRD)       | ZrTiO <sub>4</sub> , Zr <sub>0.75</sub> Ti <sub>0.25</sub> O <sub>2</sub> , Hf <sub>6</sub> Ta <sub>2</sub> O <sub>17</sub> , NbC <sub>0.5</sub>   | Zr <sub>6</sub> Nb <sub>2</sub> O <sub>17</sub> , HfTiO <sub>4</sub> , TiTa <sub>2</sub> O <sub>7</sub> , HfO <sub>2</sub>  |
| <b>1800 °C</b>              | <b>0.1% O<sub>2</sub></b>  |   |
| Microstructure              | Dense external oxide scale with larger embedded carbide grains   |   |
| Elemental composition       | Oxygen-rich regions are primarily rich in Hf, Zr and Ti up to 10 minutes. Embedded carbide regions are Ta- and Nb-rich. Ti-rich band observed at oxide/substrate interface. Very small amounts (~1-2 at%) Ta observed in the oxide adjacent to the Ta/Nb carbide grains near the surface after 15 minutes. |   |
| Phases detected (SAED, XRD) | (Nb,Ta) <sub>6</sub> C <sub>5</sub> , (Nb,Ta) <sub>2</sub> C, Zr <sub>0.42</sub> Ti <sub>0.58</sub> O <sub>2</sub> , Zr <sub>0.75</sub> Ti <sub>0.25</sub> O <sub>2</sub>  |   |

Table 3.6: Summary of the microstructure, elemental composition and oxide phases formed on (HfZrTiTaNb)B<sub>2</sub> after oxidation at 1500 °C, 1700 °C and 1800 °C in 0.1%O<sub>2</sub> and 1%O<sub>2</sub>. XRD phases reported are those detected after 5 minutes in 1%O<sub>2</sub> and 15 minutes in 0.1%O<sub>2</sub>.

| <b>1500 °C</b>        | <b>0.1% O<sub>2</sub></b>  | <b>1%O<sub>2</sub></b>  |
|-----------------------|--|---|
| Microstructure        | Mostly dense external scale. Oxide/substrate interface is characterized by partially oxidized diboride grains surrounded by oxides, and voids.   | External scale with rounded morphology consistent with formation of a melt and large pores (~10-20µm). Oxide/substrate interface is characterized by partially oxidized diboride grains surrounded by oxides.     |
| Elemental composition | Hf, Zr rich external oxide and interspersed with Ta, Nb rich boride grains at the oxide/substrate interface. Ta, Nb rich borides near the substrate.   | Porous external scale contains Hf, Zr, Ti and small amounts of Ta (4-6 at%). Oxide/substrate interface is characterized by partially oxidized Ta and Nb boride grains surrounded by group IV oxides and porosity. |
| Phases detected (XRD) | (Nb,Ta) <sub>3</sub> B <sub>4</sub> , Ti <sub>0.6</sub> Ta <sub>0.4</sub> O <sub>2</sub> , HfO <sub>2</sub> , Zr <sub>0.75</sub> Ti <sub>0.25</sub> O <sub>2</sub>   | TiNb <sub>2</sub> O <sub>7</sub> , HfO <sub>2</sub> , Zr <sub>0.75</sub> Ti <sub>0.25</sub> O <sub>2</sub> , HfTiO <sub>4</sub> , TiO <sub>2</sub> , Ta <sub>2</sub> O <sub>5</sub>                               |
| <b>1700 °C</b>        | <b>0.1% O<sub>2</sub></b>  | <b>1%O<sub>2</sub></b>  |
| Microstructure        | Mostly dense external scale, with bright (per backscatter image) phases embedded in oxide. Similar morphology seen in intergranular regions near surface.  | Thinner, dense external scale. Oxide/substrate interface is characterized by large (~10-20 µm) voids and partially oxidized grains surrounded by oxides. Liquid boron observed in pores and voids.                |
| Elemental composition | The oxides are rich in Hf and Zr. The bright phases embedded in the oxides are Ta and Nb rich borides. Ti is observed both in the oxide and boride.  | Oxides are rich in Hf, Zr and Ti. Partially oxidized grains are rich in Ta and Nb, with some Ti observed also in the diboride.  |
| Phases detected (XRD) | ZrTiO <sub>4</sub> , ZrO <sub>2</sub> , Zr <sub>0.9</sub> Ti <sub>0.1</sub> O <sub>2</sub> , Ta <sub>3</sub> B <sub>4</sub> , Ta <sub>3</sub> B <sub>2</sub> and TaB   | Ta <sub>3</sub> B <sub>4</sub> , HfO <sub>2</sub> , ZrO <sub>2</sub> , (Zr,Ti)O <sub>2</sub>  |
| <b>1800 °C</b>        | <b>0.1% O<sub>2</sub></b>  |   |
| Microstructure        | Non-uniform oxidized layer on surface. Where an oxide is observed, it is similar to that formed on the carbide: a two-phase scale with bright (per backscatter image) phases embedded in scale. Large voids are also observed. |   |
| Elemental composition | The oxides are rich in Hf and Zr. The bright phases embedded in the oxides are Ta and Nb rich borides. Ti is primarily observed in the oxide.  |   |
| Phases detected (XRD) | TaB, ZrO <sub>2</sub> , (Zr, Hf)TiO <sub>4</sub>   |   |

In summary, (HfZrTiTaNb)C exhibited porous and intergranular oxide formation at 1500 °C and 1700 °C. Mainly intergranular oxidation was observed at short times in 1500 °C

in 0.1%O<sub>2</sub> and 1700 °C at all oxygen partial pressures. A porous external scale formed at longer times at 1500 °C in 0.1%O<sub>2</sub>, and at all times in 1%O<sub>2</sub>. Denser oxides formed at 1800 °C and 0.1%O<sub>2</sub>, with some porosity in the surface regions. (HfZrTiTaNb)B<sub>2</sub> exhibited a combination of external scale and partially oxidized region marked by porosity and voids. At 1500 °C and 1%O<sub>2</sub>, the external scale was porous and exhibited large pores on the order of tens of microns. At 1700 °C and 1%O<sub>2</sub>, the external scale was thinner, and partially oxidized region is thicker compared to the 1500 °C case. At 1800 °C and 0.1%O<sub>2</sub>, the morphology mimics that observed on the carbide oxidized under the same conditions.

The composition of the oxides that formed on (HfZrTiTaNb)C and (HfZrTiTaNb)B<sub>2</sub> was generally dominated by group IV elements as there was a strong tendency towards preferential oxidation (several EDS and XRD results provided in Appendix C illustrate this very well). The trends predicted and validated in the Chapter 2, wherein the thermodynamic stabilities are expected to drive the oxidation behavior of the high entropy materials, are exhibited in all the conditions tested for the carbides and the borides, i.e., Hf and Zr oxidized preferentially, followed by Ti, then Ta and Nb.

The extent to which the group V elements were observed in the oxide formed on (HfZrTiTaNb)C was related to the oxidation morphology for a given temperature and pO<sub>2</sub>. Both Ta and Nb were observed in the oxide scale at 1500 °C, while mainly Ta was observed at 1700 °C. Ta and Nb oxides are accompanied by observations of microstructure consistent with liquid oxide formation. At 1700 °C where intergranular oxidation dominated the morphology of the oxidized regions, the porosity and liquid oxide formation combined to open large voids in the material, leading to accelerated degradation. Insignificant amounts of Ta or Nb were observed in the oxide at 1800 °C at short times, while Ta- and Nb-rich carbides were retained in the oxide scale even near the surface.

On the other hand,  $(\text{HfZrTiTaNb})\text{B}_2$  oxidized to form group IV-rich oxides in almost all conditions, with the exception occurring at  $1500^\circ\text{C}$  in  $1\%\text{O}_2$  wherein group V elements were observed in the scale. Thus, variation in the morphology of the oxidized high entropy carbides and borides are related to the changing composition of the oxide scale as the substrate oxidizes.

### *Destabilization of substrate solid solution*

The oxidized  $(\text{HfZrTiTaNb})\text{C}$  exhibits evidence of destabilization of the solid solution phase at the oxide/substrate interface. At  $1700^\circ\text{C}$  in  $0.1\%\text{O}_2$ ,  $1800^\circ\text{C}$  in  $0.1\%$  and  $0.5\%$   $\text{O}_2$ , a fine-scale microstructure of partially oxidized carbide embedded in oxides is observed (Figure 3.23) at the oxide/substrate interface. A Ti-rich band was also observed at the oxide/substrate interface as a dark band (in backscatter) at the oxide/substrate interface, shown in Figure 3.24 for the  $1800^\circ\text{C}$  case. There is no appreciable change in the overall oxide thickness or the thickness of the dark, Ti-rich band between the 10 and 15 minute exposures (Figure 3.25).

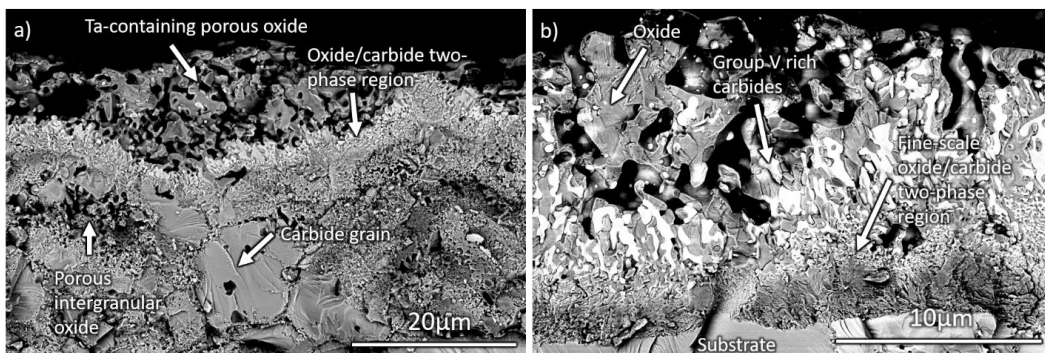


*Figure 3.23: Cross-section backscattered electron images of  $(\text{HfZrTiTaNb})\text{C}$  oxidized in  $0.1\%\text{O}_2$  for 15 minutes at (a)  $1700^\circ\text{C}$  and (b)  $1800^\circ\text{C}$ . Region shown is near the oxide/gas interface.*

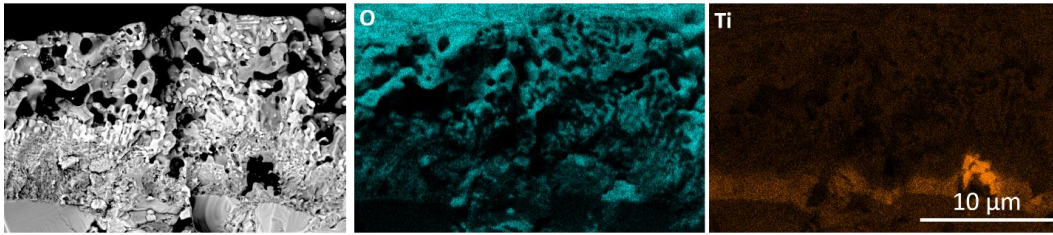


Figure 3.24: Backscattered electron image of the cross-section of the oxidized region formed on (HfZrTiTaNb)C at 1800 °C in 0.1%O<sub>2</sub> after 10 minutes, along with O and Ti EDS maps.

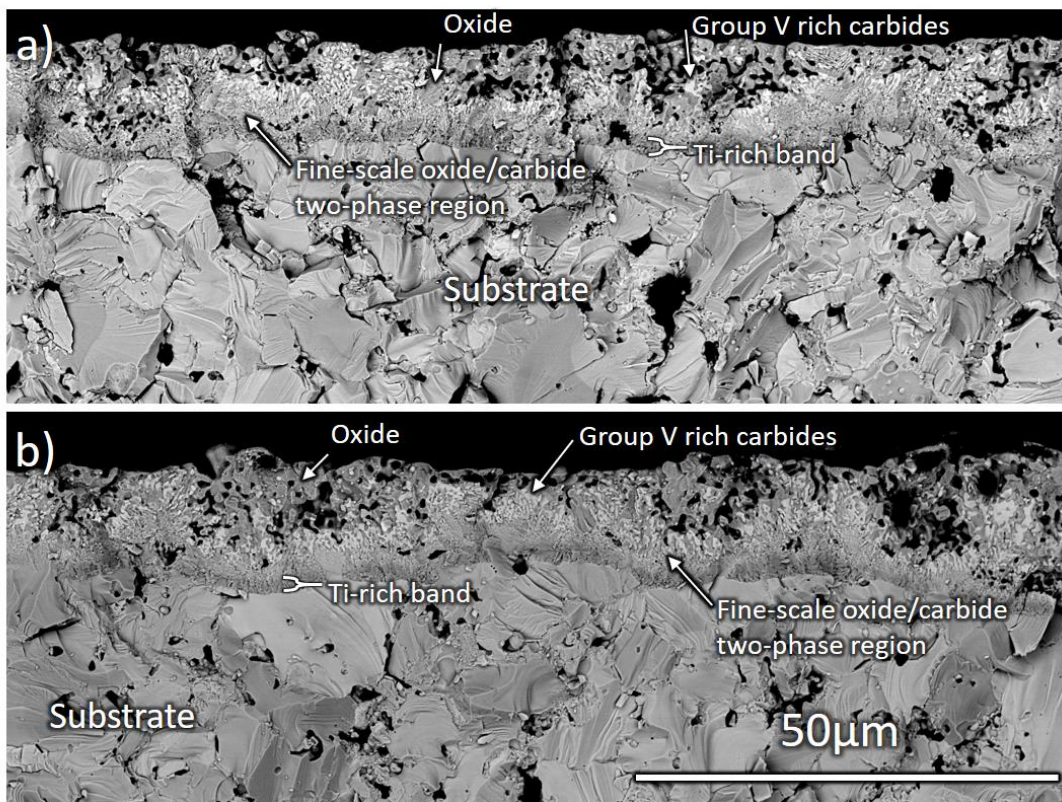


Figure 3.25: Cross-section backscattered electron images of (HfZrTiTaNb)C oxidized at 1800 °C in 0.1%O<sub>2</sub> for (a) 10 minutes and (b) 15 minutes. Region shown is near the oxide/gas interface.

The composition and structure of the Ti-rich band is consistent with TiC. The Ti-rich band formed after a 10-minute exposure at 1800 °C in 0.1%O<sub>2</sub> was analyzed using selected

area diffraction at low magnification on a focus-ion beam milled TEM foil obtained from the oxidized specimen. The pattern obtained (Figure 3.26) is consistent with the [100] zone axis for a rock-salt structure, with a lattice parameter of  $4.32\text{\AA}$ , which is a good match for the lattice parameter for  $\text{TiC}^{161}$ .

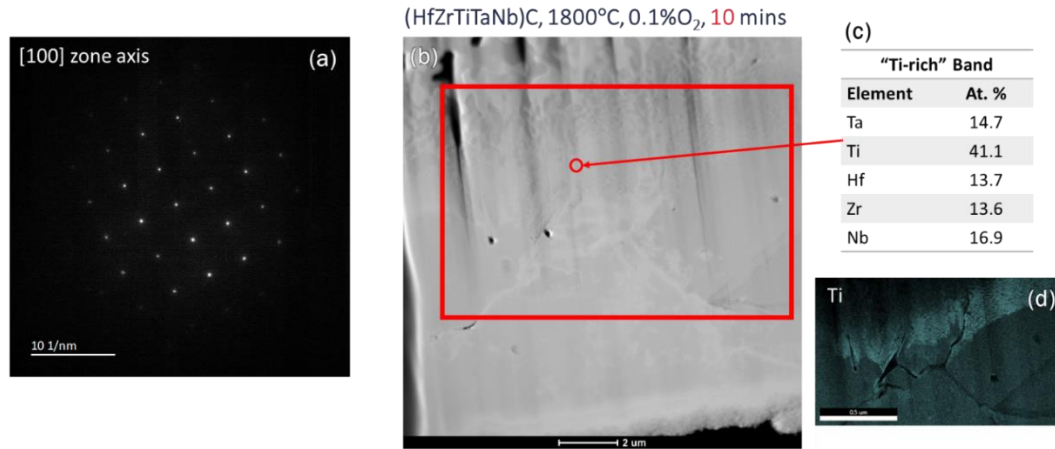


Figure 3.26: Ti-rich band formed on  $(\text{HfZrTiTaNb})\text{C}$  exposed to  $0.1\% \text{O}_2$  for 10 minutes in  $0.1\% \text{O}_2$  at the oxide-substrate interface: (a) selected area diffraction pattern, (b) STEM-EDS image (c) EDS point analysis, and (d) EDS map of the Ti rich region. Image in (b) and EDS work in (c) and (d) conducted by University of Alabama.

Analysis at higher magnification, however, reveals evidence of two phases in the Ti-rich band. A higher magnification bright field TEM image was obtained from the Ti-rich region, shown in Figure 3.27. The microstructure is indicative of phase separation. A convergent beam electron diffraction (CBED) pattern was obtained from the darker phase (Figure 3.27 (b)) in what appears to be a two-phase region. This pattern is also consistent with rock-salt titanium carbide, with a lattice parameter of  $4.36\text{\AA}^{161}$ . The brighter phase, likely group V carbide, is similar to the larger bright phase seen in electron image in Figure 3.24 nearer the surface representing the oxide/gas interface.

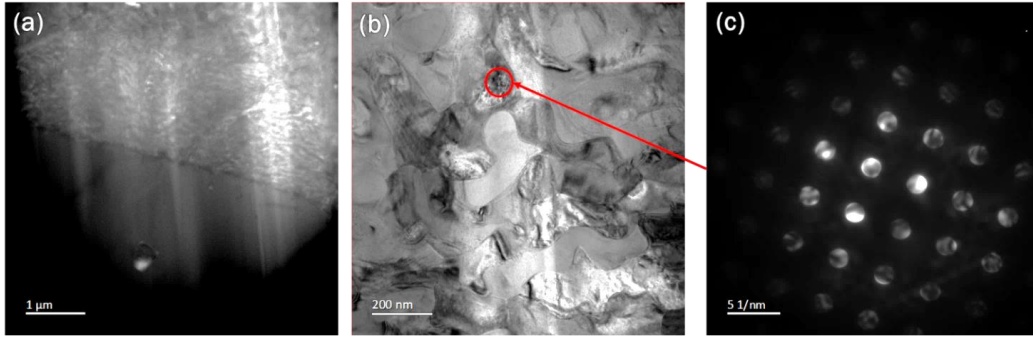


Figure 3.27: Ti-rich band formed on (HfZrTiTaNb)C exposed to 0.1%O<sub>2</sub> for 10 minutes in 0.1%O<sub>2</sub> at the oxide-substrate interface: (a) low magnification bright field TEM image, (b) higher magnification bright field TEM image in the Ti rich region, (c) CBED pattern obtained from one of the phases in the two-phase region seen in (b) consistent with TiC.

The bright phases indicated by EDS maps obtained of the foil (Figure 3.28) to be group V sub-stoichiometric carbide regions are embedded within the group IV-rich oxides. This was further confirmed by selected area diffraction (SAED) patterns obtained for the oxygen deficient region as shown in Figure 3.29. The structure indicated by the selected area diffraction pattern shown in Figure 3.29 is a good match for  $\beta$ -Nb<sub>2</sub>C<sup>123</sup> with a lattice parameter close to Ta<sub>2</sub>C, which is consistent with EDS data. Other patterns obtained from the bright regions also suggest sub-stoichiometric group V carbides (Ta, Nb), such as Nb<sub>6</sub>C<sub>5</sub> (detected by XRD, see Table 3.5), wherein ordering of C vacancies produce superlattice reflections. Combined, the microstructure and electron diffraction data suggest that upon preferential oxidation of Hf and Zr from the high entropy carbide, the solid solution phase is destabilized, resulting in a group IV rich (TiC) phase, and group V ((Ta,Nb)<sub>2</sub>C or (Ta,Nb)<sub>6</sub>C<sub>5</sub>) phases form.

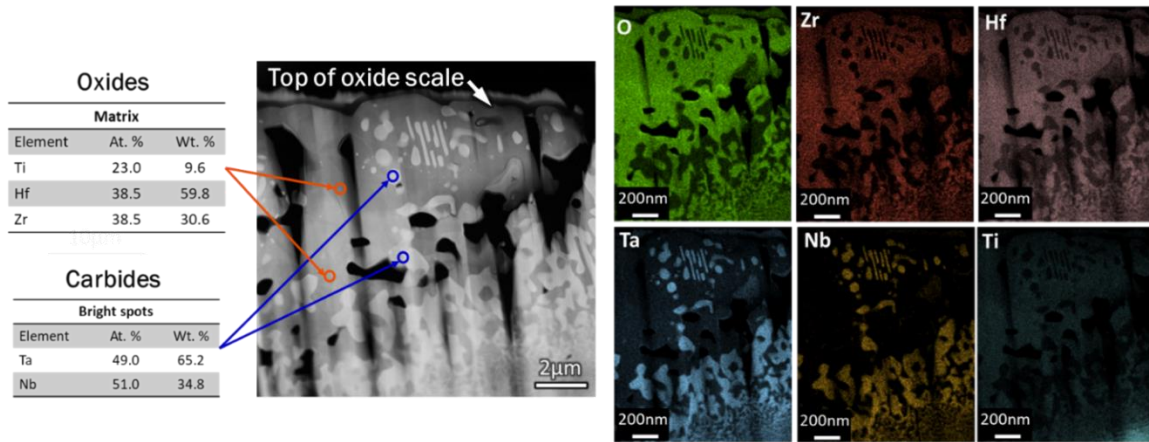


Figure 3.28: STEM-HAADF and TEM-EDS maps of FIB lift-out obtained from (HfZrTiTaNb)C oxidized at 1800 °C in 0.1%O<sub>2</sub> for 10 minutes. Only group IV elements present in the oxide-rich regions. TEM-EDS work conducted by University of Alabama.

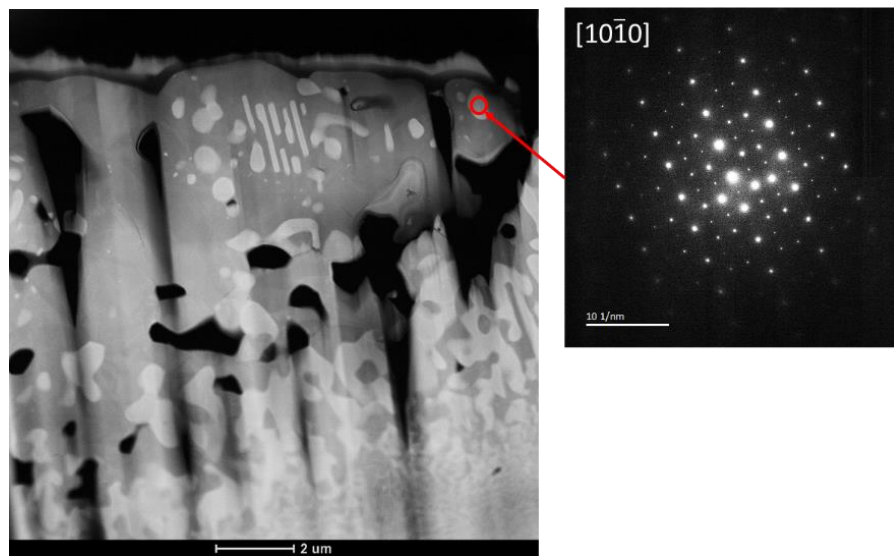
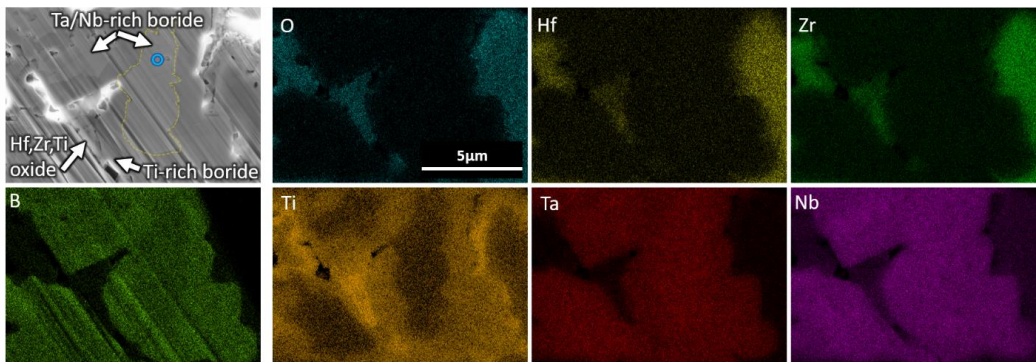


Figure 3.29: Selected area diffraction pattern obtained from a bright region near the surface of the oxidized region formed on (HfZrTiTaNb)C exposed to 0.1%O<sub>2</sub> for 10 minutes in 0.1%O<sub>2</sub> consistent with Nb<sub>2</sub>C or Ta<sub>2</sub>C. Image shown here obtained from University of Alabama.

Similarly, evidence for the destabilization of the solid solution is observed in the partially oxidized region formed on  $(\text{HfZrTiTaNb})\text{B}_2$  after exposure at  $1700^\circ\text{C}$  in  $1\%\text{O}_2$  for five minutes. This sample was discussed in detail in Chapter 2. The EDS maps are reproduced here in Figure 3.30 and annotation added. This map indicates that while Ti is found primarily in the oxide, it is partially retained as a boride phase. The electron image shows atomic number contrast coinciding with the Ti map. The interface between the Ti-rich and Ti-deficient region is sharp, suggesting that the middle of the grain is a different phase. XRD results (Table 3.6) confirm the presence of other Ta (or Nb) rich borides, confirming the destabilization of the main diboride solid solution. As with the carbide, this destabilization is attributed to the preferential oxidation of group IV elements.



*Figure 3.30: Elemental backscattered image of a FIB lift out taken from a  $(\text{HfZrTiTaNb})\text{B}_2$  sample oxidized at  $1700^\circ\text{C}$  in  $1\%\text{O}_2$  for 5 minutes along with the Hf, Zr, Ti, Ta, Nb, B and O EDS maps. Ti-deficient, Ta/Nb-rich boride outlined in pale yellow in one region to indicate region of interest but left un-outlined in another region highlight the sharp interface.*

### *Oxygen transport in carbides*

The oxidation of the high entropy carbides appears to occur via oxygen transport into the carbide material via grain boundaries at short times and then from the grain boundaries into the grain at longer times. Table 3.5 shows that this transport via grain boundary oxidation

is observed at 1500°C and 1700°C in various  $pO_2$ s and exposure times. While a porous external scale forms eventually at 1500°C, intergranular oxidation is observed to be the dominant morphology at 1700°C at all times and oxygen partial pressures. This inward transport of oxygen combined with the varying composition of the scale at different temperatures is believed to be responsible for the temperature dependence of morphology observed on the carbides after oxidation exposures.

Oxygen transport inward is supported by observations of oxygen intensity in the elemental EDS maps taken in the regions underneath the Hf-rich oxide in the oxygen affected grains, suggesting oxycarbide formation, oxygen dissolution in the carbide or the formation of oxides interspersed with carbides on a much finer scale than observable in the SEM. Shown in Figure 3.31 are examples from carbide specimens oxidized in 0.1%  $O_2$  at 1500°C, 1700°C and 1800°C for five minutes (shortest exposures at these conditions). The intensity of the oxygen maps indicates highest intensity on the surface and at grain boundaries, and regions of slightly lesser intensity in the subsurface regions, or in the grains adjacent to the oxygen maps. The yellow arrows shown in the figures indicate the direction of proposed oxygen transport. Intergranular oxide is clearly seen in Figure 3.31 (a) – (b). Maps for Hf, the element with the most thermodynamically favored oxide, and Nb, the element with the least thermodynamically favored oxide, are also shown for reference. Regions with high Hf and O intensity coinciding indicate oxide formation in the (HfZrTiTaNb)C specimens tested in this study.

The subsurface oxygen containing region is most obvious in Figure 3.31 (c) wherein a thin Hf-rich oxide layer is observed on the surface with an oxygen enriched subsurface region, five microns in thickness. Hf and Nb appear similarly distributed in the regions exhibiting oxygen intensity in these subsurface regions. Moreover, XRD results from this specimen presented in Figure 3.32 show no indication of Nb oxides for this condition. In fact, Nb sub-stoichiometric carbides are indicated ( $Nb_6C_5$  from PDF no. 04-007-6990; peak locations also

match Nb<sub>2</sub>C from Smith et al<sup>123</sup>). It is known from samples tested at 10 and 15 minutes that Hf is among the elements that oxidize preferentially, and Nb exists mainly as sub-stoichiometric carbides embedded in the oxide scale, so Nb oxides are unlikely. O intensity in Nb-rich regions in samples where Nb oxides are not detected (via XRD), and in samples in which group V elements are primarily observed in the carbides at longer times, are consistent with O transport occurring into the carbide possibly via dissolution.

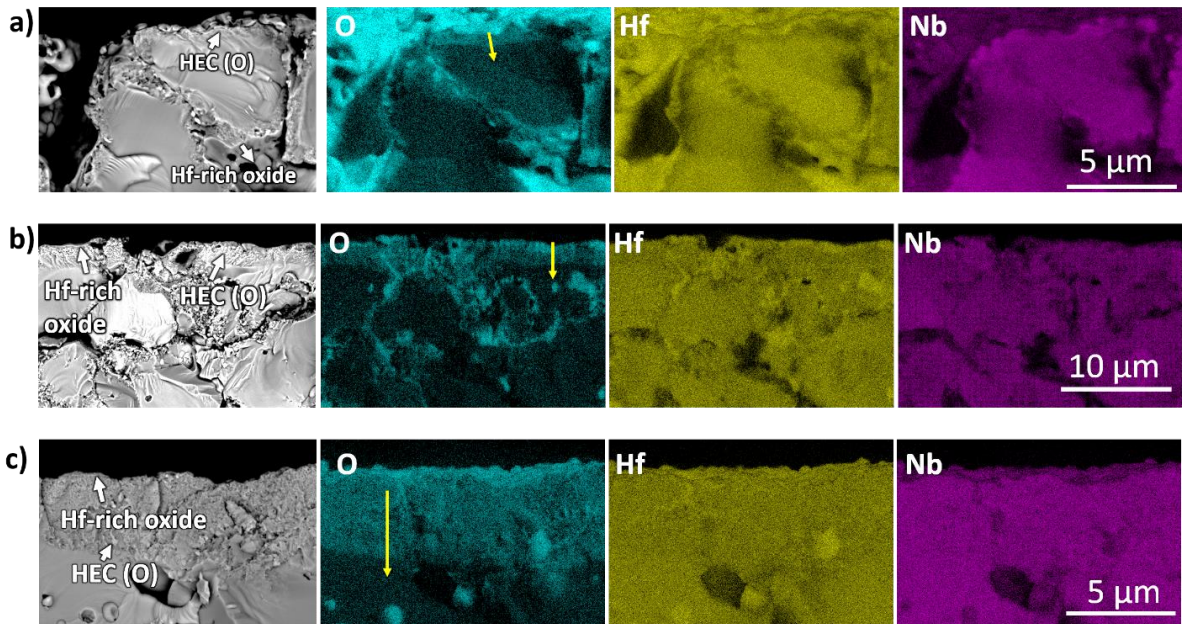


Figure 3.31: Backscattered electron image and O, Hf and Nb elemental maps for (HfZrTiTa)C oxidized in 0.1%O<sub>2</sub> for 5 minutes at (a) 1500 °C, (b) 1700 °C and (c) 1800 °C. Yellow arrows show the direction of proposed oxygen transport. HEC =High entropy carbide, (HfZrTiTa)C.

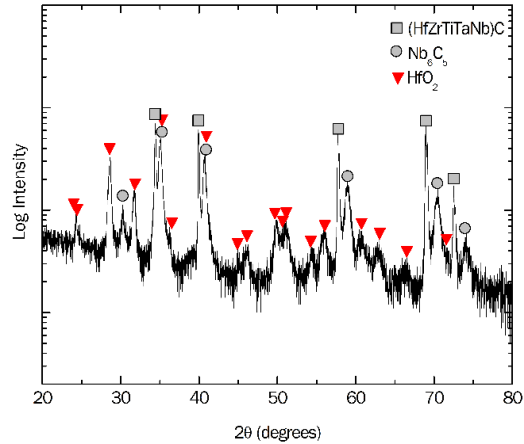


Figure 3.32: XRD data obtained from a (HfZrTiTaNb)C oxidized at 1800 °C in 0.1%O<sub>2</sub> for five minutes. XRD was obtained using micro-focused optics.

### Liquid oxide formation in carbides

The differences between oxidation morphologies observed for the carbide exposed at 1500 °C and 1700 °C can be elucidated by considerations of liquid oxide formation. Oxidation kinetics at 0.1%O<sub>2</sub> are slowed enough that the microstructural evolution for both temperatures can be observed. A transition from grain boundary-oxide dominated to porous external scale formation was observed in the specimen tested at 1500 °C in 0.1%O<sub>2</sub> after 10 minutes. The oxidized region in cross-section is shown in Figure 3.33 (a) and compared to a sample tested at 1700 °C also in 0.1%O<sub>2</sub> for 10 minutes. Figure 3.33(a) shows that the intergranular oxides formed for the 1500 °C case are porous, and a fine-scale porosity can be observed in the inner region of the grains near the surface. In contrast, the surface oxide formed at 1700 °C (Figure 3.33 (b) ) appears denser and the interior of the grain is largely unaffected. Surface oxidation at 1500 °C and 1700 °C extensive and group V (Ta, Nb) are observed as oxides (Table 3.5, Figure 3.33). At 1500 °C, Nb oxides and eutectics of Nb oxides melt (Nb<sub>2</sub>O<sub>5</sub>-TiO<sub>2</sub> eutectics from 1467 ° to 1477 °C<sup>162</sup>, Nb<sub>2</sub>O<sub>5</sub>-ZrO<sub>2</sub> eutectics at 1436 °C<sup>75</sup>). However at 1700C, Ta oxides in addition to Nb oxides result in liquid oxide formation (Ta<sub>2</sub>O<sub>5</sub>-TiO<sub>2</sub> eutectic at 1621 °C, Tm for TiTa<sub>2</sub>O<sub>7</sub> is 1674 °C<sup>120</sup>). These low melting Ta-containing phases result in a more protective

oxide around each grain limiting intragranular oxidation at 1700 °C, however it precludes the formation of an external scale. This protection is not available at 1500 °C resulting in extensive intragranular oxidation. The combination of oxygen transport inward via grain boundaries, preferential oxidation and changing chemical make-up of the oxide results in non-uniform modes of attack. This in turn results in temperature dependent morphologies observed in the carbide.

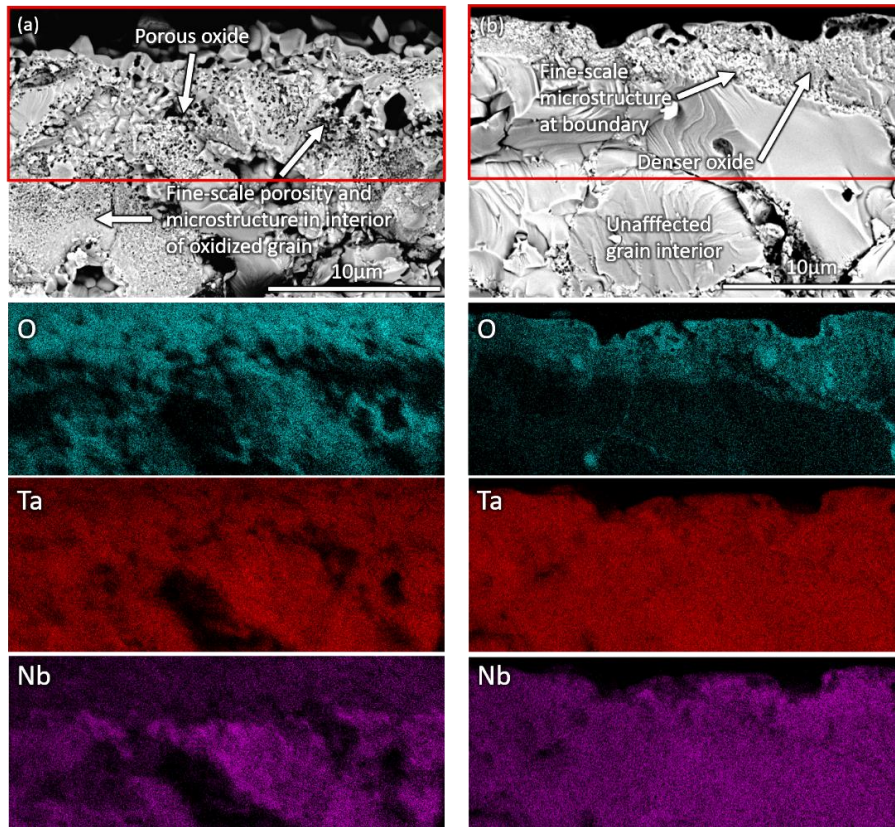


Figure 3.33: Cross-section backscattered electron images and O, Ta and Nb EDS maps of (HfZrTiTaNb)C oxidized in 0.1%O<sub>2</sub> for 10 minutes at (a) 1500 °C and (b) 1700 °C. Region shown is near the oxide/gas interface.

#### **Borides: boria formation**

The formation of boria is a significant factor to be considered in the oxidation resistance and mechanisms of diborides. The retention of boria on the surface of the oxidized

(HfZrTiTaNb)<sub>2</sub>B<sub>2</sub> is affected by temperature, as expected. The oxidized (HfZrTiTaNb)<sub>2</sub>B<sub>2</sub> shows evidence of boria retained on the surface of the sample at 1700 °C (Figure 3.34). Figure 3.35 shows detailed cross-section images of a boride sample tested in 1%O<sub>2</sub> at 1700 °C, showing porous regions filled with a product with glassy appearance (under secondary electron imaging), with morphology consistent with solidified melt. This same product appears to fill the region under the surface oxide. Combined with plan view images (Figure 3.34), the cross-section images indicate the formation of pore-filling boria. XRD data (summarized in Table 3.6) are consistent with the EDS maps, showing Ta (or possibly Ta and Nb) borides, along with group IV rich oxides.

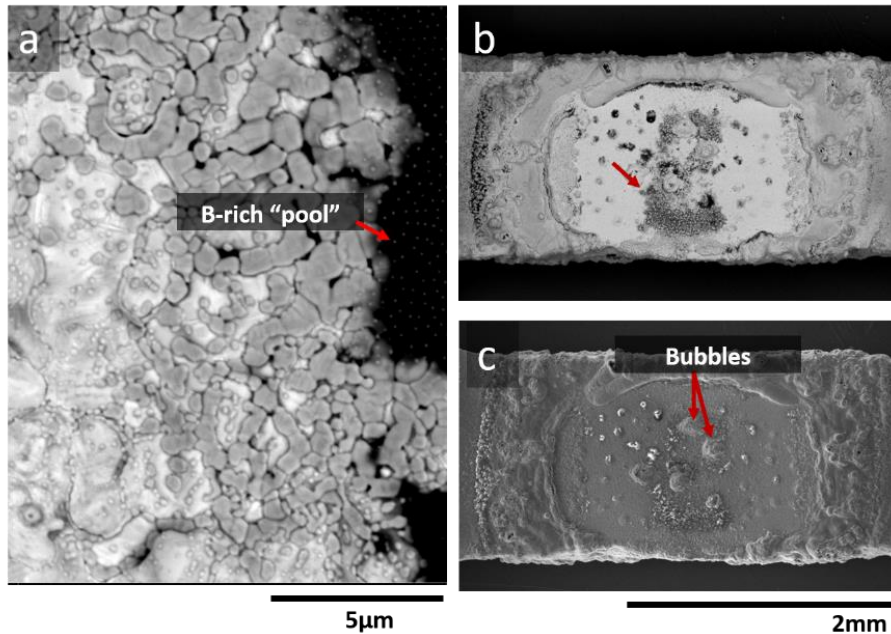


Figure 3.34: (a) Detailed backscattered electron plan view image of the pyrometer sighting zone on (HfZrTiTaNb)<sub>2</sub>B<sub>2</sub> oxidized in 1%O<sub>2</sub> at 1700 °C for 5 minutes, showing boria rich pools (dark regions in (a) and (b)) that appear glassy in the SEM. (b) and (c) are backscattered electron and secondary images showing a low magnification view of the hot zone bubbles.

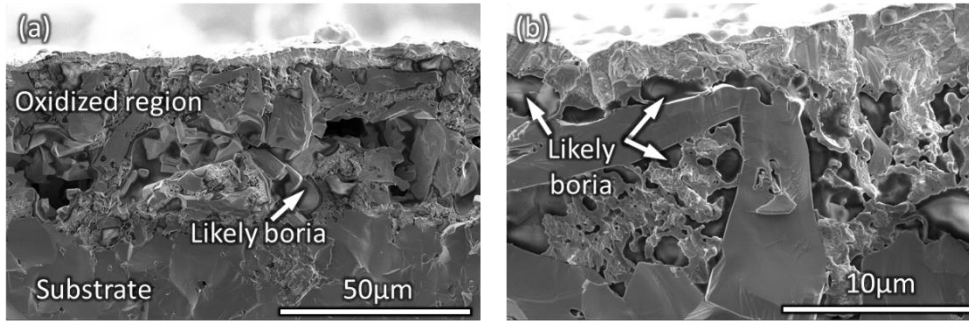


Figure 3.35:  $(\text{HfZrTiTaNb})\text{B}_2$  oxidized in 1% $\text{O}_2$  at 1700 °C for 5 minutes. (a) shows a lower magnification cross-section secondary electron image of the microstructure; (b) shows a higher magnification image of the region near the surface.

In contrast, the microstructure on the surface of  $(\text{HfZrTiTaNb})\text{B}_2$  after oxidation at 1800 °C in 0.1% $\text{O}_2$  for 15 minutes (Figure 3.36) shows faceted grains, porosity and no discernible bubbles. Analysis of the morphology in cross section (example shown in Figure 3.22(f) ) does not readily reveal any evidence of solidified boria, suggesting forms and volatilizes rapidly under this testing condition.

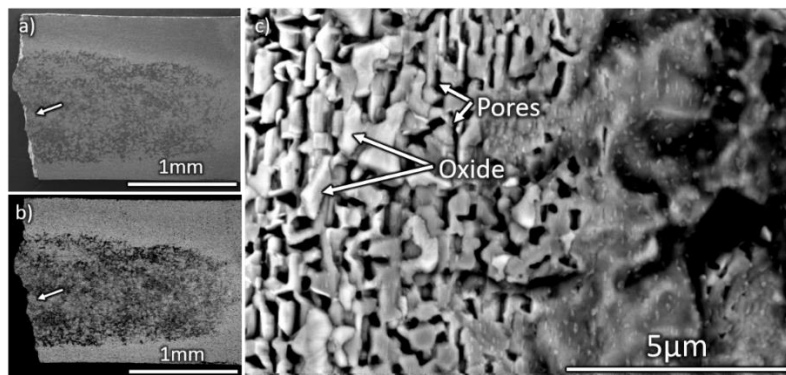


Figure 3.36: Low magnification (a) secondary and (b) backscattered electron plan view images of the pyrometer sighting zone on  $(\text{HfZrTiTaNb})\text{B}_2$  oxidized in 1% $\text{O}_2$  Ar at 1800 °C for 15 minutes. (c) High magnification backscattered image of the microstructure in the region indicated by white arrows in (a) and (b).

### 3.4. Discussion

#### 3.4.1. Oxide/substrate compositional and microstructural changes

The oxide scale and substrate composition change with time due to preferential oxidation, which then changes the oxygen transport inwards. In addition, the formation of liquid oxides changes the protective capability of the oxide scale. At short times (two minutes in 1%O<sub>2</sub> or five minutes in 0.1%O<sub>2</sub>), any oxide that forms on the carbides is enriched in the group IV elements and is porous, due to CO(g) evolution. Table 2.2, which summarizes melting temperatures of the oxides by different elemental additions, shows that increasing amounts of Ti, Ta and Nb, can result in liquid oxides in the experimental temperature ranges (1500-1800 °C). At 1500 °C, mainly Nb containing oxides result in oxides that melt at or below 1500 °C. Indeed, at 1500 °C, Nb is observed in the oxidized regions (Table 3.5, Figure 3.22). The combination of a liquid oxide and gaseous evolution result in large pores in the external scale that is seen in Figure 3.22 (a). Similarly, at 1700 °C, Ta incorporation in the oxide scale resulted in densification and melt formation, leading to slower oxidation of the carbide grains and delaying the formation of an external oxide scale, as shown in Figure 3.33(b). After five minutes at 1%O<sub>2</sub>, the intergranular regions not only exhibit solidified melts (Figure 3.22 (b)), due to both Ta and Nb contributing to lowering the melting temperature of the oxide, but also large voids which would act as fast pathways for oxidant ingress. Thus, intergranular oxidation continues to occur until the sample fails. While small amounts of elements such as Ti or Ta can help promote sintering of the oxide or closing of the pores in the short term, at longer times further oxidation of the group V elements in particular is detrimental to the oxidation behavior of the high entropy carbide (Table 2.2). The addition of group V elements, like Ta, to Hf or Zr UHTCs have been proposed to improve oxidation resistance, either through the reduction of oxygen vacancies, sintering of an otherwise porous scale or the formation of complex oxides like Hf<sub>6</sub>Ta<sub>2</sub>O<sub>17</sub>. While complex oxides and some densification of the oxide was observed (Table 3.5), excessive addition of group V elements also resulted in the promotion of liquid oxide

formation and persistence of intergranular oxidation, as seen in the 1700 °C case. The oxidation resistance improved markedly under conditions where the oxidation of Ta and Nb were limited, such as at 1800 °C for up to 15 minutes. At 1800 °C, the densification of the Hf, Zr and Ti oxide, likely due to Ti oxides lowering the melting temperature of Hf/Zr oxides (eutectic at 1740 °C,  $T_m(\text{TiO}_2) = 1857^\circ\text{C}$ ), results in the mitigation of further liquid oxide formation from the oxidation of the group V elements. Figure 3.37 summarizes the evolution of the microstructures observed on the carbides at each experimental temperature that results from the melt formation at different temperatures.

At 1800 °C, the oxide phase(s) in both the carbide and boride primarily consist of group IV elements, and sub-stoichiometric Nb/Ta carbides or borides, depending on the material, can be seen even close to the oxide/gas interface. This suggests that rapid densification of the oxide phases occurs and slows down the oxidation of Ta and Nb from the carbide, relative to the lower temperatures. This densification may take place due to formation of liquid oxides in areas where the oxide is Ti-rich ( $T_m^{\text{TiO}_2} = 1857^\circ\text{C}$ ), or sintering where the oxide is Hf/Zr-rich. A denser, more protective scale would lower the partial pressure of oxygen at the substrate interface, limiting the oxidation of the group V elements as predicted by the preferential oxidation FactSage calculations in the previous chapter.

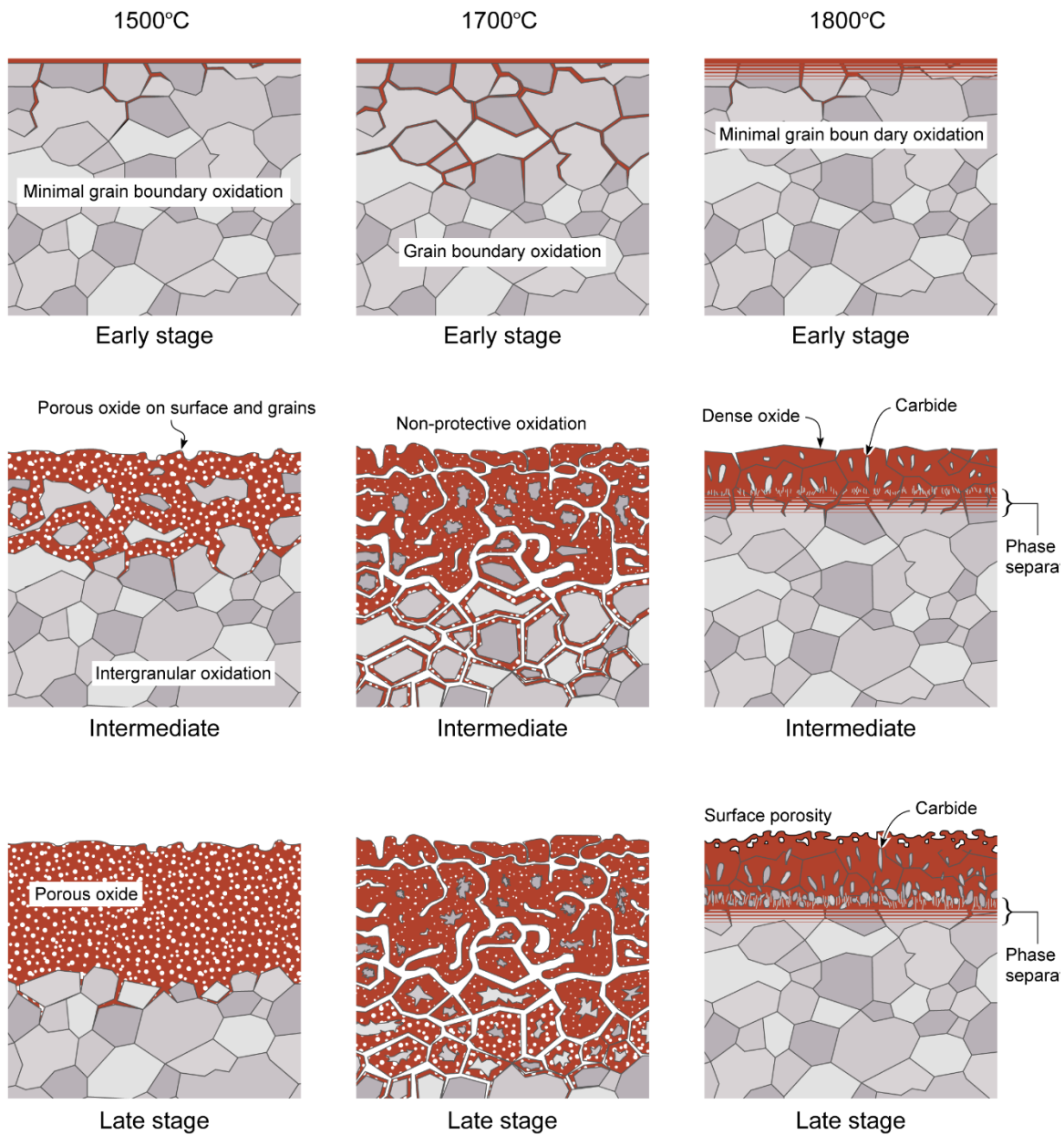


Figure 3.37: Summary of the evolution of microstructures observed on  $(\text{HfZrTiTaNb})\text{C}$ , based on observations at 1500 °C, 1700 °C and 1800 °C in 0.1% and 1% $\text{O}_2$ .

The formation of liquid bororia alongside the metal oxides at the experimental temperatures influenced the microstructure and composition formed in the oxidized regions on the diborides. The relative amounts of group IV and V oxides present in the oxide scale varied

with temperature, as with the carbides. While the external scale formed on the 1500 °C case showed Ta and Nb in the oxide, the external scale became thinner with increasing temperature and more group IV-rich. The oxide formed on the borides was deficient in group V elements compared to the carbides at 1700 °C and 1800 °C. Below the external scale, a region of partially oxidized grains consisting of Ta and Nb borides was observed. Liquid oxide that is likely boria rich, occupying channels in the oxide or in the large voids observed at the oxide/substrate interface slowed down oxidant ingress (Figure 3.35). It is possible that liquid boria in the oxidized regions offered some measure of protection against further oxidation, but this improvement was also observed at 1800 °C, where there was no direct evidence of boria solidified from melt as observed in the 1700 °C case. The materials tested here also have B<sub>4</sub>C as a secondary phase, so additional boria (l,g) production and CO (g) evolution is expected, which would explain the large voids observed, especially when compared to the morphology observed on the sample prepared from sintered commercial powders (Figure 3.15, Figure 3.16).

#### 3.4.2. Destabilization of the solid solution in high entropy carbides and borides due to preferential oxidation

In both the carbide and boride cases, there is evidence of the destabilization of the solid solution carbide or boride phase as a result of the preferential oxidation. For the carbide, after oxidation at 0.1%O<sub>2</sub> where the reactions have been slowed enough to observe the effects on the substrate, fine scale structure in the vicinity of a Ti-rich region is indicative of phase separation to TiC and (Ta,Nb)<sub>2</sub>C or (Ta,Nb)<sub>6</sub>C<sub>5</sub>. This effect was observed at 1700 °C and above in 0.1%O<sub>2</sub>, and shown for the 1800 °C case in Figure 3.24, Figure 3.27 and Figure 3.29. Figure 3.27 shows the Ti-rich rock-salt carbide and an Nb and Ta rich sub-stoichiometric carbide (Figure 3.29). Computational work performed by Oses et al.<sup>163</sup> indicates that the most stable

carbide in the Nb-C system is the Nb<sub>6</sub>C<sub>5</sub> phase as opposed to NbC, suggesting there is a driving force to form the metal-rich carbide. Further, consideration of the relative thermodynamic stabilities of Ta and Nb oxides along with that of CO(g) using an Ellingham diagram (Figure 3.41) and data from the FactPS databases<sup>30</sup> shows that CO(g) is thermodynamically favored over Ta<sub>2</sub>O<sub>5</sub> and Nb<sub>2</sub>O<sub>5</sub> at the experimental temperatures.

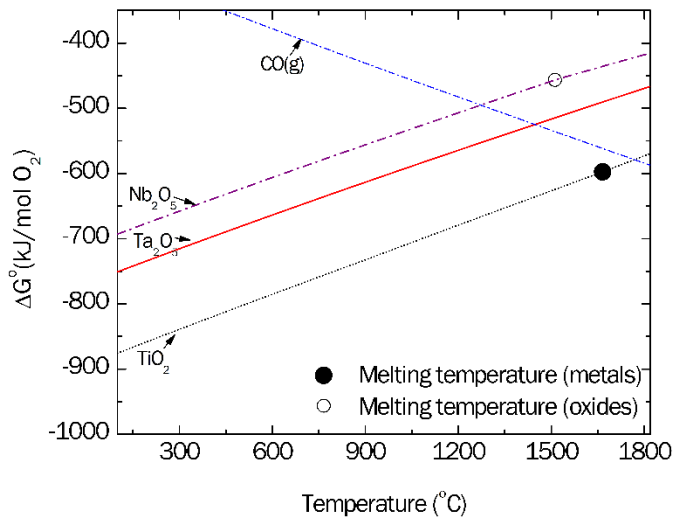


Figure 3.38: Ellingham diagram comparing the thermodynamic favorability of CO(g) to TiO<sub>2</sub>, Nb<sub>2</sub>O<sub>5</sub> and Ta<sub>2</sub>O<sub>5</sub>.

An Nb-C-O ternary phase diagram (T=1800 °C-2000 °C), based on the work of Fromm et al.<sup>164</sup> and Ono et al.<sup>165</sup> and reproduced in Figure 3.39, shows as the system becomes more metal-rich, the coexistence of Nb<sub>2</sub>C with the rocksalt NbC and niobium oxide is predicted. This is consistent with the results showing the rocksalt + A<sub>2</sub>C phase in the Ti-rich band, where A = Ta, Nb (Figure 3.29).

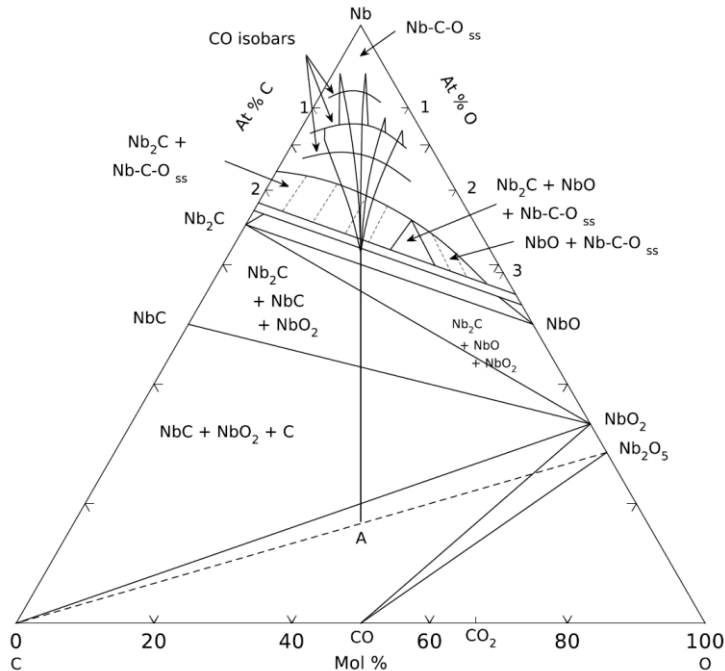


Figure 3.39: Ternary phase equilibria for Nb-C-O ( $T=1800^{\circ}\text{C}-2000^{\circ}\text{C}$ ) obtained from the Phase Equilibria Diagrams Database (NIST Standard Reference Database 31), The American Ceramic Society and the National Institute of Standards and Technology, 2020. Figure Number 92-184.

After oxidation of the diboride at  $1700^{\circ}\text{C}$ , two phases are observed in a partially oxidized grain: a Ti-rich boride phase forms at the interface between group V-rich borides and group IV-rich oxides (Figure 3.30). Additionally, an  $A_3B_4$  phase, where  $A = \text{Ta}$  or  $\text{Nb}$ , is detected by XRD after oxidation of  $(\text{HfZrTiTaNb})\text{B}_2$  at  $1500^{\circ}\text{C}$  and  $1700^{\circ}\text{C}$  (Table 3.6), while  $\text{TaB}$  is detected after oxidation at  $1800^{\circ}\text{C}$ . Based on considerations outlined in the prior chapter, this phase separation is attributed to preferential oxidation of Hf and Zr resulting in the reduction of configurational entropy stabilizing the five-component solid solution. Like the discussion for the carbide case above, it is possible to gain insight the ternary diagram for Ti-Nb-B, reproduced here in Figure 3.40 based on the work of Witusiewicz et al.<sup>116</sup>. By analogy to the carbide system, if the high entropy diboride solid solution is destabilized, other boride phases such as



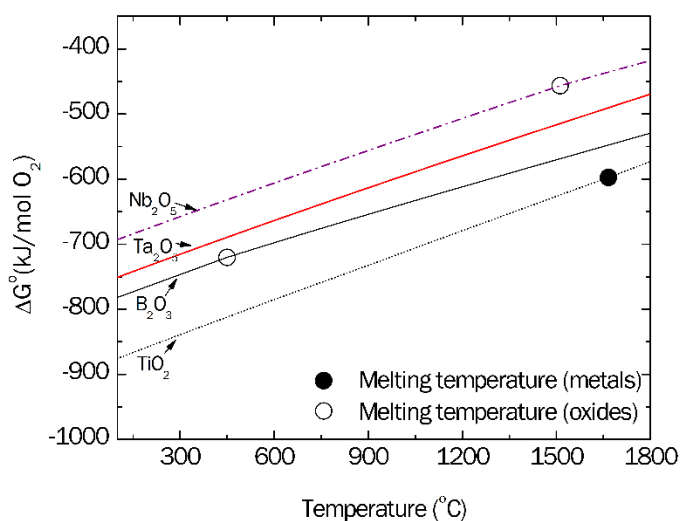


Figure 3.41: Ellingham diagram comparing the thermodynamic favorability of  $B_2O_3$  to  $TiO_2$ ,  $Nb_2O_5$  and  $Ta_2O_5$ .

### 3.4.3. Possible rate controlling mechanisms

#### 1500 °C and 1700 °C

The oxidation kinetics (Figure 3.17 and Figure 3.19) indicate a time dependence that lies between linear and parabolic for both the carbides and borides in most cases, even when a denser oxide near the reaction interface is observed (1800 °C). The carbides exhibit intergranular oxidation and porous oxide formation due to evolution of CO (g) at 1500 °C and 1700 °C at all times, and on the surface after oxidation at 1800 °C after 15 minutes. Like the carbides, the borides exhibit porosity, void formation and mixed boride/oxide oxidation affected regions, although liquid boria formation at 1700 °C and below may fill any open pores. Given that the quantification of the time dependence is based on material consumption, and therefore is reflective of an oxidized region with mixed morphology, this translates to mixed transport paths for the oxidant, particularly for the carbides. Therefore, a time-dependence intermediate between linear and parabolic is not surprising. Time dependence between linear

and parabolic can indicate reaction control, solid state diffusion through a solid, liquid or porous boundary with constant thickness, or gas phase diffusion.

The carbides exhibit a  $pO_2$  dependence of 0.59 to 0.7 (power law exponents), while the borides exhibit a  $pO_2$  dependence of 0.93 to 1.01. An oxygen partial pressure dependence is expected in several cases: if the oxidation behavior is reaction controlled, if solid state diffusion through a p-type oxide is operative, if ionic or molecular oxidant transport through a liquid product is rate controlling, molecular oxidant transport through a porous oxide or if gas phase diffusion is operative. The  $pO_2$  dependence observed for the carbides and diborides are much larger than would be expected for an ionic transport mechanism either through liquid or solid, which would exhibit  $pO_2$  dependence on the order of  $1/6$  to  $1/4$ . A  $pO_2$  dependence for the oxidation of Hf and Zr refractory metal diborides and HfC has previously been observed. Holcomb observed a  $pO_2$  dependence for the oxidation of hafnium carbide<sup>135</sup>. The  $pO_2$  dependence in that study was attributed to a gaseous diffusion through a network of pores and the existence of a reaction front where CO (g) and O<sub>2</sub> (g) react to form CO<sub>2</sub>. The model predicted a linear dependence on  $pO_2$ , which is not the case for the carbides here. The carbides exhibit a porous external scale at 1500 °C, and the  $pO_2$  dependence for this temperature is essentially the same as that for 1700 °C, where intergranular porosity and even voids are observed. Thus, transport through a porous oxide is possible, which is also supported by the microstructure. A gas phase diffusion mechanism is also supported by  $pO_2$  dependence on the order observed here, and this would be consistent with the observed microstructure.

The linear  $pO_2$  dependence observed for the diborides is consistent with results in the literature for ZrB<sub>2</sub><sup>166</sup>. Table 3.1 shows that molecular transport of oxidant through a liquid product results in a linear  $pO_2$  dependence. This is consistent with Parthasarathy et al.'s model<sup>8</sup> for the rate controlling mechanism for the oxidation of refractory metal diborides, which was based on the Tokuda's findings for the permeation of oxygen through liquid boron<sup>167</sup>. While

the  $pO_2$  dependence for the diborides may support transport through boria as a rate limiting step, the linear (or close to linear) rate kinetics suggests that a layer of constant thickness is needed. The data obtained in this study does not provide insight into this.

The oxidation rates for both compositions drop off significantly at 1800 °C, indicating a change in mechanism that happens for both the carbide and the boride, with the boride still exhibiting lower material consumption. Therefore, mechanisms for results at 1800 °C are considered separately in the next subsection. Below 1800 °C in 0.1% $O_2$ , a weak temperature dependence is observed for the carbides and diborides (Figure 3.21), which is inconsistent with an activated process such as a reaction controlled mechanism or diffusion through a solid/liquid, but would be expected for a gas phase diffusion mechanism<sup>156</sup>. Further, reaction rates are far more rapid than diffusion processes at these experimental temperatures and are therefore unlikely to be rate controlling. Linear kinetics are also consistent with gas-phase diffusion. For the carbides, microstructural features such as large pores and intergranular voids observed at 1500 ° and 1700 °C support gas phase diffusion as the rate controlling mechanism. For the diborides, porosity on the order of tens of microns is observed in the scale at 1500 °C that could be transport paths for gaseous reactants. Large voids are also observed in a mixed boride/oxide region at the oxide/substrate interface, however there is evidence that these are at least partially filled by liquid boria at 1700 °C (Figure 3.35).

### 1800 °C

Given the rate reduction at 1800 °C accompanied by changes in microstructure observed in the oxidized regions on both the high entropy carbides and diborides, the possible mechanism or mechanisms controlling the oxidation of high entropy carbides and diborides are expected to be different than observed at 1500 °C and 1700 °C. The oxide scales formed on the carbides (Figure 3.25) are denser, although some porosity appears on the surface after 15

minutes. They are also primarily rich in group IV oxides, and leaner in group V oxides at 1800 °C compared to the results at lower temperatures. At these higher temperatures, and given the microstructures observed, it is reasonable to consider that diffusion through the denser group IV rich oxide in both the carbide slows oxidant ingress. The overall thickness of the oxidized region and the denser Ti-rich band observed in the carbide in which phase separation is observed do not appreciably change between the 10 and 15 minute exposures (Figure 3.25). Linear rates can be expected for solid-state diffusion of oxygen through the oxidized region if the diffusion distance does not change. Thus, either diffusion through the Ti-rich band or through the external oxide scale to the reaction interface could be rate controlling at this condition. The strong  $pO_2$  dependence observed at this temperature is inconsistent with this proposed mechanism; however, this is only based on two data points, and includes data from experiments at 0.5% $O_2$ , which should be considered with care. While Ta was not observed in detectable amounts in the oxide after the carbide was exposed to 1800 °C in 1% $O_2$  for 10 minutes, small amounts of Ta (~1-2at%) were observed on the surface after 15 minutes of oxidation, coinciding with the appearance of some porosity at the oxide/gas interface. This suggests that the scale composition and microstructure is evolving due to group IV depletion and group V enrichment of the underlying carbide. If diffusion through the dense scale is rate controlling and assuming the thickness of this layer remains unchanged, then it is possible to expect the rates to change as the oxide composition and microstructure evolves, possibly explaining the time dependence being between linear and parabolic. If, on the other hand, the Ti-rich, phase separated band is rate-controlling, then oxidation at longer times will continue to exhibit linear kinetics. Further work at temperatures at and above 1800 °C is needed.

The diborides exhibit similar microstructures and time dependence as the carbide at 1800 °C; however, they do not exhibit a similar Ti-rich band. A dense region of interpenetrating oxides and borides is observed, like the carbides after oxidation at this temperature, along with some void formation. As the partially oxidized boride grains are surrounded by thin layers of

oxide (Figure 3.22 (f)), and given the time dependence being between linear and parabolic, it is possible that diffusion through the group-IV rich oxide is rate controlling. The origin of the voids is not immediately obvious, although outgassing of volatile species, such as boria gas or carbon monoxide from the B<sub>4</sub>C phases (Equation (3.1)), or pullout of the partially oxidized boride grain during the fracture process may explain their presence. Further work is needed to determine if the original diboride phase is destabilized, forming the Ti-rich and Nb-Ta-rich boride observed at 1700 °C (Figure 3.30).

#### *Implications for group IV+V HE-UHTCs*

The oxidation of the diborides resulted in the formation of a solid skeleton structure containing HfO<sub>2</sub>- and ZrO<sub>2</sub>-rich oxides and Ta- and Nb- rich borides, with pores and channels filled by boria. Similar microstructures have been previously observed for the diborides, and is likely a consequence of limited group IV oxide solubility in liquid boria, such as the ZrO<sub>2</sub>-B<sub>2</sub>O<sub>3</sub> case presented by Karlsdottir and Halloran.<sup>168</sup> On the other hand the formation of liquid oxides is particularly detrimental in the case of the carbides compared to the diborides. In the carbides, group IV+V oxide interactions occur over a wide range of compositions that result in eutectic liquids<sup>75,76</sup> destabilizing the solid structure of the group IV-rich oxides.

The oxidation behavior of (HfZrTiTaNb) carbide and boride at 1800 °C elucidates a potential path for the design of HE-UHTCs. The thermodynamically driven behavior of HE-UHTCs results in the formation of group IV oxides, which are stable and have high melting temperatures. Group V elements are retained as carbides (or borides). The preferential oxidation behavior at these ultra-high temperatures can be leveraged to design materials with the desired oxide composition, morphology and therefore behavior, e.g. a dense Hf/Zr rich oxide. The ideal material will likely be non-equimolar, reducing liquid oxide forming

constituents, whose composition can be tuned by using the thermodynamic approach outlined in Chapter 2.

### 3.5. Conclusions

The potential mechanisms operative during the oxidation of high entropy ceramics were studied. The group IV+V compositions (HfZrTiTaNb)C and (HfZrTiTaNb)B<sub>2</sub> were exposed to 1500 °C, 1700 °C and 1800 °C in 0.1-1% O<sub>2</sub> (balance Ar) for times up to fifteen minutes. The oxidation kinetics, oxide composition and post-oxidation microstructure were characterized using SEM, EDS, TEM and SAED.

Preferential oxidation is observed in both the group IV+V carbides and borides. This resulted in the following effects: (i) Temperature dependent microstructures related to the composition of the oxide; (ii) destabilization of the solid solution carbide or boride substrate; and (iii) liquid oxide formation combined with gaseous oxide formation resulting in porosity and voids in the carbides and borides below 1800 °C.

A time dependence that lies between linear and parabolic were observed at all temperatures for both the high entropy carbide and diboride. A weak temperature dependence was observed below 1800 °C, at which point a sharp reduction in rate was observed for both the carbide and diboride. A strong pO<sub>2</sub> dependence (power law exponents of 0.59 to 1.7) was also observed. The microstructure, time, temperature and pO<sub>2</sub> dependence suggest that gas phase diffusion or transport through pores are likely rate controlling mechanisms for the oxidation of the high entropy carbides at 1500 ° and 1700 °C. The microstructure, pO<sub>2</sub> dependence, and time dependence for the oxidation of diborides strongly suggest molecular oxidant transport in liquid boron as a possible mechanism, although the weak temperature dependence indicates that gas phase transport cannot be ruled out.

The microstructure and temperature dependence of the oxidation rates indicated a change in mechanism at 1800 °C. For the carbides, the time dependence and the observation of a denser group IV-rich scale and microstructural features of relatively constant thickness (such as the Ti-rich band) support a solid-state diffusion mechanism. For the borides, boron volatility was expected to be significant at these higher temperatures, and the microstructure mimics that observed in the carbide. Thus, it is also possible that solid state diffusion through the group IV-rich oxide surrounding group V-rich borides in the oxidized region is rate-limiting in this regime.

### 3.6. Future Work

The oxidation of high entropy UHTCs at temperatures of 1500-1700 °C results in intergranular oxidation in the carbides. Further studies conducted at temperatures below 1800 °C should utilize additional methods of quantification for oxidation behavior, e.g., external scale thickness measured separately from grain boundary oxide thickness. Future studies using ternaries are also recommended to minimize the chemical complexity better enabling determination of the oxidation mechanisms (particularly the HfTaTi) system. Further studies are specifically recommended at temperatures of 1800 °C and above, as a change in oxidation mechanism is observed: oxygen diffusion through the bulk may dominate over intergranular oxidation.

Consideration of the kinetics showed that variations in processing and the presence of secondary phases from processing such as B<sub>4</sub>C or Hf/Zr oxides, can convolute the determination of mechanisms in the refractory high entropy carbides and borides. Effects such as intergranular oxidation, liquid and gaseous oxide formation are all important effects in these materials at the temperature ranges of interest; therefore, minimizing these secondary phases is important. In the case of the carbides, the prevalence of intergranular oxidation and the

necessity of forming an external scale to mitigate continuous material degradation via grain boundaries suggests promoting the formation of an external scale as fast as possible. Therefore, an improvement of synthesis methods to refine grain size is recommended.

Additionally, while the resistive heating system presents numerous advantages (Chapter 4), challenges such as temperature fluctuations, changes in resistance due to secondary phases from processing could be improved via refinement of the PID settings for each material system or going to larger specimen sizes. The current system was limited by the upper limit of the transformer current output. A larger current output ( $>120\text{A}$ ) would enable thicker cross-sections, which could expand the experimental range, such as the ability to conduct longer exposures at higher  $p\text{O}_2\text{s}$  and higher temperatures. Finally, the uncertainty in the material consumption measurements due to examination of fracture cross-sections was not quantified. The FIB process is time consuming and cost-prohibitive for preparation of samples with dimensions above tens of microns. Comparison of these versus polished cross-sections could help elucidate these errors.

## 4. Comparison of Oxidation Resistance of (HfZrTiTaNb) Carbide and Diboride to Other UHTC Compositions

### 4.1. Introduction

Chapter 2 outlined the periodic trends observed in the oxidation of the elemental systems being considered for the high entropy approach. Given the trends discussed in that chapter, a systematic study for the design of an oxidation resistant HE-UHTC, was considered as follows:

- Group IV + V elements, which form solid and liquid oxides, wherein liquid phase sintering could be promoted, but may be prone to the formation of oxides with low melting eutectics
- Group IV + VI elements, which form solid and volatile oxides, i.e., the group VI elements will form volatile oxides which will leave the system, and the solid group IV oxides remain behind
- Group IVs + V + VI combination
- Baseline ZrC and ZrB<sub>2</sub> with no group V or VI additions

Results discussed in Chapter 3 for the group IV+V combination shows that the oxidation behavior of the solid solution closely matches the design considerations from the constituent elements, i.e., the formation of group V oxides, for example, promoted the formation of oxides with low melting temperatures that resulted in a decrease in oxidation resistance of the material. Designing a high entropy ceramic from the collection of group IV, V and VI elements with the requirement of forming oxides with high melting temperatures necessitates starting with the group IV elements, Hf, Zr and Ti. The other two ceramic components, assuming the choices are limited to the palette of group IV, V and VI transitional metals must be chosen from

Ta, Nb, Mo and W. It is important to consider whether the thermodynamic considerations discussed in Chapter 2 can be extended to compositions with group VI additions and determine whether they will oxidize to form volatile products.

While the high entropy approach expands the compositional range for UHTCs, it also complicates the oxidation behavior of UHTCs. Chapter 3 shows that the high entropy material tested did not oxidize uniformly, and instead exhibited preferential oxidation, destabilizing the underlying solid solution phase. This behavior can be beneficial when the formation of oxides with favorable properties (e.g., high melting temperatures) are formed, as was observed after oxidation at 1800 °C. In other cases, i.e. at 1700 °C, the high entropy approach was detrimental to the oxidation resistance of the material, as demonstrated by the extensive grain boundary oxidation. The high entropy approach should therefore be compared to the behavior of traditional UHTCs, such as ZrB<sub>2</sub> and ZrC, to gauge the potential of this strategy over the current state-of-the-art.

The objectives of this study were to (a) measure the oxidation resistance of HfZrTiTaMo and HfZrTiMoW carbides and borides by measuring material consumption after tests in similar conditions, and then comparing these to the group IV+V compounds (Hf, Zr, Ti, Ta and Nb) discussed in chapter 3, (b) explore the compositional effects on the oxidation resistance as described by the periodic trends previously observed, (c) determine whether the preferential oxidation behavior is also observed in other compositions and (d) compare the oxidation of HE-UHTCs to a unary group IV carbide and diboride, ZrC and ZrB<sub>2</sub>.

Chapter 3 addressed the addition of group V elements to group IV based UHTCs. The addition of molybdenum to Hf and Zr based UHTCs has mainly been in the form of MoSi<sub>2</sub><sup>169-174</sup>. The oxidation behavior of MoSi<sub>2</sub> containing boride materials has typically been characterized by the observation of silica along with the group IV rich condensed phase oxide<sup>175</sup>, although small amounts of condensed MoO<sub>x</sub> and MoO<sub>3</sub> have been observed<sup>176</sup>. Materials containing boron

typically form a borosilicate glass along with Mo-B rich phase<sup>172,173,176</sup>, but at ultra-high temperatures (1800 °C), the borosilicate glass layer is “turbulent” due to the evolution of the gaseous Si, B and Mo oxides<sup>176</sup>, suggesting that the formation of a scale may be disrupted by these volatile gases. Dehdashti et al.<sup>177</sup> explored the addition of Mo to ZrB<sub>2</sub> and found that Mo in the boria scale stabilized the boria scale at higher temperatures, resulting in improved oxidation resistance. The Hf and Zr carbides with MoSi<sub>2</sub> additions have been characterized by porous scales and it is thought that volatile Mo oxides escape through these pores<sup>175</sup>. A ZrC-Mo cermet was tested and found to form MoO<sub>3</sub>, which readily volatilizes; additionally, peeling of the oxide scale<sup>178</sup>, described by Wuchina et al.<sup>2</sup> as a phenomenon wherein the oxide spontaneously spalls off the substrate, was observed.

W additions to ZrB<sub>2</sub> have been explored, and it was found that W additions improved the oxidation resistance of ZrB<sub>2</sub><sup>179</sup>; this improved resistance was, similarly to studies done with Mo, attributed to higher stability of the liquid boria. WC and WB additions to HfB<sub>2</sub>-SiC were found to improve oxidation resistance of HfB<sub>2</sub>-SiC at 2000 °C by promoting liquid phase sintering of the HfO<sub>2</sub> scale<sup>180</sup>. Similarly the improved oxidation resistance of ZrB<sub>2</sub> with WC additions was attributed to the W-assisted densification of the ZrO<sub>2</sub> rich scale<sup>92</sup>, although this was later questioned after detailed microstructural analysis performed by Silvestroni et al.<sup>93</sup>.

Phase diagrams for the oxides of Mo and Hf, or Mo and Zr, are not available. However, the phase diagrams for W oxides and HfO<sub>2</sub> (shown for reference in Figure 4.1), as well as W oxides and ZrO<sub>2</sub> exist and show limited solubility of the W oxide in the group IV oxides<sup>181</sup>. Complex oxide formation is possible, as are low melting eutectics (>1231 °C). The coexistence of ZrO<sub>2</sub> and W oxides as separate phases at temperatures higher than this, along with the volatility of W oxides, suggest that W oxides would readily volatilize, leaving behind ZrO<sub>2</sub> (and by similitude, likely HfO<sub>2</sub>).

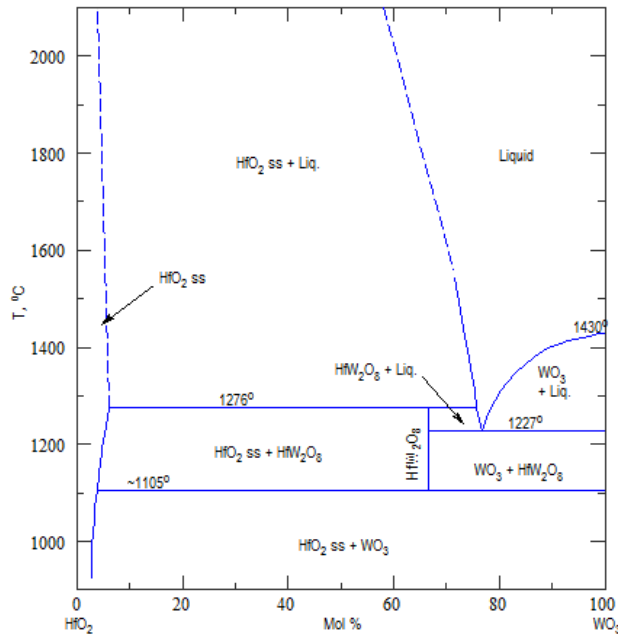


Figure 4.1: Pseudobinary phase diagram for HfO<sub>2</sub>-WO<sub>3</sub> from Chang et al.<sup>181</sup> and obtained from the Phase Equilibria Diagrams Database (NIST Standard Reference Database 31), The American Ceramic Society and the National Institute of Standards and Technology, 2020. Figure Number 04445.

#### 4.2. Methodology

ZrB<sub>2</sub> and ZrC were tested at 1500 °C, 1700 °C, and 1800 °C in 0.1%, 0.5% and 1% O<sub>2</sub> (balance Ar), the same conditions explored in Chapter 3 using the resistive heating system described therein, to provide a baseline comparison. IV+V+VI and IV+VI carbides and borides ((HfZrTiTaMo)C, (HfZrTiTaMo)B<sub>2</sub>, (HfZrTiMoW)C, and (HfZrTiMoW)B<sub>2</sub>) were all tested in 1%O<sub>2</sub> and 1700 °C, conditions in which the IV+V (HfZrTiTaNb)C and (HfZrTiTaNb)B<sub>2</sub> exhibited the poorest oxidation resistance.

All materials were made at UCSD. The ZrC, (HfZrTiTaMo)C and (HfZrTiMoW)C compositions were synthesized at UCSD by sintering commercial powders in the same manner

as discussed in Chapter 3. The  $(\text{HfZrTiTaMo})\text{B}_2$  and  $\text{ZrB}_2$  compositions were synthesized by sintering powders made via borocarbothermal reduction, as described in Chapter 3. The  $(\text{HfZrTiMoW})\text{B}_2$  was synthesized by adding 1 wt% graphite to  $\text{TiB}_2$ ,  $\text{ZrB}_2$ ,  $\text{MoB}_2$ ,  $\text{HfB}_2$  and  $\text{W}_2\text{B}_5$  commercial powders, and performing a high energy ball milling step prior to consolidation via SPS. The elemental distribution and XRD patterns for the high entropy compounds prior to oxidation are of interest and presented in the results. These spark-plasma sintered pellets were then machined into dogbones by Bomas Machine Specialties, and tested using the resistive heating system, as discussed in Chapter 3. The IV+V+VI and IV+VI carbides and diborides were exposed at  $1700^\circ\text{C}$  in 1%  $\text{O}_2$  for five minutes.  $\text{ZrC}$  and  $\text{ZrB}_2$  were tested at  $1500^\circ\text{C}$ ,  $1700^\circ\text{C}$  and  $1800^\circ\text{C}$  in 0.1%, 0.5% and 1%  $\text{O}_2$  (balance Ar) for times of 5-15 minutes. After oxidation exposures, all samples were fractured in the hot zone. The cross-sections were examined using the SEM and EDS, and the material consumption was measured using oxygen EDS maps. The oxidized samples were also characterized using XRD.

## 4.3. Results

### 4.3.1. Starting materials (high entropy compositions)

#### *High entropy carbides*

Figure 4.2 shows generally even distribution of all the metallic species in  $(\text{HfZrTiTaMo})\text{C}$ . Some intensity variation is noted for hafnium and molybdenum. Analysis of the XRD pattern (Figure 4.3) shows only one set of peaks consistent with rocksalt structure, although some asymmetry is observed, especially at higher two-theta angles. Analysis of this asymmetry during peak fitting indicates that this asymmetry may be due to lattice parameter variation in composition in the specimen (Figure 4.2). No peaks due to retained Hf and Zr oxides are observed.

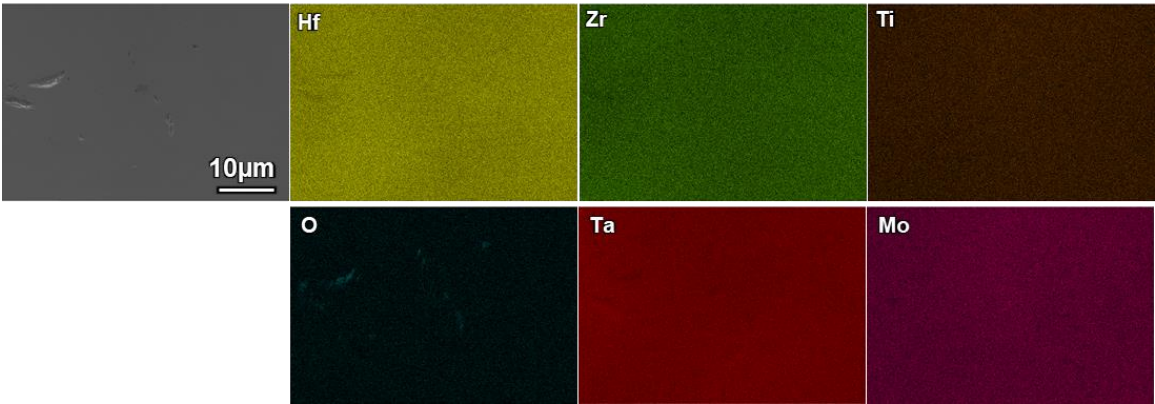


Figure 4.2: Secondary electron image and EDS maps for (HfZrTiTaMo)C before oxidation.

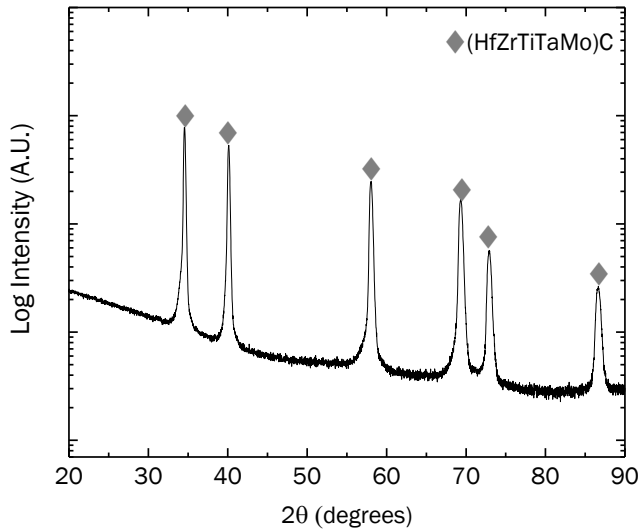


Figure 4.3: XRD pattern obtained from (HfZrTiTaMo)C before oxidation showing one set of peaks

Figure 4.4 shows elemental clustering of the metallic species in the (HfZrTiMoW)C sample. One phase appears to be rich in Hf and Zr, another rich in Mo and Ti, and possibly a third rich in Ti and W. Analysis of the XRD pattern (Figure 4.5) shows only one set of peaks consistent with the rocksalt structures, although these peaks appear broad and asymmetric,

especially at higher two-theta angles. Similar to the (HfZrTiTaMo)C case, the asymmetry observed may be due to slight lattice parameter variation. No peaks due to retained Hf and Zr oxides are observed.

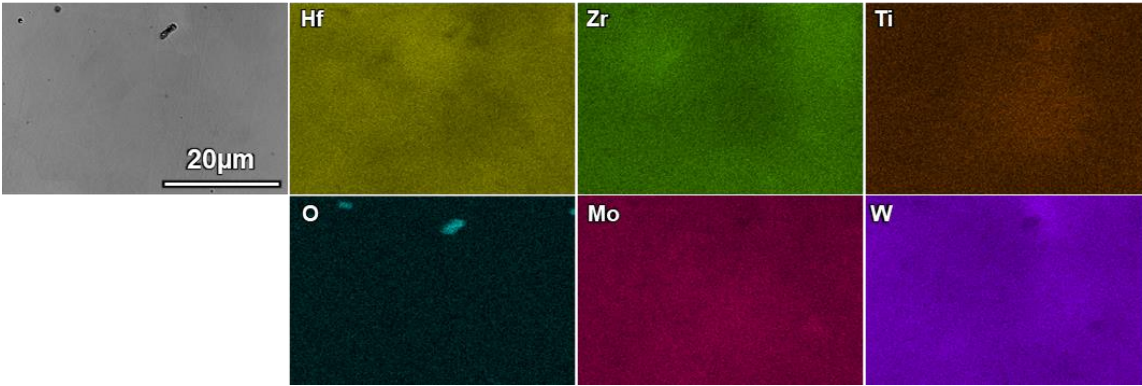


Figure 4.4: Secondary electron image and EDS maps for (HfZrTiMoW)C before oxidation.

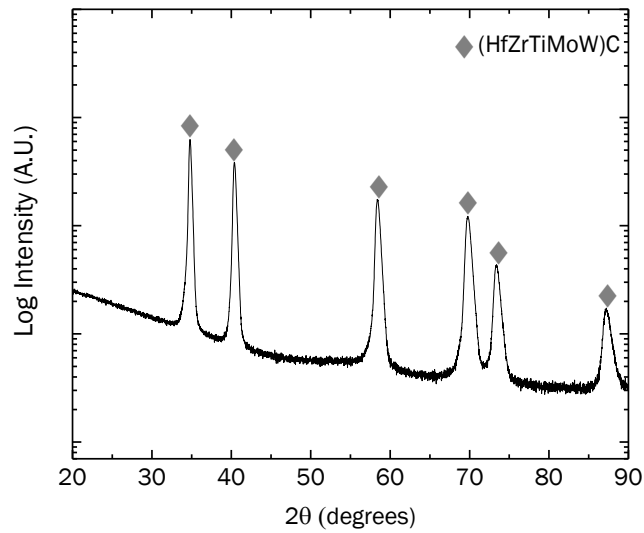


Figure 4.5: XRD pattern obtained from (HfZrTiMoW)C before oxidation showing one set of peaks

### High entropy borides

The high entropy diboride  $(\text{HfZrTiTaMo})\text{B}_2$  exhibited uniform elemental distribution of all the metallic elements (Figure 4.6) and relative densities of 99% or greater, with less than 1vol% of  $\text{B}_4\text{C}$  retained as a secondary phase, as described by Gild et al.<sup>157</sup>. A single-phase high entropy diboride is confirmed by XRD analysis (Figure 4.7) showing the hexagonal  $\text{AlB}_2$ -type structure.

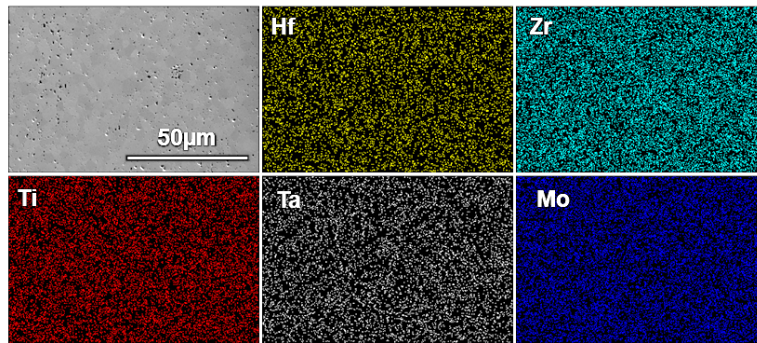


Figure 4.6: Secondary electron image and EDS maps for  $(\text{HfZrTiTaMo})\text{B}_2$  before oxidation. Analysis and data obtained from UC-San Diego.

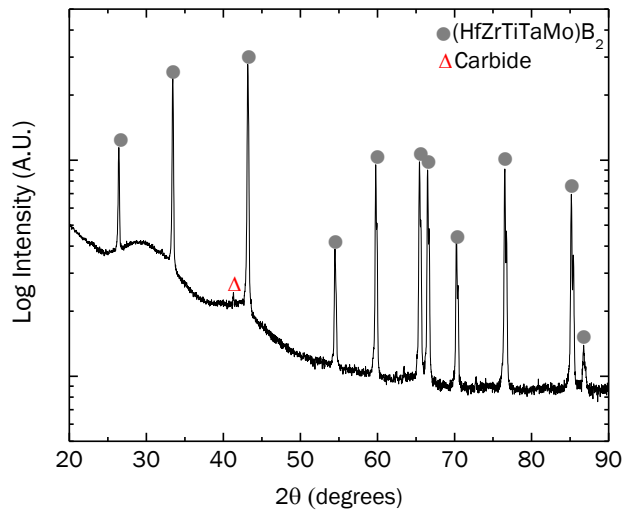


Figure 4.7: XRD pattern for  $(\text{HfZrTiTaMo})\text{B}_2$  before oxidation showing one set of peaks. Analysis and data obtained from UC-San Diego.

The  $(\text{HfZrTiMoW})\text{B}_2$  composition does not form a single-phase diboride. At least a second W-rich phase is observed. The elemental distribution of the phases is shown in Figure 4.8. The XRD pattern also confirms the presence of a second boride phase, apparent as the bright phase in Figure 4.8, the approximate composition of which is given by point EDS analysis (Figure 4.9). These results show that the main diboride phase is deficient in Mo and W, relative to the equimolar case, and is richer in the group IV elements. The second phase is rich in W, contains roughly equal amounts of Mo and Ti, and to a slightly lesser extent Hf and Zr. The elemental distributions in Figure 4.7 also indicate possible clustering of Mo and Zr in the main diboride phase.

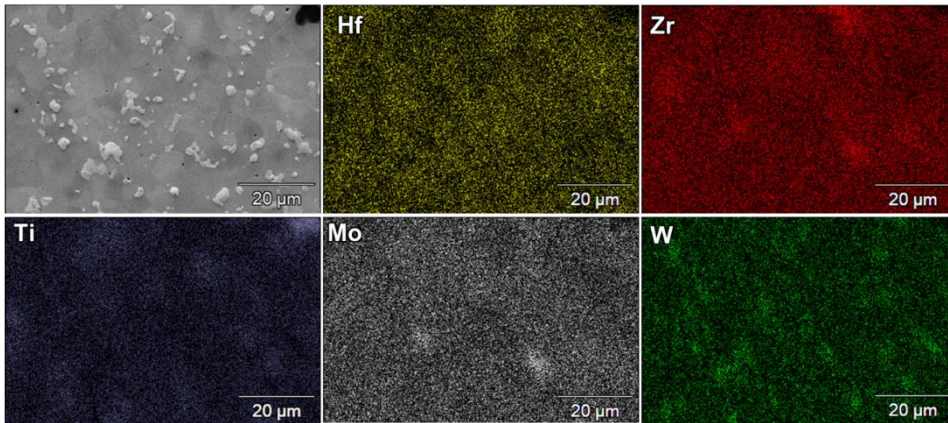


Figure 4.8: Secondary electron image and EDS maps for  $(\text{HfZrTiMoW})\text{B}_2$  before oxidation.

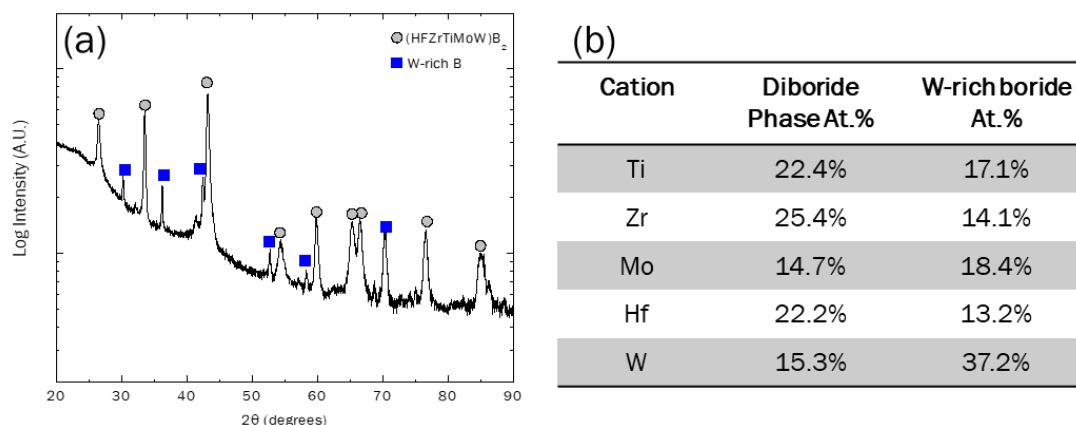


Figure 4.9: (a) XRD pattern for  $(\text{HfZrTiMoW})\text{B}_2$  before oxidation, (b) Point EDS analysis showing approximate breakdown of elemental concentration in each phase. Data obtained from UC-San Diego.

#### 4.3.2. Oxidation Results

A quantitative comparison of material consumption for all high entropy compositions as well as  $\text{ZrC}$  and  $\text{ZrB}_2$  is provided in Table 4.1 for five minute exposures at  $1700^\circ\text{C}$  in  $1\%\text{O}_2$ . Results are plotted in Figure 4.10. The results show that the borides consistently exhibited better oxidation resistance under these conditions compared to the carbides. The different boride compositions also performed similarly, when compared with each other and  $\text{ZrB}_2$ . The material consumption values for the high entropy carbide compositions generally exhibited poorer oxidation resistance compared to  $\text{ZrC}$ , except for  $(\text{HfZrTiMoW})\text{C}$ , which exhibited only slightly higher material consumption compared to  $\text{ZrC}$ .  $(\text{HfZrTiTaMo})\text{C}$ , or the group IV+V+VI composition, exhibited the highest material consumption. The oxidation products and microstructure will be discussed in more detail in the following sections.

Table 4.1: Material consumption values measured for different compositions tested at 1700 °C in 1% O<sub>2</sub> for 5 minutes.

| Material                               | Material Consumption (μm) | Std. Dev. (μm) |
|--|---------------------------|----------------|
| <b>Carbides</b>                        |                           |                |
| ZrC                                    | 74                        | 8              |
| (HfZrTiTaNb)C                          | 125                       | 5              |
| (HfZrTiTaMo)C                          | 155                       | 13             |
| (HfZrTiMoW)C                           | 95                        | 9              |
| <b>Borides</b>                         |                           |                |
| ZrB <sub>2</sub>                       | 61                        | 3              |
| (HfZrTiTaNb)B <sub>2</sub> (BW Pellet) | 50                        | 4              |
| (HfZrTiTaMo)B <sub>2</sub>             | 62                        | 4              |
| (HfZrTiMoW)B <sub>2</sub>              | 55                        | 2              |

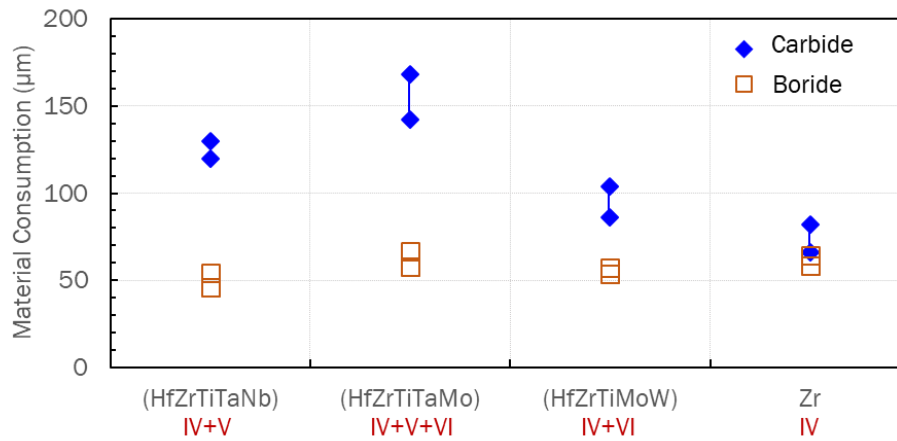


Figure 4.10: Plot showing material consumption measured for different compositions tested at 1700 °C in 1% O<sub>2</sub> for 5 minutes. Each data “point” is a range of values covering the average and standard deviation of measured material consumption. Closed blue diamonds indicate carbides and open orange squares indicate diborides.

### High entropy carbides

The group IV+VI composition, (HfZrTiMoW)C, exhibited better oxidation resistance compared to the group IV+V composition, (HfZrTiTaNb)C. The oxide formed on (HfZrTiTaMoW)C is mostly dense, although a few cracks and porosity are observed (Figure 4.11). A higher

magnification view shows that the oxide scale consists of two phases: one that is oxygen rich and contains group IV elements, and one that is carbon-rich and contains Mo and W (Figure 4.12 and Figure 4.13).

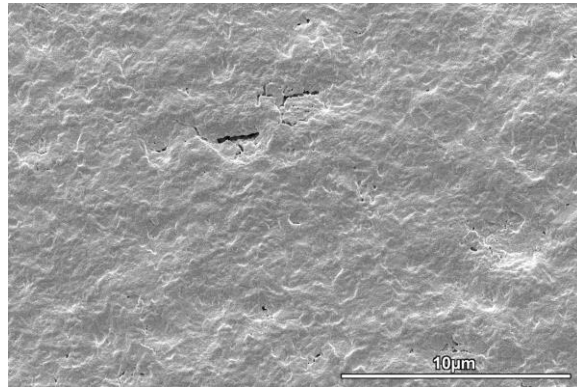


Figure 4.11: Secondary electron image in plan view of the oxide formed in the pyrometer sighting zone on (HfZrTiMoW)C after exposure to 1%O<sub>2</sub> at 1700 °C for five minutes.

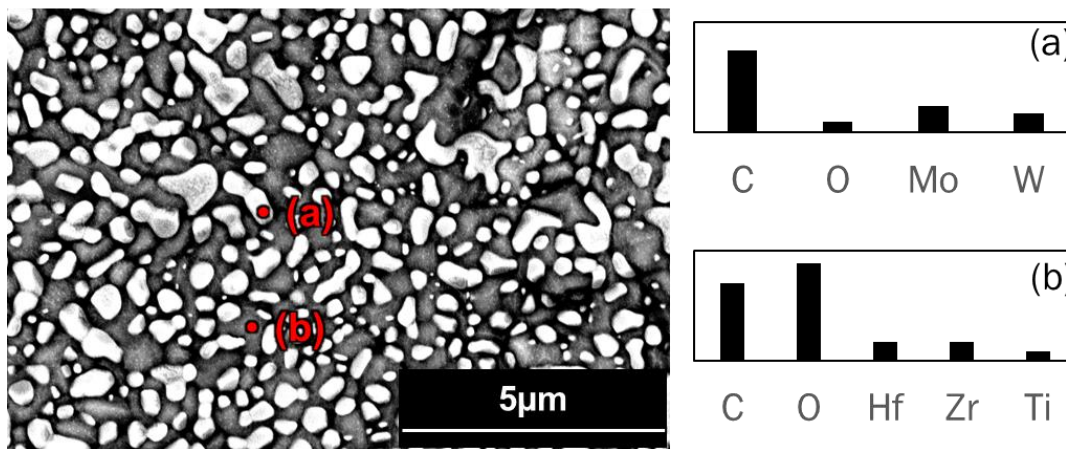
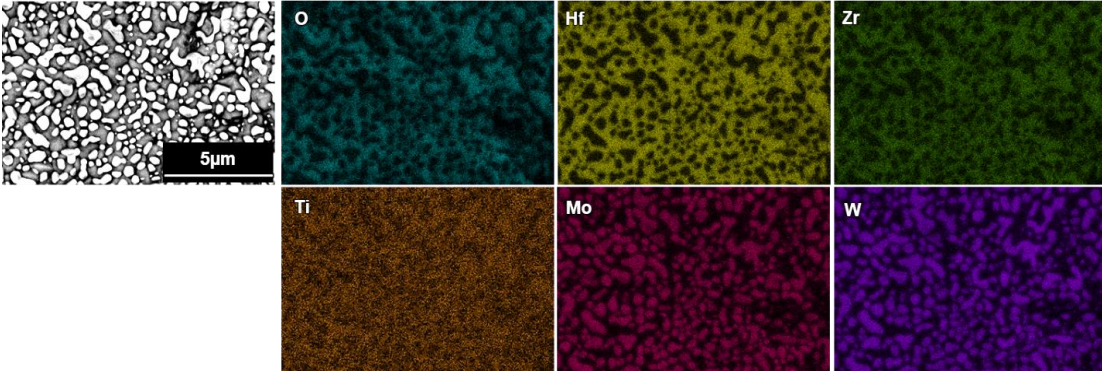


Figure 4.12: Back-scattered electron image in plan view of the oxide formed in the pyrometer sighting zone on (HfZrTiMoW)C after exposure to 1%O<sub>2</sub> at 1700 °C for five minutes, along with EDS point analysis showing the elemental composition of the two phases present, (a) and (b).



*Figure 4.13: Back-scattered electron image in plan view of the oxide formed in the pyrometer sighting zone on (HfZrTiMoW)C after exposure to 1%O<sub>2</sub> at 1700 °C for five minutes, along with EDS maps showing the distribution of the two phases present.*

The cross-section view of the oxidized (HfZrTiMoW)C is shown in Figure 4.14 at the oxide-gas interface. An oxidized region on the surface appears dark in the back-scattered electron image (Figure 4.14 (a)). At higher magnification, the back-scattered electron image shown in Figure 4.14 (b) shows that the two-phase group VI-rich carbide/group IV-rich oxide microstructure seen on the surface is present at varying depths in the oxidized region starting at the oxide/gas interface. This region is best highlighted by the Hf and Mo maps. Below this two-phase region, the grains have a uniform appearance. EDS mapping shows that the elemental distribution in the single-phase oxidized region, is uniform as well. Figure 4.14 (a) shows how far O has penetrated into the substrate, and Figure 4.14 (b) shows the two-phase region at the top of the scale. Due to topography, it is difficult to determine the extent of O intensity variation within the oxidized region shown. The two-phase region also exhibits some porosity through its thickness.

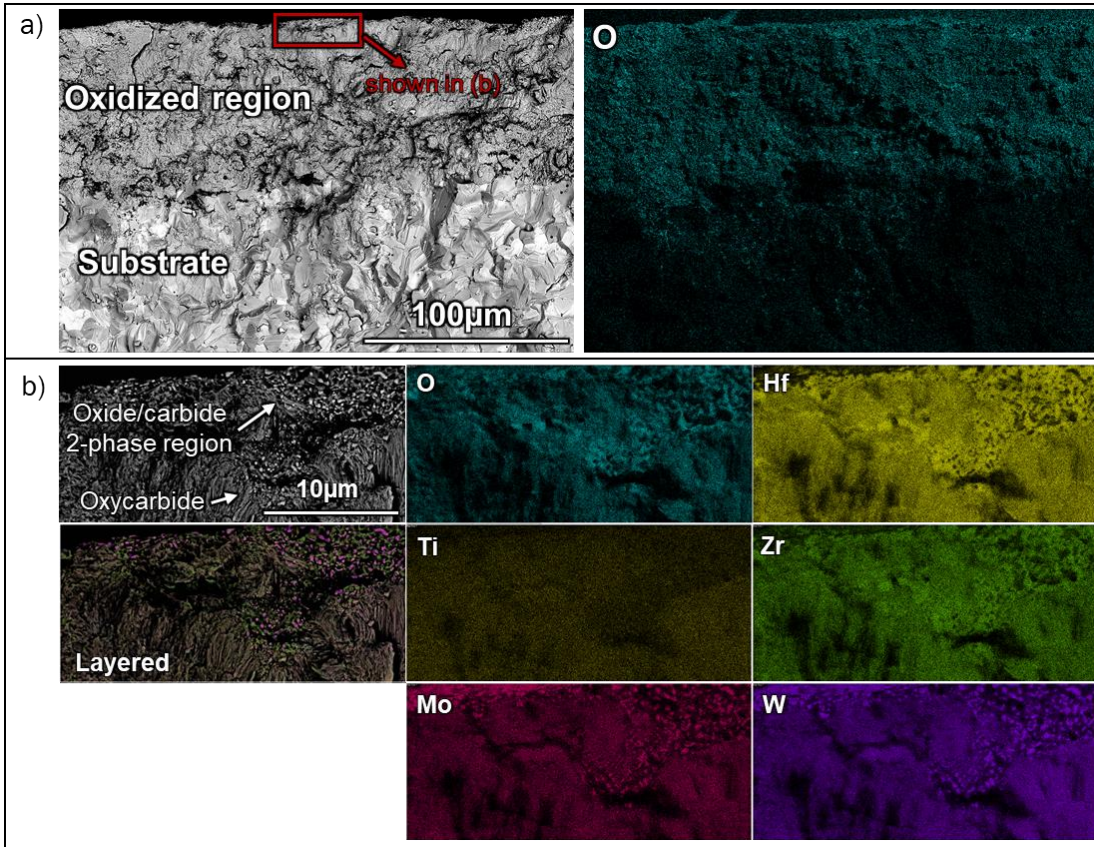


Figure 4.14: Cross-section view, of (HfZrTiMoW)C oxidized at 1700 °C in 1%O<sub>2</sub>/Ar for five minutes. (a) Lower magnification back-scattered electron image and oxygen map, (b) Higher magnification of the top of the oxide scale (near gas/oxide interface) along with Hf, Zr, Ti, Mo and W elemental maps. The layered map superimposes data from all five metallic elements as well as oxygen.

The two-phase Mo-rich/Hf-rich region seen on the surface and shown in Figure 4.14(b) also appears at what may be former grain boundaries. Figure 4.15 shows this, as well as elemental analysis showing that the phases are a group IV-rich oxide and a group VI-rich partially oxidized carbide. Based on examination of the oxide-substrate interface, oxygen is transported from the surface, to grain boundaries and into the grain (Figure 4.16).

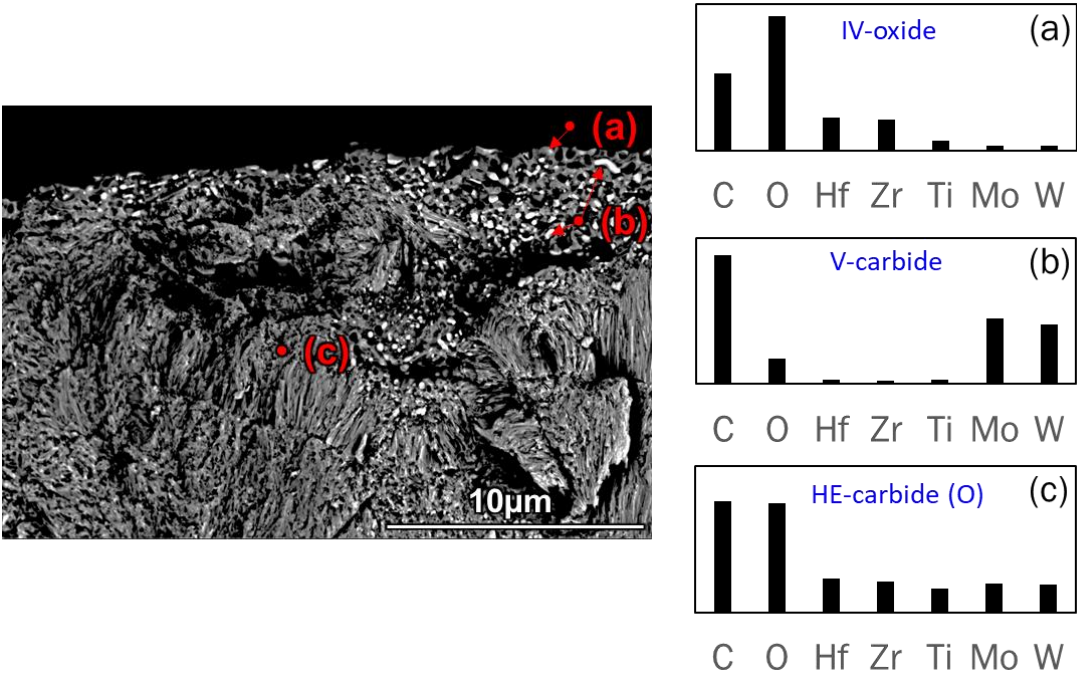


Figure 4.15: Back-scattered electron image, cross-section view, of (HfZrTiMoW)C oxidized at 1700°C in 1%O<sub>2</sub>/Ar for five minutes, and EDS point analysis for (a) the dark phase at the top of the scale, (b) the bright phase at the top of the scale, and (c) the partially oxidized single phase high entropy carbide region adjacent to the two-phase region.

These results indicate that the material oxidizes by oxygen dissolution in the high entropy carbide grain. A two-phase oxidized region is also observed, with the group IV elements selectively oxidizing to form Hf, Zr and Ti oxides, leaving behind Mo-rich carbides or oxycarbides as confirmed by XRD (Figure 4.17). As previously discussed in Chapters 2 and 3, XRD analysis for these materials are challenging at best due to multiple possible overlaps. Additionally, it is well known that peak discrimination between rocksalt carbide or oxycarbide is quite difficult. The XRD results should therefore be considered with care, although the results appear consistent with EDS results.

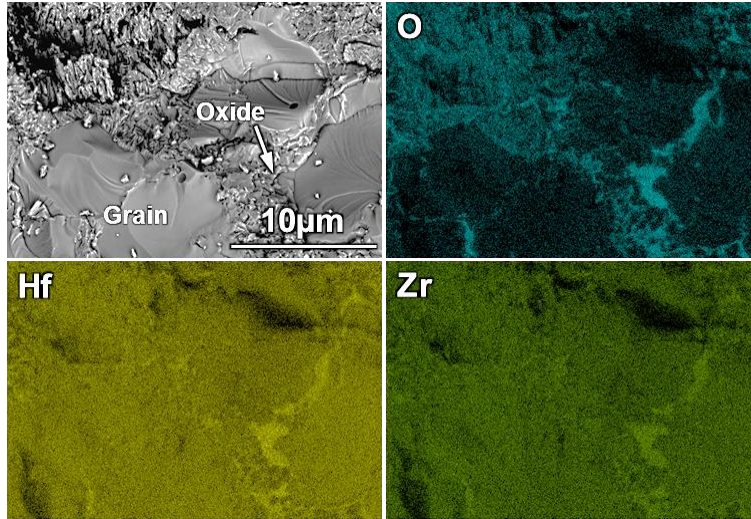


Figure 4.16: Back-scattered electron image of grains at the oxide-substrate interface in cross-section of (HfZrTiMoW)C oxidized at 1700 °C in 1%O<sub>2</sub> for five minutes, along with O, Hf and Zr elemental maps showing intergranular oxidation.

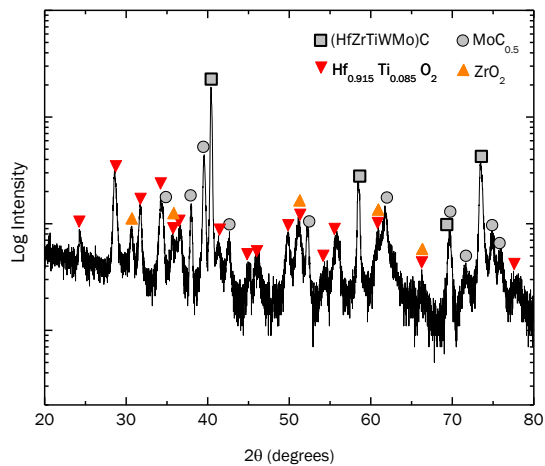


Figure 4.17: XRD data collected from (HfZrTiMoW)C oxidized at 1700 °C in 1%O<sub>2</sub> for five minutes, using micro-focus optics.

Mo and W are not present in the condensed oxide; however, there is evidence that some oxidation of Mo and W occurred. Figure 4.18 shows the microstructure and representative, semi-quantitative elemental composition of deposits on the alligator clips

holding the sample in place. The deposits appear to be  $(\text{Mo,W})\text{O}_3$  or similar, suggesting that group VI oxides formed from the carbide grains on the surface, volatilized and deposited on the much cooler clips.

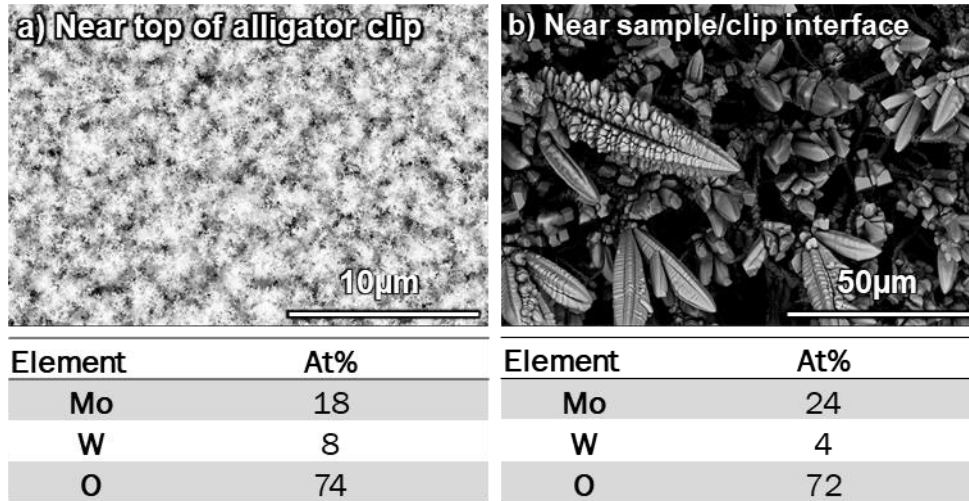


Figure 4.18: Back-scattered electron images in plan view of the oxides that volatilized and deposited on the alligator clips holding the sample in place. (a) Microstructure and semi-quantitative point-EDS analysis of the oxide deposited near the top of the alligator clip (away from the sample), and (b) microstructure and semi-quantitative point EDS analysis of the oxide deposited near the sample/clip interface.

The group IV+V+VI carbide,  $(\text{HfZrTiTaMo})\text{C}$ , which exhibited the highest material consumption of the compositions tested, also shows a two-phase microstructure on the surface (Figure 4.19). The brighter phase is oxygen deficient and likely a carbide containing mostly Mo and some Ta. The oxide phase is mostly rich in Hf, Zr and Ti, with minimal amounts ( $\sim 1$  at%) of Ta (Figure 4.19).

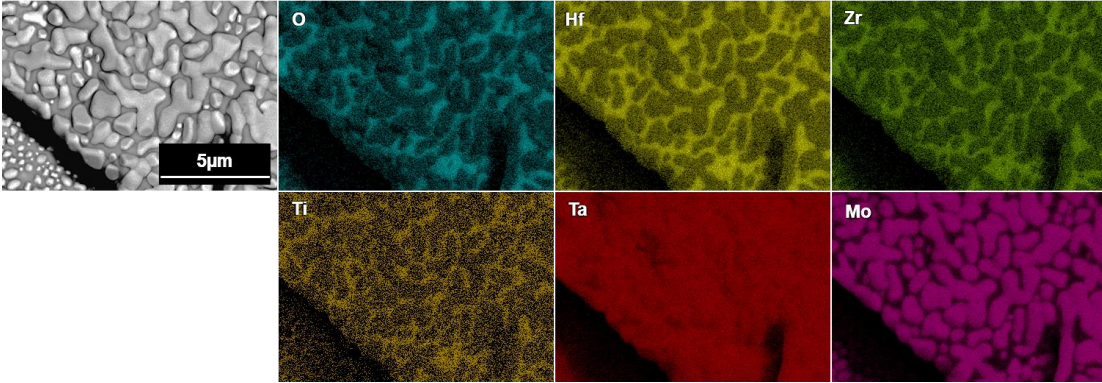


Figure 4.19: Back-scattered electron image in plan view of (HfZrTiTaMo)C oxidized at 1700 °C in 1%O<sub>2</sub> for five minutes, along with elemental EDS maps.

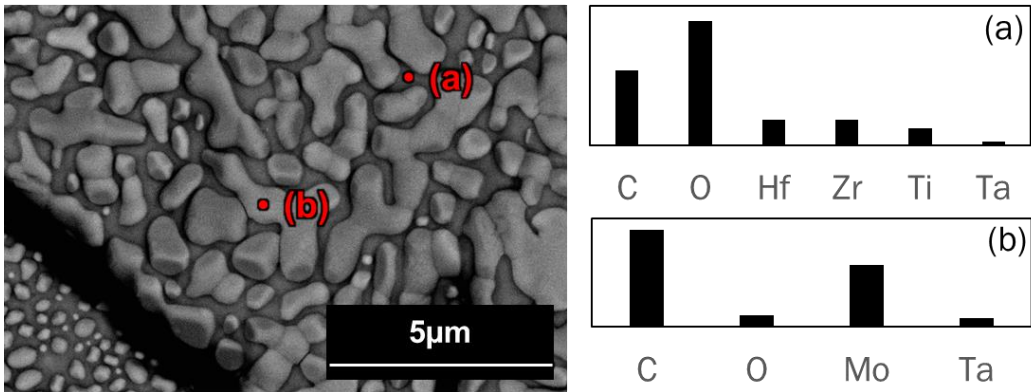


Figure 4.20: (Left) Backscattered electron image in plan view of (HfZrTiTaMo)C oxidized at 1700 °C in 1%O<sub>2</sub> for five minutes. (a) and (b) are EDS point analysis of the (a) dark, oxide phase and (b) bright, carbide phase.

The cross-section view shows a two-phase oxidized region as well. The oxide-rich regions appear to have much less porosity than (HfZrTiMoW)C, particularly around the bright grains seen in Figure 4.21 (a), where they appear quite dense. Intergranular voids, however, are observed. Near these intergranular voids, rounded features consistent with possible solidified melt was observed (Figure 4.21 (a) ). One of the phases has an elemental composition (Figure 4.21 (c)) similar to the dark gray oxide region on the surface shown in Figure 4.20, containing Hf, Zr and Ti, with ~1-2 at% Ta. The second phase is Mo and Ta rich,

and O deficient (Figure 4.21 (d)). XRD analysis (Figure 4.22) is consistent with a (Mo,Ta)C phase present along with Hf, Zr and Ti rich oxides.

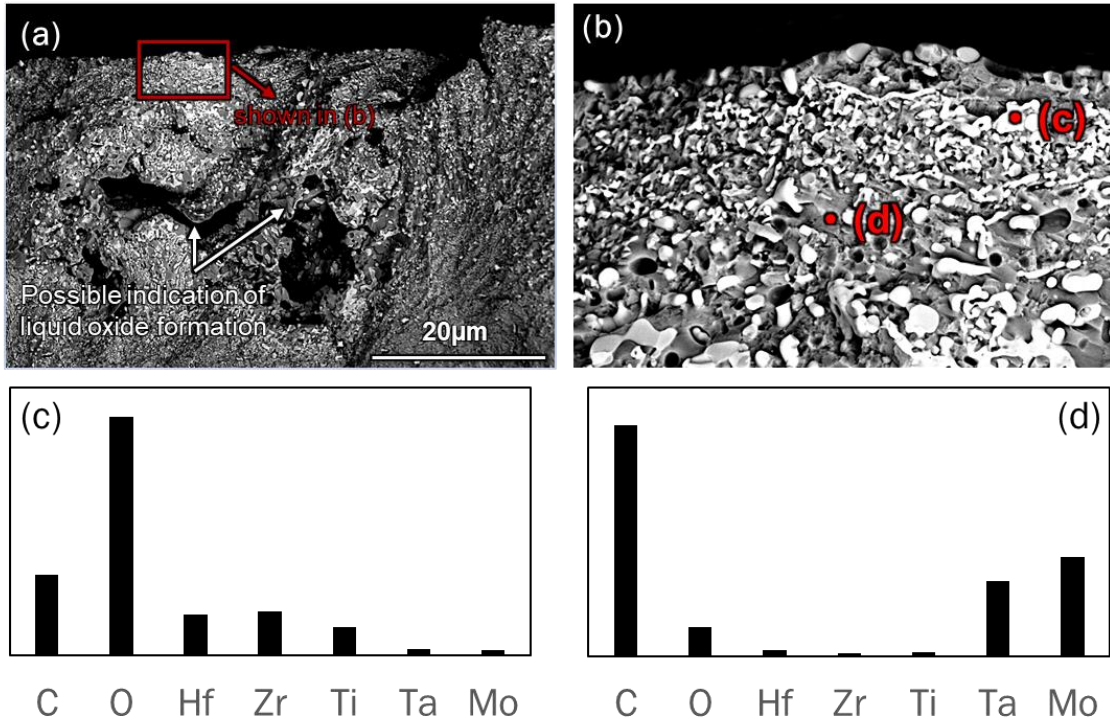


Figure 4.21: (HfZrTiTaMo)C oxidized at 1700 °C in 1%O<sub>2</sub>/Ar for 5 minutes. (a) lower magnification back-scattered electron image of the oxidized region in cross-section at the oxide/gas interface; (b) higher magnification back-scattered electron image of the oxidized region in cross-section at the oxide/gas interface; (c) and (d) show point EDS analysis of the dark and bright regions in (b), respectively. Each EDS data set is averaged over a minimum of five like points.

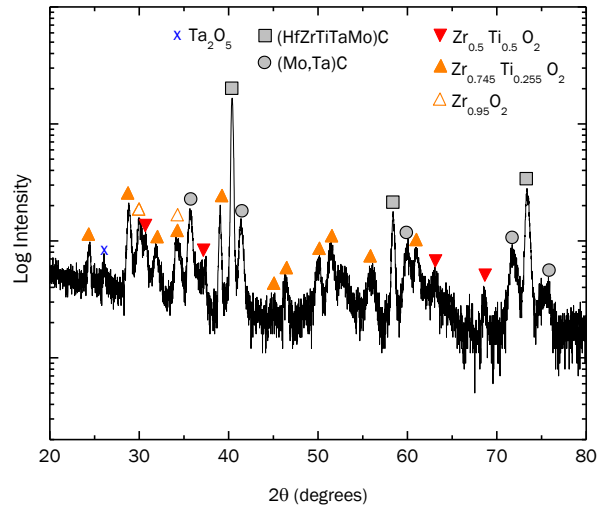


Figure 4.22: XRD data collected from  $(HfZrTiTaMo)C$  oxidized at  $1700\text{ }^\circ\text{C}$  in  $1\%O_2$  for five minutes, using micro-focus optics.

As with the other high entropy carbides, this composition exhibits intergranular oxidation as well. Figure 4.23 shows the oxide/substrate interface exhibiting oxidation along the grain boundaries.

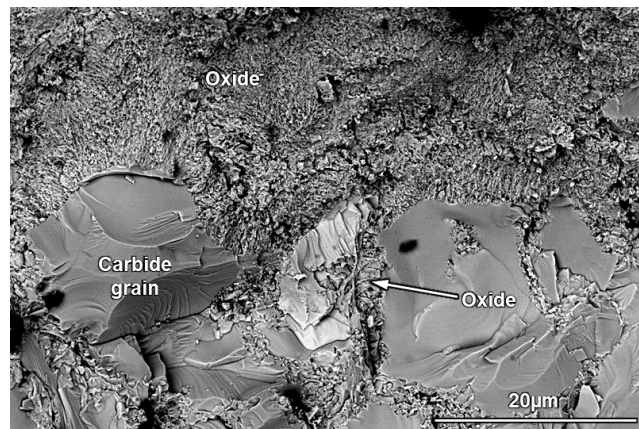


Figure 4.23: Backscattered electron image in cross-section view of  $(HfZrTiTaMo)C$  oxidized at  $1700\text{ }^\circ\text{C}$  in  $1\%O_2/Ar$  for 5 minutes, at the oxide/substrate interface.

### High entropy diborides

The oxidized surface of  $(\text{HfZrTiTaMo})\text{B}_2$  exhibited bubbles and dark, glassy appearing regions that are likely solidified boria melt (Figure 4.24). Large bubbles are also apparent on the surface.

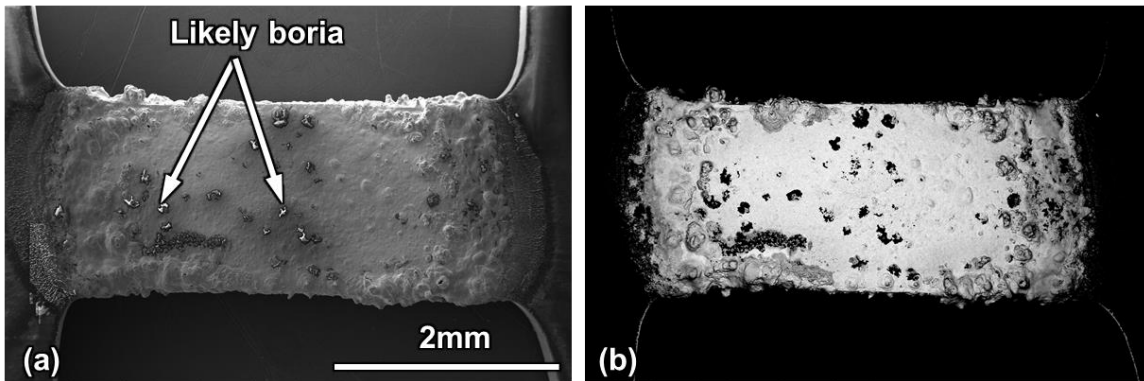


Figure 4.24: (a) Secondary electron, and (b) backscattered electron image of  $(\text{HfZrTiTaMo})\text{B}_2$  in plan view after exposure at  $1700^\circ\text{C}$  in  $1\%\text{O}_2/\text{Ar}$  for five minutes.

Examination of the oxide scale in the pyrometer sighting zone at higher magnification (Figure 4.25) shows the oxide is mostly composed of group IV elements, most notably Hf and Zr. Bubbles and cracks were also observed. Minimal Mo and Ta-containing phases are observed on the surface, in contrast with the carbide case. The Mo-rich phase also appears to contain B (Figure 4.25 (b)) and is deficient in O, indicating a Mo boride phase on the surface. XRD data (Figure 4.26) also indicates that  $\text{MoB}$  exists in oxidized region; however XRD could be detecting phases beneath the surface. XRD analysis also indicates that the oxide consists primarily of group IV elements, although a small  $\text{Ta}_2\text{O}_5$  peak appears, detectable when the XRD data is plotted logarithmically. The primary oxide phase is  $\text{HfO}_2$ , which could be  $(\text{Hf,Zr, Ti})\text{O}_2$  based on EDS data. EDS analysis of the specimen in cross-section (Figure 4.27) also shows Mo and Ta rich grains that could be  $(\text{Mo, Ta})\text{B}$  or  $(\text{Mo,Ta})\text{B}_2$ .

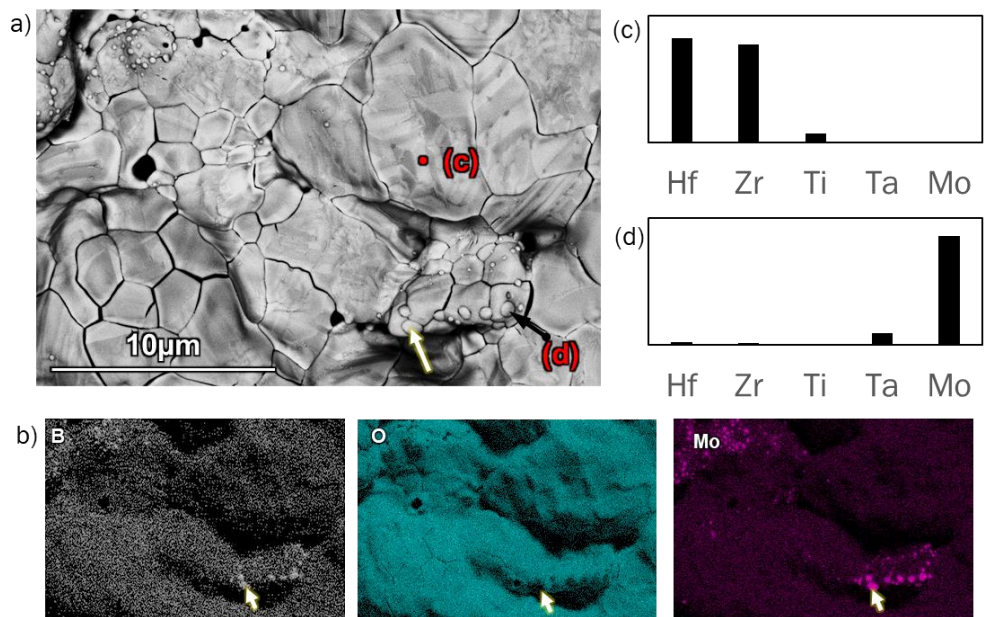


Figure 4.25: (a) Backscattered electron image and (b) B, O and Mo EDS maps in plan view of  $(\text{HfZrTiTaMo})\text{B}_2$  oxidized at  $1700^\circ\text{C}$  in  $1\%\text{O}_2$  for five minutes. (c) and (d) show point EDS analysis of the two phases observed on the surface, respectively. Arrows show a Mo-rich feature.

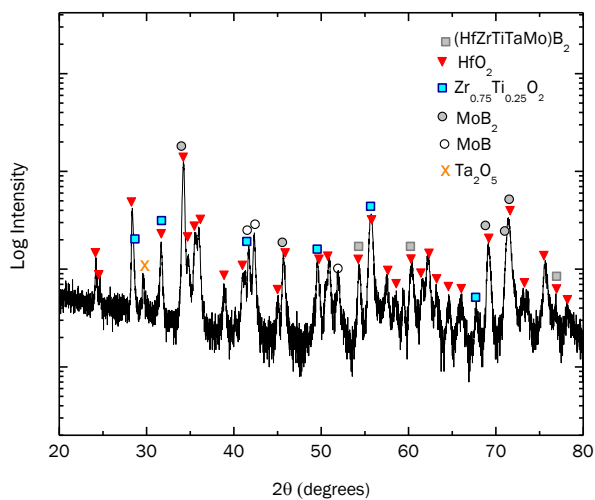


Figure 4.26: XRD data collected from  $(\text{HfZrTiTaMo})\text{B}_2$  oxidized at  $1700^\circ\text{C}$  in  $1\%\text{O}_2$  for five minutes, using micro-focus optics.

The surface layer contains mostly Hf and Zr oxide, beneath which a void can be seen that may contain boria. Beneath this void, a fine-grained, partially oxidized region exists, depleted in Hf and Zr. The fine bright grains shown in the partially oxidized region in Figure 4.27 are primarily rich in Mo and Ta, contain very little (~1-3 at% Ti) and are deficient in O.

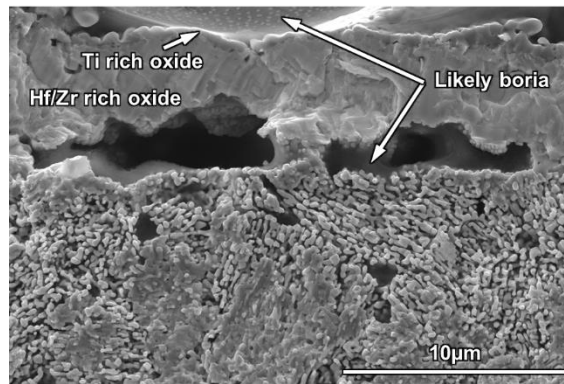


Figure 4.27: (a) Secondary electron image of  $(\text{HfZrTiTaMo})\text{B}_2$  in cross-section, near the oxide/gas interface.

Like the  $(\text{HfZrTiTaMo})\text{B}_2$  samples, the surface of the  $(\text{HfZrTiMoW})\text{B}_2$  sample shows possible retained boria and bubble formation, indicating escape of gaseous oxides.

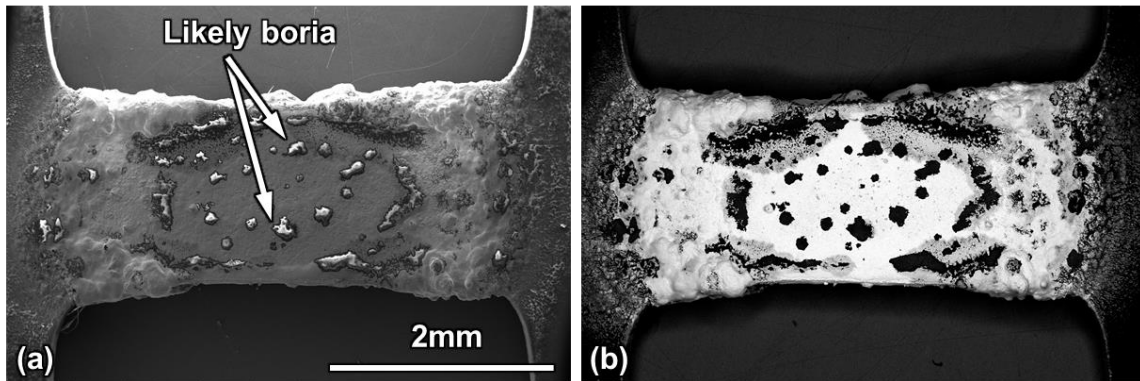


Figure 4.28: (a) Secondary electron, and (b) backscattered electron image of  $(\text{HfZrTiMoW})\text{B}_2$  in plan view after exposure at 1700 °C in 1%  $\text{O}_2/\text{Ar}$  for five minutes.

SEM and EDS point analysis show that the surface oxide in the pyrometer sighting zone consists of Hf, Zr and Ti oxide (Figure 4.29). The secondary W-rich phase, present in the pre-oxidized specimen appears to be retained even at the surface. As boron is both difficult to detect via EDS and tends to overlap with zirconium's low-energy peak, EDS analysis is not conclusive as to the extent of oxidation of this secondary phase.

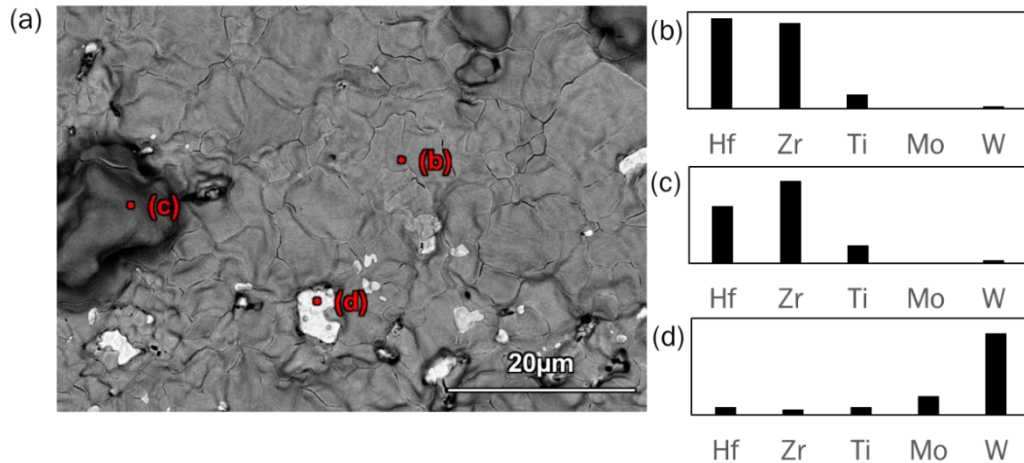


Figure 4.29: (a) Backscattered electron image in plan view of  $(\text{HfZrTiMoW})\text{B}_2$  oxidized at  $1700\text{ }^\circ\text{C}$  in  $1\%\text{O}_2$  for five minutes. (b), (c) and (d) show point EDS analysis of the phases observed on the surface.

Examination of the specimen in cross-section (Figure 4.30) after oxidation shows the W-rich secondary phase to be present in the oxidized region, and the matrix (high entropy diboride phase) to have oxidized around it. An external scale consisting of group IV elements, like the  $(\text{HfZrTiTaMo})\text{B}_2$  sample, is apparent, as is the fine scale microstructure in the oxidation affected zone. Voids are also present underneath the external oxide scale. XRD analysis (Figure 4.31) confirms that a  $\text{HfO}_2$  scale formed (likely  $(\text{Hf,Zr,Ti})\text{O}_2$ ), and coexists with W-rich borides, including the secondary phase from the pre-oxidized sample.

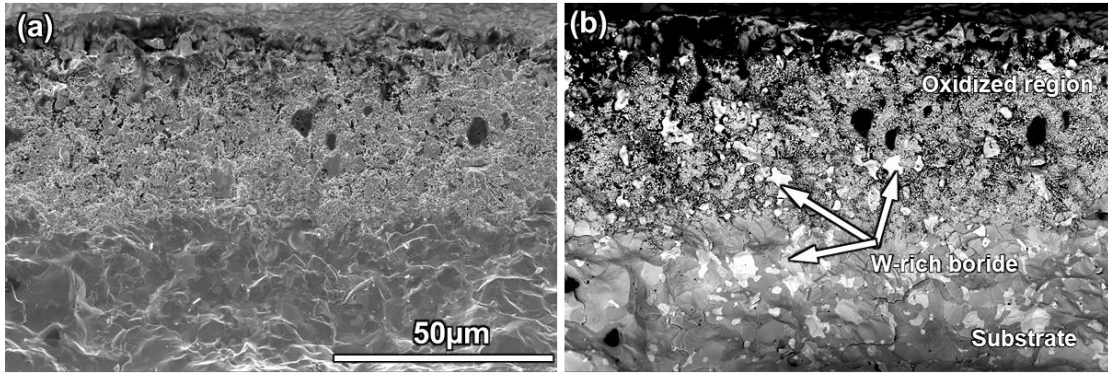


Figure 4.30: (a) Secondary electron and (b) backscattered electron image of  $(\text{HfZrTiMoW})\text{B}_2$  in cross-section, after oxidation exposure at  $1700\text{ }^\circ\text{C}$  in  $1\%\text{O}_2/\text{Ar}$  for five minutes.

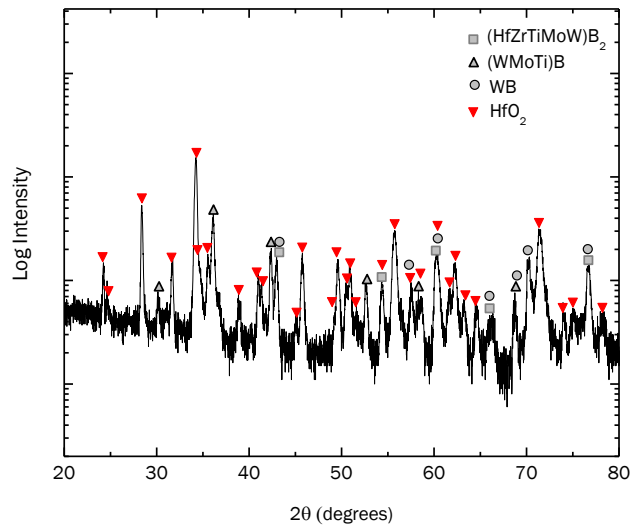


Figure 4.31: XRD data collected from  $(\text{HfZrTiMoW})\text{B}_2$  oxidized at  $1700\text{ }^\circ\text{C}$  in  $1\%\text{O}_2$  for five minutes, using micro-focus optics

#### Comparison to baseline: $\text{ZrC}$ and $\text{ZrB}_2$

The preceding sections describe the oxidation behavior of IV+VI and IV+V+VI high entropy carbide and boride compositions. A common observation was the preferential

oxidation of some components, resulting in an oxidation region often characterized by partially oxidized material depleted in one or more elements. This section describes results from similar oxidation tests conducted on ZrC and ZrB<sub>2</sub> obtained from UCSD, as a baseline for the high entropy materials. Although most of the high entropy compositions detailed above were only tested under one condition for comparison, detailed comparisons to (HfZrTiTaNb) carbide and diboride were conducted for a range of conditions. Material consumption results from these tests provide insight and are presented in Figure 4.32.

ZrC exhibited lower material consumption than (HfZrTiTaNb)C in almost all conditions tested. The exceptions here are at 1800 °C in 0.1%O<sub>2</sub> and 1500 °C in 1%O<sub>2</sub>. Zirconium diboride exhibited similar oxidation resistance to (HfZrTiTaNb)B<sub>2</sub> in both the 0.1% and 1% O<sub>2</sub> tests, and better oxidation resistance in the 0.5%O<sub>2</sub> tests. Figure 4.10 shows that the high entropy diborides in general perform similarly to ZrB<sub>2</sub>, in terms of material consumption.

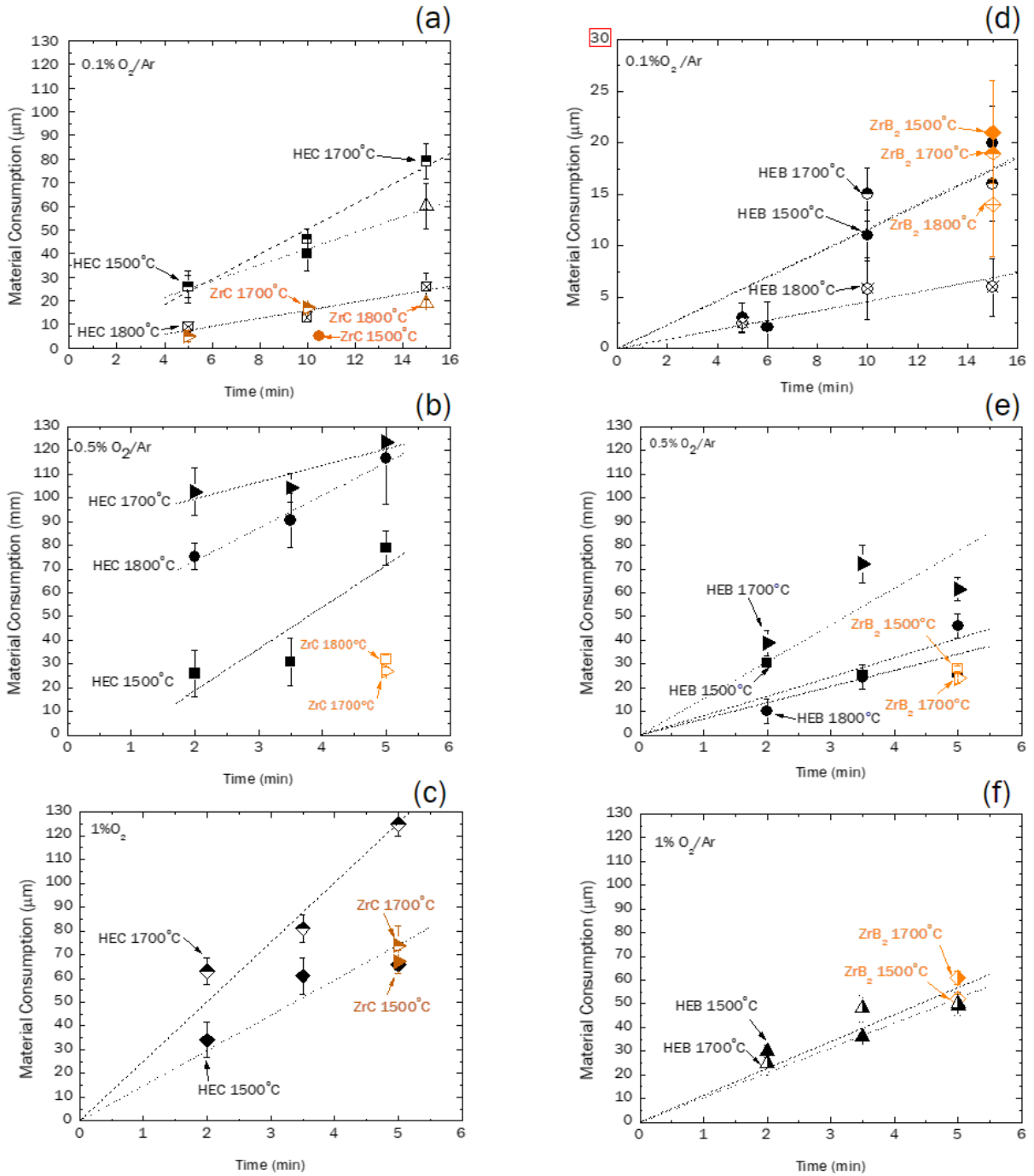


Figure 4.32: Material consumption plots for samples oxidized in 0.1%O<sub>2</sub>, 0.5%O<sub>2</sub> and 1%O<sub>2</sub>, comparing (a)-(c) ZrC to (HfZrTiTaNb)C, and (d)-(f) ZrB<sub>2</sub> to (HfZrTiTaNb)B<sub>2</sub>. ZrC and ZrB<sub>2</sub> data are shown in orange. The red box in plot (d) is to highlight the y-axis scale change.

The partial pressure dependence for the oxidation of (HfZrTiTaNb) carbide and diboride were also compared with those for ZrC and ZrB<sub>2</sub> and are shown in Figure 4.33. The plots show that (HfZrTiTaNb)C exhibits a shallower pO<sub>2</sub> dependence at 1700 °C compared to ZrC, indicating that a different oxidation mechanism is likely operative. The pO<sub>2</sub> dependence for (HfZrTiTaNb)B<sub>2</sub> is not significantly different from that of ZrB<sub>2</sub> indicating that similar mechanisms may be operative.

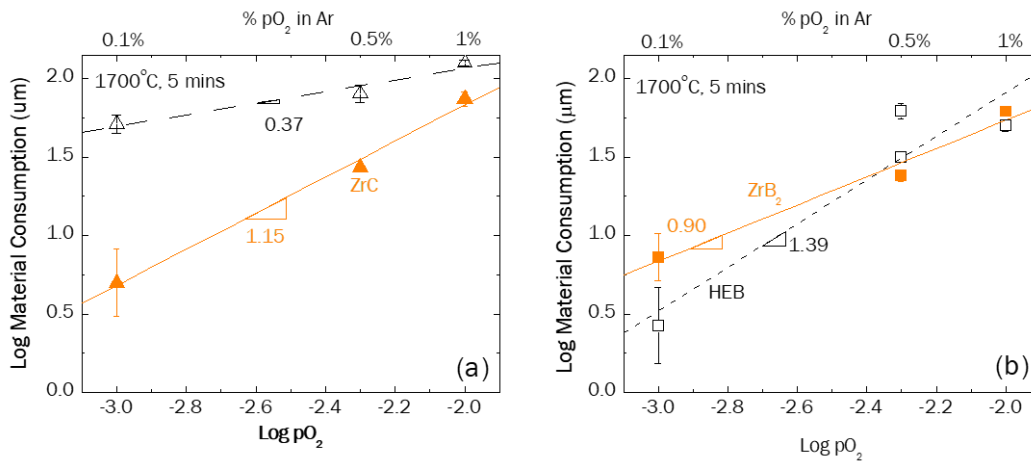


Figure 4.33: Partial pressure of oxygen dependence of (a) ZrC compared to (HfZrTiTaNb)C, and (b) ZrB<sub>2</sub> compared to (HfZrTiTaNb)B<sub>2</sub> based on material consumption at 1700 °C in 1%O<sub>2</sub> after exposure for five minutes.

Cross-section images are shown in Figure 4.34 for the ZrC samples that exhibited similar material consumption to (HfZrTiTaNb)C at 1500 °C, 1%O<sub>2</sub>, and 1800 °C, 0.1%O<sub>2</sub>. The sample tested at 1500 °C exhibits a porous surface oxide and partially oxidized ZrC grains beneath this surface oxide. The interface between the oxidation affected region and unoxidized ZrC is sharp. The grains in the oxidation affected regions show some porosity in the oxidation affected region (Figure 4.34 (b)). The sample tested at 1800 °C exhibits a much thinner

oxidized region, with a dense surface oxide and a thin layer of porous oxide underneath. Intergranular oxidation is not apparent for this case.

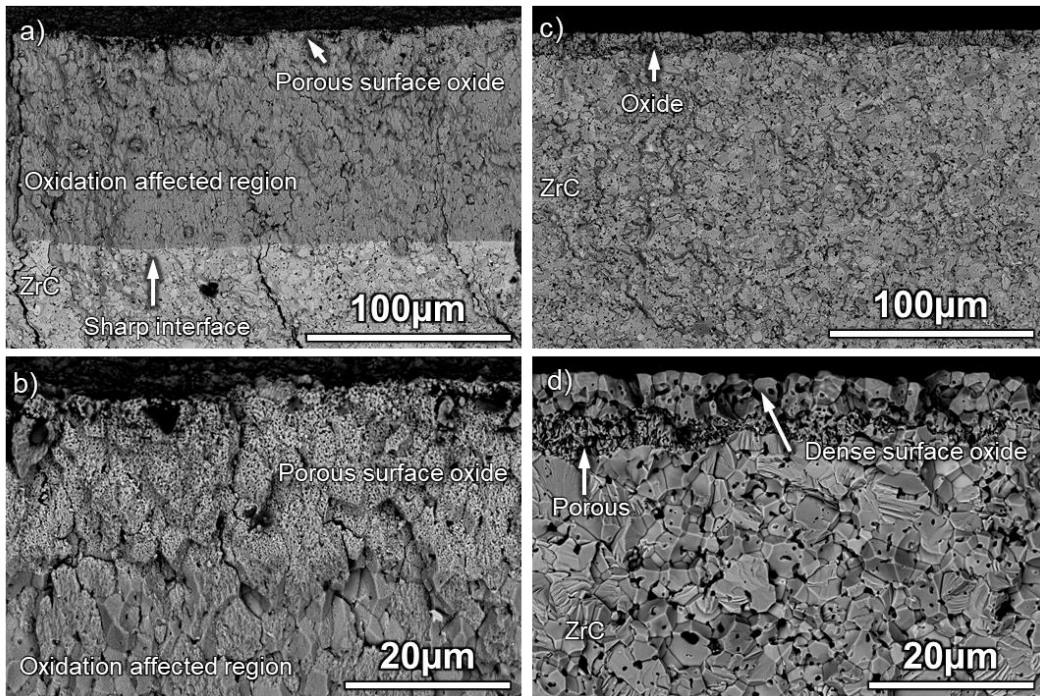


Figure 4.34: Backscattered electron images of cross-sections for (a)-(b) ZrC exposed to 1500 °C in 1%O<sub>2</sub> for five minutes and (c)-(d) ZrC exposed to 1800 °C in 0.1%O<sub>2</sub> for fifteen minutes.

The microstructure formed on ZrC after oxidation in 1700 °C, 1%O<sub>2</sub> for five minutes is shown in Figure 4.35. A porous scale is observed on the surface. Underneath this is a large region of partially oxidized, also porous, carbide between the external scale and substrate, similar to the sample tested at 1500 °C and 1%O<sub>2</sub> (Figure 4.34 (a)). There exists a clear interface between the unoxidized and oxidized regions, and intragranular oxidation shows evidence of bulk diffusion. However, while zirconium carbide exhibited lower material consumption in 1%O<sub>2</sub>, the sample itself exhibited pitting, extreme brittleness and began to disintegrate a few hours after testing (sample image shown in Figure 4.36). In comparison, the high entropy carbide compositions did not exhibit this behavior.

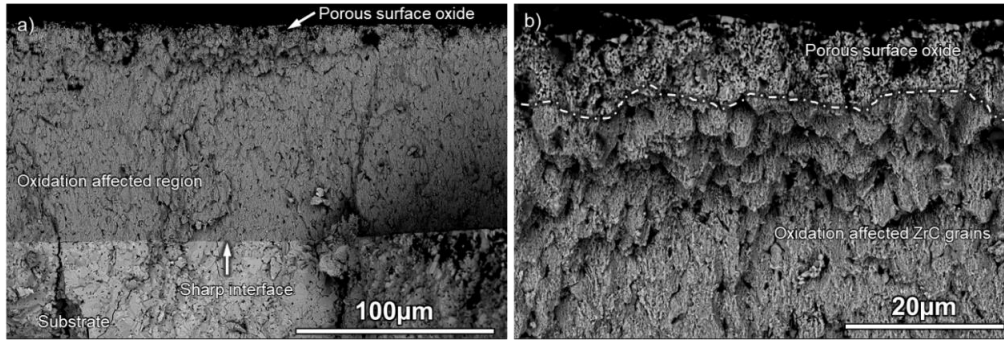


Figure 4.35: Backscattered electron images of ZrC oxidized at 1700 °C in 1%O<sub>2</sub>/Ar for five minutes. (a) shows a lower magnification image of the specimen in cross-section, and (b) shows a higher magnification image of the top of the scale (oxide/gas interface).

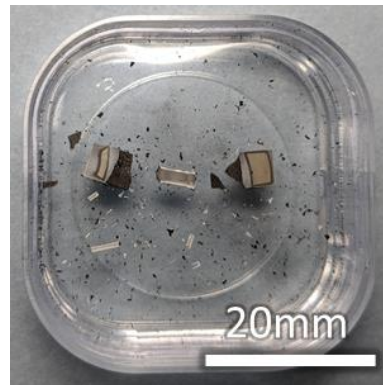


Figure 4.36: Macro image in plan view of a ZrC specimen after a few hours of sitting in ambient conditions following exposure to 1700 °C in 1%O<sub>2</sub> for five minutes.

The ZrB<sub>2</sub> specimens tested performed similarly to (HfZrTiTaNb)B<sub>2</sub> as well as the other high entropy diboride compositions. Per analysis performed at UCSD, the ZrB<sub>2</sub> synthesized for these studies contained ~4-5 vol% B<sub>4</sub>C after spark plasma sintering (SPS) consolidation like the (HfZrTiTaNb)B<sub>2</sub> samples tested in Chapter 3. (In contrast the (HfZrTiTaMo)B<sub>2</sub> contained less than 1 vol% B<sub>4</sub>C as a secondary phase due to a reduced amount of the sintering aid used in

the synthesis and the  $(\text{HfZrTiMoW})\text{B}_2$  contained less than 1 vol% graphite). The material consumption upon oxidation was compared for  $(\text{HfZrTiTaNb})\text{B}_2$  synthesized with sintered commercial powders<sup>15</sup>, sintered borocarbothermally reduced powders and  $\text{ZrB}_2$  synthesized via borocarbothermally reduced powders. The data are plotted in Figure 4.37. The data show that the  $(\text{HfZrTiTaNb})\text{B}_2$  synthesized from commercial powders exhibited higher material consumption when exposed to 1700 °C in 1%O<sub>2</sub> compared to  $\text{ZrB}_2$ . The same tests conducted on samples synthesized via the borocarbothermal reduction route exhibited material consumption, comparable to that observed for  $\text{ZrB}_2$ . The samples tested at 0.5% O<sub>2</sub> and higher exhibited columnar  $\text{ZrO}_2$  scales (example shown in Figure 4.38). At 1800 °C in 0.1%O<sub>2</sub>, a denser surface oxide was observed. Voids near the surface are also observed.

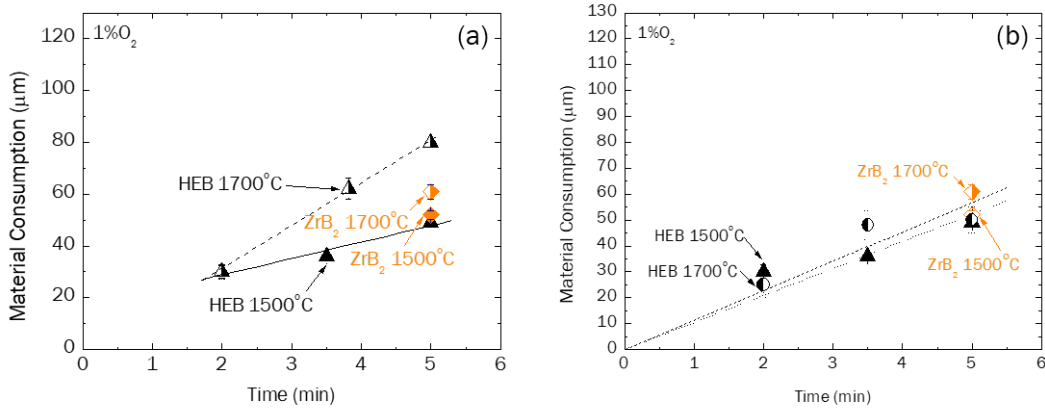


Figure 4.37: (a) Material consumption plotted for  $(\text{HfZrTiTaNb})\text{B}_2$  (labeled HEB) synthesized using commercial powders, compared to  $\text{ZrB}_2$  synthesized via borocarbothermal reduction. (b) Material consumption plotted for  $(\text{HfZrTiTaNb})\text{B}_2$  (labeled HEB) synthesized via borocarbothermal reduction, compared to  $\text{ZrB}_2$  synthesized via borocarbothermal reduction.

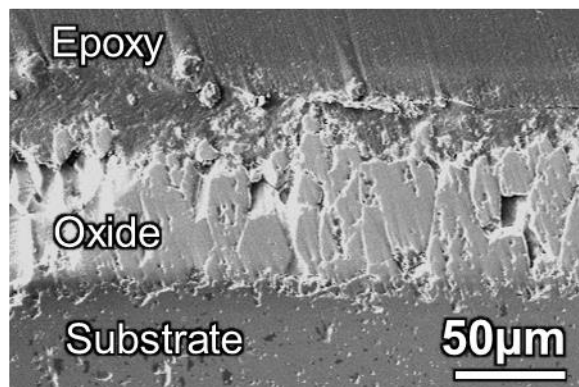


Figure 4.38: Secondary electron image of a polished cross-section of a  $ZrB_2$  sample oxidized at  $1700\text{ }^\circ\text{C}$  in  $1\%\text{O}_2$  for five minutes.

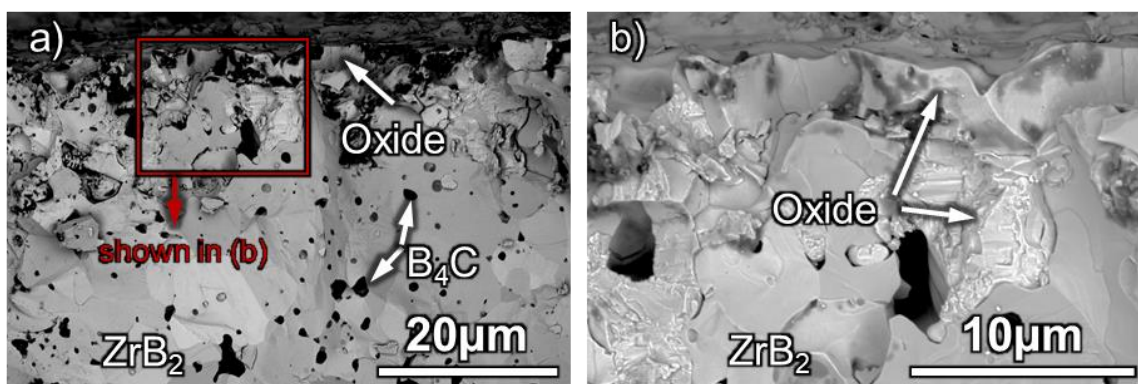


Figure 4.39: Backscattered electron images of a fracture cross-section of a  $ZrB_2$  sample oxidized at  $1800\text{ }^\circ\text{C}$  in  $0.1\%\text{O}_2$  for 15 minutes. (a) shows a lower magnification view, and (b) shows a higher magnification view of the oxide scale at the oxide/gas interface of the red-outlined region in (a).

The dark phases shown on the surfaces (gas/oxide interface) in Figure 4.39 and Figure 4.40 are likely boria, based on the morphology, the fact that it fills in open areas, and the low average Z indicated by the contrast in a backscattered image.

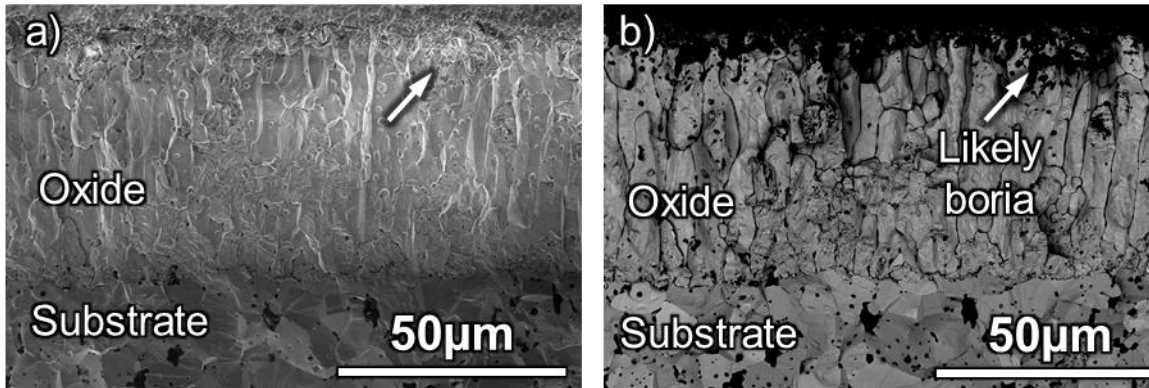


Figure 4.40: (a) Secondary electron image and (b) backscattered electron image of the same fracture cross-section of  $ZrB_2$  after exposure at  $1500^\circ C$  in  $1\%O_2$  for five minutes. Arrow in (a) shows the same region marked by the arrow in (b) and indicate region that likely contains boria.

#### 4.4. Discussion

##### 4.4.1. Carbides

As with  $(HfZrTiTaNb)C$ , both  $(HfZrTiTaMo)C$  and  $(HfZrTiMoW)C$  oxidized preferentially according to the relative thermodynamic favorabilities discussed in Chapter 2, with group IV oxides dominating in the oxide scales, and Ta, Mo and W (in their respective materials) following. This is not to say that at these conditions, the group V and VI elements did not oxidize. Evidence for  $Ta_2O_5$  is seen in XRD data (Figure 4.22), as well as evidence of Mo and W oxides (Figure 4.18).

$(HfZrTiMoW)C$  exhibited lower material consumption, only slightly more than  $ZrC$ , compared to the other high entropy compositions. The morphology exhibited by this high entropy composition mimicked that of  $ZrC$ , showing a region of oxygen dissolved in the carbide phase and a porous external scale (Figure 4.14 and Figure 4.15). This is a promising result, as  $(HfZrTiMoW)C$  did not exhibit the pesting behavior observed for  $ZrC$ . This pesting behavior was

previously reported for ZrC after oxidation exposures<sup>166,182</sup>, and may be due to deeper oxygen penetration via grain boundaries than observable by the characterization techniques used.

Apparent oxygen dissolution in the high entropy carbide was not observed for (HfZrTiTaNb)C (described in Chapter 3) to the extent and depth observed for (HfZrTiTaMo)C and (HfZrTiMoW)C. It is unknown whether group VI additions promote oxygen dissolution in carbides. A cursory review of the literature did not reveal any observations of oxygen dissolution in group VI carbides<sup>183-186</sup>, and an understanding of the dissolution of oxygen in refractory carbides and the formation of oxycarbides is a key knowledge gap in the area of oxidation of refractory carbides. The more “complete” transport of oxygen in the high entropy carbide grains for (HfZrTiTaMo)C and (HfZrTiMoW)C appears to result in a more uniform mode of attack, relative to (HfZrTiTaNb)C. As discussed in Chapter 3, after exposure at 1700 °C in 1%O<sub>2</sub> after five minutes, an external scale was not formed to mitigate the rapid oxygen diffusion and reaction via grain boundaries in (HfZrTiTaNb)C (external scales were observed at 1500 °C and 1800 °C). This more uniform attack may be partially responsible for the lower material consumption observed for (HfZrTiMoW)C.

While the surface on (HfZrTiMoW)C exhibits a mostly dense scale (Figure 4.11), examination in cross-section reveals some porosity, which is similar to that formed on ZrC, except for the presence of (Mo,W) carbide phase. Oxidation of this phase results in volatile oxides that leave the system (Figure 4.18), which was expected. Both Mo and W were observed in the deposits on the cooler clips, suggesting that both group VI elements oxidized, although more Mo is observed in the deposits, which may be an indication of Mo oxides being more volatile than W oxides as proposed through thermochemical analyses<sup>44</sup>. W additions are also known to promote densification of the group IV oxides<sup>92,180</sup>, and these may explain the mostly dense appearance of the group IV-rich oxide at the surface, particularly around the group VI-

rich carbide grains. It is not surprising, then, that this preferential oxidation of the group IV elements results in behavior similar to ZrC.

In contrast, both (HfZrTiTaNb)C and (HfZrTiTaMo)C exhibited significantly more extensive intergranular oxidation, voids at grain boundaries and possible melting of the oxide phases (see Chapter 3 and Figure 4.21). W (and perhaps by similitude, Mo) oxides show limited solubility in group IV oxides (example phase diagram shown in Figure 4.1) especially at 1700 °C, are liquid at the test temperature and readily volatilize. The result is densification due to liquid phase sintering in the short term, without excessive liquid oxide formation. Ta<sub>2</sub>O<sub>5</sub> is not as volatile and forms solid solutions or ordered compounds with group IV oxides<sup>76</sup>, which means that at the high temperatures of interest, it can persist in the oxide scale and promote liquid oxide formation. Consideration of ZrC material consumption compared to (HfZrTiTaNb)C (Figure 4.32), and comparison of the morphologies of the oxidized regions suggests that these intergranular voids in the Ta-containing high entropy compounds accelerate material consumption relative to ZrC and (HfZrTiMoW)C. The shallower pO<sub>2</sub> dependence observed for the high entropy carbide (HfZrTiTaNb)C versus that of ZrC (Figure 4.33) could be indicative of the fast pathways that these intergranular voids present. At 1800 °C and 0.1%O<sub>2</sub>, the oxidation resistance of (HfZrTiTaNb)C was similar to ZrC, likely due to the preferential formation of Hf and Zr oxides, and the lack of significant amounts of Ta in the oxide scale.

#### 4.4.2. Diborides

As with the carbides, the high entropy diborides oxidized similarly (relative to each other), with a group IV rich external scale (Figure 4.26 and Figure 4.31). The borides generally also exhibited lower material consumption than the carbides. All exhibit a partially oxidized region depleted in group IV elements and rich in group V and VI borides (depending on composition). The (HfZrTiTaMo)B<sub>2</sub> specimen, which contained less B<sub>4</sub>C as a secondary phase in the starting

material, did not exhibit the large voids (Figure 4.27) in the partially oxidized region seen after oxidation of  $(\text{HfZrTiTaNb})\text{B}_2$  synthesized via borocarbothermal reduction, in Chapter 3 (Figure 3.15, Figure 3.16, Figure 3.22). The microstructure in the partially oxidized region formed on  $(\text{HfZrTiTaMo})\text{B}_2$  is more reminiscent of the partially oxidized region formed after exposing  $(\text{HfZrTiTaNb})\text{B}_2$  (Figure 3.16) synthesized using commercial powders: relatively fine boride grains and porosity. This partially oxidized region is also similar to that formed on  $(\text{HfZrTiMoW})\text{B}_2$ , except for the retention of the secondary W-rich phase (Figure 4.30). It is not clear to what extent the segregation of preferential segregation of W (in particular) to this phase affected the material consumption results, although this secondary phase also contained appreciable amounts of the group IV elements. Further, this latter diboride material contained graphite instead of  $\text{B}_4\text{C}$  as a secondary phase in the as-synthesized specimen. The fine-grained microstructure in the partially oxidized regions due to the lower amounts of these secondary phases is more desirable as it is less dependent on the presence of liquid boria for oxidation resistance, which presumably cannot be relied upon in the conditions encountered in hypersonic flight. All the high entropy compositions and  $\text{ZrB}_2$  exhibit evidence of boria solidified from the melt on the surface, and possibly in the partially oxidized regions as well. The similarity of the material consumption (Figure 4.10) and morphology of the oxidation affected regions among the high entropy borides suggests that the preferential oxidation of group IV elements along with the formation of boria could control the oxidation behavior of these compounds. This would also explain the similarity in material consumption between  $\text{ZrB}_2$  and the high entropy materials, as well as the similarity in  $p\text{O}_2$  dependence of the material consumption between  $(\text{HfZrTiTaNb})\text{B}_2$  and  $\text{ZrB}_2$  (Figure 4.33). At  $1800^\circ\text{C}$ , the oxidation resistance of  $(\text{HfZrTiTaNb})\text{B}_2$  was likewise similar to  $\text{ZrB}_2$ .

#### 4.4.3. Design of oxidation-resistant HE-UHTCs

The high entropy approach to the design of UHTCs, considered for the benefits that were proposed in the high entropy materials literature reviewed in Chapter 1, has been explored in this dissertation. A large advantage to this approach is the expansion of compositional space for UHTCs. However, the thermodynamic analyses conducted and presented in Chapter 2 suggest that the effect of configurational entropy in stabilizing the solid solution phase in a high entropy carbide or boride is negligible compared to the large, negative free energies of the oxidation reactions. Nevertheless, high entropy compositions may still be pursued for potential improvements or tailoring of other properties, such as mechanical and thermal properties<sup>113,157,187</sup>.

Also in Chapter 2, the periodic trends in oxidation behavior and oxide stabilities of the group IV, V and VI oxides were noted, and predicted to result in a tendency towards preferential oxidation occurring in these materials and destabilization of the underlying solid solution phase. These predictions were experimentally verified as discussed in Chapters 2 and 3 as well as this one. The mechanisms for the oxidation of high entropy carbides and diborides along with compositional effects were probed in Chapters 3 and 4. These findings provide some insight into future directions for the design of oxidation resistant UHTCs.

First, the preferential oxidation of elements suggests that the group IV elements, particularly Hf and Zr, which have the highest melting temperatures of the elements of interest, will form. These oxides are porous when formed on the carbide, and denser when formed on the diboride. A dense, adherent and solid scale is required for oxidation resistance. As the effects of CO(g) and volatile B<sub>2</sub>O<sub>3</sub> (l,g) in forming a porous or otherwise disrupted scale cannot be discounted, the addition of elements that promote densification or sintering at ultra-high temperatures (UHTs) is required. Work in Chapter 3 show that this densification may be promoted by Ti in the oxide at temperatures above 1800 °C. The group V additions, Ta and Nb

have been shown to promote liquid oxide formation which, which, combined with effects such as gaseous (CO(g)) and volatile (MoO<sub>3</sub> (g)) oxide evolution, resulted in large intergranular voids which was ultimately detrimental to the oxidation resistance of high entropy carbides. Ta additions were also proposed to promote the formation of complex oxides such as Hf<sub>6</sub>Ta<sub>2</sub>O<sub>17</sub>, which may promote oxidation resistance. However, while there is evidence for the presence of such complex oxides, the results discussed here and in Chapter 3, as well as in a more recent HfC-TaC oxidation study<sup>137</sup> show that excess Ta additions in materials that oxidize intergranularly (such as UHTC carbides) result in “premature” densification of the intergranular oxides (before an external scale can form) and liquid oxide formation.

The additions of group VI oxides show that porosity due to volatile oxides is observed on the surface of the scale, but the mode of attack was more uniform. While preferential oxidation was observed, a region of phase separation was not observed in these conditions for the (HfZrTiTaMo)C and (HfZrTiMoW)C, as was observed for (HfZrTiTaNb)C. It is not clear whether this would be expected from available data on the phase equilibria between Mo- and W-containing ceramics and oxygen. Any detrimental effects due to the non-group IV elements present in the oxide phase, in this case Mo and W, was minimized due to (a) their oxides having limited solubility in group IV oxides, being volatile and leaving the system, and (b) their preferential retention as a carbide phase. The material consumption data confirms that at the conditions tested, the formation of volatile oxides over liquid is desirable; group VI additions are preferable. This is especially true for conditions that likely prevail during hypersonic flight. Thus, the group IV+VI elemental combination is a promising route for the design of HE-UHTCs.

Further, while preferential oxidation may be considered to result in destabilization of the solid solution phase, it may also be a beneficial effect if the oxidation of non-group IV elements are limited, such as observed after the 1800 °C tests on (HfZrTiTaNb)C in Chapter 3 and the results presented here for (HfZrTiMoW)C. The concept behind the compositional balance

diagram and its extension using computational tools can help tailor high entropy UHTC compositions away from the starting equimolar compositions or the five components discussed in this dissertation, that may then aid in tailoring this preferential oxidation to limit non-group IV oxide formation.

All the diborides tested for this dissertation work exhibited similar material consumption. The work performed and presented in Chapter 3 and the microstructures observed and presented in this chapter suggest that liquid boria plays a significant role in the ultra-high temperature oxidation behavior of refractory metal diborides. While borides have exhibited superior oxidation resistance compared to carbides in most of the results presented, this effect is not expected to hold at temperatures in excess of the boria boiling point ( $>1860^{\circ}\text{C}^{133,147}$ ) at 1 atm. The extent to which this might be the case needs to be further probed in experiments at higher temperatures. It should be noted that the results presented in this dissertation were partially from samples wherein the presence of secondary phases such as  $\text{B}_4\text{C}$  may obscure a better understanding of the performance of pure metal diborides. Recent improvements in the synthesis of high entropy diborides to minimize secondary phases<sup>157</sup> should be leveraged to confirm these results.

#### 4.5. Conclusions

The more favorable oxidation resistance of high entropy diborides versus high entropy carbides follows the trend observed for monocarbides and monodiborides for samples tested at  $1700^{\circ}\text{C}$  and  $1\%\text{O}_2$ . Improvement in oxidation resistance and similarity to the material consumption exhibited by Zr-based compounds at  $1800^{\circ}\text{C}$  is particularly significant for  $(\text{HfZrTiMoW})\text{C}$ , where the oxide scale is dense and primarily rich in Hf and Zr. This suggests that any beneficial effect, such as the proposed scale densification due to the presence of Mo and W, are not significant; however, this is a promising start for further refinement.

(HfZrTiMoW)C exhibited better oxidation resistance compared to the Ta containing high entropy carbides. The addition of Ta promotes the formation of liquid oxides, which results in intergranular voids presenting fast pathways for oxidant ingress. The addition of group V elements to HE-UHTCs, at least in equimolar concentrations, is not recommended. The oxidation behavior and resistance of the high entropy diborides are very similar to each other and  $ZrB_2$ , likely due to the formation of Hf and Zr rich external scales and boria, suggesting that more work is needed to improve high entropy compositions over the baseline monodiboride. All the high entropy compositions exhibited preferential oxidation according to the thermodynamic framework outlined in Chapter 2.

#### 4.6. Recommendations for future work

The improved oxidation resistance of (HfZrTiMoW)C relative to the main compositions explored in this dissertation, (HfZrTiTaNb)C, suggests that this is a promising composition for further exploration, particularly at temperatures greater than 1800 °C. A deeper understanding of the oxygen solubility, and the formation of Mo and W oxides is needed, as well as how these may vary with composition, temperature and oxygen partial pressure in order to understand how these might influence the oxidation resistance of this high entropy composition. Tests at lower partial pressures where kinetics are much slower would also aid in determining whether phase separation, as observed for (HfZrTiTaNb)C, occurs for the group VI compositions.

The precise nature of the influence of liquid boria in the oxidation of high entropy diborides is still little understood, particularly the formation of partially oxidized regions depleted in Hf, Zr and Ti. As this appears to be prevalent across three different high entropy compounds, a deeper understanding of this behavior may be necessary to aid in the design of oxidation resistant high entropy diborides. As with the carbides, the oxidation behavior of high entropy

diborides at 1800°C and above, where the influence of boria on the oxidation behavior is expected to be reduced, should also be explored.

## 5. Analysis of Test Specimen Temperature Gradients in the Resistive Heating System

### 5.1. Introduction

Hypersonic vehicles traveling in the upper atmosphere at speeds greater than Mach 5 create shock waves that lead to ultra-high temperatures at the sharp nose and wing leading edges. The need for advanced materials that can withstand ultra-high temperatures<sup>188</sup> in these oxidizing environments is currently unmet. The ability to conduct controlled ultra-high temperature oxidation studies of novel ceramics and alloys is therefore of interest to the aerospace community.

Ultra-high temperature testing presents many challenges. Reliable temperature control and measurement is required. Environment control, such as known partial pressures of oxygen ( $pO_2$ ) may be key to elucidating degradation mechanisms, particularly for materials with rapid oxidation rates. Additionally, given increased reactivity and reaction rates at high temperatures, container contamination and interaction with the material being tested are often issues<sup>189</sup>.

An experimental set-up, shown in Figure 5.1, addresses the above issues for oxidation tests on ultra-high temperature ceramics. The base configuration of the system was first introduced by Halloran et al.<sup>158</sup> to conduct studies on  $ZrB_2$ -SiC ceramics in air for temperatures up to 2000 °C. The system employs Joule heating, wherein a high current is passed through a conductive sample and the intrinsic resistivity of the material results in self-heating. The current is controlled by a combination of a micro-optical infrared pyrometer and a PID controller.

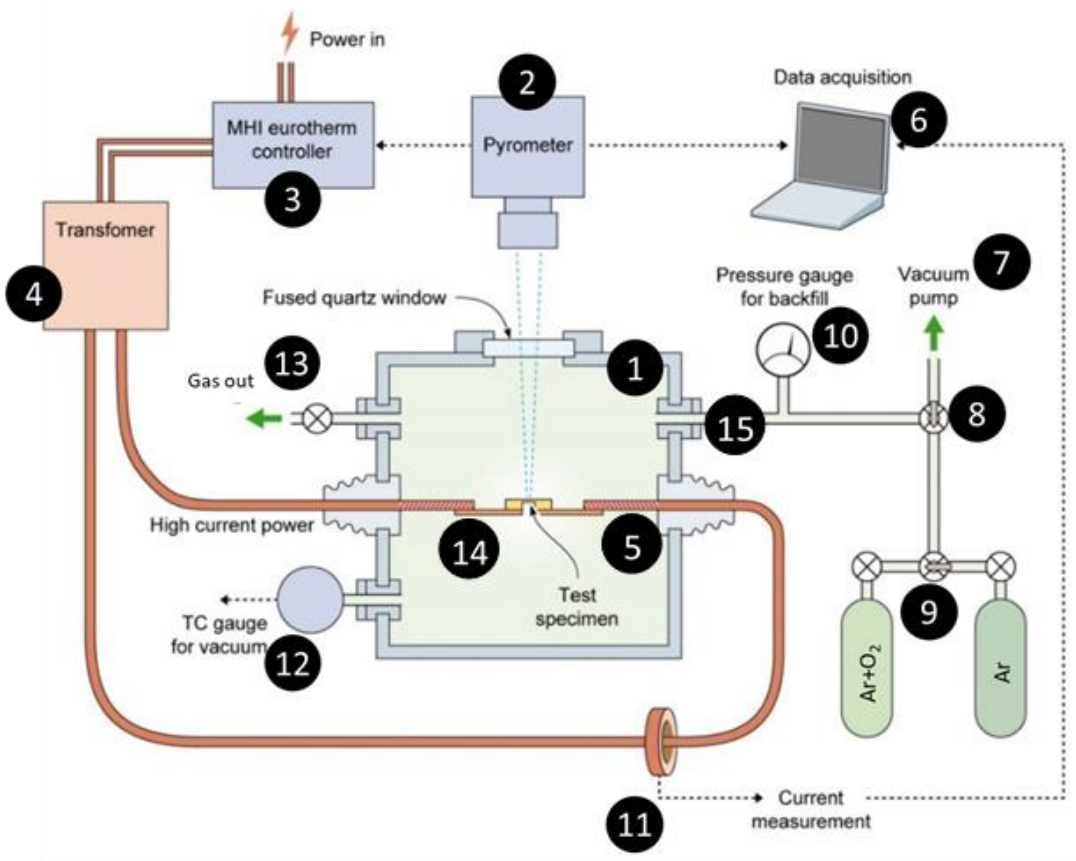


Figure 5.1: Resistive heating system schematic. (1) Chamber (2) pyrometer (3) heater + Eurotherm controller unit (4) transformer (5) copper electrodes (6) data acquisition computer (7) vacuum pump (8) valve to vacuum pump (9) valve for switching between gas tanks (10) backfill pressure gauge (11) current transducer (12) thermocouple gauge for vacuum readout (13) gas out/exhaust (14) flattened copper wires (15) gas inlet to chamber. Adapted from Shugart et al.<sup>159</sup>

The design for such a system was subsequently modified by Shugart et al.<sup>190</sup> (Figure 5.1) to (a) introduce the use of an emissivity correcting pyrometer, (b) conduct these tests in a closed chamber to enable testing in controlled oxygen partial pressures, and (c) conduct  $^{18}\text{O}_2$  double-oxidation studies to elucidate diffusion mechanisms. Other modifications of the concept have been made to run mechanical tests at high temperatures<sup>191</sup>. The advantages of such a system includes the ability to control the test environment and minimize contamination of the test

volume with other materials. The test configuration results in temperature gradients axially. In the case of oxidation experiments, the growth of an oxide scale and subsequent consumption of the base material can also result in temperature gradients through the thickness of the sample. These temperature gradients have not been defined and concerns exist that the surface temperatures reported in prior work may be significantly different than the oxide/substrate interface. Furthermore, there are concerns that the oxidation mechanisms may be different for Joule heating than for radiative/convective heating reported in other studies and of primary importance for hypersonic applications.

The objective of this study is to computationally evaluate temperature gradients in the test specimens to understand any artifacts of the test procedure on oxidation results. The temperature at the reaction front, in this case, the oxide-substrate interface, is critical toward elucidating oxidation mechanisms. Modelling the temperature gradient through the oxide and along the long axis of the specimen are both needed to interpret the oxidation results. In this work, a thermal-electric finite element analysis of the specimen is conducted in order to compute the oxide/substrate interface temperature. Several oxide thicknesses were analyzed to correlate the measured surface temperature with the interface temperature based on the thickness of the oxide. Additionally, the axial temperature gradients were evaluated as a function of oxide thickness and temperature. Finally, the current densities were calculated, and results considered in the context of its influence on mass (or ion) transport.

## 5.2. Resistive heating system

The resistive heating system (RHS, Figure 5.1), uses a dogbone shaped specimen as seen in Figure 5.2. The pyrometer sighting zone, approximately 1.5 mm in diameter, is delineated by an orange circle in that schematic. Flattened copper wires (approximately 1.1 x 2.7 x 20mm) are placed in contact with the copper electrodes with custom mechanical lugs

(Figure 5.3). The parts of the copper wire in contact with the sample are covered in platinum foil (0.05mm thick, Alfa Aeser Premion™, Fisher Scientific). The sample is loaded straddling the two copper wires, Figure 5.1. Contact between the sample legs and the copper wires is ensured by using modified alligator clips, Figure 5.4. The teeth are removed and the inner surfaces are isolated with thin yttria-stabilized zirconia plates (cut to approximately 0.4 x 3 x 9 mm, material from Ortech Advanced Ceramics, Sacramento, CA), which are adhered to the alligator clips using a cyanoacrylate adhesive (Ted Pella, Redding, CA).

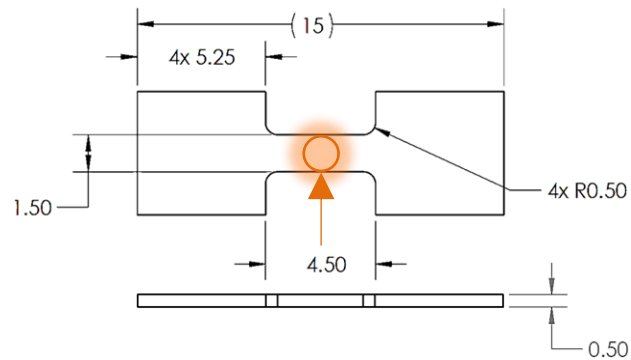


Figure 5.2: Test specimen configuration and dimensions. Orange circle and arrow indicate the approximate size and location of the hot zone, or the area of the sample known to be at the test temperature. Estimated size of the hot zone is 1.5mm, which is also the spot size of the pyrometer.

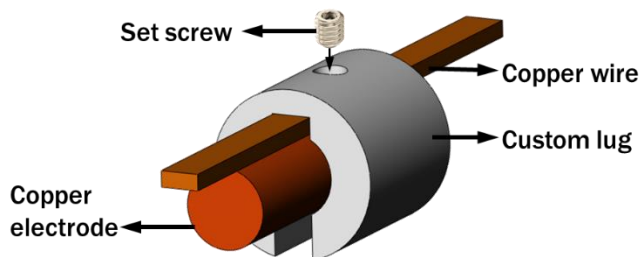


Figure 5.3: Model of the custom lug designed by and obtained from Tanner Fitzgerald at the University of Virginia Department of Materials Science. Copper electrode and wires are indicated in Figure 5.1 as labels 5 and 14 respectively.

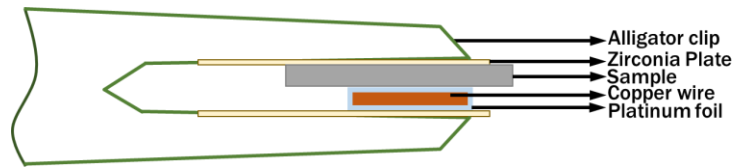


Figure 5.4: Schematic showing sample clamping configuration during test set-up.

The pyrometer is aligned with the center of the thin section of the specimen (orange outlined region in Figure 5.2) through a fused quartz window. The chamber is then sealed with copper gaskets and Conflat flanges (MDC Vacuum, Hayward, CA) evacuated and purged with argon several times before being backfilled with Ar (Ultra-high purity grade, Praxair, Danbury, CT). The exhaust ball valve (Figure 5.1, label 13) opened to allow Ar flow, prior to heating. Gas flow is maintained between 950-1000 sccm throughout the test. The inlet gas tubing (smooth bore 306 stainless steel per ASTM A213) has an inner diameter of 0.194". The free stream gas velocity in the tubing prior to entering the chamber is calculated to be approximately 87 cm/s for a volumetric flow of 1L/min. The chamber (Figure 5.5) has a complex cross section; the chamber opening on either side of the sample is 0.75 inches. At this chamber opening, the cross-sectional area is 11.4 cm<sup>2</sup> and the calculated free stream gas velocity is 5.9 cm/s for the same volumetric flow.

The pyrometer (Figure 5.1, label 2) (Pyrofiber Lab PFL-0865-0790-2500C311, Pyrometer Instrument Company, Ewing Township, NJ) works in conjunction with the MHI heater + Eurotherm controller (Figure 5.1, label 3) to control the ramp and dwell temperature of the specimen according to the set program. Shugart found previously during calibration tests conducted by melting platinum and palladium wires that the pyrometer reading was 16-28°C lower than the known melting temperatures of those elements<sup>192</sup>. A transducer is placed on a lead cable exiting the transformer and provides a measurement of the current in the line,

visualized using LabView. AC currents of 30 to 120 A have been used to resistively heat the materials being tested. The data were used to refine the PID settings for a given material.

Temperature and current read-outs (Figure 5.1, label 6) were used to refine the program. The test temperature is achieved in approximately two minutes, and dwell time at test temperature ranged from 2-30 minutes. When the program reached the dwell stage, the current was allowed to stabilize before the valve (Figure 5.1, label 9) was switched from Ar to the oxidizing gas, an O<sub>2</sub>+Ar mixture. Gas mixture compositions ranged from 100 ppm O<sub>2</sub> to 1% O<sub>2</sub> in Ar. At completion of the desired test duration, the heater was turned off and the gas valve switched back to Ar.

Gas flows from the inlet (Figure 5.1, label 15) to the outlet (Figure 5.1, label 13) across the surface of the sample, as indicated by Figure 5.6. The pyrometer was aligned to sight on the surface of the specimen through the fused quartz window in the chamber. When the oxidizing gas is turned on, an oxide forms on the surface. The changing emissivity of the sample due to oxidation is corrected for by the pyrometer and the accompanied software. The required correction is determined by measuring the difference between the energies of a pulsed laser sent to the target and that of the reflected laser signal. This difference allows for the calculation of absorptivity and therefore emissivity. The measured radiance is then corrected with this emissivity value with reference to black body radiance<sup>193</sup>.

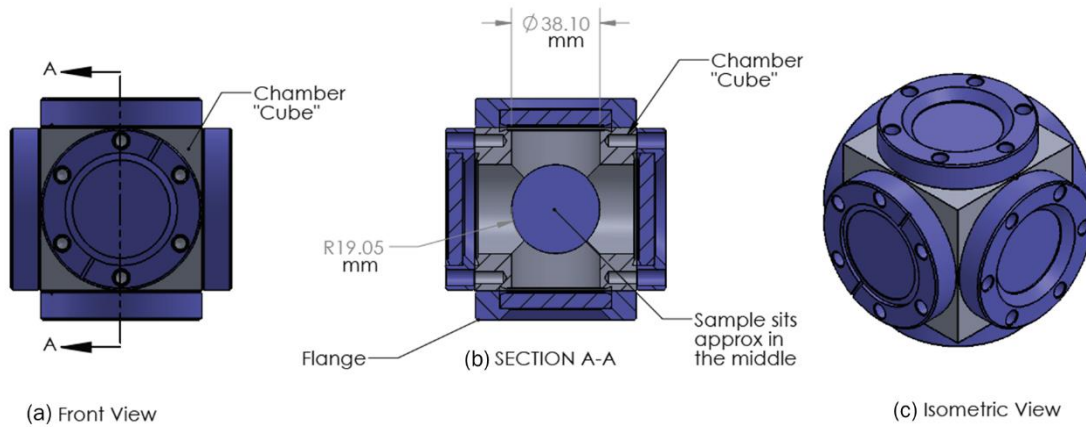


Figure 5.5: (a) Front view of the chamber used in the resistive heating set-up, (b) section view cut along the line shown in (a), and (c) isometric view of the chamber.

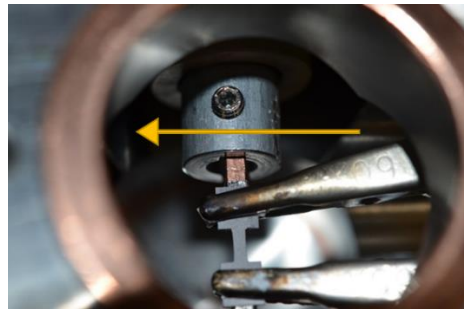
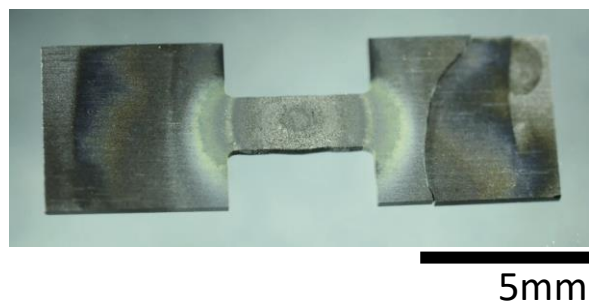


Figure 5.6: Direction of gas flow across sample, indicated by the yellow arrow.

Specimens tested in this system include high entropy ultra-high temperature ceramic ((HfZrTiTaNb)C, (HfZrTiTaNb)B<sub>2</sub>, (HfZrTiTaMo)C, (HfZrTiTaMo)B<sub>2</sub>, (HfZrTiMoW)C, (HfZrTiMoW)B<sub>2</sub>), ZrC and ZrB<sub>2</sub> and ZrB<sub>2</sub>-SiC. Samples are fabricated into pucks or bars via spark plasma sintering (SPS)<sup>15,114,126</sup>. The sintered materials were then machined by grinding, by Bomas Machine Specialties (Somerville, MA), into the bridge geometry<sup>159</sup> previously used and the dogbone configuration shown below (Figure 5.2).

The larger cross-sectional area at the ends of the specimen allow for the ends to remain cooler than the hot zone (estimated temperatures presented in the results section). This results in a large temperature gradient along the length of the sample, from the hot zone outwards. This temperature gradient is evident in the varicolored oxide formation on an (HfZrTiTaNb)C sample oxidized at 1700 °C in 1%O<sub>2</sub> for five minutes (Figure 5.7). The midsection of the specimen is suspended, preventing interaction with any container material.



*Figure 5.7: (HfZrTiTaNb)C oxidized at 1700 °C in 1%O<sub>2</sub> for five minutes using the resistive heating system. Note color and oxide gradient from center outward, indicating the temperature gradient and formation of different oxides.*

The sample is heated and held at test temperature via Joule heating. During the test, an oxide forms, which has different electrical and thermal properties compared to the base material. The pyrometer, which operates on an infrared wavelength, sights on the surface of the oxide. The base material is expected to be more conductive, and as such conducts most of the current, and therefore may heat up more than the oxide. This results in temperature gradient through the thickness of the oxide. This is illustrated in the schematic in Figure 5.8 and Figure 5.9.

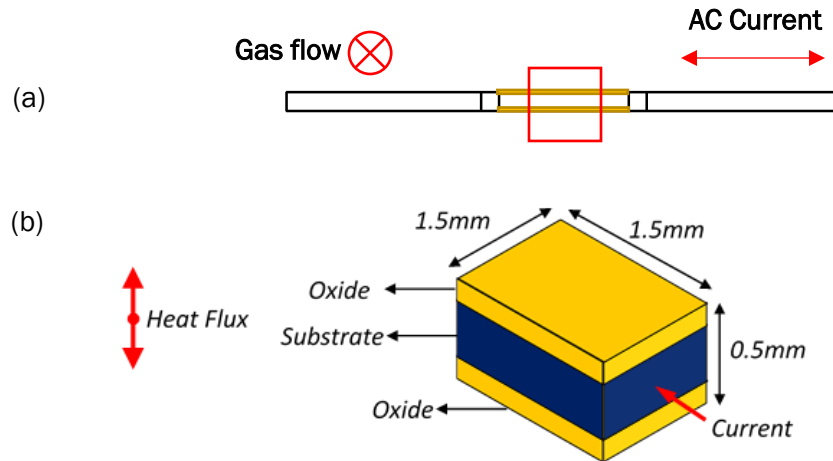


Figure 5.8: (a) Side view of the dogbone specimen. Yellow regions indicate, schematically, the formation of an oxide on the top and bottom surfaces of the sample (oxide growth on the side not shown for clarity). The red box shows, also schematically the hot zone region. (b) Volume element of the region inside the red box in (a). The yellow indicates the oxide. (not drawn to scale). Directions of the current and gas flow are shown. Gas flow is into the page.

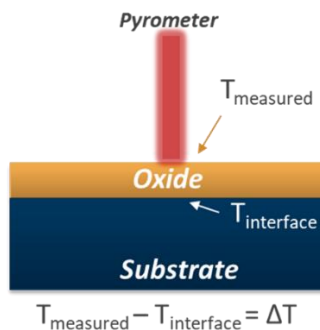
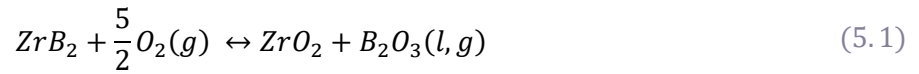


Figure 5.9: Schematic showing the potential temperature differential resulting from the oxide growth.  $T_{\text{measured}}$  is the known temperature given by the pyrometer reading, which is sighting on the surface.  $T_{\text{interface}}$  is the unknown temperature at the region of interest, i.e., the oxide-substrate interface.

### 5.3. Estimated temperature gradient through oxide thickness

A preliminary, analytical estimate of the  $\Delta T$  through the oxide thickness was conducted for  $ZrO_2$  formation on  $ZrB_2$  with the following assumptions and simplifications. Oxidation of  $ZrB_2$  occurs via reaction (5.1).



The presence of  $B_2O_3$  (l,g) was neglected for this analysis, which is a reasonable assumption due to the high vapor pressure of  $B_2O_3$ . Heat flux along the length of the sample was considered insignificant compared to the heat flux through the thickness of the sample and was therefore neglected. A DC current of 75A was assumed instead of AC current. The following energy balance equation was used<sup>194</sup>

$$kV \frac{d^2T}{dx^2} + I^2R = 0 \quad (5.2)$$

where  $k$  = thermal conductivity,  $V$  = volume,  $T$  = temperature,  $x$  = dimension in direction of the oxide through thickness,  $I$  = current,  $R$  = overall resistance.

The oxide was assumed to be dense, stoichiometric and adherent in this initial approximation so that thermal boundary conductance could be neglected. In addition, heat transfer via radiation from the surface and convection due to gas flow was also neglected for this estimate. Oxide thickness was taken to be 30  $\mu m$  per side. The electrical resistivity value for polycrystalline hot-pressed  $ZrB_2$  was extrapolated from values in literature<sup>195</sup> and was found to be  $2.5 \times 10^{-5} \Omega cm$  at 1700°C. The electrical resistivity for  $ZrO_2$  was estimated to be 2.64  $\Omega cm$  also based on the literature value<sup>196</sup> for the yttria-stabilized zirconia (YSZ) with the lowest yttria content (7 mol%) in that study at 1500K. It is readily apparent from Equation 5.2 that the current flowing through the oxide will be insignificant based on the relative resistivities of  $ZrO_2$  and  $ZrB_2$ , indicating that the electrical resistivity of  $ZrO_2$  layer is not a significant consideration

in the calculation of the overall resistivity,  $R$ . Most of the electrical power, or the second term in the energy balance equation is generated in the boride and is dissipated via heat. It was assumed that the entirety of the boride region was isothermal, so that this power is available and present to contribute to the heat flux at the oxide/substrate interface.

It was further assumed that the heat flux in the direction from the oxide/substrate interface to the oxide/gas interface dominates in the system. This is not unreasonable, given that gas is flowing across the oxide/gas interface at  $\sim 5.9$  cm/s. Linearizing the energy balance equation allows the estimation of  $\Delta T$ , or  $T_{\text{measured}} - T_{\text{interface}}$ . The thermal conductivity of yttria stabilized  $\text{ZrO}_2$  was estimated from literature<sup>197-199</sup> to range mostly from  $1.5$  to  $3 \text{ W m}^{-1} \text{ K}^{-1}$  in various studies looking at porosity effects, yttria content or synthesis method; atmospheric plasma sprayed YSZ was closer to  $1 \text{ W m}^{-1} \text{ K}^{-1}$ . The value of  $2.17 \text{ W m}^{-1} \text{ K}^{-1}$  for fully dense 8 mol% YSZ (at highest temperature measured, 1273K) was chosen to be as consistent as possible with the case chosen from the literature for electrical resistivity. However, this value is also similar to 3 mol% YSZ with 19% porosity. The thermal conductivity values for monoclinic  $\text{ZrO}_2$  are closer to  $4 \text{ W m}^{-1} \text{ K}^{-1}$ ,<sup>197</sup> indicating that this is a conservative estimate. Equation (5.2) was solved for  $\Delta T$ ; it does not require the specification of a test temperature, although the electrical resistivity value of  $\text{ZrB}_2$  at  $1700^\circ\text{C}$  was used. These preliminary calculations yield  $\Delta T$  to be  $\sim 20\text{K}$ , which will be compared with the more rigorous model described next.

#### 5.4. Thermal electric model of RHS specimen temperature gradients

This section was completed in collaboration with Dr. Michael Dion from Materials Research & Design (Wayne, PA). Figure 5.10 shows a flowchart of the model developed.

#### 5.4.1. Modeling work

##### *Computational fluid dynamics (CFD) analysis*

The CFD analysis uses a constant outer surface temperature and computed the total heat loss to the flowing gas. The CFD analysis was performed using US3D code<sup>200</sup> with the viscosity gradient computed using a weighted least squares viscosity model. The goal of this analysis was to obtain heat transfer coefficients as a function of specimen surface temperature. The heat transfer coefficients were used as a boundary condition in the thermal electric model (Figure 5.10). The analysis did not include radiation to the chamber walls. The effects of radiation were subtracted from the computed total heat flux before computing the heat transfer coefficients. Because radiation is not included in the CFD analysis, it must be accounted for separately in the finite element analysis.

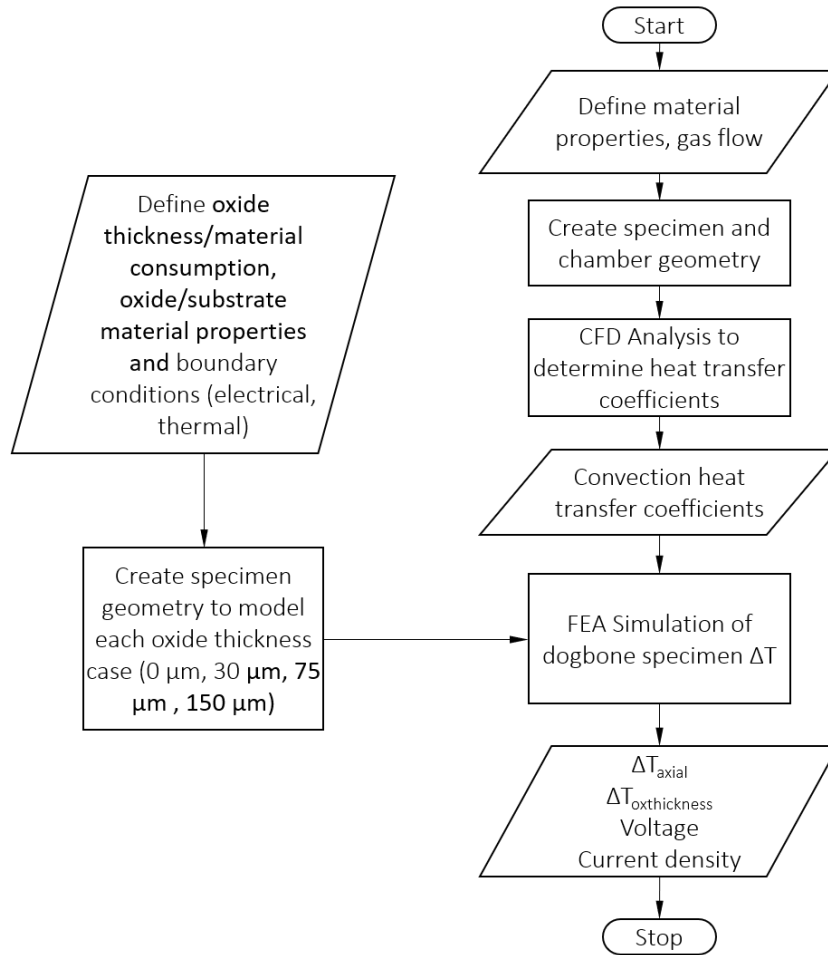


Figure 5.10: Flowchart summarizing the thermal gradients in RHS dogbone analysis process.

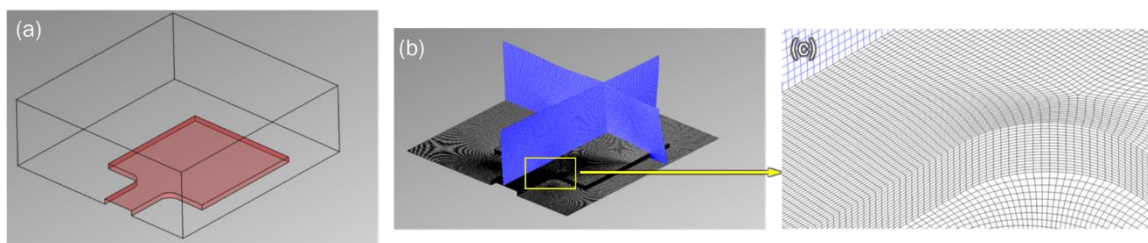


Figure 5.11: (a) Geometry of the grid used for CFD analysis, (b) smoothed grid, and (c) close-up of the smoothed grid.

Quarter symmetry of the specimen was modeled to minimize CFD computation. Link3D was used to generate topology on the specimen and then smooth the grid. The smoother showed strong signs of convergence with a residual of  $\sim 1.0$  smoothed to a residual of  $\sim 1 \times 10^{-8}$ . Calculated grid orthogonality and stretching as well as visual inspection verified a good grid was generated. CFD analysis was run on five different surface temperatures to obtain heat fluxes over the part. All four cases started with room temperature gas throughout the fluid with a velocity of 5 cm/s. The simulation was then run to find the equilibrium between the hot surface and the fluid. All simulations showed good convergence properties. Heat flux and heat transfer coefficients generated by CFD analysis are shown in Table 5.1.

*Table 5.1: Results obtained from the CFD analysis for the heat flux and transfer coefficients*

| Surface Temperature (°C) | Averaged Heat Flux (kW/m <sup>2</sup> ) | Radiation Heat Flux (kW/m <sup>2</sup> ) | Computed Heat Transfer Coefficient (W/m <sup>2</sup> -C) |
|--------------------------|---|--|--|
| 750                      | 70.85                                   | 14.35                                    | 77.61  |
| 1000                     | 147.18                                  | 45.36                                    | 104.11   |
| 1250                     | 237.12                                  | 110.74                                   | 102.91   |
| 1500                     | 374.91                                  | 229.63                                   | 98.29  |
| 2000                     | 860.24                                  | 725.76                                   | 67.99  |

#### *FEA Analysis*

ANSYS Workbench 19.0 was utilized to perform the Thermal-Electric analysis, available only as a steady-state analysis, limiting the current application to DC currents. The oxide/substrate specimens were modeled as snapshots in time, with uniform oxide thickness on the top and bottom surfaces. Based on previous laboratory tests, the oxide forms mostly in the gauge section of the specimen. Additionally, for this material system, the volume change

during the oxidation process is assumed to be insignificant, although molar volume expansion of ~14% has been reported<sup>201</sup> upon oxidation of ZrB<sub>2</sub>. Thus, in the model, oxide thickness is equal to substrate thickness loss—the outer model dimensions remain constant regardless of oxide thickness.

The finite elemental analysis uses the thermal boundary conditions computed using CFD analysis (previous section), the material properties of ZrB<sub>2</sub> and ZrO<sub>2</sub>, and oxide thickness/material consumption to compute axial and through-thickness temperature gradients for a given current. Current needs to be provided as an input in the ANSYS Thermal-Electric model. Thermal and electrical properties used in the model<sup>195,196,202,203</sup> for both ZrB<sub>2</sub> and ZrO<sub>2</sub>, assumed to be dense and polycrystalline, are summarized in Table 5.2. A temperature-dependence for ZrB<sub>2</sub> resistivity was identified in the literature<sup>195</sup>. No such relationship was identified for ZrO<sub>2</sub>. The inclusion of temperature dependent ZrB<sub>2</sub> resistivity significantly increased the solution time. To mitigate this, the models were analyzed with a single resistivity at a temperature of 1700 °C. Like the preliminary calculations, the oxide was assumed to be dense and adherent.

*Table 5.2: Values of thermal properties used for the FEA study*

| Temperature (°C) | ZrB <sub>2</sub> |   | ZrO <sub>2</sub> |                        |
|------------------|------------------|---|------------------|------------------------|
|                  | k (W/m-K)        | $\rho$ ( $\times 10^{-5}$ $\Omega$ -cm) | k (W/m-K)        | $\rho$ ( $\Omega$ -cm) |
| 23.9             | 66.34            | 0.779                                   | 1.73             | 2.64                   |
| 537.8            | 67.07            | 1.300                                   | 1.85             | 2.64                   |
| 1093.3           | 69.81            | 1.863                                   | 1.96             | 2.64                   |
| 1648.9           | 86.54            | 2.437                                   | 2.16             | 2.64                   |
| 2204.4           | 122.02           | 2.990                                   | 2.94             | 2.64                   |

The thickness of the hot zone was held constant, i.e., any oxide formation is assumed to replace the substrate without any volume change. The Joule heating was modeled in steady-state conditions to obtain “snapshots” in time. Four cases for oxide thickness were chosen: 0 $\mu$ m, 30 $\mu$ m, 75 $\mu$ m and 150 $\mu$ m, which span the range of experimental observations across the different materials tested. The surface temperature dependence on current was obtained by iterating the model for different current values.

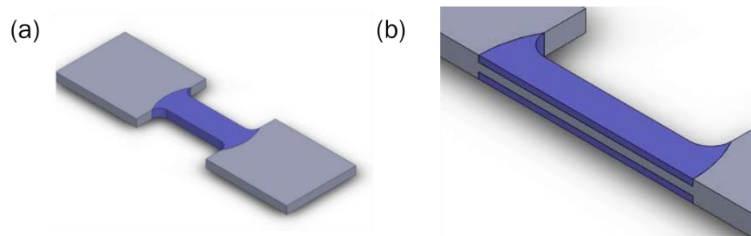


*Figure 5.12 (a) Model created and used for the FEA study. (b) Section view of the model used for the FEA study. The dark purple region indicates the oxide, gray region indicates the substrate. 150 $\mu$ m model is shown.*

The thermal boundary conditions consisted of radiation and convection. The radiation boundary condition was applied to all surfaces except the ends of the specimen where the electrical loads were applied. An emissivity of 0.8, which is expected for ZrO<sub>2</sub><sup>204</sup>, was applied to all surfaces. The convective boundary condition relied on the CFD results. The heat transfer coefficients, shown in Table 5.1 are dependent on the surface temperature of the specimen. The free gas temperature is assumed to be at room temperature, 22 °C. The electrical loads consist of an applied current and a specified voltage. The current is applied at one end of the specimen (Figure 5.13). While an alternating current is applied in the experimental set-up, the finite element is limited to direct current. The DC equivalent current (RMS) was computed by multiplying the peak AC current by  $\sqrt{2}/2$ . A voltage of 0 V, required to ground the model, was applied to the specimen as shown in Figure 5.13.

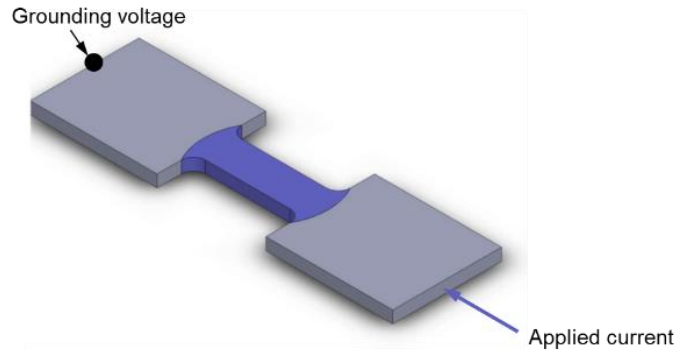


Figure 5.13: Diagram showing the locations and direction of the electrical loads

## 5.5. Results

Figure 5.14 plots the current and temperature as an example for an actual test run for  $ZrB_2$  oxidation. Table 5.3 summarizes actual temperature data collected from a series of  $ZrB_2$  oxidation tests. This table also lists material consumption, which is determined by taking half the difference of the measured thickness of the unoxidized material and the original, unoxidized cross section thickness (Figure 5.15). These data were the basis for the models that were built.

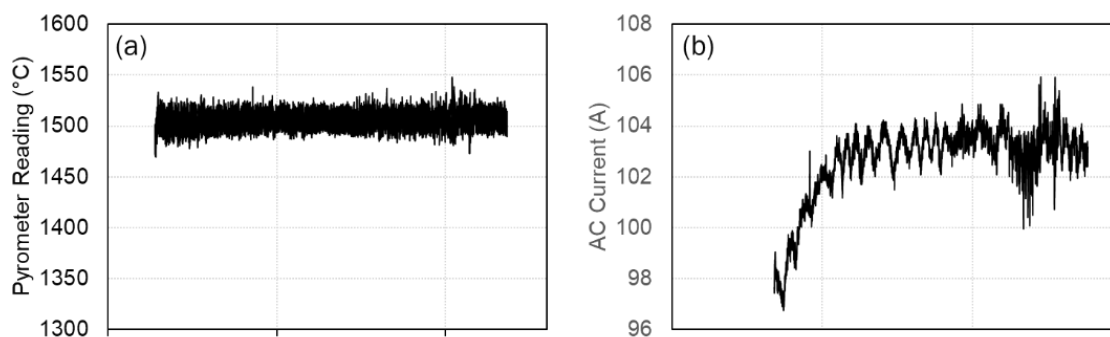


Figure 5.14: (a) Pyrometer reading of sample surface and (b) current transducer reading from lead wires, during the 15 minute "isothermal" oxidation test of  $ZrB_2$  exposed to  $0.1\%O_2$ .

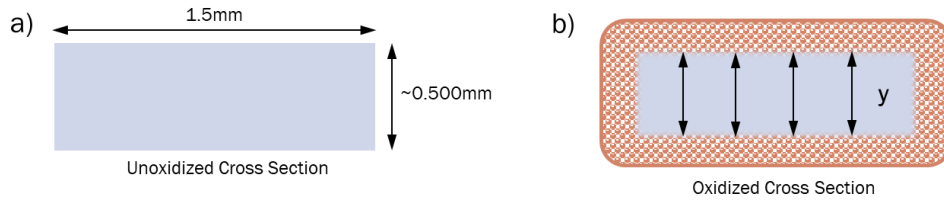


Figure 5.15: Schematic showing the cross section of the dogbone across the zone of interest (a) before oxidation, and (b) after oxidation. The solid, blue areas indicate unoxidized material, while the orange patterned areas indicate oxidized material. Material consumption is defined as half of the thickness,  $y$ , of the remaining, unoxidized material subtracted from the original thickness.

Table 5.3: Actual material consumption observed on  $ZrB_2$  tested in the resistive heating system.

| Sample                    | Average T (°C) | Standard Dev. (°C) | Exposure Time (min) | Consumption (μm) | Standard Dev. (μm) |
|---------------------------|----------------|--------------------|---------------------|------------------|--------------------|
| ZrB <sub>2</sub> -18B DB5 | 1504           | 12                 | 15                  | 21               | 5.0                |
| ZrB <sub>2</sub> -18B DB6 | 1697           | 46                 | 15                  | 19               | 2.5                |
| ZrB <sub>2</sub> -18B DB7 | 1803           | 99                 | 15                  | 14               | 2.6                |
| ZrB <sub>2</sub> -18B DB2 | 1701           | 35                 | 5                   | 61               | 2.8                |

Figure 5.16 shows the morphology of the oxidized region on a sample tested at 1504 °C for 15 minutes. The oxide that forms is mostly dense, with some porosity on the surface. The oxide is adherent, and the thickness is similar to the estimated material consumed as shown in Table 5.3.

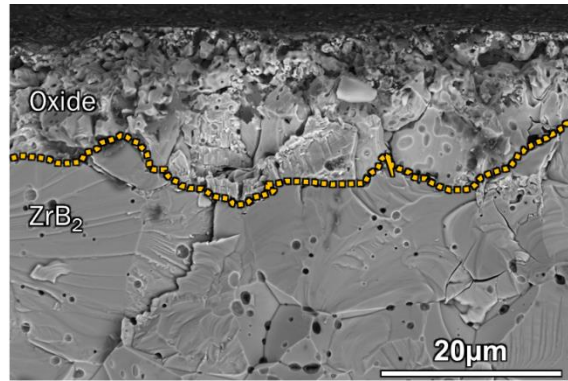


Figure 5.16: Combined backscattered electron and secondary electron image of the fracture cross section of an oxidized  $ZrB_2$  specimen ( $ZrB_2$ -18B DB5), after exposure to 0.1% $O_2$  for 15 minutes at a nominal temperature of 1500 °C.

Figure 5.17 shows an example of the results of the temperature distributions calculated using the simulation, for the case of a 30 $\mu$ m oxide at a surface temperature of 1500 °C. The resulting temperature distributions and gradients could explain any variations in oxidation behavior along the axis of the dogbone, as seen in Figure 5.7.

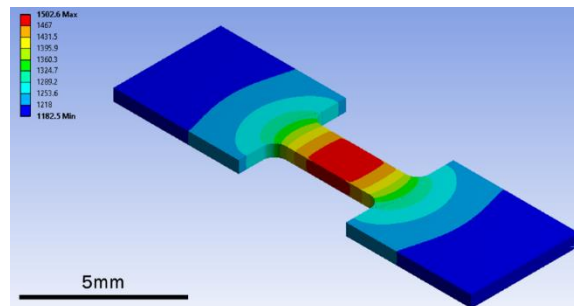


Figure 5.17: Example simulation result for the case of  $ZrB_2$  with a 30 $\mu$ m oxide/material consumption at 1500 °C.

Figure 5.18 shows the surface and oxide-substrate interface temperature results for currents ranging from 60 to 150A calculated in 10A increments. These plots were then used to interpolate the current values for the nominal surface temperatures of 1500 °C, 1700 °C

and 1800 °C for each oxide thickness. Using these interpolated current values as inputs for each target surface temperature and oxide thickness, the model was used to then calculate the axial and through thickness temperature gradients for these conditions. The current values and resultant gradients are shown in Figure 5.19.

Each discrete oxide thickness modeled can be considered as snapshots in time. From the results shown in Figure 5.19, an understanding of the temperature gradients through the oxide thickness can be determined as a function of oxide thickness, i.e., as the oxide “grows”. The current required to maintain the surface temperature at the target test temperature are plotted as a function of oxide thickness in Figure 5.20 (a). The  $\Delta T$  through the oxide thickness for the currents required to maintain nominal surface temperatures of 1500°, 1700° and 1800 °C, respectively, are plotted in Figure 5.20 (b). These show that the temperature differential grows on the order of 0.3-0.4 °C per  $\mu\text{m}$  of oxide thickness in the temperature regime of interest. While a drop in current is calculated and expected, Figure 5.14 shows that for oxidation experiments on  $\text{ZrB}_2$ , a small current increase is seen at the beginning, but which then stays relatively constant during the test duration.

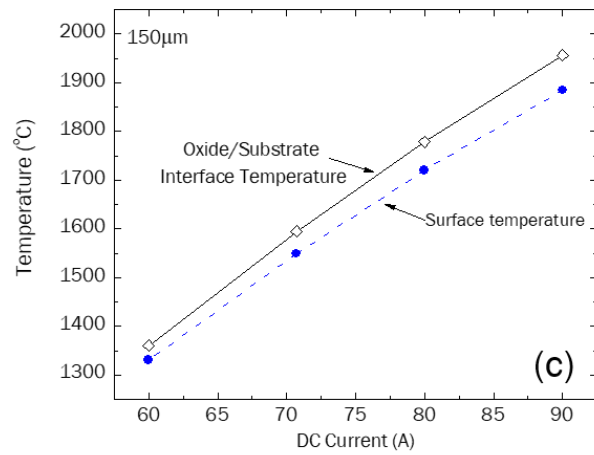
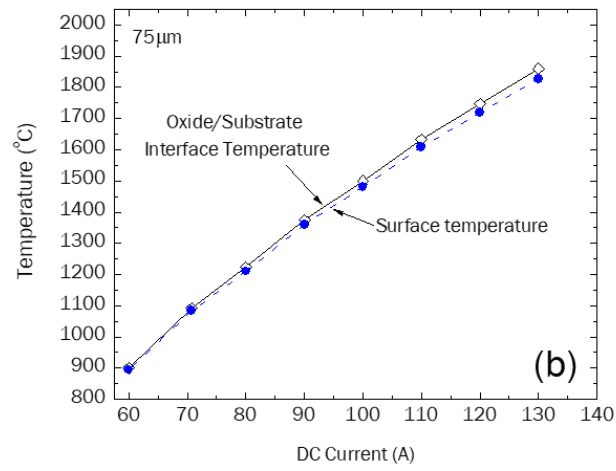
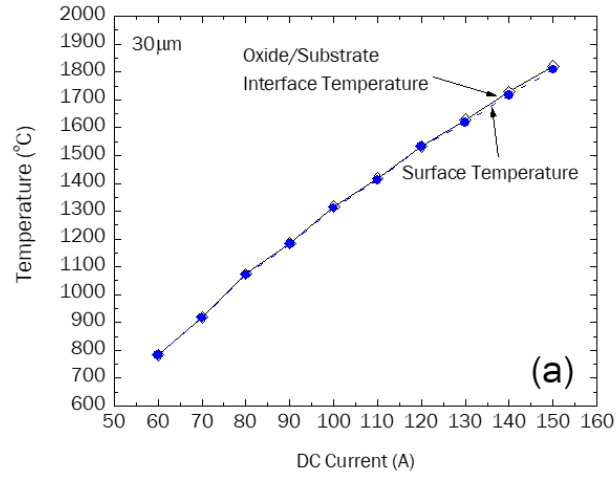


Figure 5.18: Surface and oxide/substrate interface temperatures obtained from the model for (a) 30  $\mu\text{m}$  oxide thickness (or 30  $\mu\text{m}$  material consumption), (b) 75  $\mu\text{m}$  and (c) 150  $\mu\text{m}$ .

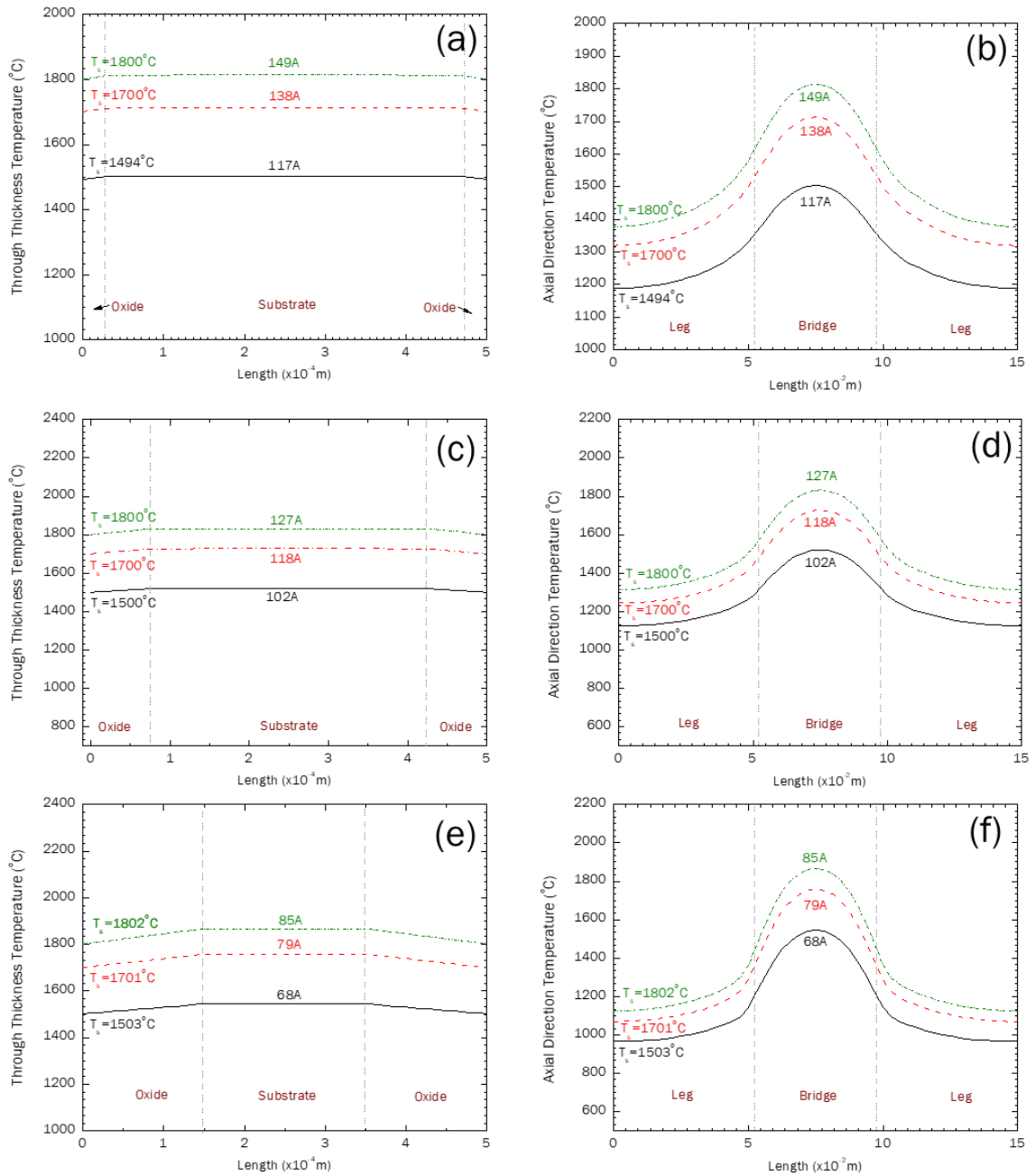


Figure 5.19: Temperature gradients through the thickness of the gauge section and axial length, respectively for (a-b) 30 μm oxide thickness (or 30μm material consumption), (c-d) 75 μm and (e-f) 150 μm.

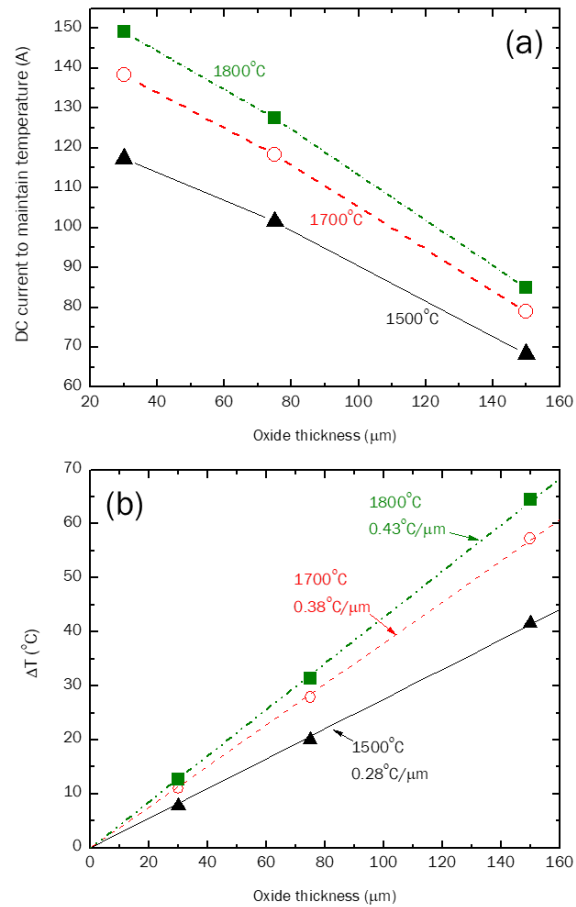


Figure 5.20: (a) Current variation as the oxide thickness grows to maintain the given surface temperatures (1500°C, 1700°C, 1800°C), (b) temperature differential through the oxide thickness as a function of oxide thickness. Lines shown in (b) are best fit lines.

### Current density

The simulation also allows the determination of current densities in the regions of interest. This parameter is of interest as electromigration, i.e., ion displacement and mass transport, can occur as a result of high current densities ( $>10^8 \text{ A/m}^2$ )<sup>205</sup>. Results for the two extreme cases under consideration, i.e. 1500°C for 30μm and 1800°C for 150μm, are presented in Figure 5.21. The calculated current densities are highest in the substrate, on the order of  $10^8 \text{ A/m}^2$ . The current density in the oxide is  $\sim 60\text{-}70 \text{ A/cm}^2$ .

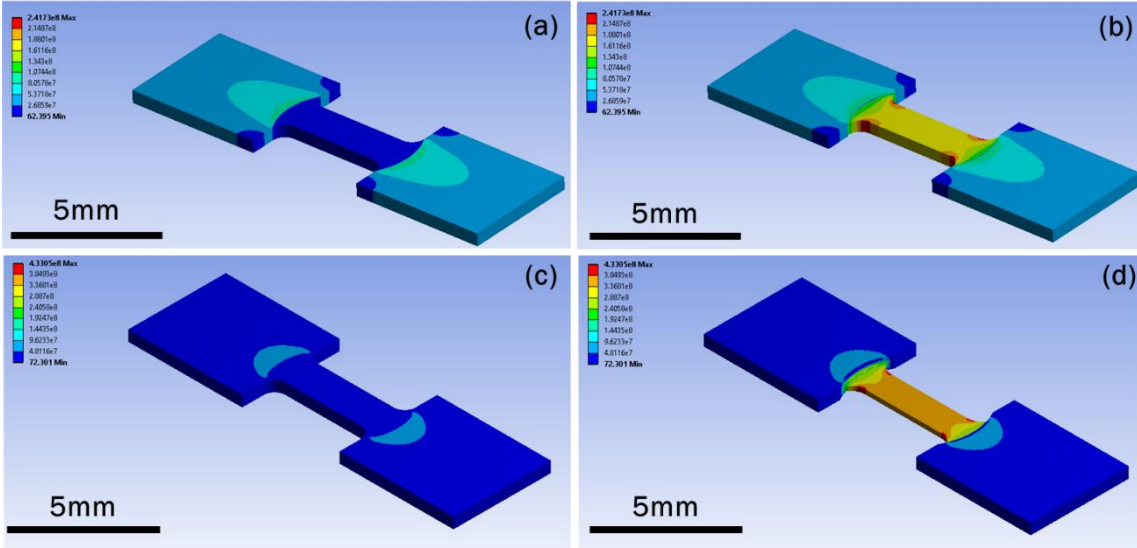


Figure 5.21: Total current density ( $A/m^2$ ) for sample with:  $30 \mu m$  oxide thickness at  $1500^\circ C$  (a) with the oxide visible, (b) oxide hidden to show the current density distribution in the substrate; and for a sample  $150 \mu m$  oxide thickness at  $1800^\circ C$  (c) with the oxide visible, (d) oxide hidden to show the current density distribution in the substrate.

## 5.6. Discussion

The simulations are based on similar material assumptions as the preliminary analytical calculations but considered heat transfer to the chamber and to the gas during the experiment and convective cooling. Nevertheless, these simulations provide results that are on the same order of magnitude as Equation (5.2).

The current dependence on the oxide thickness confirms that most of the current is conducted through the base material (diboride in this case), and such a dependence can be used to monitor the extent of oxidation observed during the test. The current density results confirm that the highest current densities are observed in the base material. This is advantageous as many oxides can have ionic character; the very small current densities preclude the possibility of ion displacement due to high currents. The current densities in the base material are on the order of  $10^8 A/m^2$ . Current densities higher than this are needed to

result in mass transport, as discussed by Tu et al.<sup>205</sup> Shugart et al.<sup>159</sup> compared the morphology of ZrB<sub>2</sub>-SiC exposed to oxidizing conditions in the box furnace and the resistive heating system for exposures at 1500 °C for 20 minutes. No artifacts in the oxide composition and morphology were observed in the samples tested in the RHS relative to those tested in the box furnace.

The lateral hot zone, as shown by the axial plots (Figure 5.19 (b), (d) and (f)) are expected to be within the pyrometer sighting zone of 1.5mm. Taking the case of the 75µm oxide at a surface temperature of 1800 °C, the zone of 1800 °C±10 °C is approximately 1.97mm in length. This hot zone decreases negligibly with increasing temperature and oxide thickness, with the worst case (among those calculated) being 1.9mm in length for the 150µm case at a surface temperature of 1802 °C.

The results show that the temperature differentials through the oxide thickness are generally on the order of the standard deviation in temperature measurement and the uncertainty of pyrometer reading for typical oxide thicknesses observed (Table 5.3). The  $\Delta T$  through the oxide thickness increases as a function of test temperature. The maximum differential was obtained in the extreme case of 150µm and 1800 °C surface temperature, where  $\Delta T=65$  °C. The highest material consumption for ZrB<sub>2</sub> in the tests conducted was 61 µm, well below 150µm. Tests conducted on ZrB<sub>2</sub>-SiC exhibited oxide thicknesses on the order of 18.1 µm (combined borosilicate and ZrO<sub>2</sub> layer thicknesses)<sup>159</sup>. Most material consumption values for ultra-high temperature carbide or boride ceramics observed were below 100µm. The highest material consumption observed thus far was on the order of 125 µm for (HfZrTiTaNb)C tested in 1%O<sub>2</sub> for 5 minutes at 1700 °C (Figure 5.7), as discussed in Chapter 3; however, much of the oxidized region consisted of intergranular oxidation<sup>206</sup>, instead of a dense 125µm scale (also discussed in Chapters 2 and 3).

## 5.7. Conclusions

The models developed and presented confirm that the through oxide temperature differentials are on the order of the standard deviation in measured temperatures for most observed conditions, and the RHS is therefore a viable method to test UHTC for oxidation resistance. Further, the study outlined above can be used to account for these differentials, and more rigorously define the experimental conditions such that the target test temperature occurs at the oxide/substrate interface. These models provide an understanding of the temperature ranges to be considered when evaluating temperature dependencies. Finally, consideration of calculated current densities even in the extreme cases suggest that mass transport via electromigration is not expected to occur.

The simulations conducted in this study provide an important understanding of the temperature gradients observed in using resistive heating to conduct oxidation experiments. These results will enable precise tailoring of the experimental conditions required to conduct these oxidation experiments. They further confirm that the temperature differences between oxide and reaction interface are on the order of the other uncertainties inherent in this technique. The advantages of conducting oxidation experiments in the RHS, on the other hand, are numerous, including a hot zone free of contamination and controlled experimental environments. Therefore, the use of resistive heating is a valid method to conduct oxidation experiments on UHTCs.

## 6. References

1. Opeka, M. M., Talmy, I. G. & Zaykoski, J. A. Oxidation-based materials selection for 2000°C + hypersonic aerosurfaces: Theoretical considerations and historical experience. *J. Mater. Sci.* **39**, 5887–5904 (2004).
2. Wuchina, E., Opila, E., Opeka, M., Fahrenholtz, W. & Talmy, I. UHTCs: ultra-high temperature ceramic materials for extreme environment applications. *Electrochem. Soc. Interface* **16**, 30 (2007).
3. Squire, T. H. & Marschall, J. Material property requirements for analysis and design of UHTC components in hypersonic applications. *J. Eur. Ceram. Soc.* **30**, 2239–2251 (2010).
4. Paul, A. *et al.* UHTC composites for hypersonic applications. (2012).
5. Monteverde, F., Savino, R., Fumo, M. D. S. & Di Maso, A. Plasma wind tunnel testing of ultra-high temperature ZrB<sub>2</sub>–SiC composites under hypersonic re-entry conditions. *J. Eur. Ceram. Soc.* **30**, 2313–2321 (2010).
6. Mungiguerra, S. *et al.* Ultra-High-Temperature Ceramic Matrix Composites in Hybrid Rocket Propulsion Environment. in (American Institute of Aeronautics and Astronautics, 2018).
7. Levine, S. R. S., Singh, M. & Opila, E. J. Robust UHTC for Sharp Leading Edge Applications. (2003).
8. Parthasarathy, T. A., Rapp, R. A., Opeka, M. & Kerans, R. J. A model for the oxidation of ZrB<sub>2</sub>, HfB<sub>2</sub> and TiB<sub>2</sub>. *Acta Mater.* **55**, 5999–6010 (2007).
9. Shimada, S., Nakajima, K. & Inagaki, M. Oxidation of Single Crystals of Hafnium Carbide in a Temperature Range of 600° to 900°C. *J. Am. Ceram. Soc.* **80**, 1749–1756 (1997).
10. Bargeron, C. B., Benson, R. C., Jette, A. N. & Phillips, T. E. Oxidation of Hafnium Carbide in the Temperature Range 1400° to 2060°C. *J. Am. Ceram. Soc.* **76**, 1040–1046 (1993).

11. Yeh, J.-W. Alloy Design Strategies and Future Trends in High-Entropy Alloys. *JOM* **65**, 1759–1771 (2013).
12. Miracle, D. B. High-Entropy Alloys: A Current Evaluation of Founding Ideas and Core Effects and Exploring “Nonlinear Alloys”. *JOM* 1–7 (2017).
13. Rost, C. M. *et al.* Entropy-stabilized oxides. *Nat. Commun.* **6**, (2015).
14. Castle, E., Csanádi, T., Grasso, S., Dusza, J. & Reece, M. Processing and Properties of High-Entropy Ultra-High Temperature Carbides. *Sci. Rep.* **8**, 8609 (2018).
15. Gild, J. *et al.* High-Entropy Metal Diborides: A New Class of High-Entropy Materials and a New Type of Ultrahigh Temperature Ceramics. *Sci. Rep.* **6**, (2016).
16. Alling, B., Högborg, H., Armiento, R., Rosen, J. & Hultman, L. A theoretical investigation of mixing thermodynamics, age-hardening potential, and electronic structure of ternary  $M_{11-x}M_2x$  $B_2$  alloys with  $AlB_2$  type structure. *Sci. Rep.* **5**, 9888 (2015).
17. Miracle, D. B. & Senkov, O. N. A critical review of high entropy alloys and related concepts. *Acta Mater.* **122**, 448–511 (2017).
18. Pickering, E. J. & Jones, N. G. High-entropy alloys: a critical assessment of their founding principles and future prospects. *Int. Mater. Rev.* **61**, 183–202 (2016).
19. Zhang, Y. *et al.* Microstructures and properties of high-entropy alloys. *Prog. Mater. Sci.* **61**, 1–93 (2014).
20. Rost, C. M., Rak, Z., Brenner, D. W. & Maria, J.-P. Local structure of the  $Mg_xNi_xCo_xCu_xZn_xO$  ( $x=0.2$ ) entropy-stabilized oxide: An EXAFS study. *J. Am. Ceram. Soc.* **100**, 2732–2738 (2017).
21. Schön, C. G., Duong, T., Wang, Y. & Arróyave, R. Probing the entropy hypothesis in highly concentrated alloys. *Acta Mater.* **148**, 263–279 (2018).
22. Gorr, B. *et al.* Phase equilibria, microstructure, and high temperature oxidation resistance of novel refractory high-entropy alloys. *J. Alloys Compd.* **624**, 270–278 (2015).

23. Sims, C. T. A History of Superalloy Metallurgy for Superalloy Metallurgists. in *Superalloys 1984 (Fifth International Symposium)* 399–419 (TMS, 1984).
24. Young, D. J. *High Temperature Oxidation and Corrosion of Metals*. (Elsevier, 2008).
25. Ellingham, H. J. T. Reducibility of oxides and sulfides in metallurgical processes. *J Soc Chem Ind* **63**, 125–133 (1944).
26. Gleeson, B. 1.09 Thermodynamics and Theory of External and Internal Oxidation of Alloys. *Shreirs Corros.* 182–184 (2010).
27. Birks, N., Meier, G. H. & Pettit, F. S. *Introduction to the High Temperature Oxidation of Metals*. (Cambridge University Press, 2006).
28. Gorr, B. *et al.* High-Temperature Oxidation Behavior of Refractory High-Entropy Alloys: Effect of Alloy Composition. *Oxid. Met.* 1–11 (2017).
29. Senkov, O. N., Wilks, G. B., Miracle, D. B., Chuang, C. P. & Liaw, P. K. Refractory high-entropy alloys. *Intermetallics* **18**, 1758–1765 (2010).
30. C. W. Bale, E. Bélisle, P. Chartrand, S. A. Deckerov, G. Eriksson, K. Hack, I. H. Jung, Y. B. Kang, J. Melançon, A. D. Pelton, C. Robelin and S. Petersen, FactSage Thermochemical Software and Databases - Recent Developments, Calphad, vol. 33, pp 295-311, 2009.
31. Smeltzer, W. W. & Young, D. J. Oxidation properties of transition metals. *Prog. Solid State Chem.* **10**, 17–54 (1975).
32. Pujilaksono, B., Jonsson, T., Halvarsson, M., Svensson, J.-E. & Johansson, L.-G. Oxidation of iron at 400–600 °C in dry and wet O<sub>2</sub>. *Corros. Sci.* **52**, 1560–1569 (2010).
33. Yurek, G. J., Hirth, J. P. & Rapp, R. A. The formation of two-phase layered scales on pure metals. *Oxid. Met.* **8**, 265–281.
34. Wagner, C. Contribution to the Theory of Formation of Oxidation Films. *Z Phys Chem B* **21**, 25 (1933).

35. Kofstad, P. High-temperature oxidation of titanium. *J. Common Met.* **12**, 449–464 (1967).
36. Chen, R. Y. & Yeun, W. Y. D. Review of the High-Temperature Oxidation of Iron and Carbon Steels in Air or Oxygen. *Oxid. Met.* **59**, 433–468 (2003).
37. Kofstad, P. *High temperature corrosion*. (Elsevier Applied Science ; Sole distributor in the USA and Canada, Elsevier Science Pub. Co., 1988).
38. Wallwork, G. R. & Jenkins, A. E. Oxidation of Titanium, Zirconium, and Hafnium. *J. Electrochem. Soc.* **106**, 10–14 (1959).
39. Kofstad, P. & Espevik, S. Kinetic study of high-temperature oxidation of hafnium. *J. Common Met.* **12**, 382–394 (1967).
40. Belle, J. & Mallett, M. W. Kinetics of the High Temperature Oxidation of Zirconium. *J. Electrochem. Soc.* **101**, 339–342 (1954).
41. Cubicciotti, D. The Oxidation of Zirconium at High Temperatures. *J. Am. Chem. Soc.* **72**, 4138–4141 (1950).
42. Kofstad, P., Anderson, P. B. & Krudtaa, O. J. Oxidation of titanium in the temperature range 800–1200°C. *J. Common Met.* **3**, 89–97 (1961).
43. Poland, D. E., Kuriakose, A. K. & Margrave, J. L. The Oxidation of Titanium Monoxide at High Temperatures. *J. Phys. Chem.* **69**, 158–160 (1965).
44. Gulbransen, E. A. Thermochemistry and the Oxidation of Refractory Metals at High Temperature. *CORROSION* **26**, 19–28 (1970).
45. Kubaschewski, O. & Hopkins, B. E. Oxidation mechanisms of niobium, tantalum, molybdenum and tungsten. *J. Common Met.* **2**, 172–180 (1960).
46. Clenny, J. T. & Rosa, C. J. Oxidation kinetics of niobium in the temperature range of 873 to 1083 K. *Metall. Trans. A* **11**, 1385–1389 (1980).
47. Stringer, J. The vanadium-oxygen system—a review. *J. Common Met.* **8**, 1–14 (1965).

48. Price, W. R. & Stringer, J. The oxidation of vanadium at high temperatures. *J. Common Met.* **8**, 165–185 (1965).
49. Price, W. R. & Stringer, J. Oxidation of Vanadium in the Liquid Oxide Region. *Nature* **212**, 1356–1356 (1966).
50. Mukherjee, A. & Wach, S. P. Kinetics of the oxidation of vanadium in the temperature range 350–950°C. *J. Common Met.* **92**, 289–300 (1983).
51. Mukherjee, A. & Wach, S. P. An investigation of the kinetics and stability of VO<sub>2</sub>. *J. Common Met.* **132**, 107–113 (1987).
52. Westman, S. On the lower oxides of vanadium. *Acta Chem Scand.* **17**, 749–752 (1963).
53. Bartlett, R. W. Molybdenum Oxidation Kinetics at High Temperatures. *J. Electrochem. Soc.* **112**, 744–746 (1965).
54. Gulbransen, E. A., Andrew, K. F. & Brassart, F. A. Oxidation of Molybdenum 550° to 1700°C. *J. Electrochem. Soc.* **110**, 952–959 (1963).
55. Berkowitz-Mattuck, J. B., Büchler, A., Engelke, J. L. & Goldstein, S. N. Mass-Spectrometric Investigation of the Oxidation of Molybdenum and Tungsten. *J. Chem. Phys.* **39**, 2722–2730 (1963).
56. Rosner, D. E. & Allendorf, H. D. Kinetics of High-Temperature Oxidation of Molybdenum by Dissociated Oxygen. *J. Chem. Phys.* **40**, 3441–3442 (1964).
57. Jones, E. S., Mosher, Capt. J. F., Speiser, R. & Spretnak, J. W. The Oxidation of Molybdenum. *Corrosion* **14**, 20–26 (1958).
58. Peterson, R. C. & Fassell, W. M. *High Pressure Oxidation of Metals. Molybdenum in Oxygen.* (1954).
59. Gulbransen, E. A. & Andrew, K. F. Kinetics of the Oxidation of Pure Tungsten from 500° to 1300°C. *J. Electrochem. Soc.* **107**, 619–628 (1960).

60. Gulbransen, E. A., Andrew, K. F. & Brassart, F. A. Kinetics of Oxidation of Pure Tungsten, 1150°–1615°C. *J. Electrochem. Soc.* **111**, 103–109 (1964).
61. Harvey, F. J. High temperature oxidation of tungsten wires in O<sub>2</sub>-Ar mixtures. *Metall. Trans.* **4**, 1513–1517 (1973).
62. Sikka, V. K. & Rosa, C. J. The oxidation kinetics of tungsten and the determination of oxygen diffusion coefficient in tungsten trioxide. *Corros. Sci.* **20**, 1201–1219 (1980).
63. Schissel, P. O. & Trulson, O. C. Mass-Spectrometric Study of the Oxidation of Tungsten. *J. Chem. Phys.* **43**, 737–743 (1965).
64. Kellett, E. A. & Rogers, S. E. The Structure of Oxide Layers on Tungsten. *J. Electrochem. Soc.* **110**, 502–504 (1963).
65. Webb, W. W., Norton, J. T. & Wagner, C. Oxidation of Tungsten. *J. Electrochem. Soc.* **103**, 107–111 (1956).
66. Courtright, E. L. Engineering Property Limitations of Structural Ceramics and Ceramic Composites Above 1600°C. in *Proceedings of the 15th Annual Conference on Composites and Advanced Ceramic Materials: Ceramic Engineering and Science Proceedings 1725–1744* (Wiley-Blackwell, 2008).
67. Courtright, E. L., Graham, H. C., Katz, A. P. & Kerans, R. J. Ultrahigh Temperature Assessment Study: Ceramic Matrix Composites. Final report (Report number: ADA262740). Battelle Pacific Northwest Labs., Air Force Wright Laboratory, Richland, WA (1992).
68. Rosa, C. J. Oxidation of zirconium—A critical review of literature. *J. Common Met.* **16**, 173–201 (1968).
69. Haul, R. & Dümbgen, G. Sauerstoff-selbstdiffusion in Rutilkristallen. *J. Phys. Chem. Solids* **26**, 1–10 (1965).

70. Kapoor, R. & Oyama, S. T. Measurement of solid state diffusion coefficients by a temperature-programmed method. *J. Mater. Res.* **12**, 467–473 (1997).
71. Chen, W. K. & Jackson, R. A. Diffusion of Oxygen in Near-Stoichiometric  $\alpha$ -Nb<sub>2</sub>O<sub>5</sub>. *J. Chem. Phys.* **47**, 1144–1148 (1967).
72. Giber, J. & Oechsner, H. Dissolution of anodic Ta<sub>2</sub>O<sub>5</sub> layers into polycrystalline tantalum. *Thin Solid Films* **131**, 279–287 (1985).
73. Stroud, J. E., Tripp, W. C. & Wimmer, J. M. Defect Structure of Ta<sub>2</sub>O<sub>5</sub>. *J. Am. Ceram. Soc.* **57**, 172–175 (1974).
74. Chandrasekharan, R., Park, I., Masel, R. I. & Shannon, M. A. Thermal oxidation of tantalum films at various oxidation states from 300 to 700°C. *J. Appl. Phys.* **98**, 114908 (2005).
75. Roth, R. S. & Coughanour, L. W. Phase equilibrium relations in the systems titania-niobia and zirconia-niobia. *J. Res. Natl. Bur. Stand.* **55**, 209 (1955).
76. McCormack, S. J. *et al.* In-situ determination of the HfO<sub>2</sub>–Ta<sub>2</sub>O<sub>5</sub>-temperature phase diagram up to 3000°C. *J. Am. Ceram. Soc.* **102**, 4848–4861 (2019).
77. Rosa, C. J. Oxygen diffusion in alpha and beta titanium in the temperature range of 932° to 1142°C. *Metall. Trans.* **1**, 2517–2522 (1970).
78. Coutures, J. P. & Coutures, J. The System HfO<sub>2</sub>-TiO<sub>2</sub>. *J. Am. Ceram. Soc.* **70**, 383–387 (1987).
79. Noguchi, T. & Mizuno, M. Phase Changes in the ZrO<sub>2</sub>-TiO<sub>2</sub> System. *Bull. Chem. Soc. Jpn.* **41**, 2895–2899 (1968).
80. Maister, I. *et al.* Reaction in the System HfO<sub>2</sub>-ZrO<sub>2</sub>-TiO<sub>2</sub> at 1300-2800°C. *Inorg Mater* **26**, 847–850 (1990).
81. McHale, A. E. & Roth, R. S. Investigation of the Phase Transition in ZrTiO<sub>4</sub> and ZrTiO<sub>4</sub>-SnO<sub>2</sub> Solid Solutions. *J. Am. Ceram. Soc.* **66**, C-18-C-20 (1983).

82. Magunov, R. L., Sotulo, V. S. & Magunov, I. R. Phase ratios in  $ZrO_2(HfO_2)$ - $Nb_2O_5$  systems. *Zhurnal Neorganicheskoy Khimii* **38**, 363–365 (1993).
83. Jongejan, A. & Wilkins, A. A re-examination of the system  $Nb_2O_5$ - $TiO_2$  at liquidus temperatures. *Journal of the Less Common Metals* **19**, 185–191 (1969).
84. Waring, J. L. & Roth, R. S. Effect of oxide additions on polymorphism of tantalum pentoxide (system  $Ta_2O_5$ - $TiO_2$ ). *J. Res. Natl. Bur. Stand. Sect. Phys. Chem.* **72A**, 175 (1968).
85. Roth, R. & Waring, J. Effect of oxide additions on the polymorphism of tantalum pentoxide III. Stabilization of the low temperature structure type. *J Res Natl. Bur. Stand.- Phys. Chem.* 485–493 (1970).
86. Holtzberg, F. & Reisman, A. SUB-SOLIDUS EQUILIBRIA IN THE SYSTEM  $Nb_2O_5$  - $Ta_2O_5$  . *J. Phys. Chem.* **65**, 1192–1196 (1961).
87. Cirilli, V., Burdese, A. & Brisi, C. Atti Accad. Sci. Torino, Cl. *Sci Fis Mat Nat* **95**, 197–228 (1961).
88. Waring, J. & Roth, R. Phase equilibria in the system vanadium oxide-niobium oxide. *J Res Natl Bur Std* **69**, (1965).
89. Roth, R. S., Waring, J. L. & Brower, W. S. Effect of oxide additions on the polymorphism of tantalum pentoxide. II. “Stabilization” of the high temperature structure type. *J. Res. Natl. Bur. Stand. Sect. Phys. Chem.* **74A**, 477 (1970).
90. Schadow, H., Oppermann, H. & Wehner, B. Investigations on the Quasi-binary System  $V_2O_5$ - $Ta_2O_5$ . *Crystal Research and Technology* **27**, 691–695 (1992).
91. Chang, L. L., Scroger, M. & Phillips, B. Condensed phase relations in the systems  $ZrO_2$ - $WO_2$ - $WO_3$  and  $HfO_2$ - $WO_2$ - $WO_3$ . *J. Am. Ceram. Soc.* **50**, 211–215 (1967).
92. Zhang, S. C., Hilmas, G. E. & Fahrenholtz, W. G. Improved Oxidation Resistance of Zirconium Diboride by Tungsten Carbide Additions. *J. Am. Ceram. Soc.* **91**, 3530–3535 (2008).

93. Silvestroni, L., Sciti, D., Monteverde, F., Stricker, K. & Kleebe, H.-J. Microstructure evolution of a W-doped ZrB<sub>2</sub> ceramic upon high-temperature oxidation. *J. Am. Ceram. Soc.* **100**, 1760–1772 (2017).
94. Gorr, B. et al. High temperature oxidation behavior of an equimolar refractory metal-based alloy 20Nb20Mo20Cr20Ti20Al with and without Si addition. *J. Alloys Compd.* **688**, 468–477 (2016).
95. Butler, T. M., Chaput, K. J., Dietrich, J. R. & Senkov, O. N. High temperature oxidation behaviors of equimolar NbTiZrV and NbTiZrCr refractory complex concentrated alloys (RCCAs). *J. Alloys Compd.* **729**, 1004–1019 (2017).
96. Ye, B., Wen, T., Liu, D. & Chu, Y. Oxidation behavior of (Hf<sub>0.2</sub>Zr<sub>0.2</sub>Ta<sub>0.2</sub>Nb<sub>0.2</sub>Ti<sub>0.2</sub>)C high-entropy ceramics at 1073-1473 K in air. *Corros. Sci.* **153**, 327–332 (2019).
97. Backman, L. & Opila, E. J. Thermodynamic assessment of the group IV, V and VI oxides for the design of oxidation resistant multi-principal component materials. *J. Eur. Ceram. Soc.* **39**, 1796–1802 (2019).
98. Osei-Agyemang, E. & Balasubramanian, G. Surface oxidation mechanism of a refractory high-entropy alloy. *Npj Mater. Degrad.* **3**, 20 (2019).
99. Gaskell, D. R. & Laughlin, D. E. *Introduction to the Thermodynamics of Materials*. (CRC Press, 2017).
100. Simnad, M. & Spilners, A. Kinetics and Mechanism of the Oxidation of Molybdenum. *J. Met.* **Vol: 7**, (1955).
101. Brenner, S. S. Catastrophic Oxidation of Some Molybdenum-Containing Alloys. *J. Electrochem. Soc.* **102**, 16–21 (1955).
102. Murray, J. L. & Wriedt, H. A. The O–Ti (Oxygen-Titanium) system. *J. Phase Equilibria* **8**, 148–165 (1987).

103. Bellucci, A., Gozzi, D. & Latini, A. Overview of the TiC/TiO<sub>2</sub> (rutile) interface. *Solid State Ion.* **172**, 369–375 (2004).
104. Senkov, O. N., Miracle, D. B., Chaput, K. J. & Couzinie, J.-P. Development and exploration of refractory high entropy alloys—A review. *J. Mater. Res.* 1–37 (2018).
105. Hautier, G., Fischer, C. C., Jain, A., Mueller, T. & Ceder, G. Finding Nature’s Missing Ternary Oxide Compounds Using Machine Learning and Density Functional Theory. *Chem. Mater.* **22**, 3762–3767 (2010).
106. Jain, A. *et al.* Commentary: The Materials Project: A materials genome approach to accelerating materials innovation. *APL Mater.* **1**, 011002 (2013).
107. Senkov, O. N. *et al.* Microstructure and elevated temperature properties of a refractory TaNbHfZrTi alloy. *J. Mater. Sci.* **47**, 4062–4074 (2012).
108. Senkov, O. N. & Miracle, D. B. A new thermodynamic parameter to predict formation of solid solution or intermetallic phases in high entropy alloys. *J. Alloys Compd.* **658**, 603–607 (2016).
109. Senkov, O. N., Scott, J. M., Senkova, S. V., Miracle, D. B. & Woodward, C. F. Microstructure and room temperature properties of a high-entropy TaNbHfZrTi alloy. *J. Alloys Compd.* **509**, 6043–6048 (2011).
110. Gusev, A. Phase Diagrams of the Pseudo-Binary TiC--NbC, TiC--TaC, ZrC--NbC, ZrC--TaC, and HfC--TaC Carbide Systems. *Russ J Phys Chem* **59**, 336–340 (1985).
111. Adjaoud, O., Steinle-Neumann, G., Burton, B. P. & van de Walle, A. First-principles phase diagram calculations for the HfC--TiC, ZrC--TiC, and HfC--ZrC solid solutions. *Phys. Rev. B* **80**, 134112 (2009).
112. Figure numbers 08986, 09030. *Phase Equilibria Diagrams Database (NIST Standard Reference Database 31)*, The American Ceramic Society and the National Institute of Standards and Technology (2020).

113. Sarker, P. *et al.* High-entropy high-hardness metal carbides discovered by entropy descriptors. *Nat. Commun.* **9**, 1–10 (2018).
114. Fahrenholtz, W. G., Binner, J. & Zou, J. Synthesis of ultra-refractory transition metal diboride compounds. *J. Mater. Res. FirstView*, 1–16 (2016).
115. Rudy, E. *Ternary Phase Equilibria in Transition Metal-Boron-Carbon-Silicon Systems. Part 5. Compendium Of Phase Diagram Data.* (1969).
116. Witusiewicz, V. T., Bondar, A. A., Hecht, U., Rex, S. & Velikanova, T. Ya. The Al–B–Nb–Ti system: II. Thermodynamic description of the constituent ternary system B–Nb–Ti. *J. Alloys Compd.* **456**, 143–150 (2008).
117. Jacob, K. T., Shekhar, C. & Waseda, Y. An update on the thermodynamics of Ta<sub>2</sub>O<sub>5</sub>. *J. Chem. Thermodyn.* **41**, 748–753 (2009).
118. Smith, S. J. *et al.* Heat capacities and thermodynamic functions of TiO<sub>2</sub> anatase and rutile: Analysis of phase stability. *Am. Mineral.* **94**, 236–243 (2009).
119. Ranade, M. R. *et al.* Energetics of nanocrystalline TiO<sub>2</sub>. *Proc. Natl. Acad. Sci.* **99**, 6476–6481 (2002).
120. Waring, J. & Roth, R. Effect of oxide additions on the polymorphism of tantalum pentoxide (system Ta<sub>2</sub>O<sub>5</sub>-TiO<sub>2</sub>). *Journal of Research of the National Bureau of Standards. Section A, Physics and Chemistry* **72**, 175 (1968).
121. Cacciamani, G., Riani, P. & Valenza, F. Equilibrium between MB<sub>2</sub> (M=Ti,Zr,Hf) UHTC and Ni: A thermodynamic database for the B–Hf–Ni–Ti–Zr system. *World Round Robin Semin. 2010* **35**, 601–619 (2011).
122. Lin, L., Delaey, L., Wollants, P. & Van der Biest, O. Phase diagram calculation of Ti-Zr-X systems. *J. Chim. Phys.* **90**, 175–180 (1993).

123. Smith, C. J., Weinberger, C. R. & Thompson, G. B. Phase stability and microstructural formations in the niobium carbides. *J. Eur. Ceram. Soc.* **38**, 4850–4866 (2018).
124. Park, Y. & Butt, D. P. Composition Dependence of the Kinetics and Mechanisms of Thermal Oxidation of Titanium-Tantalum Alloys. *Oxid. Met.* **51**, 383–402 (1999).
125. Toher, C., Oses, C., Hicks, D. & Curtarolo, S. Unavoidable disorder and entropy in multi-component systems. *Npj Comput. Mater.* **5**, 1–3 (2019).
126. Harrington, T. J. *et al.* Phase stability and mechanical properties of novel high entropy transition metal carbides. *Acta Mater.* **166**, 271–280 (2019).
127. McCormack, S. J. & Kriven, W. M. Crystal structure solution for the A<sub>6</sub>B<sub>2</sub>O<sub>17</sub> (A = Zr, Hf; B = Nb, Ta) superstructure. *Acta Crystallogr. Sect. B Struct. Sci. Cryst. Eng. Mater.* **75**, 227–234 (2019).
128. Kharton, V. V., Yaremchenko, A. A., Naumovich, E. N. & Marques, F. M. B. Research on the electrochemistry of oxygen ion conductors in the former Soviet Union. *J. Solid State Electrochem.* **4**, 243–266 (2000).
129. Ruh, R., Garrett, H. J., Domagala, R. F. & Tallan, N. M. The System Zirconia-Hafnia. *J. Am. Ceram. Soc.* **51**, 23–28 (1968).
130. Hautier, G., Fischer, C., Ehlacher, V., Jain, A. & Ceder, G. Data Mined Ionic Substitutions for the Discovery of New Compounds. *Inorg. Chem.* **50**, 656–663 (2011).
131. Wuchina, E. J. & Opeka, M. The Group IV Carbides and Nitrides. in *Ultra-High Temperature Ceramics* 361–390 (John Wiley & Sons, Ltd, 2014).
132. Courtright, E. L., Prater, J. T., Holcomb, G. R., Pierre, G. R. St. & Rapp, R. A. Oxidation of hafnium carbide and hafnium carbide with additions of tantalum and praseodymium. *Oxid. Met.* **36**, 423–437 (1991).

133. Metcalfe, A. G. Gas Evolution During Oxidation of Refractory Borides and Carbides at 1500{degree sign}C to 2700{degree sign}C. *ECS Trans.* **3**, 131–142 (2007).
134. Müller, F. *et al.* On the oxidation mechanism of refractory high entropy alloys. *Corros. Sci.* **159**, 108161 (2019).
135. Holcomb, G. R. The high temperature oxidation of hafnium-carbide. (1988).
136. Zhang, J., Wang, S., Li, W., Yu, Y. & Jiang, J. Understanding the oxidation behavior of Ta–Hf–C ternary ceramics at high temperature. *Corros. Sci.* 108348 (2019).
137. Zhang, C. High temperature oxidation study of tantalum carbide-hafnium carbide solid solutions synthesized by spark plasma sintering. (2016).
138. Zeng, Y. *et al.* Ablation-resistant carbide  $Zr_{0.8}Ti_{0.2}C_{0.74}B_{0.26}$  for oxidizing environments up to 3,000°C. *Nat. Commun.* **8**, 15836 (2017).
139. Opila, E., Levine, S. & Lorincz, J. Oxidation of  $ZrB_2$ - and  $HfB_2$ -based ultra-high temperature ceramics: Effect of Ta additions. *J. Mater. Sci.* **39**, 5969–5977.
140. Gasparrini, C., Chater, R. J., Horlait, D., Vandeperre, L. & Lee, W. E. Zirconium carbide oxidation: Kinetics and oxygen diffusion through the intermediate layer. *J. Am. Ceram. Soc.* **101**, 2638–2652 (2018).
141. Shimada, S. & Mochidsuki, K. The oxidation of TiC in dry oxygen, wet oxygen, and water vapor. *J. Mater. Sci.* **39**, 581–586 (2004).
142. Münster, A. Über die Oxydation metallischer Hartstoffe. *Z. Für Elektrochem. Berichte Bunsenges. Für Phys. Chem.* **63**, 807–818 (1959).
143. Desmaison-Brut, M., Alexandre, N. & Desmaison, J. Comparison of the oxidation behaviour of two dense hot isostatically pressed tantalum carbide (TaC and Ta<sub>2</sub>C) Materials. *J. Eur. Ceram. Soc.* **17**, 1325–1334 (1997).

144. Gozzi, D., Montozzi, M. & Cignini, P. L. Apparent oxygen solubility in refractory carbides. *Solid State Ion.* **123**, 1–10 (1999).
145. Shimada, S. & Inagaki, M. A kinetic study on oxidation of niobium carbide. *Solid State Ion.* **63–65**, 312–317 (1993).
146. Szokefalvi-Nagy, A. & Jehn, H. High-temperature oxidation of NbC and TaC at low oxygen pressures. *Z Met.* **75**, 389–394 (1984).
147. Cole, S. S. & Taylor, N. W. The System  $\text{Na}_2\text{O}-\text{B}_2\text{O}_3$ , IV Vapor Pressures of Boric Oxide, Sodium Metaborate, and Sodium Diborate between 1150°C and 1400°C. *J. Am. Ceram. Soc.* **18**, 82–85 (1935).
148. Silvestroni, L., Guicciardi, S., Melandri, C. & Sciti, D. TaB<sub>2</sub>-based ceramics: Microstructure, mechanical properties and oxidation resistance. *J. Eur. Ceram. Soc.* **32**, 97–105 (2012).
149. Kofstad, P. Low-pressure oxidation of tantalum at 1300°–1800°C. *J. Common Met.* **7**, 241–266 (1964).
150. Jehn, H. & Olzi, E. High temperature solid-solubility limit and phase studies in the system tantalum-oxygen. *J. Common Met.* **27**, 297–309 (1972).
151. Talmy, I. G., Wuchina, E. J., Zaykoski, J. A. & Opeka, M. M. Ceramics in the System NbB<sub>2</sub> – CrB<sub>2</sub>. in *Symposium M – Ceramic Matrix Composites–Advanced High-* vol. 365 81 (1994).
152. Opila, E. J. & Halbig, M. C. Oxidation of ZrB<sub>2</sub>-SiC. in *25th Annual Conference on Composites, Advanced Ceramics, Materials, and Structures: A: Ceramic Engineering and Science Proceedings* (eds. Singh, M. & Jessen, T.) 221–228 (John Wiley & Sons, Inc., 2001).
153. Castle, E., Reece, M., Grasso, S., Csanadi, T. & Dusza, J. High entropy transition metal carbides. (2017).
154. Harrington, T. J. High Entropy Carbides: Modeling, Synthesis, and Properties. (UC San Diego, 2019).

155. Talmy, I. G., Zaykoski, J. A., Opeka, M. M. & Dallek, S. Oxidation of ZrB<sub>2</sub> ceramics modified with SiC and group IV–VI transition metal diborides. in vol. 12 144–158 (2001).
156. Lamouroux, F., Bourrat, X., Nasalain, R. & Sevely, J. Structure/oxidation behavior relationship in the carbonaceous constituents of 2D-C/PyC/SiC composites. *Carbon* **31**, 1273–1288 (1993).
157. Gild, J. *et al.* Thermal conductivity and hardness of three single-phase high-entropy metal diborides fabricated by borocarbothermal reduction and spark plasma sintering. *Ceram. Int.* (2019).
158. Karlsdottir, S. N. & Halloran, J. W. Rapid Oxidation Characterization of Ultra-High Temperature Ceramics. *J. Am. Ceram. Soc.* **90**, 3233–3238 (2007).
159. Shugart, K. & Opila, E. SiC Depletion in ZrB<sub>2</sub>–30 vol% SiC at Ultrahigh Temperatures. *J. Am. Ceram. Soc.* **98**, 1673–1683 (2015).
160. Berkowitz-Mattuck, J. B. High-Temperature Oxidation: III . Zirconium and Hafnium Diborides. *J. Electrochem. Soc.* **113**, 908–914 (1966).
161. Duwez, P. & Odell, F. Phase Relationships in the Binary Systems of Nitrides and Carbides of Zirconium, Columbium, Titanium, and Vanadium. *J. Electrochem. Soc.* **97**, 299 (1950).
162. Jongejan, A. & Wilkins, A. L. A re-examination of the system Nb<sub>2</sub>O<sub>5</sub>-TiO<sub>2</sub> at liquidus temperatures. *J. Common Met.* **19**, 185–191 (1969).
163. Oses, C. *et al.* AFLOW-CHULL: Cloud-Oriented Platform for Autonomous Phase Stability Analysis. *J. Chem. Inf. Model.* **58**, 2477–2490 (2018).
164. Fromm, E. & Spaeth, G. Co-Equilibrium Pressure of Niobium--Oxygen Solid Solutions. (1968).
165. Ono, K., Ueda, Y. & Moriyama, J. Fundamental Study on the Production of Niobium by the Carbothermic Reduction-Electron Beam Melting Combination Method. *Trans. Jpn. Inst. Met.* **21**, 319–324 (1980).

166. Kuriakose, A. K. & Margrave, J. L. The Oxidation Kinetics of Zirconium Diboride and Zirconium Carbide at High Temperatures. *J. Electrochem. Soc.* **111**, 827–831 (1964).
167. Tokuda, T., Ito, T. & Yamaguchi, T. Self Diffusion in a Glassformer Melt Oxygen Transport in Boron Trioxide. *Z. Für Naturforschung A* **26**, 2058–2060 (1971).
168. Karlsdottir, S. N., Halloran, J. W. & Grundy, A. N. Zirconia Transport by Liquid Convection during Oxidation of Zirconium Diboride–Silicon Carbide. *J. Am. Ceram. Soc.* **91**, 272–277 (2008).
169. Sciti, D., Silvestroni, L., Guicciardi, S., Fabbriche, D. D. & Bellosi, A. Processing, mechanical properties and oxidation behavior of TaC and HfC composites containing 15 vol% TaSi<sub>2</sub> or MoSi<sub>2</sub>. *J. Mater. Res.* **24**, 2056–2065 (2009).
170. Silvestroni, L. *et al.* Ablation behaviour of ultra-high temperature ceramic matrix composites: Role of MeSi<sub>2</sub> addition. *J. Eur. Ceram. Soc.* **39**, 2771–2781 (2019).
171. Sani, E., Mercatelli, L., Sans, J.-L., Silvestroni, L. & Sciti, D. Porous and dense hafnium and zirconium ultra-high temperature ceramics for solar receivers. *Opt. Mater.* **36**, 163–168 (2013).
172. Potanin, A. Yu. *et al.* High-temperature oxidation and plasma torch testing of MoSi<sub>2</sub>–HfB<sub>2</sub>–MoB ceramics with single-level and two-level structure. *Corros. Sci.* **158**, 108074 (2019).
173. Guo, S., Mizuguchi, T., Ikegami, M. & Kagawa, Y. Oxidation behavior of ZrB<sub>2</sub>–MoSi<sub>2</sub>–SiC composites in air at 1500°C. *Ceram. Int.* **37**, 585–591 (2011).
174. Sciti, D., Balbo, A. & Bellosi, A. Oxidation behaviour of a pressureless sintered HfB<sub>2</sub>–MoSi<sub>2</sub> composite. *J. Eur. Ceram. Soc.* **29**, 1809–1815 (2009).
175. Charpentier, L., Balat-Pichelin, M., Sciti, D. & Silvestroni, L. High temperature oxidation of Zr- and Hf-carbides: Influence of matrix and sintering additive. *J. Eur. Ceram. Soc.* **33**, 2867–2878 (2013).

176. Silvestroni, L., Stricker, K., Sciti, D. & Kleebe, H.-J. Understanding the oxidation behavior of a ZrB<sub>2</sub>-MoSi<sub>2</sub> composite at ultra-high temperatures. *Acta Mater.* **151**, 216–228 (2018).
177. Kazemzadeh Dehdashti, M., Fahrenholtz, W. G. & Hilmas, G. E. Effects of transition metals on the oxidation behavior of ZrB<sub>2</sub> ceramics. *Corros. Sci.* **91**, 224–231 (2015).
178. Yung, D.-L., Maaten, B., Antonov, M. & Hussainova, I. Oxidation of spark plasma sintered ZrC-Mo and ZrC-TiC composites. *Int. J. Refract. Met. Hard Mater.* **66**, 244–251 (2017).
179. Kazemzadeh Dehdashti, M., Fahrenholtz, W. G. & Hilmas, G. E. Effects of temperature and the incorporation of W on the oxidation of ZrB<sub>2</sub> ceramics. *Corros. Sci.* **80**, 221–228 (2014).
180. Carney, C. M., Parthasarathy, T. A. & Cinibulk, M. K. Oxidation Resistance of Hafnium Diboride Ceramics with Additions of Silicon Carbide and Tungsten Boride or Tungsten Carbide. *J. Am. Ceram. Soc.* **94**, 2600–2607 (2011).
181. Chang, L. L. Y., Scroger, M. G. & Phillips, B. Condensed Phase Relations in the Systems ZrO<sub>2</sub>-WO<sub>2</sub>-WO<sub>3</sub> and HfO<sub>2</sub>-WO<sub>2</sub>-WO<sub>3</sub>. *J. Am. Ceram. Soc.* **50**, 211–215 (1967).
182. Berkowitz-Mattuck, J. B. High-Temperature Oxidation: IV . Zirconium and Hafnium Carbides. *J. Electrochem. Soc.* **114**, 1030–1033 (1967).
183. Worrell, W. L. A Thermodynamic Analysis of the Cr-Co, Mo-Co, And W-Co Systems. (1964).
184. Warren, A., Nylund, A. & Olefjord, I. Oxidation of tungsten and tungsten carbide in dry and humid atmospheres. *Int. J. Refract. Met. Hard Mater.* **14**, 345–353 (1996).
185. Newkirk, A. E. The Oxidation of Tungsten Carbide. *J. Am. Chem. Soc.* **77**, 4521–4522 (1955).
186. Kurlov, A. S. & Gusev, A. I. Oxidation of tungsten carbide powders in air. *Int. J. Refract. Met. Hard Mater.* **41**, 300–307 (2013).
187. Zhang, R.-Z. & J. Reece, M. Review of high entropy ceramics: design, synthesis, structure and properties. *J. Mater. Chem. A* (2019).

188. Silvestroni, L., Mungiguerra, S., Sciti, D., Di Martino, G. D. & Savino, R. Effect of hypersonic flow chemical composition on the oxidation behavior of a super-strong UHTC. *Corros. Sci.* **159**, 108125 (2019).
189. Margrave, J. L. High-temperature chemistry. *Access Sci.* (2014).
190. Cissel, K. S. & Opila, E. Oxygen diffusion mechanisms during high-temperature oxidation of ZrB<sub>2</sub>-SiC. *J. Am. Ceram. Soc.* **101**, 1765–1779 (2018)..
191. Morris, R. A., De Leon, N. & Thompson, G. B. Thermo-mechanical testing of tantalum carbides using a Lorentz-force, non-contact technique. *J. Eur. Ceram. Soc.* **33**, 1639–1646 (2013).
192. Shugart, K. Oxidation Behavior of Zirconium Diboride Silicone Carbide Based Materials at Ultra-High Temperatures. (University of Virginia, 2014).
193. Pyrofiber Lab. The Pyrometer Instrument Company. *Inc Bergenf. N. J.*
194. Phinney, L. M., Koppers, J. D., Clemens, R. C. & Box, P. O. Thermal Conductivity Measurements of SUMMIT™ Polycrystalline Silicon. *Sandia Report SAND 7112* (2006).
195. Rahman, M., Wang, C. C., Chen, W., Akbar, S. A. & Mroz, C. Electrical Resistivity of Titanium Diboride and Zirconium Diboride. *J. Am. Ceram. Soc.* **78**, 1380–1382 (1995).
196. Dixon, J. M., LaGrange, L. D., Merten, U., Miller, C. F. & Porter, J. T. Electrical Resistivity of Stabilized Zirconia at Elevated Temperatures. *J. Electrochem. Soc.* **110**, 276 (1963).
197. Clarke, D. R. & Phillpot, S. R. Thermal barrier coating materials. *Mater. Today* **8**, 22–29 (2005).
198. Slifka, A. J., Filla, B. J., Phelps, J. M., Bancke, G. & Berndt, C. C. Thermal Conductivity of a Zirconia Thermal Barrier Coating. *J. Therm. Spray Technol.* **7**, 43–46 (1998).
199. Schlichting, K. W., Padture, N. P. & Klemens, P. G. Thermal conductivity of dense and porous yttria-stabilized zirconia. *J. Mater. Sci.* **36**, 3003–3010 (2001).

200. Candler, G. V. *et al.* Development of the US3D code for advanced compressible and reacting flow simulations. in 1893 (2015).
201. Sarin, P. *et al.* In situ studies of oxidation of ZrB<sub>2</sub> and ZrB<sub>2</sub>-SiC composites at high temperatures. *J. Eur. Ceram. Soc.* **30**, 2375–2386 (2010).
202. Lynch, J. Engineering property data on selected ceramics volume III, single oxides. *Met. Ceram. Inf. Cent. Rep. MCIC-HB-07 Columb. OH Battelle Columb. Lab.* **122**, (1981).
203. Kosolapova, T. Y. *Handbook of high temperature compounds: properties, production, applications.* (CRC Press, 1990).
204. Solonenko, O. P. *et al.* Theoretical modeling and experimental study of thermal barrier coatings. *Mater. Trans.* **44**, 2311–2321 (2003).
205. Tu, K., Mayer, J. & Feldman, L. *Electronic Thin Film Science: For Electrical Engineering and Materials.* (1996).
206. Backman, L., Gild, J., Luo, J. & Opila, E. J. Selective Oxidation in Refractory High Entropy Materials. *ArXiv190802654 Cond-Mat* (2019).

## Appendix A: Volatility of Ta oxides

The vapor pressures of the known Ta suboxides are summarized in Table A.1 and Table A.2, calculated using FactSage, when Ta, TaC or TaB<sub>2</sub> is exposed to oxygen. Based on these values, it is unlikely that TaO or TaO<sub>2</sub> are volatile in the experimental conditions tested and discussed in Chapter 3.

*Table A.1: Partial pressure of TaO<sub>2</sub> as a function of substrate and temperature, calculated using FactSage.*

| <b>TaO<sub>2</sub></b> | <b>1500°C</b>            | <b>1600°C</b>            | <b>1700°C</b>            | <b>1800°C</b>            |
|------------------------|--------------------------|--------------------------|--------------------------|--------------------------|
| <b>Ta</b>              | 1.20 x 10 <sup>-08</sup> | 9.88 x 10 <sup>-08</sup> | 6.54 x 10 <sup>-07</sup> | 3.57 x 10 <sup>-06</sup> |
| <b>TaC</b>             | 3.34 x 10 <sup>-09</sup> | 3.43 x 10 <sup>-08</sup> | 2.76 x 10 <sup>-07</sup> | 1.72 x 10 <sup>-06</sup> |
| <b>TaB<sub>2</sub></b> | 6.00 x 10 <sup>-09</sup> | 5.27 x 10 <sup>-08</sup> | 3.68 x 10 <sup>-07</sup> | 2.11 x 10 <sup>-06</sup> |

*Table A.2: Partial pressure of TaO as a function of substrate and temperature, calculated using FactSage.*

| <b>TaO</b>             | <b>1500°C</b>            | <b>1600°C</b>            | <b>1700°C</b>            | <b>1800°C</b>            |
|------------------------|--------------------------|--------------------------|--------------------------|--------------------------|
| <b>Ta</b>              | 2.35 x 10 <sup>-09</sup> | 1.91 x 10 <sup>-08</sup> | 2.05 x 10 <sup>-10</sup> | 6.77 x 10 <sup>-07</sup> |
| <b>TaC</b>             | 5.11 x 10 <sup>-11</sup> | 7.99 x 10 <sup>-10</sup> | 9.37 x 10 <sup>-09</sup> | 7.54 x 10 <sup>-08</sup> |
| <b>TaB<sub>2</sub></b> | 2.97 x 10 <sup>-10</sup> | 2.89 x 10 <sup>-09</sup> | 2.22 x 10 <sup>-08</sup> | 1.39 x 10 <sup>-07</sup> |

## Appendix B: Pyrometer Data for Resistive Heating System Experiments

Table B.1: Average and standard deviation temperature values recorded by the pyrometer for experiments conducted on (HfZrTiTaNb)<sub>X</sub> where X=C or B<sub>2</sub>. “\*” indicates sample tested from a different batch (Batch C2) than the 2- and 3.5-minute tests (Batch C3). “s” indicates a repeat experiment with a sample from the same powder batch but different pellet IDs (BW also tested for 2 and 3.5 mins.)

| Carbides       | pO <sub>2</sub> (% in Ar) |           |           |                    |            |   |                  |              |           |
|----------------|---------------------------|-----------|-----------|--------------------|------------|---|------------------|--------------|-----------|
| Nominal T (°C) | 0.1%O <sub>2</sub>        |           |           | 0.5%O <sub>2</sub> |            |   | 1%O <sub>2</sub> |              |           |
|                | 5 min.                    | 10 min.   | 15 min.   | 2 min.             | 3.5 min.   | 5 min.  | 2 min.           | 3.5 min.     | 5 min.    |
| 1500           | 1497 ± 20                 | 1497 ± 14 | 1499 ± 15 | 1505 ± 17          | 1510 ± 16  | 1511 ± 15   | 1509 ± 16        | 1521.51 ± 12 | 1509 ± 22 |
| 1700           | 1698 ± 56                 | 1700 ± 57 | 1703 ± 56 | 1744 ± 55          | 1728 ± 63  | 1722 ± 60<br>1707 ± 33*                             | 1712 ± 51        | 1725 ± 39    | 1715 ± 34 |
| 1800           | 1798 ± 85                 | 1804 ± 85 | 1798 ± 77 | 1854 ± 140         | 1849 ± 119 | 1836 ± 88   |                  |              |           |
| Borides        | pO <sub>2</sub> (% in Ar) |           |           |                    |            |   |                  |              |           |
| Nominal T (°C) | 0.1%O <sub>2</sub>        |           |           | 0.5%O <sub>2</sub> |            |   | 1%O <sub>2</sub> |              |           |
|                | 5 min.                    | 10 min.   | 15 min.   | 2 min.             | 3.5 min.   | 5 min.  | 2 min.           | 3.5 min.     | 5 min.    |
| 1500           | 1494 ± 11<br>(6 min.)     | 1495 ± 12 | 1496 ± 10 | 1504 ± 10          | 1504 ± 10  | 1504 ± 10   | 1498 ± 9         | 1499 ± 9     | 1498 ± 8  |
| 1700           | 1688 ± 36                 | 1694 ± 36 | 1696 ± 36 | 1703 ± 37          | 1707 ± 25  | 1703 ± 27<br>(BW)<br>1699 ± 38 <sup>s</sup><br>(BY) | 1700 ± 39        | 1701 ± 38    | 1701 ± 26 |
| 1800           | 1794 ± 60                 | 1789 ± 60 | 1802 ± 65 | 1795 ± 87          | 1801 ± 81  | 1801 ± 76   |                  |              |           |

Table B.2: Average and standard deviation temperature values recorded by the pyrometer for resistive heating experiments conducted on ZrC.

| ZrC            | pO <sub>2</sub> (% in Ar) |                        |            |                    |                  |
|----------------|---------------------------|------------------------|------------|--------------------|------------------|
| Nominal T (°C) | 0.1%O <sub>2</sub>        |                        |            | 0.5%O <sub>2</sub> | 1%O <sub>2</sub> |
|                | 5 min.                    | 10 min.                | 15 min.    | 5 min.             | 5 min.           |
| 1500           |                           | 1500 ± 14<br>(10.5min) |            |                    | 1511 ± 12        |
| 1700           | 1696 ± 48                 | 1696 ± 50              |            | 1700 ± 57          | 1708 ± 43        |
| 1800           |                           |                        | 1805 ± 105 | 1804 ± 90          | 1802 ± 66        |

Table B.3: Average and standard deviation temperature values recorded by the pyrometer for resistive heating experiments conducted on ZrB<sub>2</sub>.

| ZrB <sub>2</sub> | pO <sub>2</sub> (% in Ar) |                    |                  |
|------------------|---------------------------|--------------------|------------------|
| Nominal T (°C)   | 0.1%O <sub>2</sub>        | 0.5%O <sub>2</sub> | 1%O <sub>2</sub> |
|                  | 15 min.                   | 5 min.             | 5 min.           |
| 1500             | 1504 ± 12                 | 1504 ± 9           | 1504 ± 9         |
| 1700             | 1697 ± 46                 | 1690 ± 51          | 1701 ± 35        |
| 1800             | 1803 ± 99                 |                    |                  |

Table B.4 Average and standard deviation temperature values recorded by the pyrometer for resistive heating experiments conducted on the group IV+V+VI and group IV+VI carbides and diborides for exposures at a nominal temperature of 1700 °C in 1%O<sub>2</sub> for five minutes.

| Composition                | Temperature (°C) |
|----------------------------|------------------|
| (HfZrTiTaMo)C              | 1707 ± 23        |
| (HfZrTiMoW)C               | 1720 ± 17        |
| (HfZrTiTaMo)B <sub>2</sub> | 1716 ± 25        |
| (HfZrTiMoW)B <sub>2</sub>  | 1709 ± 29        |

## Appendix C: Detailed Experimental Results from Oxidation Studies on (HfZrTiTaNb)C and (HfZrTiTaNb)B<sub>2</sub>

### C.1: (HfZrTiTaNb)C

#### 1500°C

Samples tested at 1500°C in all partial pressures of oxidation exhibited similar oxidation behavior, composition and morphology (Figure C.1). At short times, oxidation along grain boundaries were observed, consisting of initially Hf and Zr oxides, although the other elements also appear to have started oxidizing (Figure C.2, Figure C.4). The morphologies observed after 15 minutes in 0.1%O<sub>2</sub> is like that observed at 1%O<sub>2</sub> at all times. The evolution of the microstructure at 0.1%O<sub>2</sub> then provides insight as to how the material oxidizes via intergranular oxidation.

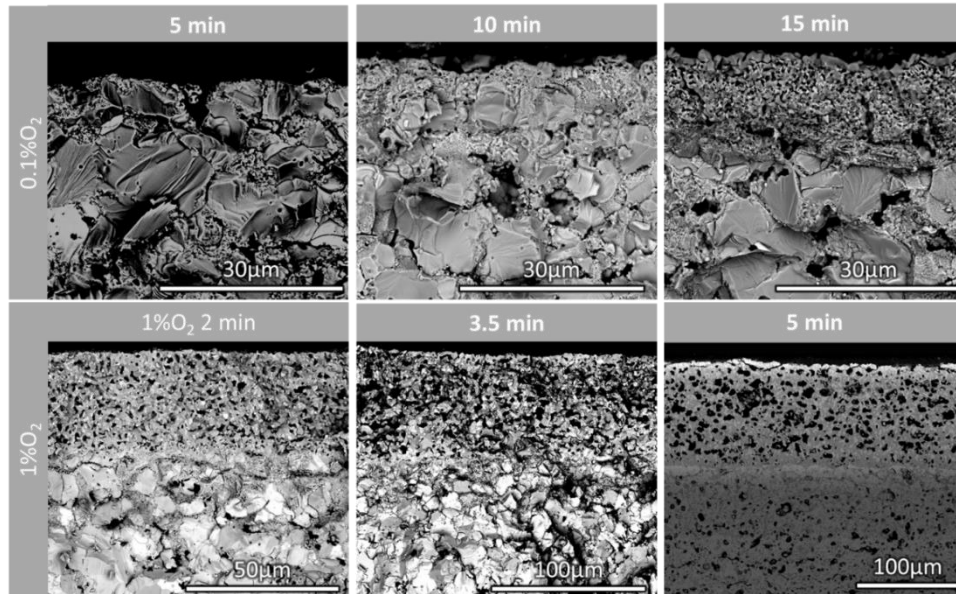


Figure C.1: (HfZrTiTaNb)C samples oxidized in (top) 0.1%O<sub>2</sub> and (bottom) 1%O<sub>2</sub>.

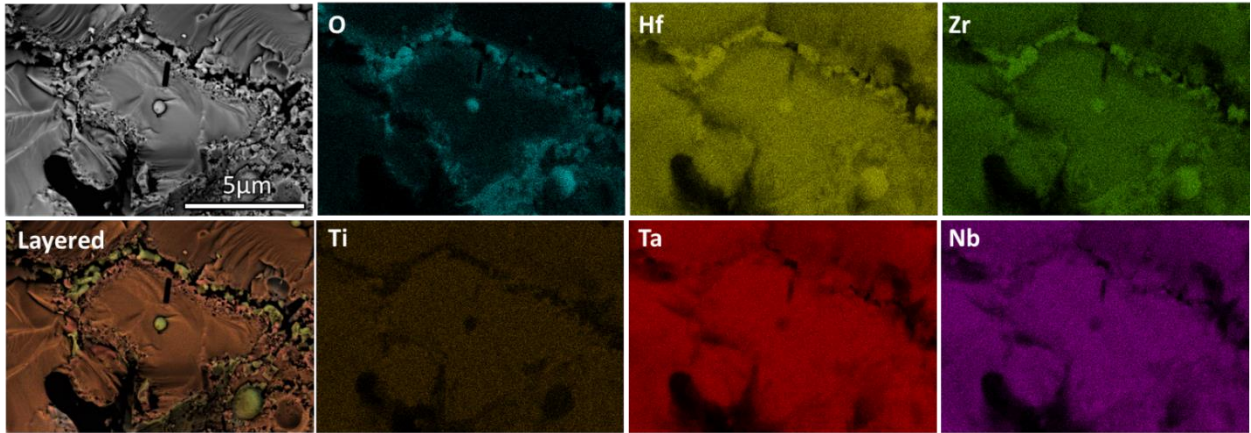


Figure C.2: Detail of oxide formed around a grain in (HfZrTiTaNb)C in the intergranularly oxidized region directly below the external scale at short times (2 minutes) in 1%O<sub>2</sub> at 1500 °C. The layered image superimposes results from all six elements.

Point EDS analysis near the surface on a carbide specimen oxidized for 5 minutes in 0.1%O<sub>2</sub> indicates that the oxygen rich regions are rich in group IV elements (Figure C.3). The oxides appear to be discontinuous and an oxygen gradient is apparent in the Hf/Zr depleted regions, or regions enriched in Ti, Ta and Nb.

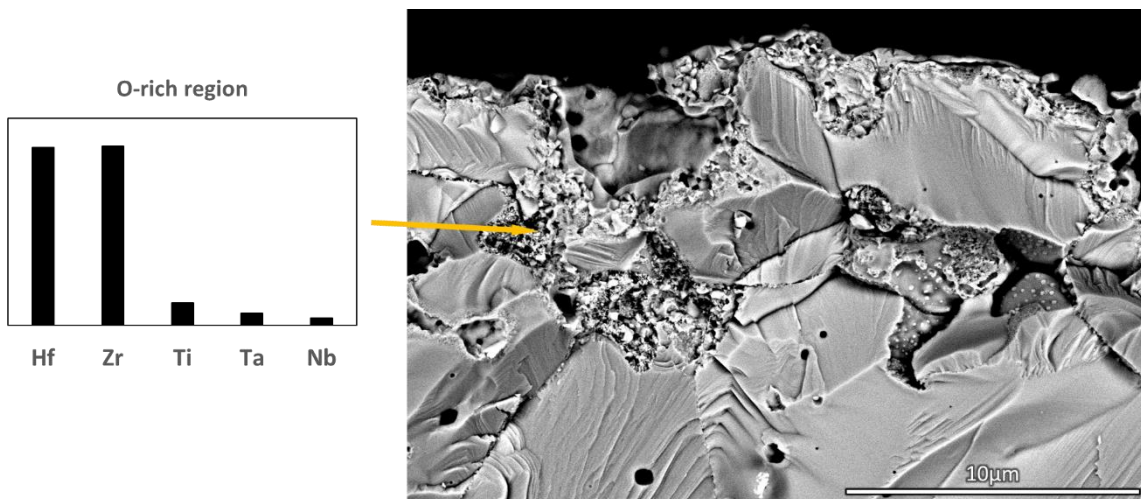


Figure C.3: Composition of intergranular oxide near the surface of (HfZrTiTaNb)C oxidized for 5 minutes in 0.1%O<sub>2</sub> at 1500 °C.

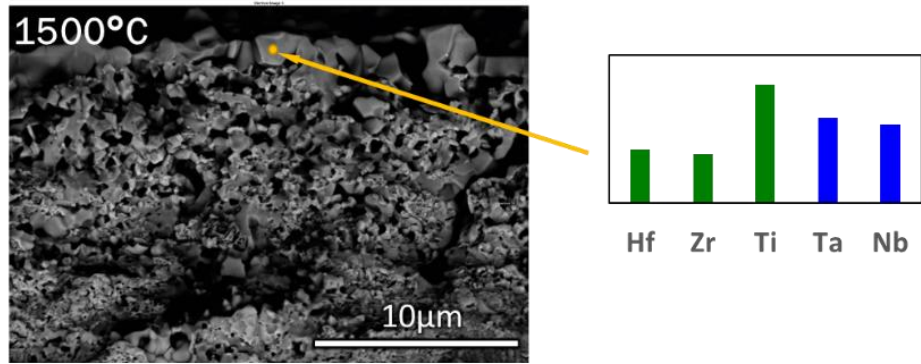


Figure C.4: Point EDS analysis near the surface on (HfZrTiTaNb)C exposed at 1500 °C in 0.1%O<sub>2</sub> after 15 minutes.

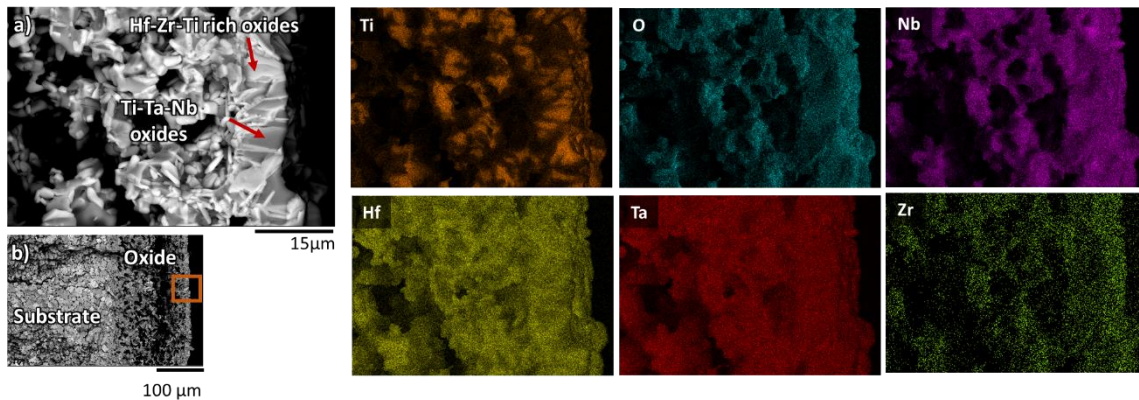


Figure C.5: (a) Backscatter electron image and EDS maps of the cross-section of (HfZrTiTaNb)C oxidized at 1500 °C in 1%O<sub>2</sub> for 5 minutes. (b) shows a lower magnification backscatter electron image at lower magnification from the same area, orange outline shows region in (a). Oxide/gas interface is to the right in this image.

Analysis of the composition of the external scale in the hot zone shows that Ta and Nb have both oxidized as well (Figure C.4). A combined consideration of the EDS data from the intergranular regions and external scale suggest that Group IV elements oxidize first, followed by Ta and Nb, respectively. This order is consistent with the relative thermodynamic stabilities of the oxides as shown in the Ellingham Diagram in the previous chapter.

The external oxide scale formed on samples at 1500 °C after 15 minutes in 0.1%O<sub>2</sub> and at all times in 1%O<sub>2</sub> was multi-phase and contained both Group IV (Hf, Zr, Ti) and Group V (Ta, Nb) elements. XRD analyses for the longest times and the bounding pO<sub>2</sub> conditions are shown in Figure C.6. Matches shown are the best available matches informed by EDS data, but ionic substitutions are likely and expected<sup>105</sup>, i.e., Ta can substitute on Nb sites, while Hf can substitute on Zr sites (or vice versa). The XRD patterns shown in Figure C.6 highlight the complex nature of determining the oxide phases present. Overlaps exist for possible compounds. Therefore, XRD analysis serves to provide i) an indication that complex oxides are possible, and ii) a comparison of product phases across different oxidation conditions. In this case, we see similar compounds present, although at the higher pO<sub>2</sub>, more peaks associated with Ti(Nb,Ta)O<sub>x</sub> appear.

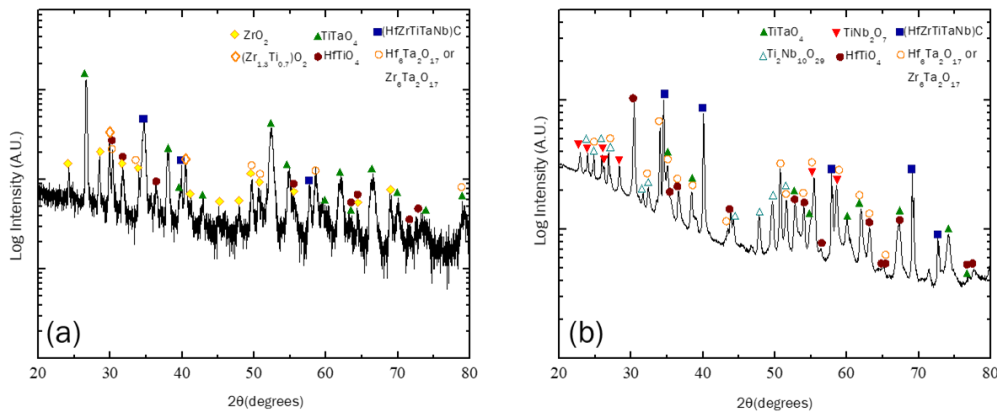


Figure C.6: X-ray diffraction patterns, plotted as log intensity versus two-theta, collected from carbide samples oxidized for (a) 15 minutes in 0.1%O<sub>2</sub> and (b) 5 minutes (1%O<sub>2</sub>). (a) was obtained using MF = microfocused optics.

## 1700 °C

SEM and EDS results for (HfZrTiTaNb)C exposed in 0.1% and 1% O<sub>2</sub> are shown in Figure C.7, Figure C.8, Figure C.9). In 0.1% O<sub>2</sub> at this temperature, there is evidence of

intragranular oxidation and an external, surface oxide scale that appears to grow with time for (HfZrTiTaNb)C, although intergranular oxidation is still observed. The external scale contains Ta and the group IV elements, is highly porous and does not form a continuous layer. Beneath the Ta-containing external scale, a Nb-rich, O-deficient layer is seen, which is comparable to the morphology seen at 1800 °C (see next section).

In 1% O<sub>2</sub> the surface oxide does not change much with time up to 5 minutes, but the grains beneath the surface oxidize further with time in addition to deeper penetration along grain boundaries. The intergranular scale formed becomes more porous as seen in the intermediate times, and increasingly enriched in the group V elements. The oxidized region at 1700 °C in 1%O<sub>2</sub> after five minutes approaches a morphology similar to that observed at 1500 °C.

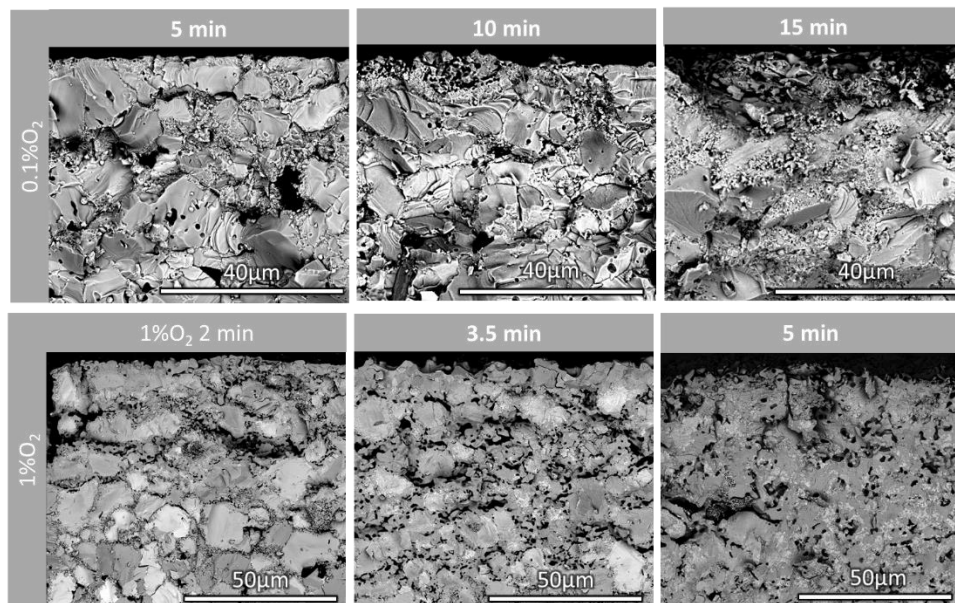


Figure C.7: Backscattered images of the oxidized (HfZrTiTaNb)C cross sections. (top) 0.1%O<sub>2</sub>, bottom 1%O<sub>2</sub>.

The morphology shown in Figure C.7 is mostly different from the 1500 °C cases, given the extensive intergranular oxidation. At 1500 °C, grain boundary oxidation was only observed at short times in all pO<sub>2</sub>s tested. At 1700 °C, grain boundary oxidation is the dominant morphology at all times. The grains near the surface approach complete oxidation after 5

minutes in 1%O<sub>2</sub>. The intergranular oxides are rich in group IV elements (Figure C.8) after two minutes oxidation in 1%O<sub>2</sub>. After five minutes the grains oxidize further, group IV elements and Ta are observed in the oxide (Figure C.9). The O deficient region is still enriched in Nb. The oxygen gradient observed in the oxygen maps at the short times indicate that these materials oxidize by oxygen transport into the grain.

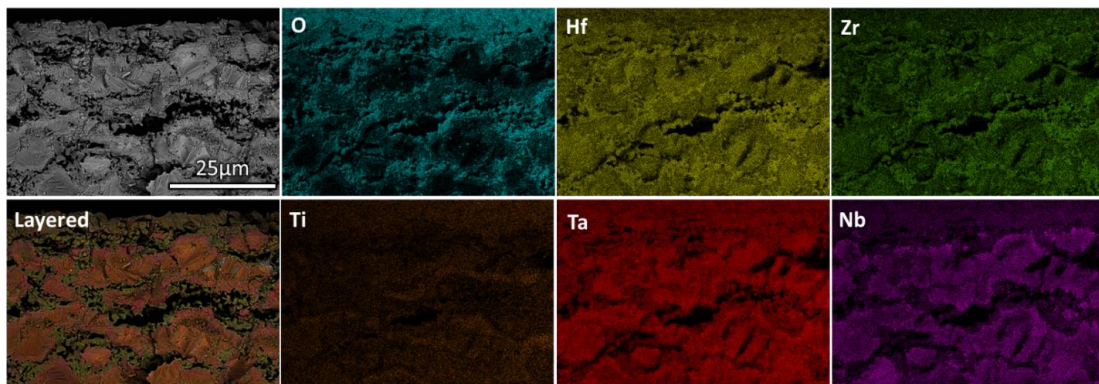


Figure C.8: Back-scattered electron micrograph and representative EDS maps showing the composition of the oxides along grain boundaries for (HfZrTiTaNb)C oxidized at 1700 °C in 1%O<sub>2</sub> for 2 minutes. The layered image superimposes results from all five elements (Hf, Zr, Ti, Ta and Nb).

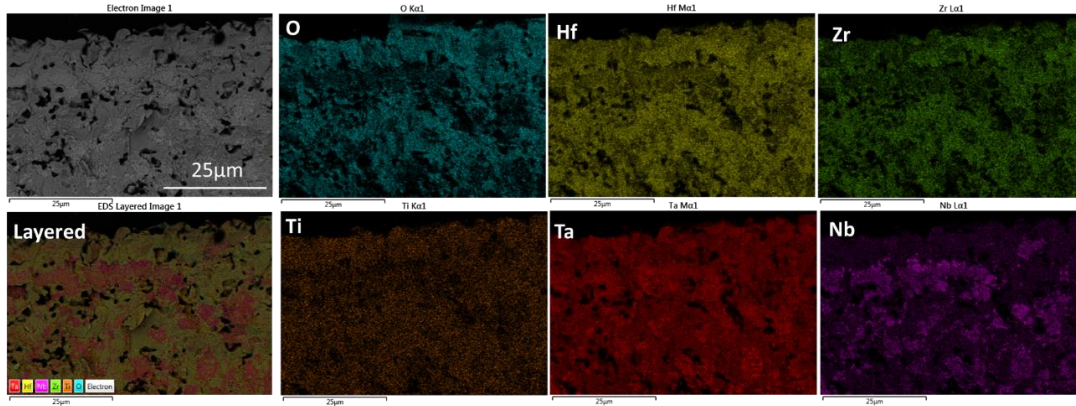


Figure C.9: Back-scattered electron micrograph and representative EDS maps showing the composition of the oxides along grain boundaries for (HfZrTiTaNb)C oxidized at 1700 °C in 1%O<sub>2</sub> for 5 minutes. The layered image superimposes results from all five elements (Hf, Zr, Ti, Ta and Nb).

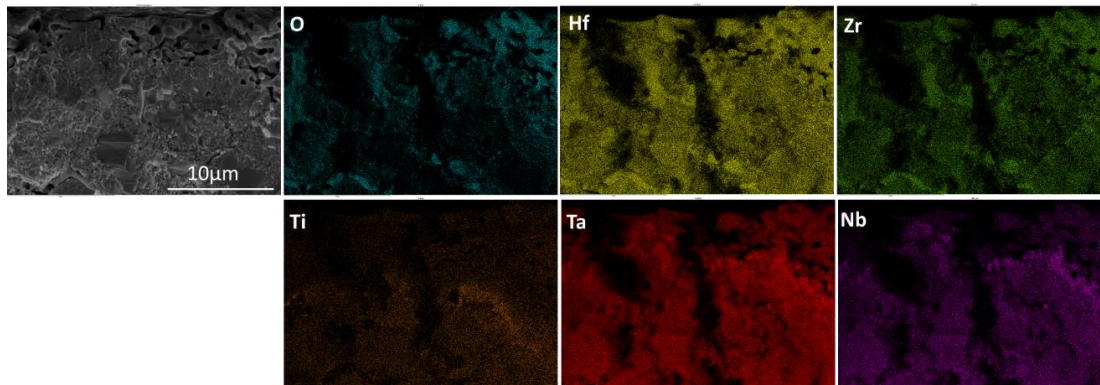


Figure C.10: Secondary electron micrograph and representative EDS maps showing the composition of the oxides along grain boundaries for (HfZrTiTaNb)C oxidized at 1700 °C in 0.1%O<sub>2</sub> for 15 minutes.

X-ray diffraction patterns (Figure C.11) confirm that group V containing oxides form. The oxidized regions are comprised of multiple phases. Similar product phases are seen for both partial pressures of oxygen tested, with the exception of TiTa<sub>2</sub>O<sub>7</sub> for the sample tested in 1%O<sub>2</sub>, which is apparent in the microstructure (Figure C.12) in plan view.

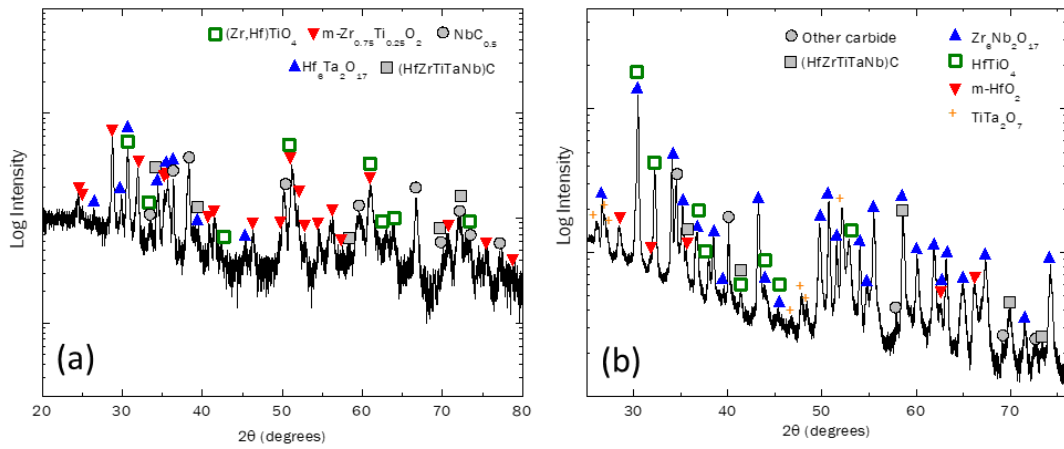


Figure C.11: X-ray diffractograms obtained from (HfZrTiTaNb)C oxidized at 1700 °C (a) 0.1%O<sub>2</sub> for 15 minutes (micro-focused optics) and (b) 1% O<sub>2</sub> for 5 minutes.

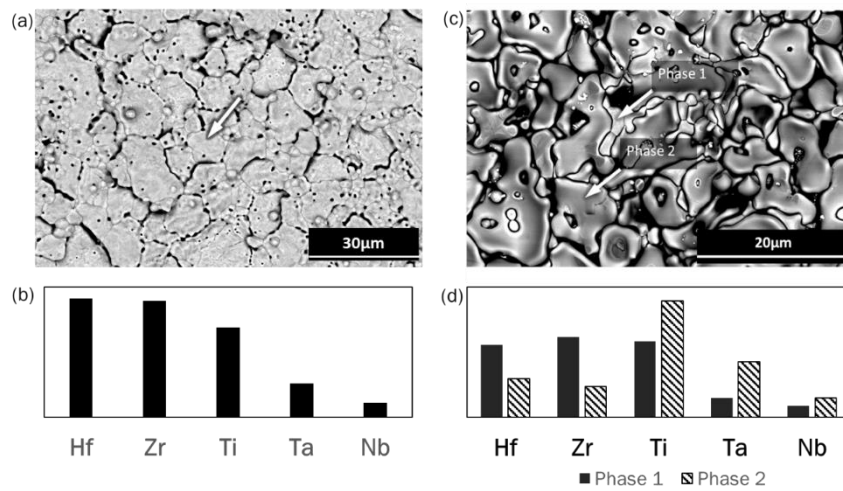


Figure C.12: Plan view for carbides oxidized at 1700 °C in (a)-(b) 0.1%O<sub>2</sub> for 15 minutes (c)-(d) 1% O<sub>2</sub> for 5 minutes. Column charts (b) and (d) show point EDS analysis for phases indicated by arrows.

## 1800 °C

For the samples tested in 0.1%O<sub>2</sub>, an external oxide scale (or oxidized region) appears to grow with time (Figure C.13). Minimal grain boundary oxidation can be seen starting 10 minutes, and an external oxide scale is observed.

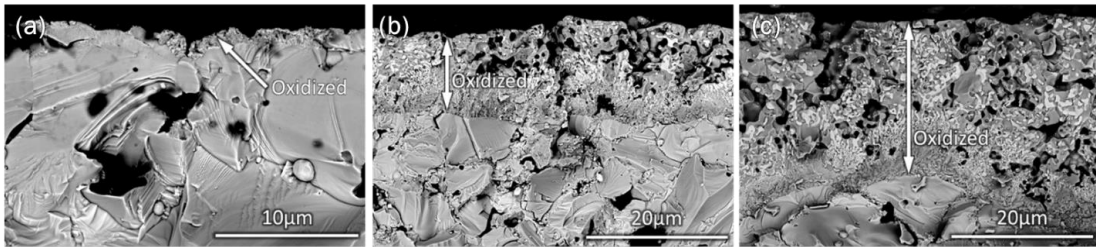


Figure C.13: Microstructural evolution with time at 1800 °C in 0.1%O<sub>2</sub> for (a) 5, (b) 10 and (c) 15 minutes.

The oxidized regions are composed of a Group IV rich oxide and Group V rich carbide, as shown by the EDS maps for the 15-minute case (Figure C.14). A Ti-rich region at the oxide/substrate interface is also observed.

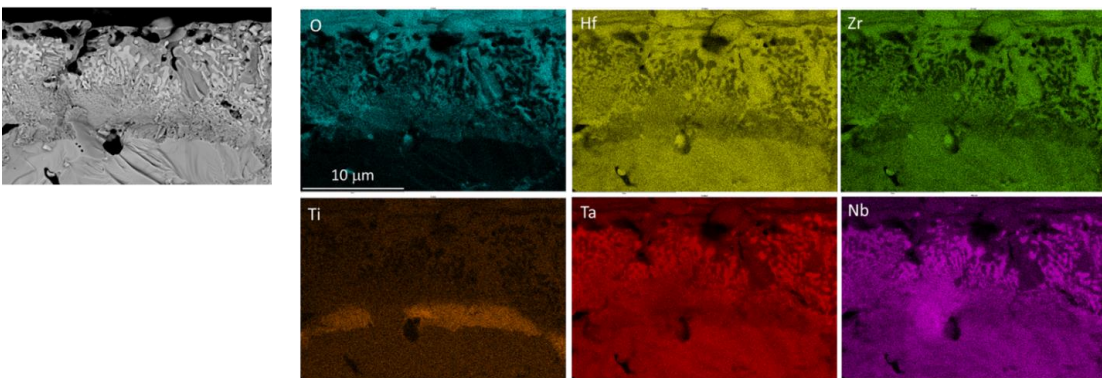


Figure C.14: Backscattered electron image and EDS maps for (HfZrTiTaNb)C oxidized at 1800 °C in 0.1%O<sub>2</sub> for fifteen minutes.

At short times (5 minutes) and in 0.1%O<sub>2</sub>, a continuous external scale is not readily apparent. At higher magnifications, EDS analysis indicates oxygen signal in the carbide, suggesting oxygen dissolution in the substrate occurs prior to external scale formation. The sample (Figure C.14) exhibits at least a two-phase scale, one of which is oxygen deficient. This oxygen-deficient region is also rich in Ta and Nb. In addition, a Ti-rich region can be observed at the oxide-substrate interface. The Ti-rich band is also observed in the ten-minute case. A TEM foil was prepared by FIB from the pyrometer sighting zone of the ten-minute sample. The ten-minute sample was chosen due to the thickness of the oxidized region being smaller than that at 15 minutes and therefore easier to perform a FIB lift-out of a region which also includes the Ti-rich zone.

The oxidized region formed on (HfZrTiTaNb)C at 1800 °C in 0.5%O<sub>2</sub> exhibits both intergranular and an external oxide scale. The scale appears to be mostly dense, although not as dense as the 0.1%O<sub>2</sub> case (Figure C.15). Oxidation via grain boundaries appears to penetrate deeper into the material in the 0.5%O<sub>2</sub> case, compared to the 0.1%O<sub>2</sub>. The time evolution of the oxide scale for the 0.5%O<sub>2</sub> case is shown in Figure C.16. The external scale due to bulk oxidation grows with time, but no significant change in the extent of intergranular oxidation is seen.

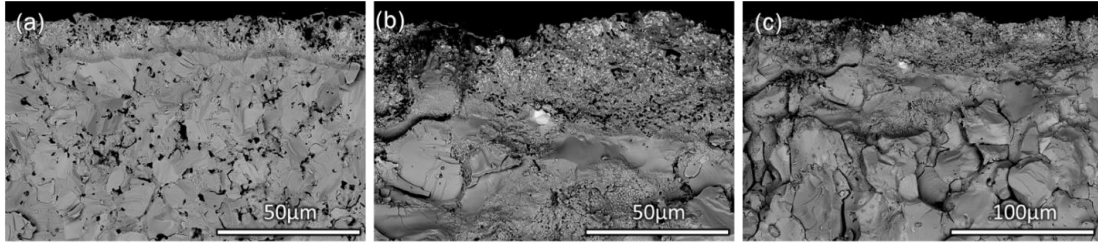


Figure C.15: Comparison of microstructure of the oxidized regions formed after exposing (HfZrTiTaNb)C at 1800 °C in 0.1%O<sub>2</sub> and 0.5%O<sub>2</sub>. Backscattered images of (HfZrTiTaNb)C oxidized in (a) 0.1%O<sub>2</sub> for 15 minutes, and (b)-(c) 0.5%O<sub>2</sub> oxidized for 5 minutes.

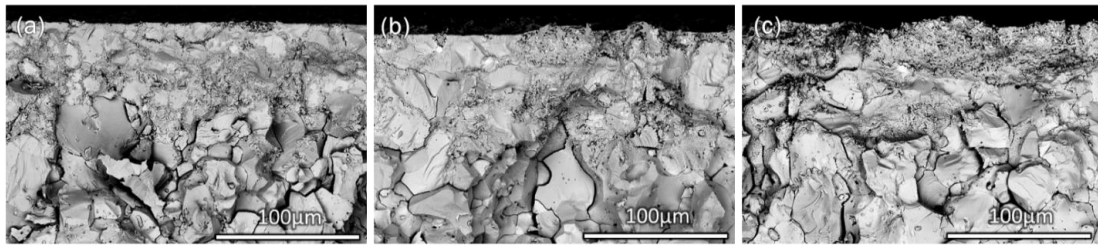


Figure C.16: Microstructural evolution of the external oxide scale formed on (HfZrTiTaNb)C at 1800 °C in 0.5%O<sub>2</sub> for (a) 2, (b) 3.5 and (c) 5 minutes.

In addition, the Ti-rich band is again observed beneath the external oxide scale (Figure C.17). The scale consists of Group IV and Group V regions, albeit on a finer scale. The external scale retains O-deficient, group V -rich phases. The morphology is comparable to the 0.1%O<sub>2</sub> case after 10 and 15 minutes.

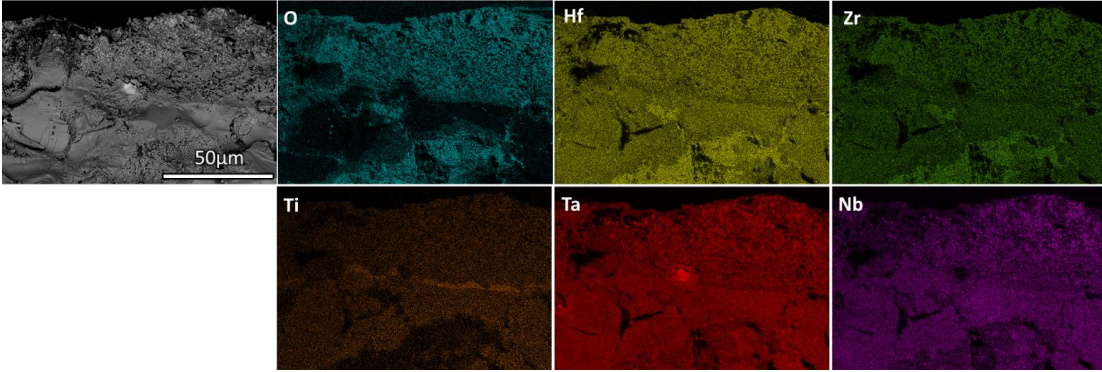


Figure C.17: Backscattered electron image and EDS maps of the oxidized region in cross-section formed on  $(\text{HfZrTiTaNb})\text{C}$  at  $1800\text{ }^\circ\text{C}$  in  $0.5\%\text{O}_2$  for 15 minutes. Note the Ti-rich band at the oxide/substrate interface

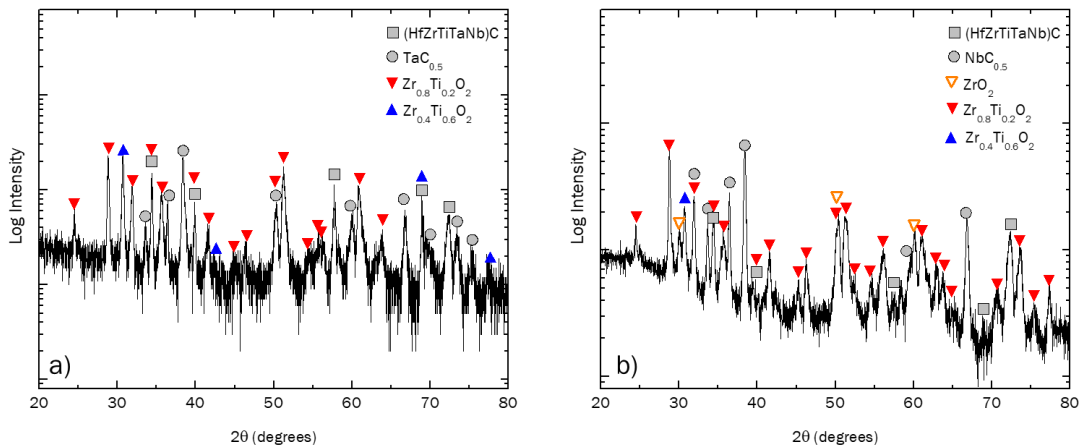


Figure C.18: X-ray diffractograms obtained from  $(\text{HfZrTiTaNb})\text{C}$  oxidized at  $1800\text{ }^\circ\text{C}$  (a)  $0.1\%\text{O}_2$  for 15 minutes (micro-focused optics) and (b)  $0.5\%\text{O}_2$  for 5 minutes.

## C.2: $(\text{HfZrTiTaNb})\text{B}_2$

### 1500 °C

The oxide morphology exhibits a porous scale and large voids, particularly at longer times. The oxidized region appears consists of an outer scale that grows with time and faceted grains at the “oxide”/substrate interface. EDS analysis indicates that partially oxidized grains exist at the interface. The different layers appear to be similar across different  $p\text{O}_2$ , only varying in relative thicknesses.

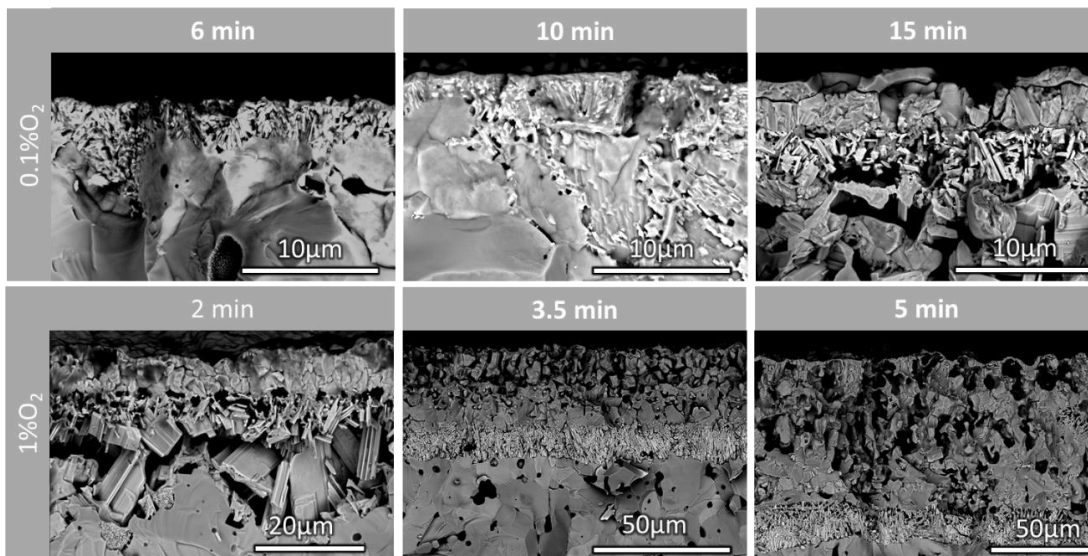


Figure C.19: Time and partial pressure dependence of the morphology of the oxidized regions formed on  $(\text{HfZrTiTaNb})\text{B}_2$  after exposure at 1500 °C in (top) 0.1%O<sub>2</sub> and (bottom) 1%O<sub>2</sub>

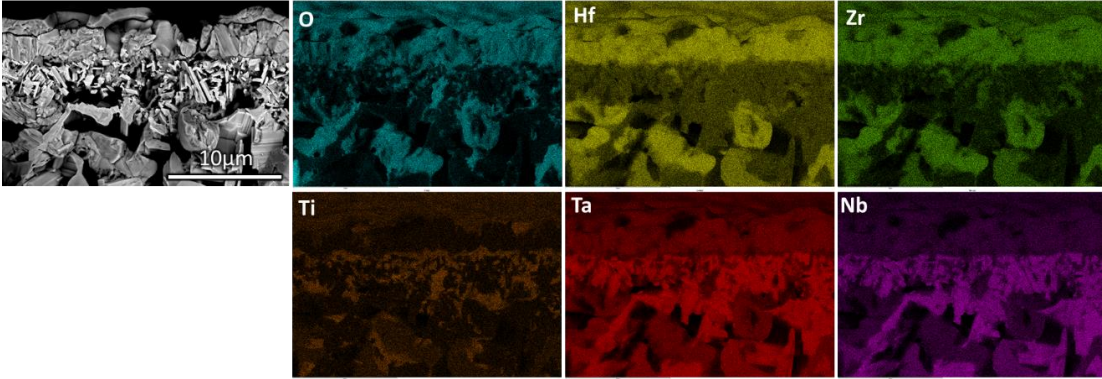


Figure C.20: Elemental EDS maps for  $(\text{HfZrTiTaNb})\text{B}_2$  oxidized in  $0.1\% \text{O}_2$  at  $1500^\circ\text{C}$  for 15 minutes.

In  $0.1\% \text{O}_2$ , Hf, Zr and Ti have oxidized, whereas the oxygen deficient grains are Ta and Nb rich. The surface of the sample exhibits a Hf/Zr rich scale.

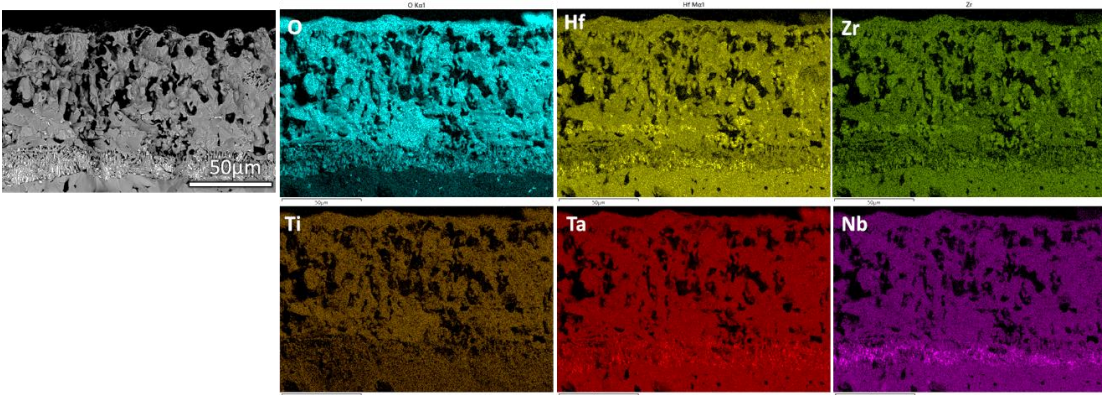


Figure C.21: Elemental EDS maps for  $(\text{HfZrTiTaNb})\text{B}_2$  oxidized in  $1\% \text{O}_2$  at  $1500^\circ\text{C}$  for five minutes.

In  $1\% \text{O}_2$  and at  $1500^\circ\text{C}$  at the longest time tested, the oxide/substrate interface region consists of Nb and Ta rich grains, above which is a multi-phase oxide apparently containing not only the Group IV elements but also Ta and Nb. Oxidation products at both oxygen partial pressures are similar (Figure C.22), with the addition of Group V elements at the higher partial pressure.

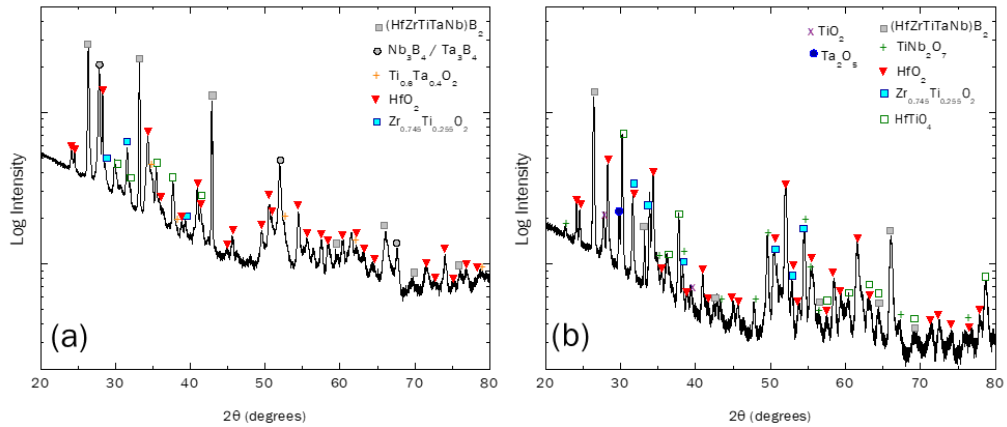
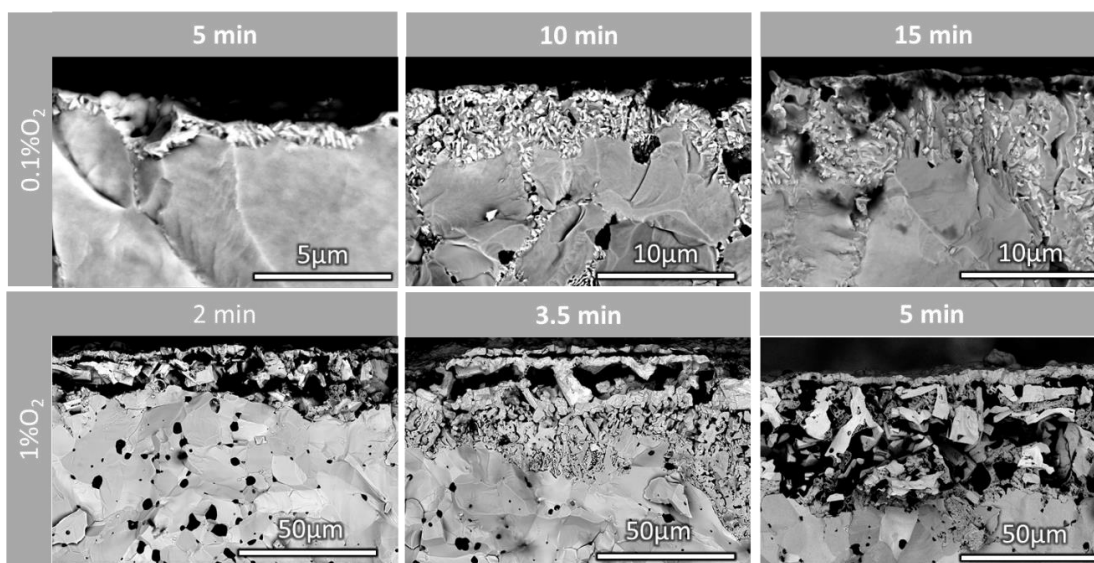


Figure C.22: XRD patterns obtained from  $(\text{HfZrTiTaNb})\text{B}_2$  obtained after exposure in (a)  $0.1\% \text{O}_2$  for 15 minutes and (b)  $1\% \text{O}_2$  for five minutes.

### 1700°C

In  $0.1\% \text{O}_2$  the oxide scale is dense and consists of oxidized regions around partially oxidized grains (Figure C.23). These latter grains consist of Ta and Nb. Intergranular oxidation is observed. The regions near or directly beneath the oxidized region does not contain boron carbide in any significant fraction.



*Figure C.23: Time and partial pressure dependence of the morphology of the oxidized regions*

The oxide is rich in Hf, Zr and Ti, and poor in Ta and Nb (Figure C.24), exhibiting similar trends as seen in most of the conditions tested. The morphology observed after oxidation in 0.1%O<sub>2</sub> is reminiscent of the microstructure seen in the oxidized carbide at 1800 °C in 0.1%O<sub>2</sub>, and at the oxide/substrate interface in (HfZrTiTaNb)C samples tested at 1700 °C in 0.1%O<sub>2</sub>.

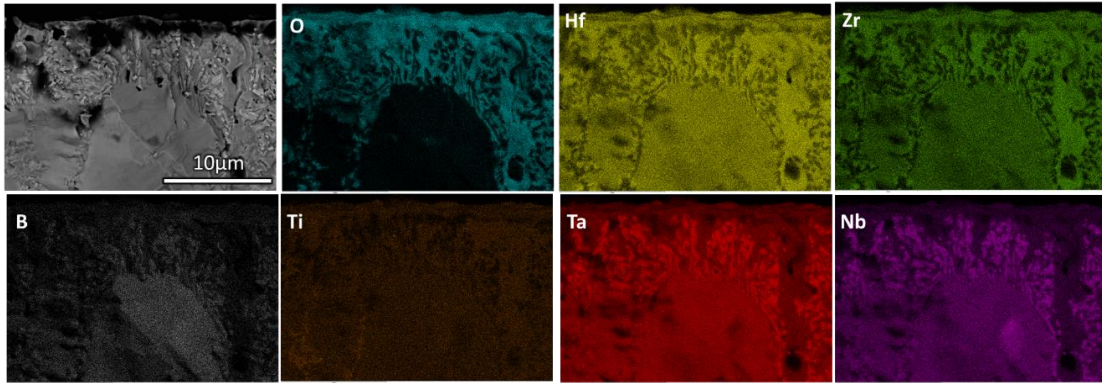


Figure C.24: Elemental EDS maps for  $(\text{HfZrTiTaNb})\text{B}_2$  oxidized in  $0.1\% \text{O}_2$  at  $1700^\circ \text{C}$  for 15 minutes.

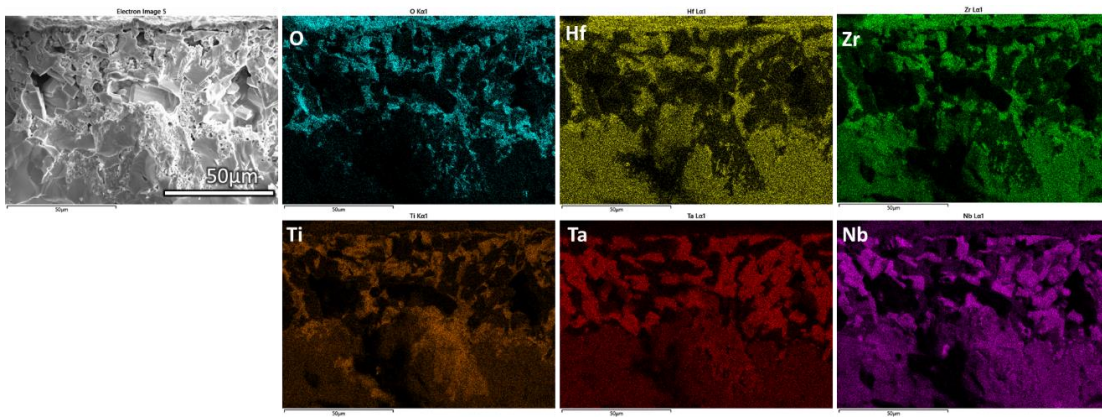


Figure C.25: Elemental EDS maps for  $(\text{HfZrTiTaNb})\text{B}_2$  oxidized in  $1\% \text{O}_2$  at  $1700^\circ \text{C}$  for five minutes.

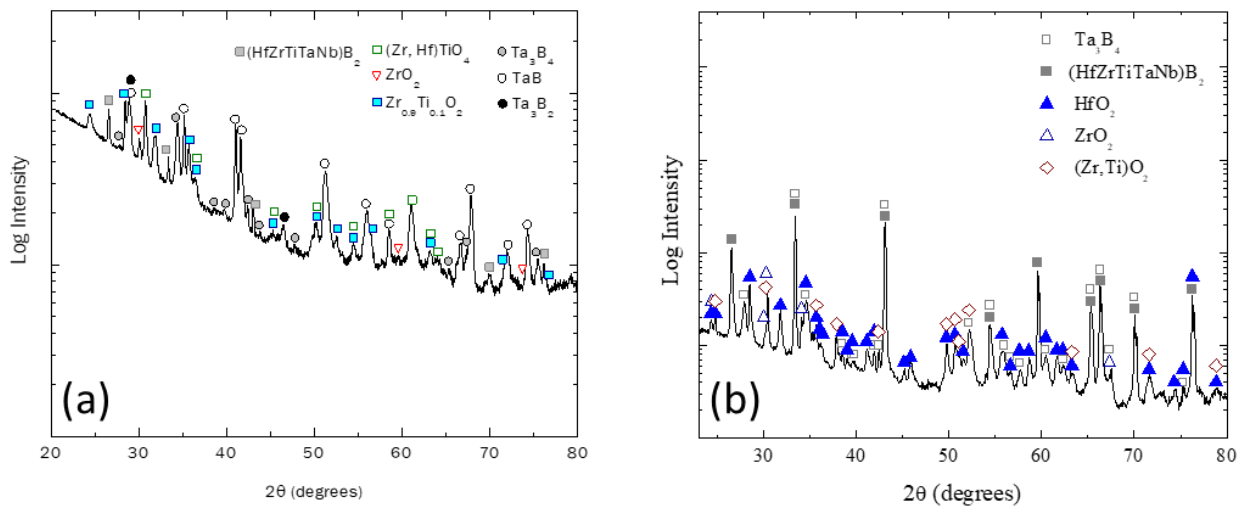


Figure C.26: XRD patterns for the longest times in (a) 0.1%O<sub>2</sub> and (b) 1%O<sub>2</sub>.

## 1800 °C

As was the case with the carbides, the scale is denser at 1800 °C compared to the 1500 °C and 1700 °C. At the fracture location, the oxidized region at the surface has a scale of varying thickness, with the thickest being near the outer edge of the sample (Figure C.28). At 0.5%O<sub>2</sub>, an external scale with morphology like the 0.1% O<sub>2</sub> cases is observed, along with intergranular oxidation. The oxide scale formed under these conditions are reminiscent of the morphology observed on the carbides tested under similar conditions. The elemental EDS maps (Figure C.29 and Figure C.30) show a morphology very similar to that seen in the carbide: an interpenetrating oxide and boride microstructure, wherein the oxide is mostly dense and fills the region around boride grains rich in Ta and Nb. XRD results (Figure C.31) confirm group IV-rich oxides and group V-rich borides.

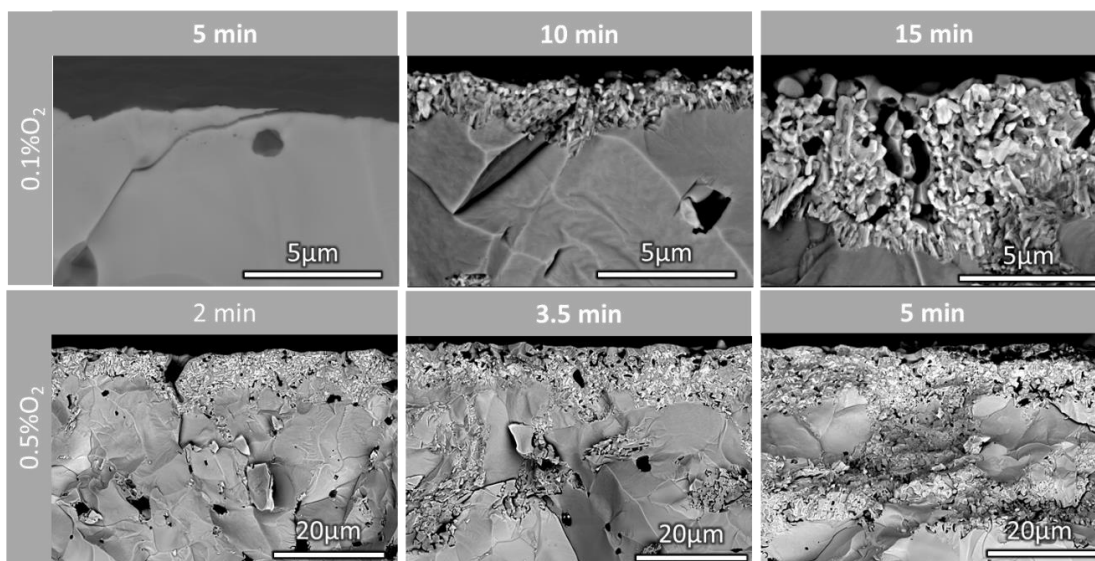


Figure C.27:  $(\text{HfZrTiTaNb})\text{B}_2$  exposed to  $1800\text{ }^\circ\text{C}$  in  $0.1\%$  and  $0.5\%$   $\text{O}_2$ . Images show time and partial pressure dependence of the morphology of the oxidized regions.

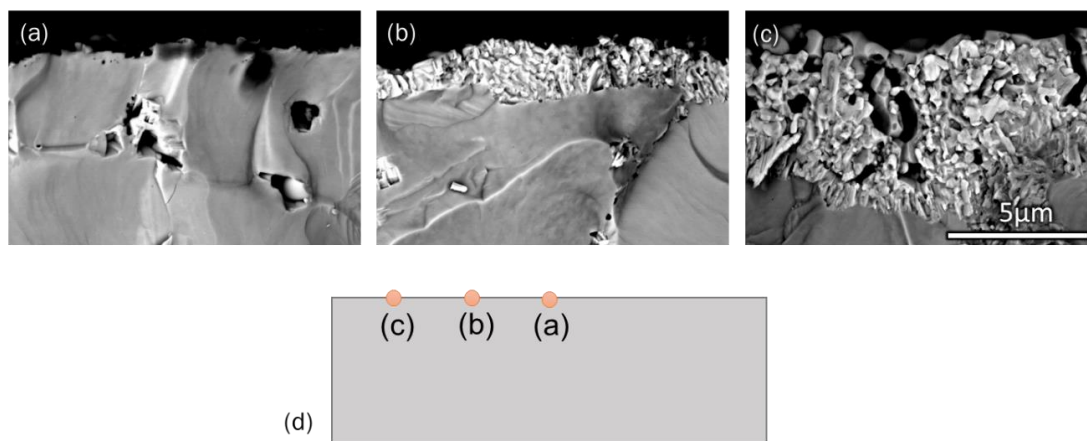


Figure C.28: Backscattered electron images of a  $(\text{HfZrTiTaNb})\text{B}_2$  sample in cross-section, oxidized in  $0.1\% \text{O}_2$  at  $1800\text{ }^\circ\text{C}$  for 15 minutes. Image (a) is in the middle of the cross-section at the oxide-gas interface, (b) is midway between the middle and outer edge of the cross-section, and (c) is closer to the edge. A schematic is shown in (d) of the cross-section of the sample, with the approximate locations of (a), (b) and (c).

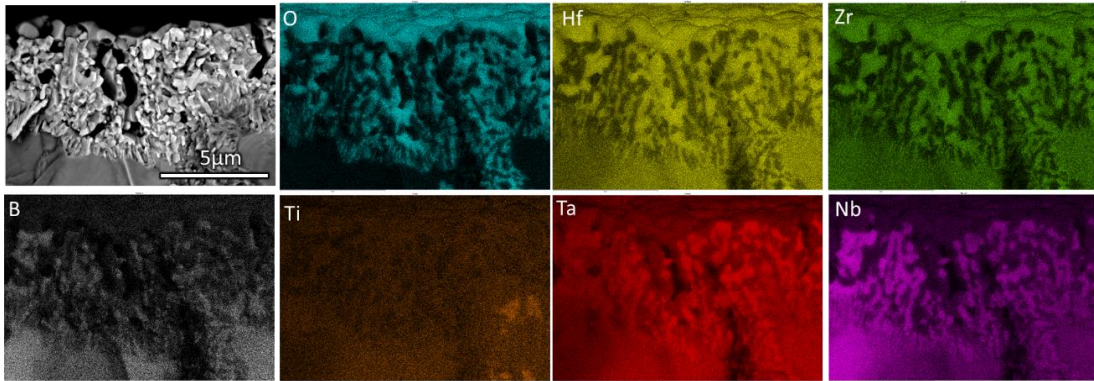


Figure C.29: Backscattered electron images of a  $(\text{HfZrTiTaNb})\text{B}_2$  sample in cross-section, oxidized in  $0.1\% \text{O}_2$  at  $1800^\circ\text{C}$  for 15 minutes along with elemental EDS maps.

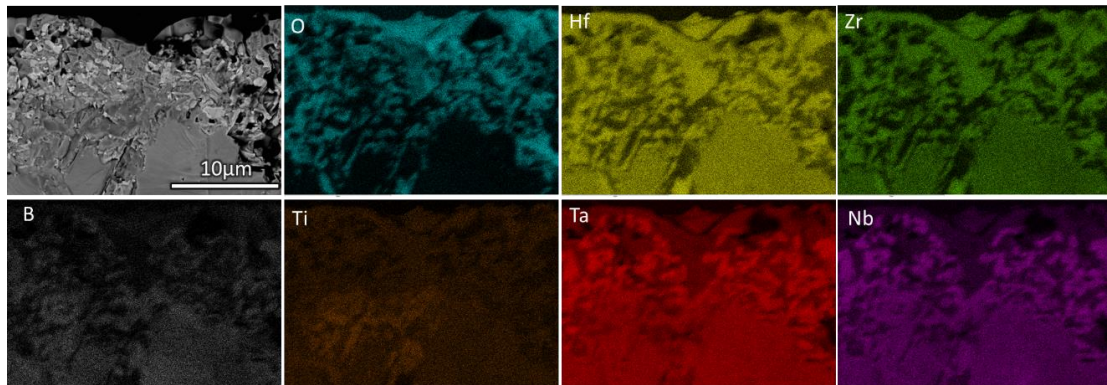


Figure C.30: Backscattered electron images of a  $(\text{HfZrTiTaNb})\text{B}_2$  sample in cross-section, oxidized in  $0.5\% \text{O}_2$  at  $1800^\circ\text{C}$  for 5 minutes along with elemental EDS maps.

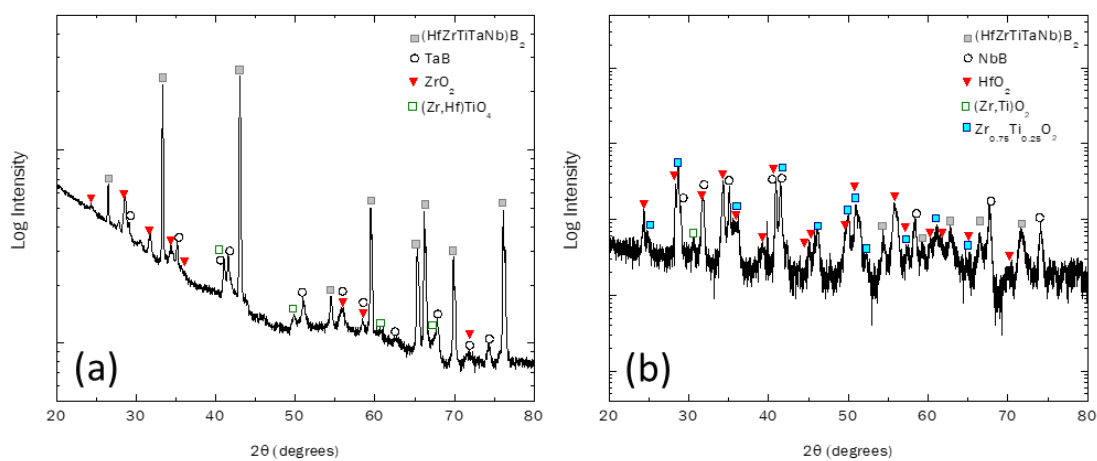


Figure C.31: XRD patterns for  $(\text{HfZrTiTaNb})\text{B}_2$  oxidized at  $1800^\circ\text{C}$  in (a)  $0.1\%\text{O}_2$  for 15 minutes and (b) (obtained using micro-focused optics)  $0.5\%\text{O}_2$  for 5 minutes.